EXPERIMENTAL STUDY OF THE PROPERTIES OF THE HIGGS BOSON

Richard David Mudd

Thesis submitted for the degree of
Doctor of Philosophy

Particle Physics Group,
School of Physics and Astronomy,
University of Birmingham.

January 25, 2016

Abstract

Measurements of Higgs boson production and decay rates are presented using the proton-proton collision data collected by the ATLAS experiment during LHC Run I, corresponding to 4.5 fb^{-1} at $\sqrt{s} = 7$ TeV and 20.3 fb^{-1} at $\sqrt{s} = 8$ TeV. Under certain assumptions, the coupling strengths of the Higgs boson to Standard Model particles are also probed.

The $H \to ZZ^{(*)} \to 4\ell$ final state, where $\ell = e, \mu$, is discussed in detail, and is observed with a significance corresponding to 8.1 standard deviations. The Higgs boson production rate, relative to the Standard Model prediction, is measured to be $\mu = 1.44^{+0.40}_{-0.33}$ at the ATLAS best-fit value for the measurement of the Higgs boson mass, $m_H = 125.36$ GeV. Grouping similar Higgs boson production modes, the production rates relative to the SM prediction for the fermionic production modes - gluon fusion and associated production with a $t\bar{t}$ or $b\bar{b}$ pair - and bosonic production modes - vector boson fusion and associated production with a W or Z boson - are measured to be $\mu_{ggF+t\bar{t}H+b\bar{b}H} = 1.7^{+0.5}_{-0.4}$ and $\mu_{VBF+VH} = 0.3^{+1.6}_{-0.9}$, respectively.

The various Higgs boson production and decay modes studied by the ATLAS experiment are also combined, where the measured overall Higgs boson rate, relative to the Standard Model prediction, is $1.18^{+0.15}_{-0.14}$. The couplings of the Higgs boson are probed in a number of benchmark models, where a good agreement with the Standard Model prediction is observed for each model considered. The Higgs boson coupling measurements are also used to place constraints on a number of beyond the Standard Model theories, and are combined with direct searches for invisible Higgs boson decays to place a limit on the Higgs boson branching ratio to invisible final states.

Declaration of author's contribution

The design and construction of the ATLAS experiment, as well as the LHC, represents the significant efforts of large number individuals over many years. Every ATLAS result, including those presented in this thesis, owe a significant debt to these efforts.

The remarkably successful operation of the ATLAS detector during the first run of the LHC, again due to the work of many people, has underpinned the entire physics programme, and I have been fortunate to have had the opportunity to contribute to this in an operational role during 2012.

Offline performance studies also play a big role in facilitating physics results, and to this end I have contributed to the Level-1 Calorimeter Trigger efficiency monitoring and the development of trigger algorithms used during the 2012 8 TeV run. I also performed a detailed study of the application of isolation criteria to electron triggers at the hardware level, work that was subsequently continued by several other collaborators and underpins the ability of ATLAS to trigger events containing $W^{\pm}$ and Z bosons in LHC Run II. This work is not described in this thesis, though several aspects are described in approved ATLAS internal documents [1, 2].

This thesis focuses on the Higgs sector, and in particular the experimental study of the coupling properties of the observed Higgs boson. Chapters 4, 5 and 6 summarise the results that I have contributed to in this area.

Chapters 4 and 5 document the ATLAS $H \to ZZ^{(*)} \to 4\ell$ analysis, where I have contributed to all ATLAS publications [3, 4, 5] and preliminary results [6] since Summer 2012. With several collaborators, I developed, maintained and ran analysis software to perform the full analysis. Though a baseline event selection for the inclusive analysis had already been defined when I started my work on this analysis,

I participated in the optimisation of the analysis, and in particular in the definition of production based categories to enable a measurement of the signal strengths of the various Higgs boson production modes. I have also contributed extensively to the data-driven background estimation, the modelling of signal and background distributions, the final statistical interpretation of results, the Higgs boson mass measurement [7] and the search for high mass resonances.

I have also been involved in the first search for Higgs boson decays to a quarkonium state plus a photon, primarily in the signal and background modelling and statistical interpretation. This work is not discussed in this thesis, and is described in Ref. [8].

I have been involved in the combination of Higgs boson decay modes and the subsequent rate and couplings measurements [9]. In particular I have performed the correlation of systematic uncertainties across different final states and performed maximum likelihood fits in a number of models, described in this thesis. This includes the combination of off-shell and on-shell analyses, and the combination of visible and invisible decay modes. I have also used the coupling measurements to study directly several beyond the Standard Model scenarios [10].

Finally, I have contributed to the overall LHC - ATLAS and CMS - Higgs boson couplings combination [11] as the ATLAS contact for the $H \to ZZ^{(*)} \to 4\ell$ channel.

Acknowledgements

Reflecting on four years that have seemed to pass very quickly, I am somewhat overwhelmed by the extent and nature of the support I have received from a great many sources. It is, of course, impossible to suitably acknowledge every individual, group and organisation to whom I am grateful. Below are some scattered thoughts, but it should be emphasised that I am truly appreciative of everyone who has played a part, large or small, in making the work described in this thesis possible.

Firstly, I gratefully acknowledge the financial support that I have received from the STFC and the University of Birmingham. The opportunity to work day-to-day on something that is simultaneously stimulating, challenging and enjoyable is rare, and this would not have been possible for me if not for this generous support.

I owe a great debt to my Ph.D. supervisors, whose guidance has been invaluable. Kostas Nikolopoulos is a remarkable physicist and person. I am thankful for his patience, his unwavering support, his advice (not always taken but always wise) and friendship. More than this, Kostas has always endeavoured to be professional, principled and empathetic and has taught me lessons reaching far beyond Particle Physics. I would also like to express my gratitude to Paul Newman and Juraj Bracinik. Paul's faith in me and enthusiasm for particle physics were key factors in bringing me to Birmingham, and I greatly appreciate the advice and support he has consistently provided since I have been here. Working with Juraj has also been an immense pleasure; he is one of the most positive, friendly and helpful people I've ever met, and helped me immensely as a newcomer to the ATLAS collaboration.

It has been my great privilege to collaborate with, learn from, and get to know many Physicists from across the world and I appreciate the many stimulating discussions I have had with members of the ATLAS collaboration. I am grateful in particular to colleagues from the working groups that I have been a part of. I am thankful to

the ATLAS Level-1 Trigger community for the friendly, welcoming and supportive environment I experienced in the early parts of my Ph.D. I am also grateful to the ATLAS Higgs boson working group, in particular the $H \rightarrow ZZ^{(*)}$ sub-group. I thank the sub-group convenors and paper editors I have had the opportunity to work closely with - Christos Anastopoulos, Stefano Rosati, Fabien Tarrade, Rosy Nikolaidou, Robert Harrington, Roberto Di Nardo and R.D. Schaffer - for their support and guidance.

I also thank Eleni Mountricha for her collaboration and patience in the early parts of my Ph.D., and Tim Adye for expert technical guidance and the many hours spent helping me. I am thankful to all of my colleagues in the particle physics group at the University of Birmingham, in particular the Birmingham ATLAS group, for the support, guidance and stimulating discussions. It has been a real privilege to have had the opportunity to work closely with my friends Andy Chisholm, Ludovica Aperio Bella and Paul Thompson.

The company of fellow Ph.D. students has contributed immensely to making the past four years an enjoyable and memorable experience. For this, I am grateful to my fellow University of Birmingham students and especially those in West 316 - Tim, Jody, Tom, Hardeep, Benedict, Andy C (again), Andrew, "Mi Amigo" Javier, Mark, Rhys, Matt, James, Andy F and Alasdair. Thanks for the Friday beers, the curries, the football and the drinks at the Belgian Bar; I had fun.

I am fortunate to have had the opportunity to spend an extended period at CERN, though this would have been very difficult if it were not for the company of the many great friends I met there, in particular those residing at Citadines in Ferney-Voltaire, especially Carl, Shaun, Gary, Sam, Nikki, "The Ravens", Jim and Craig (and everyone I've forgotten to mention). I will remember fondly the pool parties, the kebabs and, again, the drinks at the Belgian Bar.

I am grateful to my friends outside of academia, whose support, encouragement and interest has been a great motivation. I would also like to express my gratitude to my extended family, especially my grandparents and great-grandparents. This includes the Evanses, in particular Chris and Stan, who have warmly welcomed me into their family.

Most importantly, I am indebted to those closest to me. I am grateful to my parents, Jane and Steve, and my Brother, Andrew: thank you, for your love and unconditional support, for always believing in me, and for so much more. You have always inspired me. Finally, I am grateful to Sammy: thank you for everything and more. You've shared this experience with me and it hasn't always been easy - I appreciate the sacrifices that you've made and the support and love you've shown me more than I can possibly express. I couldn't imagine spending these (and the rest of my) years with anyone else.

This thesis is dedicated to my Mum and Dad, to Andrew, and to Sammy.

All I know is that I don't know nothing
... and that's fine.

Operation Ivy, "Knowledge"

Contents

CHAPTER 1

Introduction

In July 2012, the ATLAS and CMS collaborations reported the discovery of a Higgs boson with a mass, m_H, around 125 GeV [12, 13], representing the culmination of many years of searches at a number of experimental facilities, with notable recent examples being at LEP [14] and the Tevatron [15]. A summary of the ATLAS results is shown in Figure 1.1. Many subsequent analyses have been performed to test the compatibility of the observed boson's properties with those predicted by the Standard Model, some of which form the main part of this document.

Chapter 2 gives an overview of some of the relevant theoretical background, as well as the expected phenomenology of the SM Higgs sector and the details of theoretical calculations and simulations. Chapter 3 contains a brief description of the Large Hadron Collider and the ATLAS experiment, including details about the reconstruction of physics objects and the data sample used for analyses contained in this thesis.
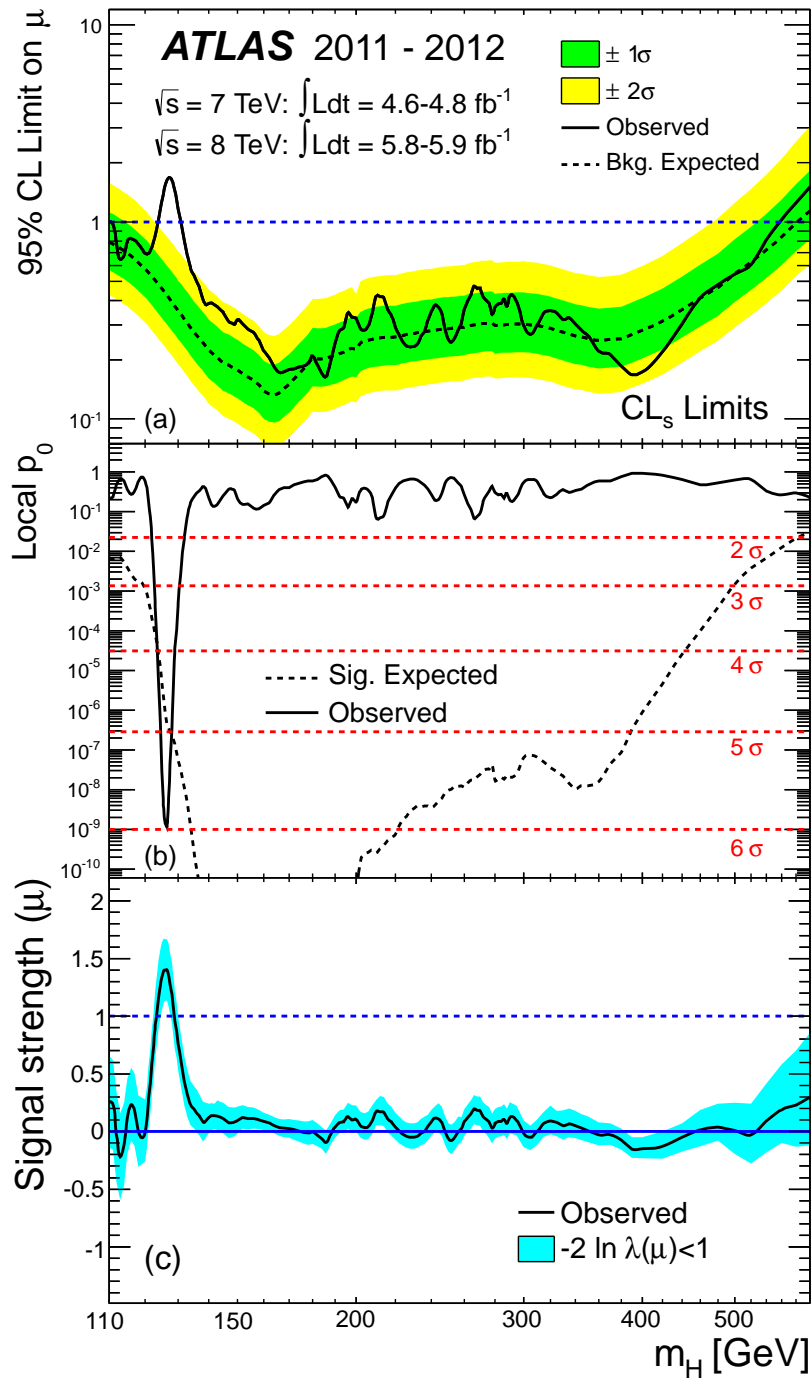
Figure 1.1: Summary of the results corresponding to the observation of the Higgs boson by the ATLAS experiment, using a combination of searches in different Higgs boson final states. a) shows the observed (solid black line) and, under the background-only hypothesis, expected (dashed black line) 95% CL$_S$ upper limits [16] on the Higgs boson signal strength (defined in Section 2.3). The green (yellow) band shows the one (two) sigma uncertainties on the expected limit. b) shows the observed (solid black line) and, under the SM Higgs boson hypothesis, expected (dashed black line) local-p_0 value (defined in Section 4.7). c) shows the best-fit value for the Higgs boson signal strength (black line) and its one sigma uncertainty (blue band). All distributions are shown as a function of the assumed Higgs boson mass, m_H. Figure from Ref. [12].

Chapters 4 and 5 discuss the ATLAS $H \to ZZ^{(*)} \to 4\ell$ analysis:

- Chapter 4 details the so-called "inclusive analysis" and the subsequent measurements of the Higgs boson mass, inclusive signal strength and differential cross sections.

- Chapter 4 focuses in detail on the "categorised analysis" used to measure the signal strengths for different Higgs boson production modes and extract the Higgs boson couplings.

Chapter 6 focuses on the measurement of the Higgs boson production and decay rates using the combination of the various decay modes and the subsequent extraction of the Higgs boson couplings. Direct constraints placed on "beyond the Standard Model" theories using the coupling measurements are also discussed.

Finally, Chapter 7 closes the thesis with some concluding remarks.

The Higgs boson

2.1   The Higgs boson and the Standard Model

In modern elementary particle physics, the current best understanding of the fundamental constituents of matter and their interactions is provided by the Standard Model (SM) [17, 18]. The SM, whose interactions are derived by imposing $SU(3)_C \otimes SU(2)_L \otimes SU(1)_Y$ local gauge symmetry, describes constituent fermions, classified into families of quarks and leptons, that are assumed to be point like and whose interactions are mediated by the strong, weak and electromagnetic (EM) forces. Each force is associated with one or more gauge boson.

The quarks - $up(u)$, $down(d)$, $charm(c)$, $strange(s)$, $top(t)$ and $bottom(b)$ - and leptons - $electrons(e)$, $muons(\mu)$, $taus(\tau)$ and $electron$, $muon$ and $tau\,neutrinos(\nu_{e/\mu/\tau})$ - are summarised in Table 2.1. The gauge bosons associated with the strong force and EM force are the $gluon(g)$ and $photon(\gamma)$ respectively and both are mass-

less. Three massive gauge bosons are associated with the weak force, the neutral Z boson ($m_Z = 91.1876 \pm 0.0021\,\text{GeV}$), and the charged W^+ and W^- bosons ($m_{W^\pm} = 80.385 \pm 0.015\,\text{GeV}$) [19].

The $SU(2)_L \otimes SU(1)_Y$ symmetry provides a unified description of the EM and weak forces in a single Quantum Field Theory, despite their significant phenomenological differences, and is discussed in Section 2.1.1. The $SU(3)$ symmetry corresponds to Quantum Chromodynamics (QCD), a non-abelian gauge theory describing the strong interaction.

Quarks and leptons are distinguished by the fact that quarks carry colour charge, whereas leptons do not; thus QCD acts only on the quark sector and is mediated by gauge bosons known as gluons. Unlike photons in Quantum Electrodynamics (QED) that do not carry electric charge, gluons do carry a colour charge and as a consequence self-interact. Only states with net-zero colour are observed in isolation, so quarks, anti-quarks and gluons appear in colour-neutral bound states known as hadrons. Up, down, charm, strange and bottom quarks all become part of bound states, a process known as hadronisation, though top quarks decay too quickly to hadronise.

In scattering experiments final state partons are typically observed as part of collimated bunches of hadrons known as jets. However, a jet is not uniquely defined, and typically an algorithm must be defined to associate constituent particles with a particular jet. Finally, since the Large Hadron Collider (LHC), described in Section 3.1, is a proton-proton ($p - p$) collider, the initial state particles are hadrons and hard collisions in fact occur between the proton constituents. As a consequence, parton distribution functions are required to describe the distribution of quarks and gluons within the protons.

Table 2.1: Mass and electric charge (in units of the electron charge) for the three families of fermions in the SM. Mass values, estimated using the $\overline{\text{MS}}$ scheme except for the top quark mass (where a direct measurement is quoted), are taken from Ref. [19]. In general, the uncertainties on the lepton masses are considerably smaller than the uncertainties on the quark masses. Neutrinos are considered massless in the SM.

	Generation					
	I		II		III	
Quarks						
Symbol	u	d	c	s	t	b
Mass	$4.8^{+0.7}_{-0.5}$ MeV	$2.3^{+0.7}_{-0.5}$ MeV	1.275 ± 0.025 GeV	95 ± 5 MeV	173.21 ± 0.51 GeV	4.18 ± 0.03 GeV
Electric Charge	$+2/3$	$-1/3$	$+2/3$	$-1/3$	$+2/3$	$-1/3$
Leptons						
Symbol	e	ν_e	μ	ν_μ	τ	ν_τ
Mass	0.51100	0	105.65 MeV	0	1776.8 MeV	0
Electric Charge	-1	0	-1	0	-1	0

2.1.1   Electroweak theory

Guided by the observed phenomenology, the theory of EW interactions is based on the $SU(2)_L \otimes SU(1)_Y$ gauge group. The physical fermions are made up of left-handed and right-handed fields; the left-handed components transform as doublets under $SU(2)$, whereas the right-handed components transform as singlets, so the weak interaction only acts on the left-handed components.

The requirement for the theory to be invariant under local gauge transformations, leads to a weak isovector $\mathbf{W}_\mu$, corresponding to $SU(2)$ with coupling constant g, and a weak isoscalar B_μ, corresponding to $U(1)$ with a coupling constant g'. At odds with experimental observations, this model alone requires both the vector bosons and the fermions to be massless since Dirac mass terms do not respect the local gauge invariance of the symmetry group.

2.1.2   The Brout-Englert-Higgs (BEH) mechanism

In the SM, the Brout-Englert-Higgs (BEH) mechanism generates masses for the vector bosons and fermions [20, 21, 22]. A complex, self-interacting $SU(2)$ scalar doublet, labelled the Higgs doublet, is introduced:

$$\phi = \begin{pmatrix} \phi^+ \\ \phi^0 \end{pmatrix}$$

with a potential, shown in Figure 2.1, given by:

$$V(\phi) = \mu^2 \phi^\dagger \phi + \frac{\lambda^2}{2}(\phi^\dagger \phi)^2$$

where choosing $\mu^2 < 0$ results in the neutral component of the doublet acquiring a non-zero vacuum expectation value, $v = \sqrt{2}\mu/\lambda \simeq 246\,\text{GeV}$. Since the ground state of ϕ is degenerate and is not symmetric under local $SU(2)_L \otimes SU(1)_Y$ gauge transformations, the symmetry is said to be spontaneously broken.
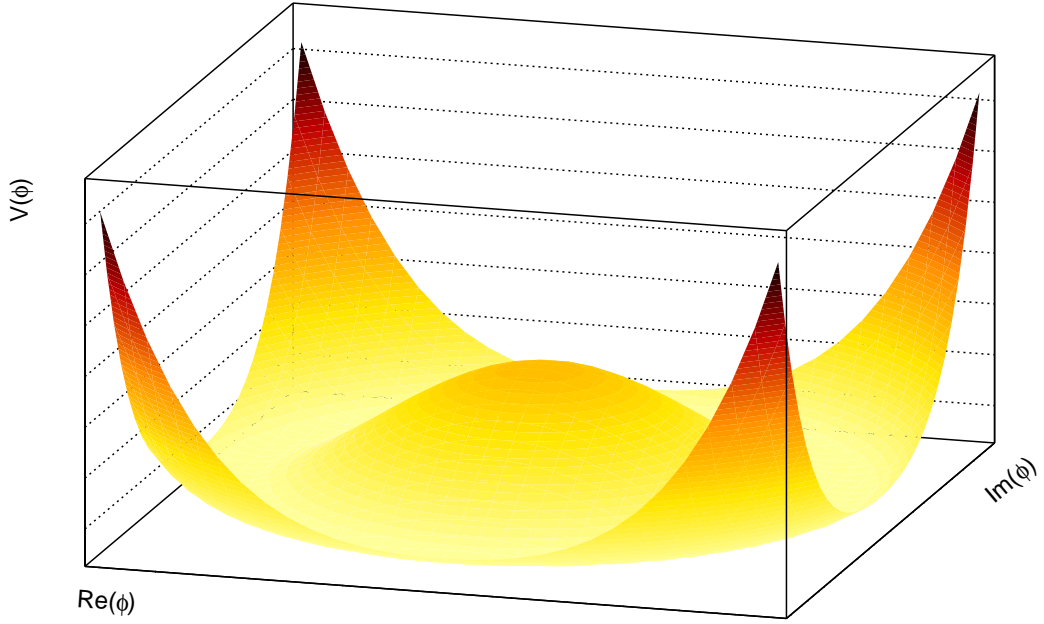
Figure 2.1: The Higgs potential, $V(\phi)$.

Three of the four $SU(2)_L \otimes SU(1)_Y$ generators are spontaneously broken, leading to the existence of three massless Goldstone bosons, associated with three of the four degrees of freedom introduced by the Higgs doublet. The Higgs field couples to the $\mathbf{W}_\mu$ and B_μ gauge fields through the kinetic term of the Higgs Lagrangian, and as a result the three degrees of freedom associated with the Goldstone bosons become the longitudinal polarisation components of the physical W and Z bosons. The fourth generator is unbroken, and corresponds to $U(1)_{EM}$, which means the photon remains massless. The remaining degree of freedom introduced by the scalar doublet corresponds to the Higgs boson itself.

After the introduction of the Higgs field, Yukawa interactions between the Higgs boson and the SM fermions can be added to the SM Lagrangian. When the Higgs field acquires a vacuum expectation value as described above, the Yukawa interaction terms generate fermion masses.

The Higgs boson itself is a massive, scalar boson, whose mass is $m_H = \sqrt{2\lambda}v$,

where v is the vacuum expectation value of the Higgs field and λ, the Higgs self coupling parameter, is a free parameter in the SM. The Higgs boson mass is hence not predicted by the SM.

For a given value of the Higgs boson mass, its couplings to SM particles are predicted, and depend linearly on the fermion mass for Higgs boson-fermion couplings, $g_{Hf\bar{f}}$, and on the boson mass squared for Higgs boson-vector boson couplings, g_{HVV}:

$$g_{Hf\bar{f}} = \frac{m_f}{v}, \quad g_{HVV} = \frac{2m_V^2}{v}$$

A further motivation for the introduction of a BEH mechanism is the preservation of unitarity in the $W^+W^- \rightarrow W^+W^-$ process, where without a Higgs boson, the scattering amplitude for the process rises at a faster rate than the total cross section. After introducing the Higgs boson, unitarity is recovered due to a series of new processes (including a Higgs boson exchange) with the same initial and final states.

2.1.3   Alternative and extended Higgs sectors

The tree level Higgs boson mass is subject to radiative loop corrections due to heavy particles, in the SM dominated by the top quark and with further significant contributions from the W and Z bosons. Such loop processes are required to be calculated up to a scale determined by the domain of the validity of the SM which, in the absence of heavy new physics, is considered to be the Planck scale, $\mathcal{O}(10^{19})$ GeV. In this case, for a physical Higgs boson mass at the electroweak scale, the stability of the Higgs boson mass is provided by a high degree of parameter fine-tuning. Several extended or alternative models for EWSB have been proposed to construct theories that are able to avoid this problem, and are also able to explain the source of EWSB.

In **Composite Higgs Models (CHM)**, the Higgs boson is not a fundamental scalar but a composite, pseudo Nambu-Goldstone boson, associated with the spontaneous breaking of a global "flavour" symmetry in a strongly interacting sector.

EWSB is generated dynamically by loop processes involving SM bosons and fermions and radiative corrections to the Higgs boson mass are saturated at a so-called compositeness scale, so the mass remains low even in the presence of heavy new physics. For **Minimal Composite Higgs Models (MCHM)**, interactions are derived by imposing $SO(5)$ gauge symmetry, and the Higgs boson couplings to vector bosons take the form:

$$g_{HVV} = g_{HVV}^{SM} \cdot \sqrt{1 - \xi}$$

where $\xi = v^2/f^2$ is a scale factor that depends on the compositness scale, f, and the SM vacuum expectation value, v. The form of the Higgs boson couplings to fermions depends on the chosen representation for fermions in the theory, and two variants of MCHM are correspondingly defined: MCHM$_4$ [23], where spinorial representations of SO(5) are chosen, and MCHM$_5$ [24, 25], where fundamental representations of SO(5) are chosen. The fermion couplings for each variant take the following form:

$$g_{Hf\bar{f}} = g_{Hf\bar{f}}^{SM} \cdot \sqrt{1 - \xi} \, (\text{MCHM}_4)$$
$$g_{Hf\bar{f}} = g_{Hf\bar{f}}^{SM} \cdot \frac{1 - 2\xi}{\sqrt{1 - \xi}} (\text{MCHM}_5)$$

The SM predictions are recovered in the limit $\xi = 0$.

A central prediction of the BEH mechanism is:

$$\rho = M_W^2 \, / \, (M_Z^2 \, \cdot \, cos^2\theta_W) = 1 \tag{2.1}$$

at tree level, where θ_W is the Weinberg angle. This parameter has been precisely measured at LEP [26]. Choosing suitable quantum numbers, this is also the case in models with additional Higgs multiplets. Several models extend the scalar sector with the introduction of further fields. In **Additional Electroweak Singlet Models**, a single, real field, transforming as a singlet under $SU(3)_C \otimes SU(2)_L \otimes SU(1)_Y$, is added to the theory [27, 28]. Both the Higgs field and the singlet field acquire

a non-zero vacuum expectation value, and the singlet state mixes with the original Higgs doublet, with the additional degree of freedom introduced giving rise to a second scalar boson.

The lighter and heavier bosons are denoted as h and H respectively, and the couplings of each to vector bosons and fermions are modified by a factor κ^2 (for h) and κ'^2 (for H). For this Higgs sector to unitarise $W^+W^- \to W^+W^-$ scattering it is required that $\kappa^2 + \kappa'^2 = 1$. Assuming SM decays modes, the branching ratios of the lighter state are identical to those in the SM, and the branching ratios of the heavy state are modified with respect to the SM predictions to take into account new kinematically accessible decay modes (including final states containing h). The transformation properties of the EW singlet under the $SU(3)_C \otimes SU(2)_L \otimes SU(1)_Y$ gauge symmetry mean that this model provides a dark matter candidate.

In **Two Higgs Doublet Models** (2HDMs) [27, 29, 30] a second complex scalar doublet is added. 2HDMs represent a wide class of models, though many introduce tree-level flavour changing neutral currents (FCNCs) which are disfavoured by experimental data. As a result, models considered are typically required to satisfy the Glashow-Weinberg condition, which states that at most one neutral Higgs field couples to fermions of a given electric charge [31, 32].

As in the SM, three degrees of freedom become the longitudinal polarisation coordinates of the W and Z bosons. Five degrees of freedom remain, and lead to five physical Higgs bosons. Two of the new states are scalar bosons (h and H), one is a neutral pseudo-scalar boson (A), and two are charged scalar bosons ($H^{\pm}$). 2HDMs are parameterised by the ratio of the vacuum expectation values of the two doublet fields:

$$tan\beta = \frac{v_2}{v_1}$$

and the mixing angle, α between the neutral scalars.

Several classes of models satisfy the Glashow-Weinberg condition and are distinguished by the way in which the light scalar boson couples to SM fermions, sum-

marised in Table 2.2. The Minimal Supersymmetric Standard model is an example of a 2HDM.

Table 2.2: Coupling scale factors, κ_V, κ_u, κ_d and κ_ℓ, that scale the SM Higgs boson coupling to vector bosons, up-type quarks, down-type quarks and leptons respectively in several classes of 2HDM [10].

Coupling scale factor	Type I	Type II	Type III	Type IV
κ_V	$\sin(\beta - \alpha)$	$\sin(\beta - \alpha)$	$\sin(\beta - \alpha)$	$\sin(\beta - \alpha)$
κ_u	$\cos(\alpha)/\sin(\beta)$	$\cos(\alpha)/\sin(\beta)$	$\cos(\alpha)/\sin(\beta)$	$\cos(\alpha)/\sin(\beta)$
κ_d	$\cos(\alpha)/\sin(\beta)$	$-\sin(\alpha)/\cos(\beta)$	$\cos(\alpha)/\sin(\beta)$	$-\sin(\alpha)/\cos(\beta)$
κ_l	$\cos(\alpha)/\sin(\beta)$	$-\sin(\alpha)/\cos(\beta)$	$-\sin(\alpha)/\cos(\beta)$	$\cos(\alpha)/\sin(\beta)$

2.2 SM Higgs boson production and decay at the LHC

Several Higgs boson production modes are relevant at the LHC. The Feynman diagrams for the Higgs boson production mechanisms considered by analyses discussed in this thesis are shown in figure 2.2.

The cross sections for Higgs boson production processes and their associated uncertainties are compiled in Refs. [33, 34]. The Higgs boson gluon fusion (ggF) cross section has been calculated to next-to-leading order (NLO) [35, 36, 37] and next-to-next-to-leading order (NNLO) [38, 39, 40] in QCD. QCD soft-gluon resummations to the Higgs boson ggF cross section have been calculated in the next-to-next-to-leading log (NNLL) approximation [41]. Finally, NLO EW corrections are also applied [42, 43]. The Vector Boson Fusion (VBF) process is calculated with full NLO QCD and EW corrections [44, 45, 46]. Approximate NNLO QCD corrections are applied [47]. For the processes where the Higgs boson is produced in association with a vector boson (WH/ZH), calculations are performed at NLO [48] and NNLO [49] in QCD, and EW radiative corrections [50] are calculated to NLO. For the process where the Higgs boson is produced in association with a pair of top quarks ($t\bar{t}H$), the cross section is calculated to NLO in QCD [51, 52, 53, 54].

Assuming a Higgs boson mass $m_{\mathrm{H}} = 125$ GeV, the QCD scale uncertainty for the
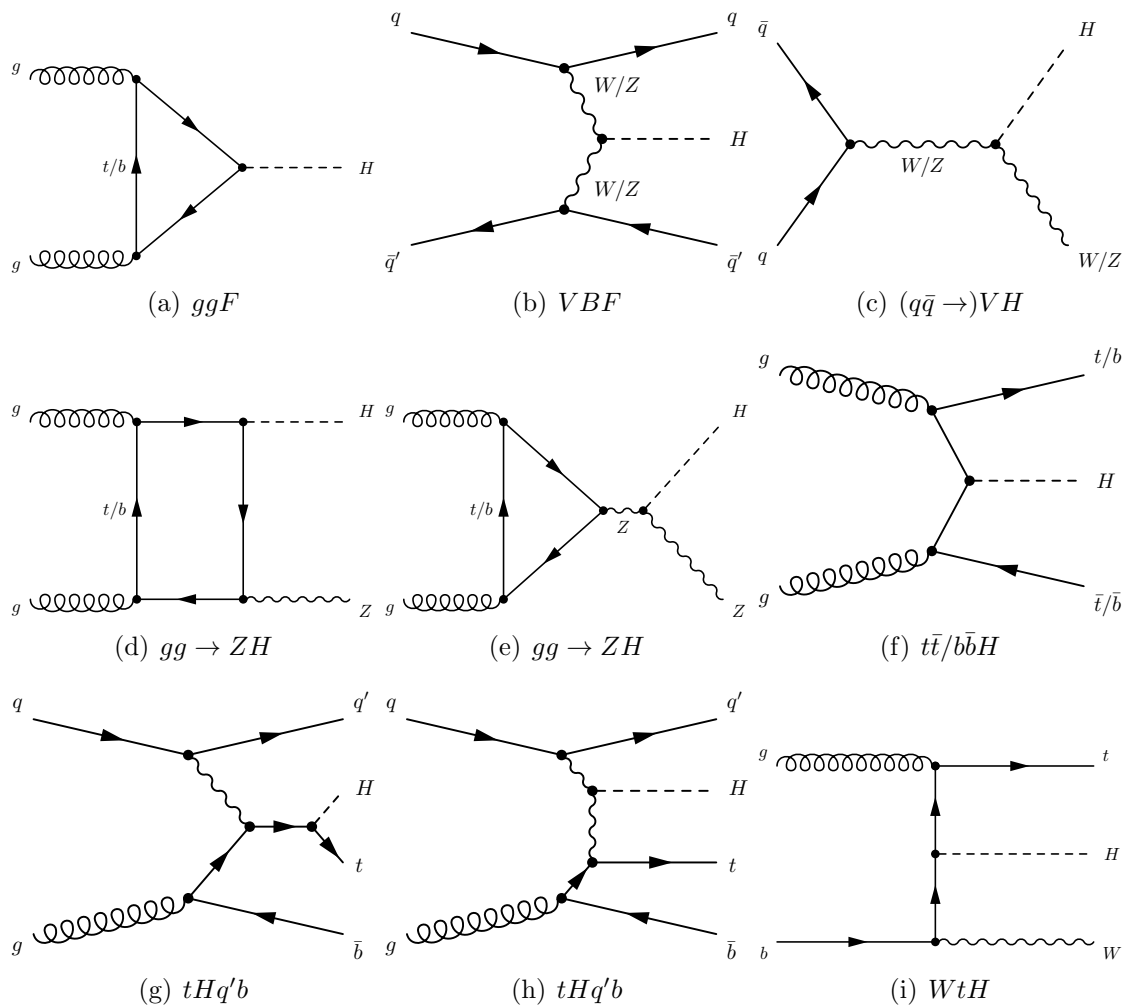
Figure 2.2: Feynman diagrams for Higgs boson production at the LHC. All production processes considered by analyses described in this thesis are shown [9].

ggF process is $^{+7}_{-8}\%$, and the corresponding uncertainty for the VBF and VH production processes is 1%. The production cross section uncertainty due to uncertainties in the parton distribution function (PDF) and α_s are $\pm 8\%$ for gluon-initiated processes and $\pm 4\%$ for quark-initiated processes, estimated using the method described in Ref [55] with the CTEQ [56], MSTW [57] and NNPDF [58] PDF sets.

The Higgs boson decay modes considered by analyses discussed in this thesis are presented in Figure 2.3.

(a) $H \to ZZ^{(*)}/WW^{(*)}$ (b) $H \to b\bar{b}/\tau\tau/\mu\mu$

(c) $H \to \gamma\gamma/Z\gamma$ (d) $H \to \gamma\gamma/Z\gamma$ (e) $H \to \gamma\gamma/Z\gamma$
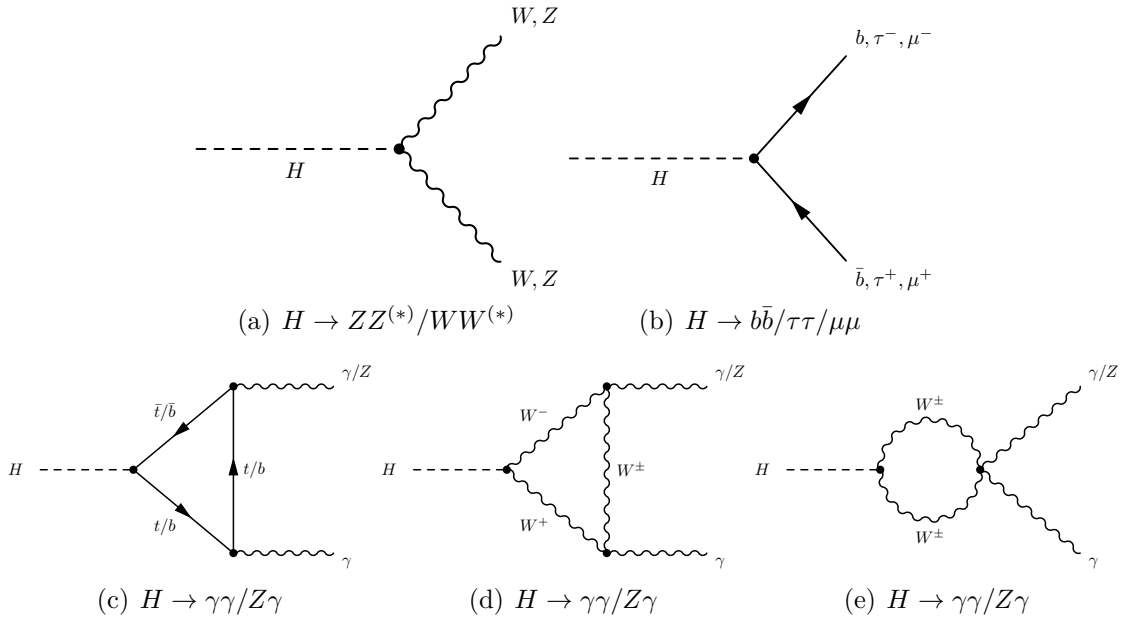
Figure 2.3: Feynman diagrams for Higgs boson decays at the LHC. All decay processes considered by analyses described in this thesis are shown [9].

The PROPHECY4F [59] program is used to calculate the partial widths to the $ZZ^{(*)}$ and $WW^{(*)}$ decay modes, accounting for interference effects between four fermion final states. The HDECAY [60] program is used to calculate the partial widths for other decay modes, and the information is combined to provide the Higgs boson branching ratios to different final states.

For the Higgs boson production and decay processes considered by analyses discussed in this thesis, the SM predictions for the cross sections and branching ratios are given in Table 2.3. For a number of Higgs boson production and decay processes, the production of the production cross section and branching ratio are shown as a

function of the Higgs boson mass in Figure 2.4.
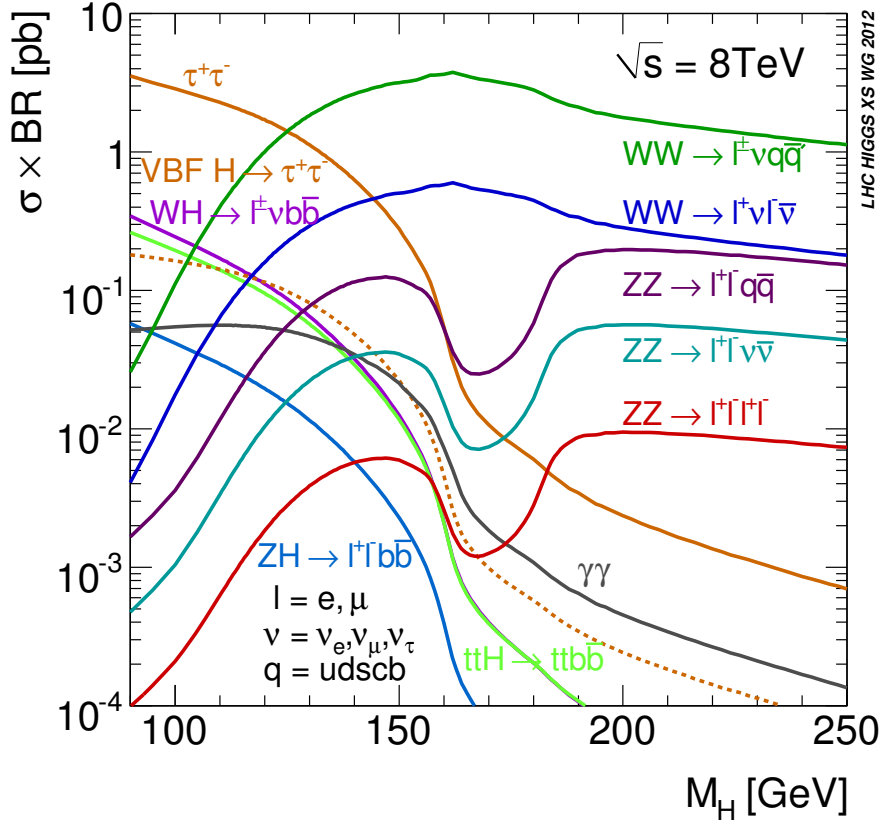
Figure 2.4: SM prediction for Higgs boson production cross section times branching ratio as a function of the Higgs boson mass for a number of processes [33].

The Higgs boson width, assuming $m_H = 125$ GeV, is $\Gamma_H = 4.15$ MeV, far beyond the experimental precision that a collider experiment could feasibly achieve. Recent studies have observed that a sizeable cross section for the off-shell production of a Higgs boson in the $H \to ZZ^{(*)}$ and $H \to WW^{(*)}$ decay modes may be observable, and under certain assumptions the combination of the on-shell and off-shell measurements may be used to indirectly constrain the Higgs boson width.

Table 2.3: SM predictions for Higgs boson production cross sections and decays branching ratios, along with their uncertainties, from Ref. [27] except for the tH production cross section, from Ref. [61]. The calculations assume a Higgs boson mass m_H=125 GeV.

Production process	Cross section (pb)		Decay channel	Branching ratio (%)
	$\sqrt{s} = 7$ TeV	$\sqrt{s} = 8$ TeV	$H \to b\bar{b}$	57.1 ± 1.9
ggF	15.0 ± 1.6	19.2 ± 2.0	$H \to WW^*$	22.0 ± 0.9
VBF	1.22 ± 0.03	1.57 ± 0.04	$H \to \gamma\gamma$	8.53 ± 0.85
WH	0.573 ± 0.016	0.698 ± 0.018	$H \to \tau\tau$	6.26 ± 0.35
ZH	0.332 ± 0.013	0.412 ± 0.013	$H \to c\bar{c}$	2.88 ± 0.35
bbH	0.155 ± 0.021	0.202 ± 0.028	$H \to ZZ^*$	2.73 ± 0.11
ttH	0.086 ± 0.009	0.128 ± 0.014	$H \to \gamma\gamma$	0.228 ± 0.011
tH	0.012 ± 0.001	0.018 ± 0.001	$H \to Z\gamma$	0.157 ± 0.014
Total	17.4 ± 1.6	22.3 ± 2.0	$H \to \mu\mu$	0.022 ± 0.001

2.3 Measurement of the Higgs boson rates and probing its couplings

Measured rates in Higgs boson analyses are presented in terms of the signal strength parameter μ, defined for a given decay mode as:

$$\mu = \frac{\sigma \cdot \mathrm{BR}}{\sigma_{SM} \cdot \mathrm{BR_{SM}}} \tag{2.2}$$

where σ is the total cross section of the Higgs boson and BR is the branching ratio for the relevant mode. For specific production modes, this may be factorised as:

$$\mu = \mu_i \cdot \mu_f \tag{2.3}$$

where $\mu_i = \sigma_i/\sigma_{i,SM}$ and $\mu_f = \mathrm{BR_f}/\mathrm{BR_{f,SM}}$ for a given production mode i and decay mode f. Since only the product $\mu_i \cdot \mu_f$ is experimentally measured, measurements of production or decay related quantites are required to make assumptions on μ_f or μ_i respectively.

To go beyond the measurement of rates and interpret the experimentally measured rates in terms of the Higgs boson couplings, the LO framework described in Ref. [27] is used. Several assumptions are implicit in the framework:

- All signals considered come from a Higgs boson-like particle, which is a single resonance near 125 GeV.

- The width of the Higgs boson is negligible, so the product $\sigma \times BR(i \to \mathrm{H} \to f)$ can be decomposed as:

$$\sigma \times BR(i \to \mathrm{H} \to f) = \frac{\sigma_i \cdot \Gamma_f}{\Gamma_\mathrm{H}}$$

  where σ_i is the production cross section, Γ_f is the partial decay width into a final state f and Γ_H the total width of the Higgs boson.

- Only modifications of absolute values of coupling strengths are considered. Modifications to the kinematic structure of processes are not considered, and the observed state is assumed to be a CP-even scalar, as predicted by the SM.

For each Higgs boson coupling with a SM particle, a coupling scale factor, κ, is defined, where the rate for a process with an initial state, i, and final states, f, is defined as follows:

$$\sigma \times BR(i \to \mathrm{H} \to f) = \frac{\sigma_{i,SM} \cdot \Gamma_{f,SM}}{\Gamma_{\mathrm{H},SM}} \cdot \frac{\kappa_i^2 \cdot \kappa_f^2}{\kappa_H^2}$$

where the squared scale factors κ_i^2, κ_f^2 and κ_H^2 scale the production cross section, partial decay width and total decay width respectively, where κ_H depends on the scale factors for all couplings contribution to the Higgs boson total width. $\kappa = 1$ corresponds to the SM prediction. The above expression assumes that only known particles contribute to the total Higgs boson decay width, and this assumption can be relaxed in the case of additional invisible or undetected Higgs boson decays,

where the Higgs boson total width becomes:

$$\Gamma_{\mathrm{H}} = \frac{\kappa_H^2}{1 - \mathrm{BR_{i.,u.}}}\Gamma_{\mathrm{H},SM}$$

For the production and decay process considered by analyses discussed in this thesis, the corresponding signal strength, written in terms of the coupling scale factors, is shown in Table 2.4.

If the particle content of loops is assumed to be the same an in the SM, the loop processes are resolved in terms of fundamental coupling scale factors as shown in Table 2.4. To allow for the presence of additional, unknown particles running in loops, effective coupling scale factors, κ_g, κ_γ and $\kappa_{Z\gamma}$, are introduced in some fits to scale the $gg \to H$, $H \to \gamma\gamma$ and $H \to Z\gamma$ processes. The $gg \to ZH$ process is always resolved in terms of the SM predicted loop content as any deviation from the SM is likely to give rise to a kinematic structure very different to the SM prediction.

Since each measured rate depends on the Higgs boson total width, which cannot be measured directly at the LHC, only measurements of ratios of coupling scale factors can be made without some assumption about the Higgs boson total width.

To measure absolute coupling scale factors, several possible assumptions can be made to constrain Γ_H:

- The Higgs boson does not decay to any additional invisible or undetected final states, i.e. $\mathrm{BR_{i.,u.}} = 0$.

- The scale factors for the ZH and WH couplings do not exceed one, i.e. $\kappa_W \leq 1$ and $\kappa_Z \leq 1$. This is motivated by the assumption that the existence of the Higgs boson solves the unitarity problem in vector boson scattering, and holds in many BSM models [27].

- Under the assumption that the equivalent coupling strengths for off-shell Higgs boson and on-shell Higgs boson production are identical, a measurement of the

Table 2.4: Higgs boson rate scalings in terms of coupling strength scale factors for the production and decay processes considered and the Higgs boson total width. Loop processes may depend on more than one coupling scale factor, and may include interference terms. The expressions are taken from Ref. [27], except for $\sigma(gg \to ZH)$, which is from Ref. [62], and $\sigma(gb \to WtH)$ and $\sigma(qb \to tHq')$, which is calculated using Ref. [61].

Production	Loops	Interference	Rate scaling in terms of coupling scale factors	
$\sigma(\text{ggF})$	✓	$b - t$	$\kappa_g^2 \sim$	$1.06 \cdot \kappa_t^2 + 0.01 \cdot \kappa_b^2 - 0.07 \cdot \kappa_t \kappa_b$
$\sigma(\text{VBF})$	-	-	$\sim$	$0.74 \cdot \kappa_W^2 + 0.26 \cdot \kappa_Z^2$
$\sigma(WH)$	-	-	$\sim$	κ_W^2
$\sigma(q\bar{q} \to ZH)$	-	-	$\sim$	κ_Z^2
$\sigma(gg \to ZH)$	✓	$Z - t$	$\kappa_{\text{ggZH}}^2 \sim$	$2.27 \cdot \kappa_Z^2 + 0.37 \cdot \kappa_t^2 - 1.64 \cdot \kappa_Z \kappa_t$
$\sigma(bbH)$	-	-	$\sim$	κ_b^2
$\sigma(ttH)$	-	-	$\sim$	κ_t^2
$\sigma(gb \to WtH)$	-	$W - t$	$\sim$	$1.84 \cdot \kappa_t^2 + 1.57 \cdot \kappa_W^2 - 2.41 \cdot \kappa_t \kappa_W$
$\sigma(qb \to tHq')$	-	$W - t$	$\sim$	$3.4 \cdot \kappa_t^2 + 3.56 \cdot \kappa_W^2 - 5.96 \cdot \kappa_t \kappa_W$
Partial decay width				
$\Gamma_{b\bar{b}}$	-	-	$\sim$	κ_b^2
Γ_{WW}	-	-	$\sim$	κ_W^2
Γ_{ZZ}	-	-	$\sim$	κ_Z^2
$\Gamma_{\tau\tau}$	-	-	$\sim$	κ_τ^2
$\Gamma_{\mu\mu}$	-	-	$\sim$	κ_μ^2
$\Gamma_{\gamma\gamma}$	✓	$W - t$	$\kappa_\gamma^2 \sim$	$1.59 \cdot \kappa_W^2 + 0.07 \cdot \kappa_t^2 - 0.66 \cdot \kappa_W \kappa_t$
$\Gamma_{Z\gamma}$	✓	$W - t$	$\kappa_{Z\gamma}^2 \sim$	$1.12 \cdot \kappa_W^2 + 0.00035 \cdot \kappa_t^2 - 0.12 \cdot \kappa_W \kappa_t$
Total decay width				
Γ_{H}	✓	$W - t$ $b - t$	$\kappa_{\text{H}}^2 \sim$	$0.57 \cdot \kappa_b^2 + 0.22 \cdot \kappa_W^2 + 0.09 \cdot \kappa_g^2 +$ $0.06 \cdot \kappa_t^2 + 0.03 \cdot \kappa_Z^2 + 0.03 \cdot \kappa_c^2 +$ $0.0023 \cdot \kappa_\gamma^2 + 0.0016 \cdot \kappa_{Z\gamma}^2 + 0.00022 \cdot \kappa_\mu^2$

off-shell Higgs boson production rate can be used to constrain the Higgs boson total width.

- If it is assumed that the Higgs boson does not decay to additional undetected final states, $\text{BR}_{\text{undet.}} = 0$, then a direct limit on Higgs boson decays to invisible final states can be used to constrain the Higgs boson total width.

As well as making measurements where each fundamental coupling is assigned a scale factor (and variations upon this discussed so far), benchmark models with reduced numbers of coupling scale factors may be probed. The benchmark models considered are discussed alongside the obtained results in Section 5.5.

2.4   Simulation

The simulation of $p - p$ collisions and the response of the ATLAS detector[1] plays a vital role in the analysis of data collected by the ATLAS experiment. A range of event generator programs, using Monte Carlo (MC) simulation to model the acceptance of events, are used to model the signal and background processes for various analyses. Event generators are used to simulate the $p - p$ interaction and the subsequent decays, as well as the parton shower, hadronisation and underlying event processes. In practice, the program used to simulate the hard interaction and the program used to simulate the other processes may be different; in this case, the latter is known as a 'showering program'. Parton distribution functions (PDFs) are used to parameterise the distribution of constituents inside the proton.

The collection of stable particles produced in the event generation process is interfaced to the ATLAS detector simulation, which uses the GEANT4 [63, 64] framework to simulate the interaction of particles passing through a detailed model of the ATLAS detector geometry and material composition. The simulation of further $p - p$ interactions in the same bunch crossing is performed by superimposing the detector

---

[1]The ATLAS detector is described in Chapter 3.

activity from simulated minimum bias events.

2.4.1   Higgs boson signal simulation

For the ggF and VBF Higgs boson production modes, the hard scatter process is modelled using the Powheg event generator program [65, 66, 67, 68, 69], which uses next-to-leading order (NLO) matrix-element calculations. Pythia8 [70, 71] is used as a showering program. For the WH and ZH processes, Pythia8 is used to simulate both the hard scatter and the parton shower at leading-order (LO). For the $H \to ZZ^{(*)} \to 4\ell$ channel, discussed in detail in this thesis, the $t\bar{t}H$ process is also simulated with Pythia8, whereas analyses specifically searching for $t\bar{t}H$ production, described in Chapter 6, use Powheg for the hard scatter and Pythia8 for showering. The $b\bar{b}H$ process is assumed to have the same acceptance and efficiency as the ggF process as the event kinematics are found to be similar, and the same Higgs boson mass dependence as the $t\bar{t}H$ process. The CT10 [72] and CTEQ6L1 [73] PDF sets are used. Table 2.5 summarises the event generators and PDF sets used for the main Higgs boson production modes.

Table 2.5: Summary of the event generators and PDF sets used to simulate Higgs boson production in $\sqrt{s} = 8$ TeV $p - p$ collisions, for the main production modes considered [9].

Production process	Event generator	Showering program	PDF set
ggF	Powheg	Pythia8	CT10
VBF	Powheg	Pythia8	CT10
WH	Pythia8	Pythia8	CTEQ6L1
$ZH: \ q\bar{q} \to ZH$	Pythia8	Pythia8	CTEQ6L1
$ZH: \ gg \to ZH$	Powheg	Pythia8	CT10
ttH	Powheg	Pythia8	CT10

The simulated samples are scaled to match the best available theoretical predictions for the production cross sections and decay branching ratios for each process, taken from Refs. [33, 34].

For the ggF production mechanism, the generated Higgs boson p_T distribution is reweighted to match the calculations from Refs. [74, 75]. The calculation includes NNLO and NNLL QCD corrections.

For the $H \to ZZ^{(*)} \to 4\ell$ channel, discussed in detail in this thesis, the production cross sections for various production modes and $H \to ZZ^{(*)} \to 4\ell$ branching ratio is presented for a series of Higgs boson mass values at 7 TeV and 8 TeV in Table 2.6.

2.4.2 Background simulation for $H \to ZZ^{(*)} \to 4\ell$

Since the $H \to ZZ^{(*)} \to 4\ell$ analysis is considered in detail in this thesis, the simulation of relevant background processes is discussed here.

The SM $q\bar{q} \to ZZ^{(*)}$ process is modelled using POWHEG [76] and the $gg \to ZZ^{(*)}$ process is modelled with gg2ZZ [77]. PDF and α_s depend on the invariant mass of $ZZ^{(*)}$ system. The QCD scale uncertainty on the expected number of $ZZ^{(*)}$ events around $m_{ZZ^{(*)}} = 125$ GeV is 5% for the $q\bar{q} \to ZZ^{(*)}$ process and 25% for the $gg \to ZZ^{(*)}$ process. The corresponding uncertainties due to the PDF scale and α_s uncertainties are 4% for $q\bar{q} \to ZZ^{(*)}$ and 8% for $gg \to ZZ^{(*)}$

The $Z + $ jets and $t\bar{t}$ background processes are simulated using ALPGEN [78] and POWHEG (interfaced to PYTHIA) respectively. The $Z+$jets sample is divided into $Z+$ light jets, including $Zc\bar{c}$ in the massless c-quark approximation and $Zb\bar{b}$ events from parton showers, and $Zb\bar{b}$ using matrix element calculations that take into account the b-quark mass. Double counting is removed using the MLM [79] matching scheme, except for b-jets, where any double counting is manually removed by requiring that $b\bar{b}$ pairs with $\Delta R = \sqrt{(\Delta\phi)^2 + (\Delta\eta)^2} > 0.4$ between the b-quarks are taken from the matrix-element calculation and b-quarks with $\Delta R < 0.4$ are taken from the parton-shower. The normalisations of the $Z + $ jets and $t\bar{t}$ background processes are estimated using data-driven methods, described in Section 4.4.

Table 2.6: SM Higgs boson production cross sections for the ggF, VBF VH, $b\bar{b}H$ and $t\bar{t}H$ production modes in 7 TeV and 8 TeV $p - p$ collisions. The $b\bar{b}H$ and $t\bar{t}H$ production cross sections are summed. The branching ratio (B) for $H \to ZZ^{(*)} \to 4\ell$ decays is also shown [4].

m_H [GeV]	ggF [pb]	VBF [pb]	WH [pb]	ZH [pb]	$b\bar{b}H/t\bar{t}H$ [pb]	$B\,(H \to ZZ^{(*)} \to 4\ell)$ $[10^{-3}]$
			$\sqrt{s} = 7$ TeV			
123	15.6 ± 1.6	1.25 ± 0.03	0.61 ± 0.02	0.35 ± 0.01	0.26 ± 0.04	0.103 ± 0.005
125	15.1 ± 1.6	1.22 ± 0.03	0.58 ± 0.02	0.34 ± 0.01	0.24 ± 0.04	0.125 ± 0.005
127	14.7 ± 1.5	1.20 ± 0.03	0.55 ± 0.02	0.32 ± 0.01	0.23 ± 0.03	0.148 ± 0.006
			$\sqrt{s} = 8$ TeV			
123	19.9 ± 2.1	1.61 ± 0.05	0.74 ± 0.02	0.44 ± 0.02	0.35 ± 0.05	0.103 ± 0.005
125	19.3 ± 2.0	1.58 ± 0.04	0.70 ± 0.02	0.42 ± 0.02	0.33 ± 0.05	0.125 ± 0.005
127	18.7 ± 1.9	1.55 ± 0.04	0.67 ± 0.02	0.40 ± 0.02	0.32 ± 0.05	0.148 ± 0.006

CHAPTER 3

The ATLAS experiment at the LHC

3.1 The LHC

The Large Hadron Collider (LHC) is a particle accelerator that occupies the underground tunnel which had previously housed the Large Electron Positron Collider (LEP) at CERN, near Geneva, Switzerland. With a circumference of 26.7 km, made up of eight straight sections and eight curved sections, it is the largest particle collider ever constructed. Protons are supplied to the LHC by the injector complex shown in Figure 3.1.

In the LHC protons are accelerated in two rings with counter-rotating beams, where superconduncting magnets are used to bend their trajectories and they are accelerated by superconducting radio frequency cavities. Protons are grouped into bunches, where the design value for the bunch spacing is 25 ns (during the first LHC run, known as 'Run I', between 2010 and 2013, 50 ns bunch spacing was used). The
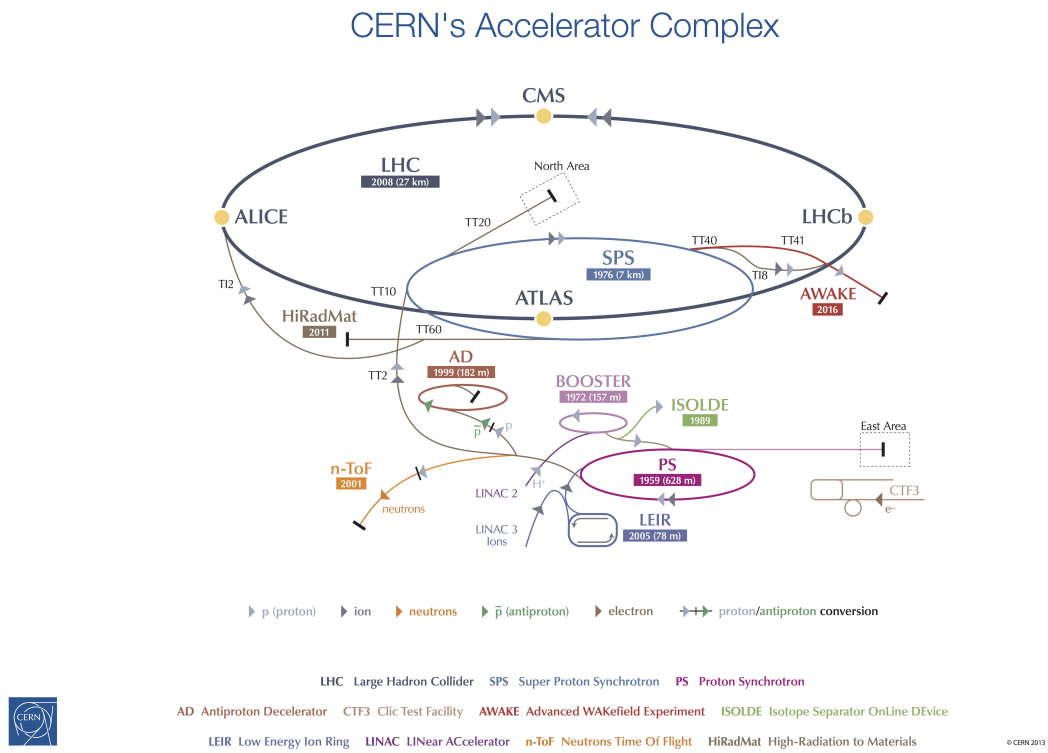
Figure 3.1: Labelled schematic diagram of the LHC injector complex.   Image ©CERN

LHC is designed to collide protons at a centre of mass energy, $\sqrt{s}$, of 14 TeV and a peak instantaneous luminosity of $\mathcal{L} = 10^{34}\,\mathrm{cm^{-2}s^{-1}}$, though during run I a maximum centre-of-mass energy of 8 TeV and a peak instantaneous luminosity of $\mathcal{L} = 7.7 \times 10^{33}\,\mathrm{cm^{-2}s^{-1}}$ were achieved. The LHC is also designed to perform ion-ion and proton-ion collisions.

There are four interaction points on the LHC ring, each surrounded by a cavern containing one of the four primary LHC experimental detectors:

- A Toroidal LHC Apparatus (ATLAS) [80] and Compact Muon Solenoid (CMS) [81] are general purpose experiments with complementary detector designs. The ATLAS experiment is discussed in more detail throughout the rest of this chapter.

- LHC beauty (LHCb) [82] is an experiment designed to study B-Physics, that is the physics of bound states involving the bottom quark. LHCb is able to make precise measurements of various processes which are sensitive to CP violation or appear in various Beyond the Standard Model (BSM) theories.

- A Large Ion Collider Experiment (ALICE) [83] is an experiment designed to study the ion-ion collisions produced at the LHC. These collisions create a high enough temperature and baryon density to create a quark gluon plasma, replicating the conditions of the early universe.

3.2 The ATLAS detector

The extensive nature of the physics programme pursued by ATLAS necessitates a detector designed to observe a wide range of final state signatures. This is achieved by a hermetic general purpose detector consisting of a series of complementary sub-components arranged in a cylindrical barrel surrounding the beam pipe with two end-caps. A computer generated image of the ATLAS detector with labelled sub-components is shown in Figure 3.2.
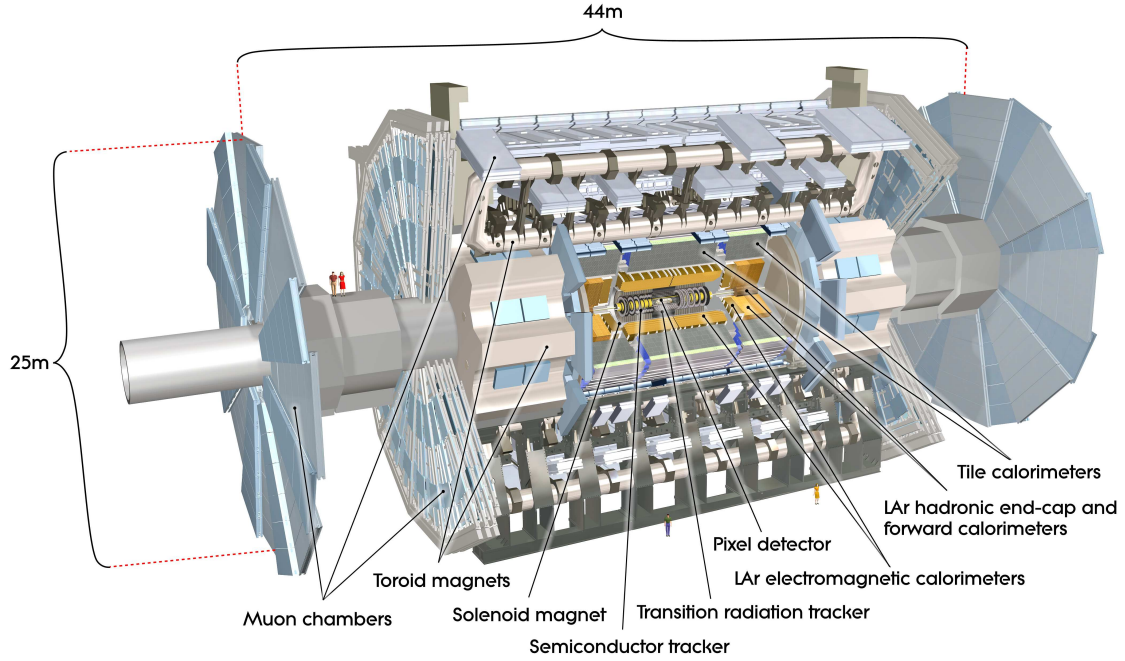
Figure 3.2: Computer generated image showing a cut-out of the ATLAS detector [80].

The following sections give a brief overview of the ATLAS detector. A detailed description may be found in Ref. [80].

3.2.1   Coordinate system and quantity definitions

The origin of the conventional ATLAS coordinate system is defined by the nominal Interaction Point (IP), where the z-axis is defined along the beam direction and the x-y plane is transverse to the beam direction. The azimuthal angle around the beam axis is labelled ϕ and the angle from the beam axis is labelled θ. The rapidity, y, is defined as:

$$y = \frac{E + p_z}{E - p_z} \tag{3.1}$$

where E is the energy of a particle travelling with momentum $\boldsymbol{p}$, and p_Z is the component of $\boldsymbol{p}$ in the direction of the beam axis. The difference in rapidity between

any two particles is invariant under boosts along the beam axis.

For highly relativistic particles, the pseudorapidity, η, is commonly used to describe the angle of particles from the beam axis:

$$\eta = -\ln \tan \frac{\theta}{2} \qquad (3.2)$$

where y and η are identical in the limit of massless particles. The quantity $\Delta R = \sqrt{(\Delta\eta)^2 + (\Delta\phi)^2}$ is often used as a measure of the angular separation between objects in the detector.

As the ATLAS detector does not have full solid angle coverage and the momenta of incoming partons are not known, it is not possible to exploit longitudinal momentum conservation. However, since the initial momentum in the transverse direction is zero, it is common to exploit momentum conservation in the transverse plane and introduce quantities such as the transverse momentum p_T, where $p_T^2 = p_x^2 + p_y^2$, and transverse energy $E_T = E\sin\theta = p_T c$. The Missing Transverse Energy (MET), with magnitude E_T^{miss}, is used to identify particles which do not interact within the detector volume, such as neutrinos.

3.2.2   Magnet system

Magnetic fields are exploited to enable measurements of the momentum of charged particles by bending their trajectory. Since the magnet system imposes geometric constraints on the other detector components, it is fundamental to the design of the entire detector. The ATLAS magnet system is composed of a thin solenoid surrounding the inner detector and three larger toroid magnets (one in the barrel and one in each end-cap) outside the calorimeters. Due to the high energy environment of the LHC, strong fields are necessary to provide sufficient bending (since the radius of curvature of a charged particle is proportional to the ratio of its transverse momentum, p_T, and the magnetic field strength, B) and this is achieved in ATLAS through the use of superconducting magnet technology.

The solenoid immerses the inner detector in a 2 T axial field and, as it sits closer to the beampipe than the calorimeters, is only 10 cm thick to minimise the effect the solenoid material has on energy measurements. The solenoid contributes $\approx$0.66 X_0 at normal incidence, where X_0 is the radiation length, the characteristic length for electromagnetic interactions in the material. The remaining magnets are designed to produce a toroidal magnetic field which traverses the muon chambers (approximately 0.5 T in the barrel region and 1.0 T in the end-caps) and hence allow an independent measurement of muon momenta.

3.2.3   Inner detector

The region of the ATLAS detector closest to the interaction point is known as the Inner Dectector (ID). It is designed to provide high precision tracking information, enabling high resolution momentum measurements of charged particles and good primary and secondary vertex identification. This is achieved in ATLAS using silicon pixel and microstrip precision detectors, in combination with the Transition Radiation Tracker (TRT). A computer generated image of the ID is shown in Figure 3.3.

The silicon pixel detectors and Semiconductor Tracker (SCT) provide precision tracking in the $|\eta|$ <2.5 region and are arranged in concentric cylinders around the beam axis in the barrel and on disks perpendicular to the beam axis in both end-caps. The pixel detectors provide the highest granularity and occupy the region radially closest to the interaction point ($45.5 < R < 242$ mm), with three cylindrical layers in the barrel and three disks in each end-cap. The pixel detector layers have intrinsic accuracies for point measurements of approximately 10 μm in the $R - \phi$ plane, while the barrel and end-cap layers provide intrinsic accuracies of 115μm in the z and R directions respectively. The innermost layer of pixels, known as the B-layer, enhances the performance of secondary vertex measurements. The pixel detector has approximately 80.4 M readout channels, around half of the ATLAS total.

6.2m

2.1m

Barrel semiconductor tracker
Pixel detectors
Barrel transition radiation tracker
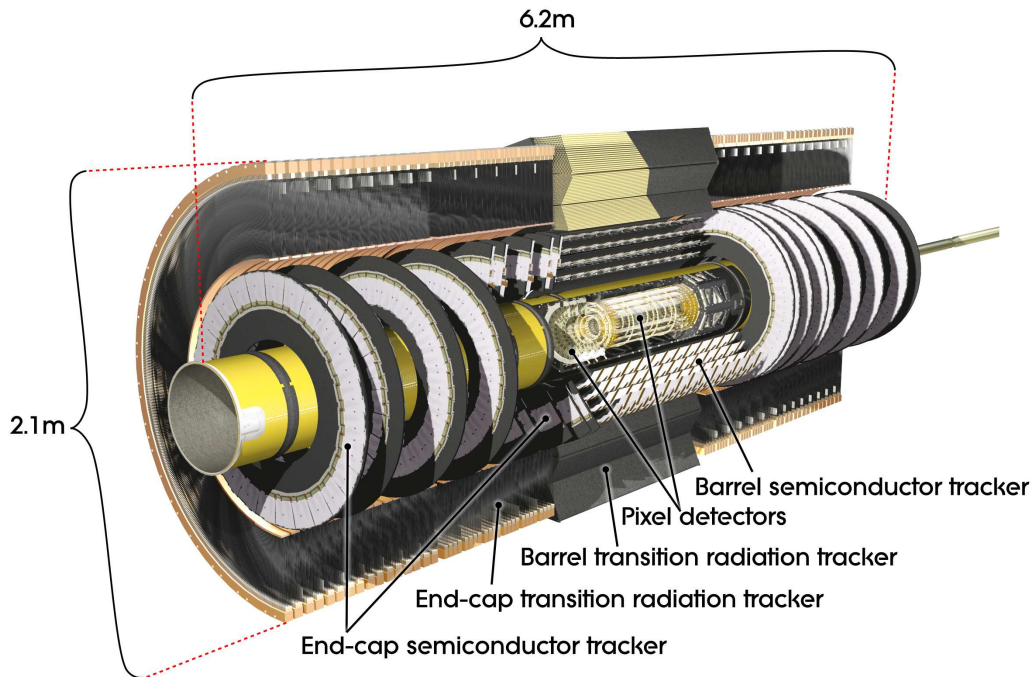End-cap transition radiation tracker
End-cap semiconductor tracker

Figure 3.3: A computer generated image showing a cut-out of the ATLAS ID [80].

The SCT modules, located in the range $255 < R < 549$ mm are arranged in four cylindrical layers in the barrel and in nine disks in each end-cap. Each layer consists of two sets of strips; a first set which is parallel to the beam direction in the barrel and perpendicular to it in the end-caps, and a second set aligned at a stereo angle of 40 mrad to the first. The strips have intrinsic accuracies of approximately 17 μm in the $R - \phi$ plane, while the barrel and end-cap layers provide intrinsic accuracies of 580μm in the z and R directions respectively.

The TRT, located in the range $554 < R < 1082$ mm in the barrel and $617 < R < 1106$ mm in the end-cap, consists of layers of gaseous straw tube elements interleaved with material inducing transition radiation (fibres in the barrel, foil in the end-caps). The straws contain a 70% Xe, 27% CO_2 and 3% O_2 gas mixture and are arranged parallel to the beam axis in the barrel and radially in wheels in the end-cap. TRT straws have an intrinsic accuracy of 130μm in $R - \phi$ and provide tracking information for $|\eta| <2.0$. Despite the lower precision per measurement of the TRT straws compared to the silicon components, the larger number of measurement points and

longer track length means that the TRT contributes substantially to momentum measurements.

The TRT also plays a role in electron identification. Photons from transition radiation typically have significantly higher energy than electrons from ionisation, and by implementing high-pass and low-pass filters in the TRT front-end electronics, discriminating power is provided. As electrons produce significant amounts of transition radiation due to their low mass, they typically produce many high threshold hits (seven to ten hits are typically expected for electrons with energies above 2 GeV).

3.2.4   Calorimeters

The ATLAS detector employs sampling calorimeter technology in the range $|\eta| < 4.9$ to absorb electrons, photons and hadronic jets within its volume, providing energy and direction measurements. The calorimeter depth is designed to fully contain electromagnetic (EM) and hadronic showers, both to enable energy measurements and to prevent the punch-through of particles to the muon system. The specific technologies employed in different parts of the calorimeter are selected based on requirements relating to physics processes of interest and the radiation environment. The main Liquid Argon (LAr) EM calorimeter covers the pseudorapidity range $|\eta| < 3.2$. For hadronic calorimetry, a scintillator-tile calorimeter is used in an extended barrel region ($|\eta| < 1.7$) and LAr calorimeters are used in the end-caps. LAr calorimeters are used for both EM and hadronic calorimetry in the forward region up to $|\eta| < 4.9$. A fine granularity is implemented in the η region matching the ID, allowing for precision measurements of electrons and photons. A computer generated image of the ATLAS Calorimeters is shown in Figure 3.4.
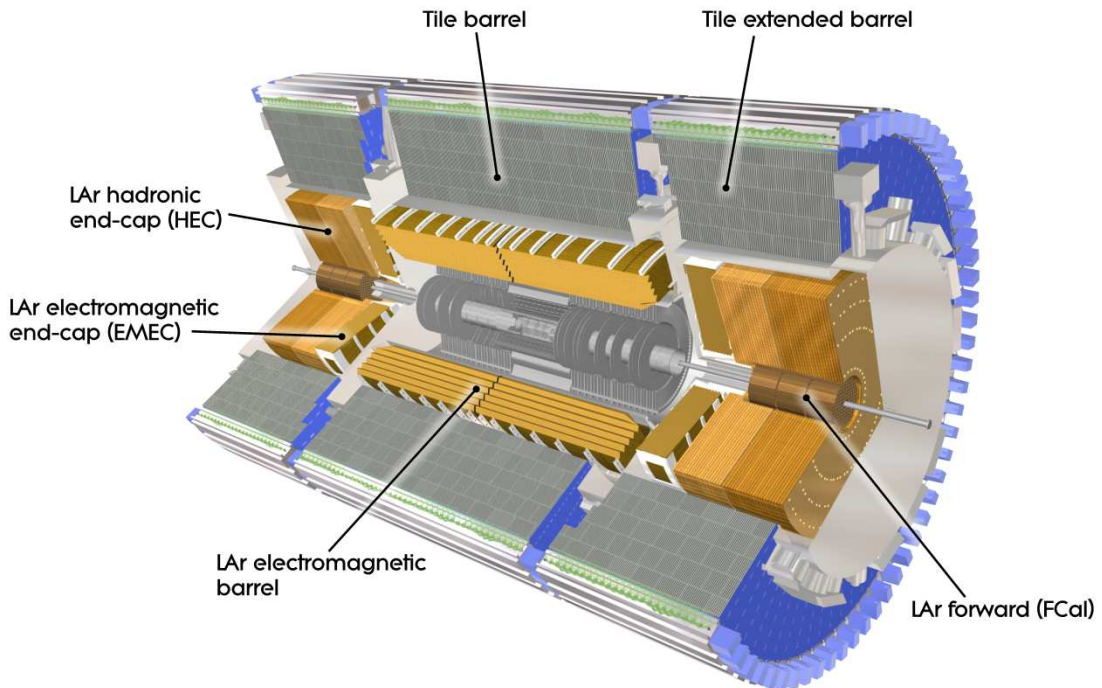
Figure 3.4: A computer generated image showing a cut-out of the ATLAS Calorimeters [80].

Electromagnetic LAr calorimeter

The EM calorimeter, with a barrel section and two end-cap sections, uses lead absorber plates and LAr as the active detection material, where the absorbers and Kapton electrodes are accordion shaped, avoiding azimuthal cracks in coverage which would degrade the calorimeter energy resolution and allowing fast readout (see Figure 3.5).The thickness of lead in the absorber layers is designed to optimise the calorimeter energy resolution. In the fine granularity region, the EM calorimeter is arranged in three segmented layers (decreasing in granularity with distance from the IP) to allow measurements of the energy and direction of EM showers. The remainder of the EM calorimeter has two layers. An additional LAr pre-sampler detector, positioned closer to the beam pipe than the solenoid, is present in the region $|\eta| < 1.8$ to correct for the energy lost by electrons and photons in the magnet. The total thickness of the EM calorimeter is $> 22\ X_0$ in the barrel and $> 24\ X_0$ in the end-caps.

Figure 3.5: Diagram of a barrel module of the LAr calorimeter, showing the accordion geometry and the granularity in η and ϕ [80].

The resolution of a sampling calorimeter can be parameterised by:

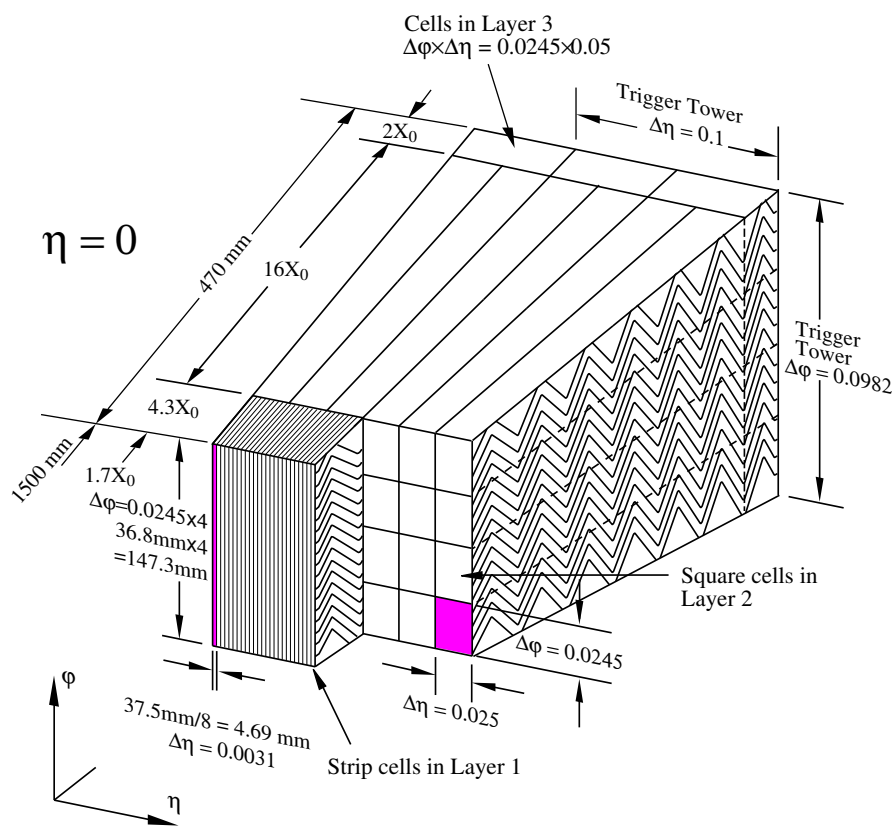$$\frac{\sigma_E}{E} = \frac{a}{\sqrt{E}} \oplus \frac{b}{E} \oplus c \qquad (3.3)$$

where a, b and c are known as the *stoachastic*, *noise* and *constant* terms respectively. For the ATLAS LAr calorimeter, typical parameter values are $a = 0.1\sqrt{\text{GeV}}$, $b = 0.17\,\text{GeV}$ and $c = 0.7\,\%$ (where E has units of GeV) [84].

Hadronic calorimeters

The Tile Calorimeter (TileCal), with steel absorbing layers and scintillating tiles as active material, consists of a barrel section ($|\eta| < 1.0$) and two extended barrel sections ($0.8 < |\eta| < 1.7$) and is also segmented in three layers. The hadronic end-cap calorimeter uses LAr technology with copper absorbing layers, and has two wheels, each segmented in two layers, in each end-cap.

In total, the ATLAS calorimeter comprises 9.7 nuclear interaction lengths (λ, the characteristic length for hadronic interactions) of active material in the barrel and $10\,\lambda$ in the end-caps, enough to reduce the punch-through of jets to the muon system to a level significantly lower than the irreducible background from prompt and decay muons.

The energy resolution of the TileCal for hadronic jets is approximately:

$$\frac{\sigma_E}{E} = \frac{0.5}{\sqrt{GeV}} \oplus 0.03 \qquad (3.4)$$

where E has units of GeV [85].

Forward calorimeter

The ATLAS Forward Calorimeter (FCal) is a LAr calorimeter consisting of three modules in each end-cap. The first module is made of copper and is optimised to measure electromagnetic interactions, whereas the other modules are made of tungsten and measure hadronic interactions.

3.2.5   Muon spectrometer

The ATLAS Muon Spectrometer (MS), composed of separate precision tracking and triggering chambers, provides a second measurement of muon momenta based on tracks bent by the toroid magnets, whose configuration is designed to produce a field orthogonal to the muon trajectories where possible. The bending occurs due to the barrel toroid for $|\eta| < 1.4$ and due to the end-cap toroids for $1.6 < |\eta| < 2.7$. In the region $1.4 < |\eta| < 1.6$, muon trajectories are bent by a combination of the fields from both the barrel and end-cap magnets. The MS is able to make standalone measurements of muon momenta over a wide range (≈ 3 GeV - ≈ 1 TeV), with a transverse momentum resolution of approximately 10% for 1 TeV muons.

The tracking chambers are arranged in three cylindrical layers, placed on and between the toroid coils in the barrel region, and in planes perpendicular to the beam axis, in front of and behind the toroids, in the end-caps. An optical aligment system provides precise measurements of the relative alignment of chambers. Chambers overlap in ϕ, allowing further studies of chamber alignment using tracks recorded by overlapping chambers and maximising coverage. A gap in coverage exists at $\eta \simeq 0$ to allow services access to the rest of the detector and additional acceptance gaps are present due to detector support structures.

Precision tracking is provided by Monitored Drift Tube (MDT) chambers, made up of several layers of drift tubes and measuring coordinates in η, in the region $|\eta| < 2.7$. Cathode Strip Chambers (CSC), which are multiwire proportional chambers with

cathode planes segmented into orthogonal strips, are used instead in the innermost layer for $2.0 < |\eta| < 2.7$ as they give measurements of both the η and ϕ coordinates and their higher rate capability and time resolution makes them better suited to deal with the higher background rates in this region.

Chambers providing fast triggering information complement the tracking chambers in the region $|\eta| < 2.0$. Resistive Plate Chambers (RPC) are used in the barrel and Thin Gap Chambers (TGC) in the end-caps. Both types of chamber are designed to provide signals quickly enough to identify the correct bunch crossing of the event. The trigger chambers measure both track coordinates, so MDT measurements use the ϕ co-ordinate from matched trigger chamber hits to supplement the η measurement.

A computer generated image of the ATLAS Muon Spectrometer is shown in Figure 3.6.

3.2.6   Trigger and data acquisition

The nominal 40 MHz bunch crossing frequency provided by the LHC is much too high to process and store collision data from every collision event and ATLAS is limited to recording events at a rate of around 200 Hz. To achieve this level of rate reduction, ATLAS adopts a three-level trigger system where the first level is hardware-based and subsequent levels, collectively known as the Higher Level Trigger (HLT), involve the reconstruction of all or part of the event data on parallelised computing farms. A schematic representation of the structure of the ATLAS trigger is shown in Figure 3.7.

The Level-1 (L1) trigger uses reduced granularity information from the Calorimeters and MS to identify high p_T muons, electrons, photons, jets and hadronic τ decays, as well as large E_T and E_T^{miss}. It is required to make an event-by-event decision in less than 2.5 μs, where approximately 1 μs is taken up by the propagation of electric signals from the detector. The L1 trigger reduces the rate to approximately 75 kHz,
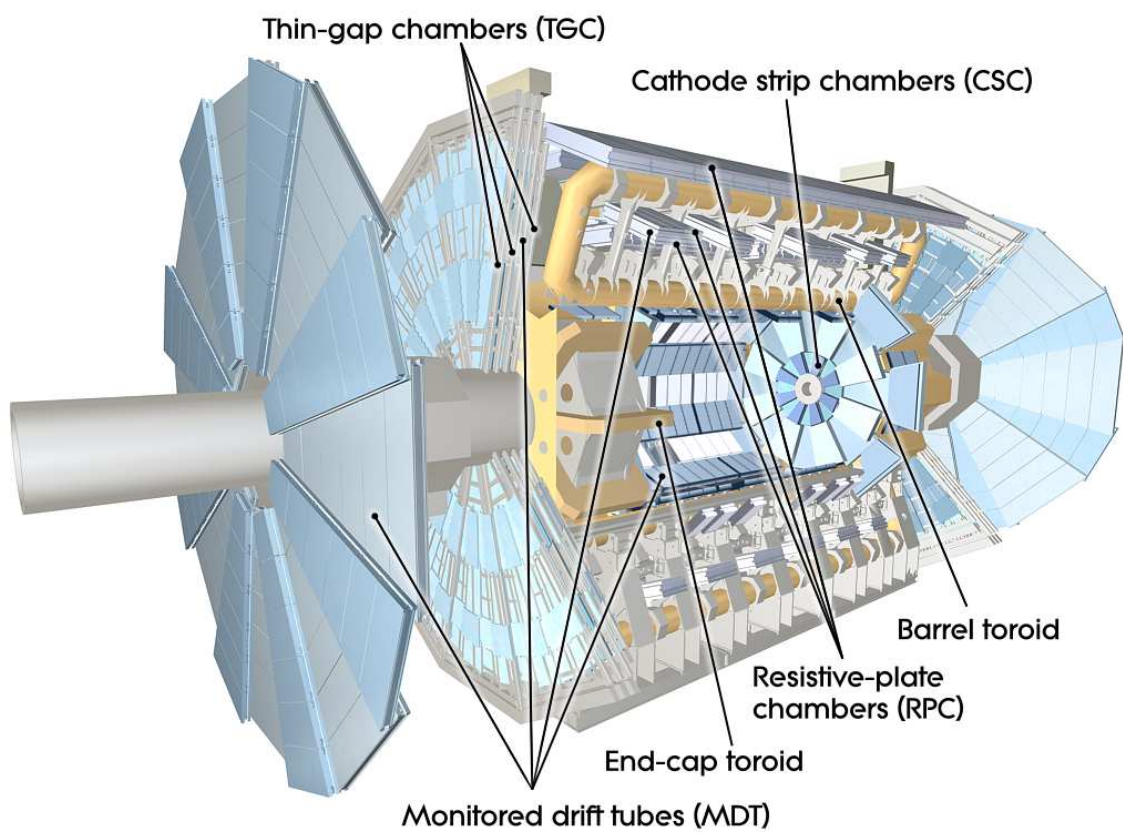
Figure 3.6: A computer generated image showing a cutout of the ATLAS MS [80].
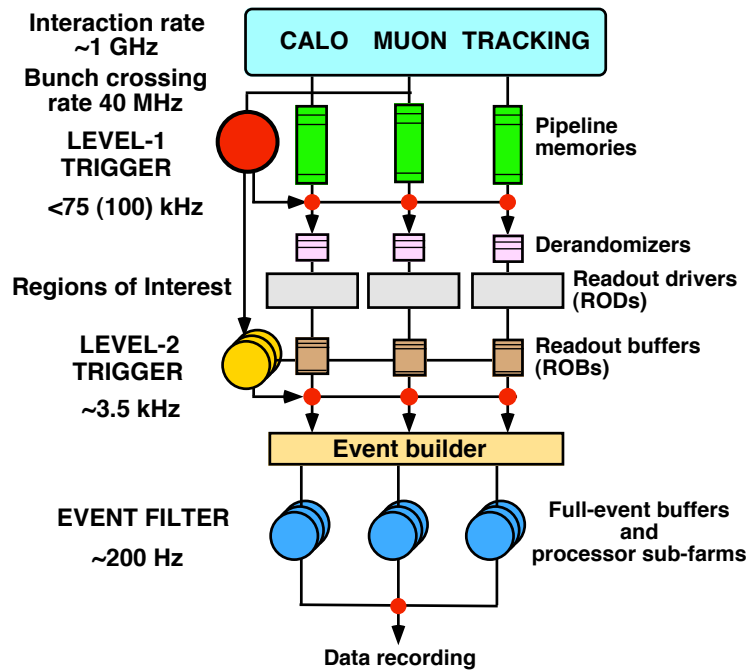
Figure 3.7: Schematic diagram of the structure of the ATLAS three level trigger system [86].

identifying Regions of Interest (RoI) - geometric detector regions with boundaries defined by $\eta - \phi$ co-ordinates - where a potentially interesting signature has ocurred.

The Level-2 (L2) trigger uses full granularity detector information from the regions defined by these RoIs, approximately 2% of the full event data on average, to further reduce the rate. The L2 trigger reduces the trigger rate to around 3.5 kHz, taking 40 ms on average to process events. In the case that an event is accepted by L2, it is then passed to the Event Filter (EF), which builds the full event and uses more sophisticated algorithms to make a final decision on whether to record an event, taking 4 s on average. The EF also tags events it selects, placing them into event streams which group events containing similar signatures to be recorded together in the same data files which are permanently stored.

The trigger efficiencies for muons and electrons at each stage of the trigger chain, are presented for the 8 TeV data in Figure 3.8.

The Data Acquisition (DAQ) system controls the movement of data through the trig-

ger system and to permanent storage and also manages the configuration and monitoring of the ATLAS detector during data-taking. The average size of a recorded event is approximately 1.3 Mb.

3.3   Data Sample

The results presented in this thesis are based on the data collected by ATLAS during LHC Run I, between 2010 and 2012, where the LHC operated first at $\sqrt{s} = 7$ TeV and later at $\sqrt{s} = 8$ TeV. Only events recorded in periods where all detector components were operating normally are considered. The cumulative collected luminosity during LHC Run I is illustrated in Figure 3.9.

The average number of interactions per bunching crossing for the $\sqrt{s} = 7$ TeV and $\sqrt{s} = 8$ TeV datasets is shown in Figure 3.10. As the LHC operated with a bunch spacing of 50 ns, rather than the design bunch spacing of 25 ns, a high number of protons per bunch was required to maintain a high instantaneous luminosity, leading to a higher average number of interactions per bunch crossing than the design value.

The $\sqrt{s} = 7$ TeV and $\sqrt{s} = 8$ TeV data samples used are summarised in Table 3.1.

Table 3.1: Summary of the $\sqrt{s} = 7$ TeV and $\sqrt{s} = 8$ TeV data samples. The "Data quality efficiency" column indicates the fraction of the delivered integrated luminosity collected when all detector components were functioning normally, and corresponds to the "Good for Physics" histogram in Figure 3.9.

Year	$\sqrt{s}$	Instantaneous peak luminosity	Average Pile-up ($< \mu >$)	Data	Data taking efficiency	Data quality efficiency
2011	7 TeV	3.65 $\times 10^{33}$cm^{-2}s^{-1}	9.1	4.5 fb^{-1}	$\approx$96.5%	$\approx$89.9%
2012	8 TeV	7.73 $\times 10^{33}$cm^{-2}s^{-1}	20.3	20.3 fb^{-1}	$\approx$95.5%	$\approx$95.3%
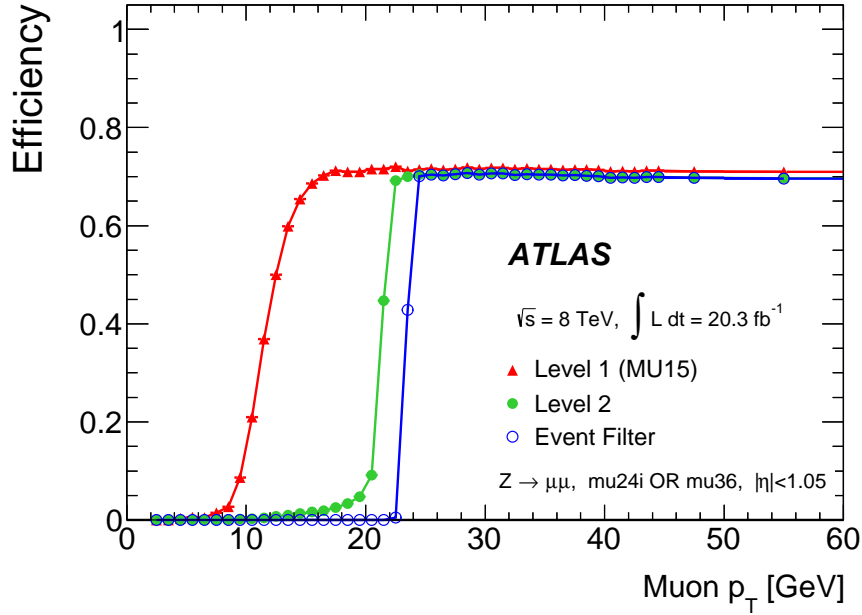
(a)
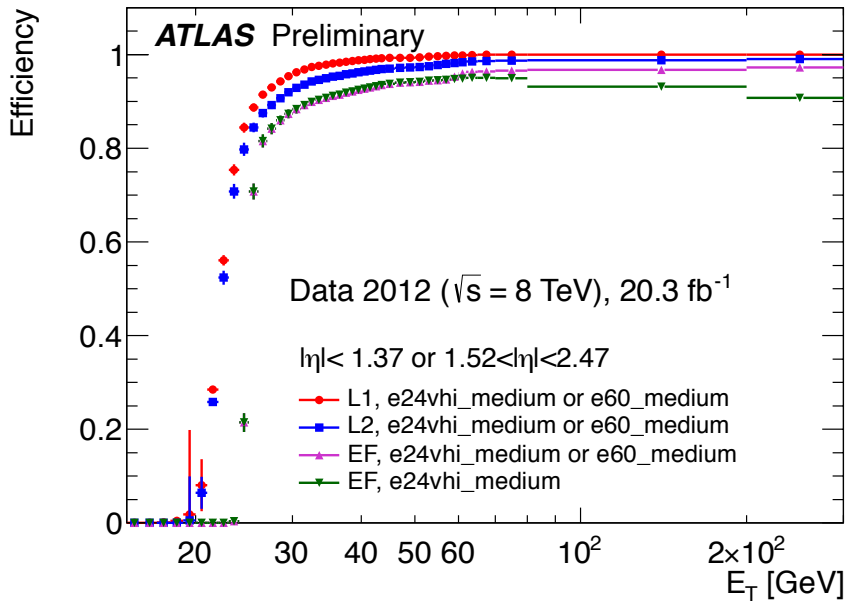
(b)

Figure 3.8: a) Muon trigger efficiency (in the barrel region, $|\eta| < 1.05$) as a function of muon p_T [87], and b) electron trigger efficiency (for the pseudorapidity regions $|\eta| < 1.37$ and $1.52 < |\eta| < 2.47$) as a function of electron E_T [88]. In both cases, the efficiency is measured in data with respect to objects selected offline using a tag-and-probe method. The reconstruction and identification of muons and electrons is described in Sections 3.4.1 and 3.4.2 respectively. The efficiency is shown separately for the L1, L2 and EF stages.

Figure 3.9: The cumulative integrated luminosity delivered by the LHC, recorded by ATLAS and passing data quality requirements as a function of time [88].

Figure 3.10: The mean number of interactions per bunch crossing for ATLAS data recorded at $\sqrt{s} = 7$ TeV and $\sqrt{s} = 8$ TeV [88].

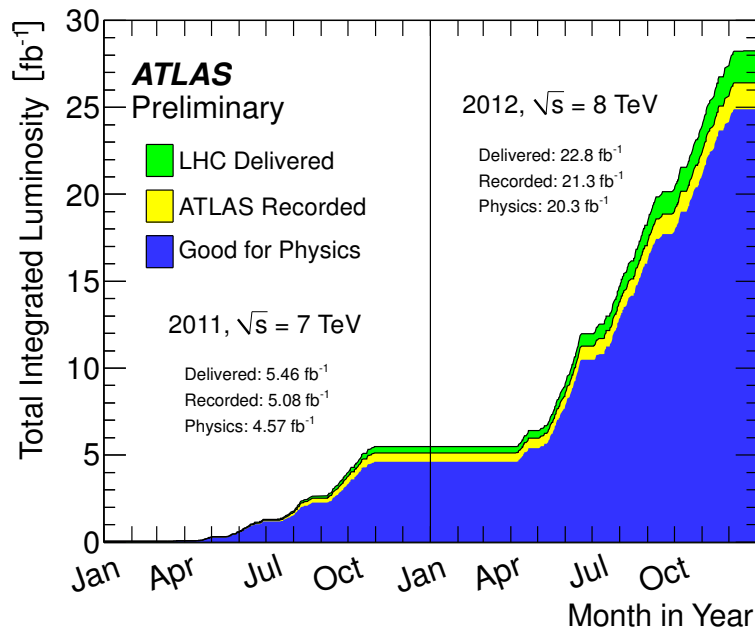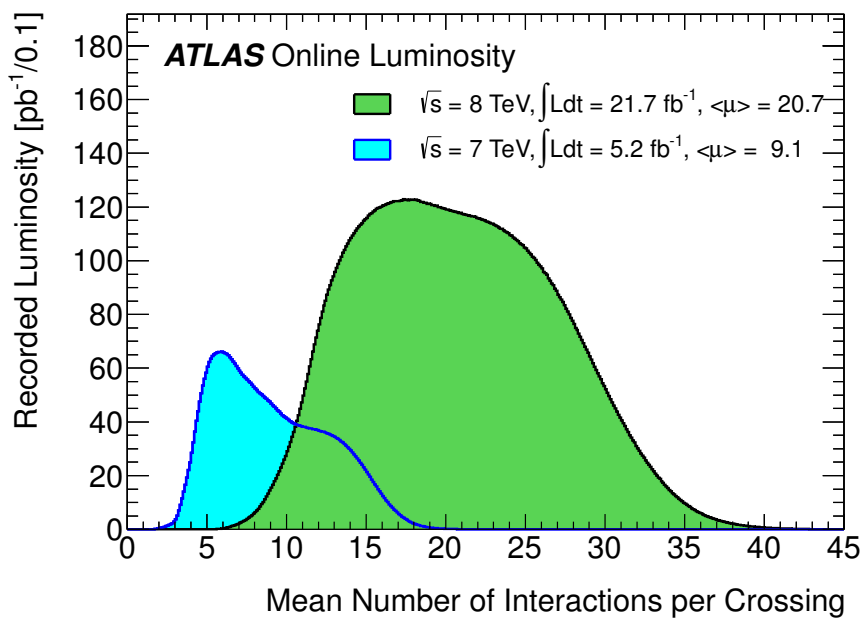### 3.3.1 Luminosity Measurement

A precise measurement of the luminosity is important for many ATLAS analyses, in particular for cross section measurements.

Using several event and particle counting algorithms with the ID, calorimeters and dedicated luminosity detectors, ATLAS monitors the luminosity delivered by the LHC by measuring the observed average number of interactions per bunch crossing. The delivered luminosity, $\mathcal{L}$, may be written as:

$$\mathcal{L} = \frac{\mu n_b f_r}{\sigma_{inelastic}} = \frac{\mu_{vis} n_b f_r}{\sigma_{vis}} \tag{3.5}$$

where n_b is the number of bunches, f_r is the LHC revolution frequency, μ is the number of inelastic interactions per bunch crossing and $\sigma_{inelastic}$ is the total inelastic cross section [89]. The number of visible inelastic interactions (excluding diffractive processes which do not register signals in the relevant detectors) and the visible inelastic cross section may be written as $\mu_{vis} = \epsilon \mu$ and $\sigma_{vis} = \epsilon \sigma_{inelastic}$ respectively, where ϵ is the efficiency of a given detector and algorithm.

Since the ATLAS monitoring measures μ_{vis}, the absolute luminosity scale is given by σ_{vis}. In terms of the accelerator parameters, the luminosity can alternatively be expressed as:

$$\mathcal{L} = \frac{n_b f_r n_1 n_2}{2\pi \Sigma_x \Sigma_y} \tag{3.6}$$

where $n_{1,2}$ are the number of protons in each bunch, and $\Sigma_{x,y}$ are the horizontal and vertical convolved beam widths [89]. The calibration of σ_{vis} is performed using dedicated beam-separation scans known as Van der Meer scans [90, 91]. Via these scans, Σ_x and Σ_y are measured directly and combining these with measurements of the bunch populations $n_{1,2}$ gives an absolute luminosity measurement.

3.4   Physics object reconstruction and identification

3.4.1   Muons

In ATLAS muon momentum is measured separately in the ID and MS. Four sets of reconstruction criteria are used depending on the information available from the various sub-detectors, resulting in four categories: combined muons (CB), stand-alone muons (SA), segment-tagged muons (ST) and calorimeter-tagged muons (CaloTag) [92]. In most cases, muons are identified by matching full or partial tracks from the MS with ID tracks. For detector regions where either the ID or MS lacks coverage, alternative strategies are used.

- **Combined muons** are the primary muon type used in ATLAS analyses, where muon candidates are identified by matching an MS track with an ID track and the track parameters are obtained by combining the two measurements. Combined muons have the highest purity of the ATLAS muon types.

- **Segment-tagged muons** are muons that have not traversed all MS stations, either because they have low p_T or because their trajectories pass through regions which are not fully instrumented. ST muons are identified using ID tracks which, when extrapolated to the MS, match with a reconstructed track segment. In this case, the track parameters of the ID track are assigned to the muon.

- **Stand-alone muons** are reconstructed using only information from the MS. The MS track is extrapolated back to the interaction point, taking into account effects from multiple scattering and energy loss in the traversed material when determining compatibility with the primary vertex. SA muons are used in the region $2.5 < |\eta| < 2.7$, outside of the geometrical acceptance of the ID.

- **Calorimeter-tagged** muons are used in the region $|\eta| < 0.1$ where the MS is only partially instrumented. Muons are reconstructed using ID tracks with

$p_T > 15$ GeV, where the track is associated with an energy deposit in the calorimeter compatible with a muon. The track parameters of the ID track are assigned to the muon.

The reconstruction of muons using information from the MS (CB, SA and ST) is performed using two separate algorithms which implement differently both the reconstruction of tracks in the MS and the combination of ID and MS information. The 'Chain 1' reconstruction algorithm combines the track parameters of the ID and MS tracks using the corresponding covariance matrices and the 'Chain 2' algorithm refits the muon track using the hits from both the ID and MS. The algorithms also use different pattern recognition strategies for building tracks in the MS. The $H \rightarrow ZZ^{(*)} \rightarrow 4\ell$ analysis, described in detail in this thesis, uses muons reconstructed with the 'Chain 1' algorithm.

The combination of muon reconstruction types results in a reconstruction efficiency of around 99% for the majority of the geometrical acceptance of the detector. The use of ST muons allows the recovery of efficiency in MS regions only partially instrumented, in particular $1.1 < |\eta| < 1.3$, and the use of CaloTag muons similarly allows for a significant increase in efficiency in the uninstrumented region $|\eta| < 0.1$. The muon reconstruction efficiency, measured using a tag-and-probe technique[1] with $Z \rightarrow \mu\mu$ events, is shown as a function of $|\eta|$ in Figure 3.11

Above $p_T \approx 20$ GeV, the muon reconstruction efficiency remains constant as a function of p_T. For low p_T, a sharp increase in the reconstruction efficiency is observed above $p_T \approx 3$ GeV, which is the momentum required for a muon to pass through the calorimeters and produce hits in at least two muon chambers. The muon reconstruction efficiency as a function of the average number of interactions per bunch crossing, $< \mu >$, is stable and above 99% except at the very highest $< \mu >$. The muon reconstruction efficiency, measured using $Z \rightarrow \mu\mu$ and $J/\psi \rightarrow \mu\mu$ decays,

---

[1] Data driven tag-and-probe methods are used in ATLAS to measure reconstruction, identification or trigger efficiencies using two-body decay processes, for example $Z \rightarrow \mu\mu$, where the 'tag' particles are used to select a sample of events and the 'probe' paricles are used for the efficiency measurement. An example implementation of this method is described in Ref. [92].
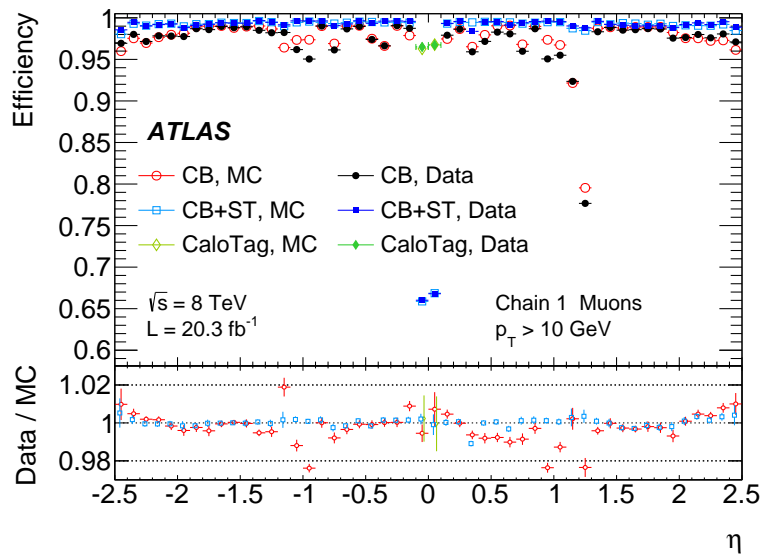
Figure 3.11:   Muon reconstruction efficiency as a function of η, measured in $Z \to \mu\mu$ events using muons with p_T >10 GeV and reconstructed using the 'Chain 1' algorithm and different muon reconstruction types. The error bars on the efficiencies represent the statistical uncertainties. The bottom panel shows the ratio between measured and predicted efficiencies. The error bars on the ratios show the total uncertainties, combining the statistical and systematic components. Figure from Ref. [92].

is shown as a function of p_T and $< \mu >$ in Figure 3.12.

(a)   (b)
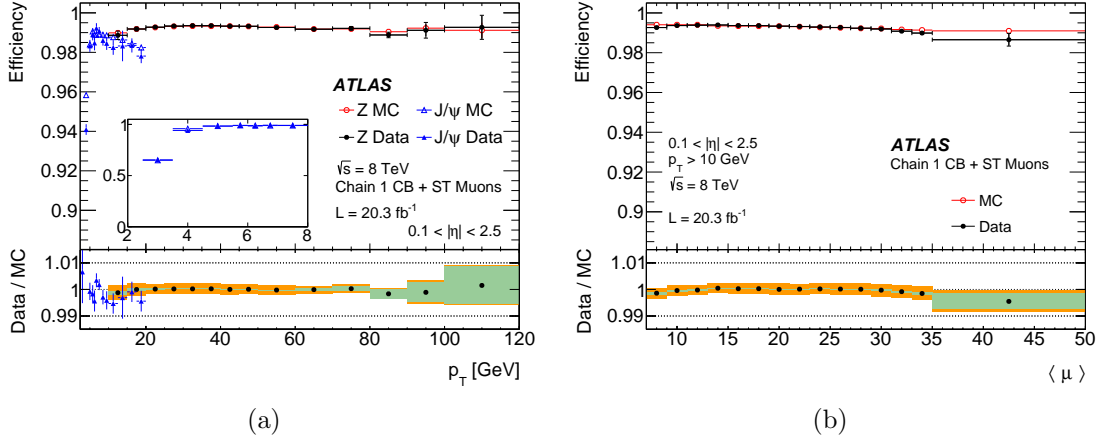
Figure 3.12:   Reconstruction efficiency for CB+ST muons reconstructed with the 'Chain 1' algorithm as a function of: a) the p_T of the muon, for muons with $0.1 < |\eta| < 2.5$ using $Z \rightarrow \mu\mu$ and $J/\psi \rightarrow \mu\mu$ decays, and b) the average number of collisions per bunch crossing, $< \mu >$ for muons with $0.1 < |\eta| < 2.5$ and $p_T > 10$ GeV. The panels at the bottom show the ratio between the measured and predicted efficiencies. The green bands show the statistical uncertainty only and the orange bands show the total uncertainty. Figure from Ref. [92].

Corrections derived from observed $Z \rightarrow \mu\mu$ and $J/\psi \rightarrow \mu\mu$ decays events are applied to the simulation of the muon reconstruction to match the momentum scale and resolution measured in data. The use of $J/\psi \rightarrow \mu\mu$ events in deriving the correction significantly improves the precision in the low momentum range, which is particularly important for the measurement of the Higgs boson mass in the $H \rightarrow ZZ^{(*)} \rightarrow 4\ell$ final state. Figure 3.13 shows a validation of this correction, where the peak position and width of the J/ψ, Z and Υ resonances in data and simulation are fitted with and without the correction applied. As Υ decays were not used in the derivation of the correction, they provide an independent validation sample.

3.4.2   Electrons

The reconstruction of electrons in ATLAS combines information from the ID and the LAr EM calorimeter, where background discrimination is provided by the shower shape information available from the calorimeter, high-threshold TRT hits and the
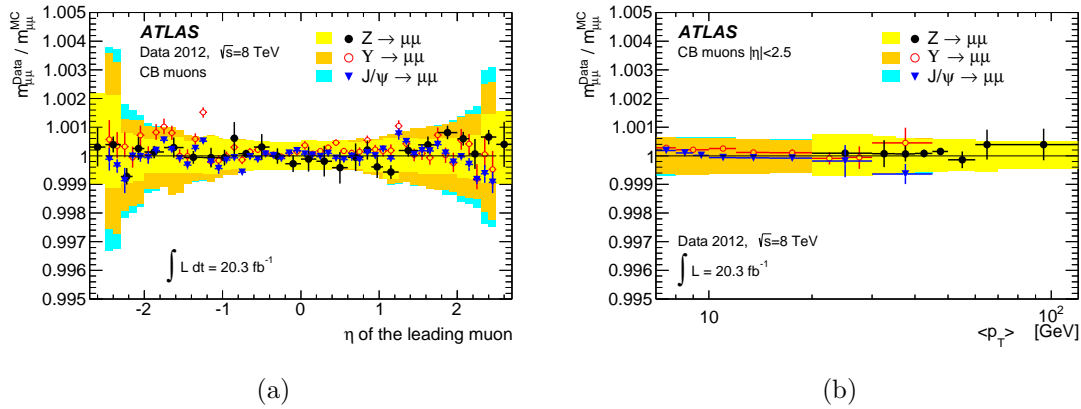
Figure 3.13:   Ratio of the reconstructed dimuon invariant mass for data to that in simulation for $Z \to \mu\mu$, $\Upsilon \to \mu\mu$ and $J/\psi \to \mu\mu$ events: (a) as a function of the η of the highest p_T muon, and (b) as a function of the average transverse momentum $< p_T >$ of the two muons. The coloured bands show the systematic uncertainty on the simulation corrections. Figure from Ref. [93].

compatibility of the tracking and calorimeter information. The details of the electron reconstruction and identification are different for the $\sqrt{s} = 7$ TeV and $\sqrt{s} = 8$ TeV datasets [94] [95].

Electron candidates are reconstructed by matching a track in the ID with a cluster of energy deposited in the EM calorimeter. The calorimeter cluster is required to satisfy a number of criteria related to its longitudinal and transverse shower profiles. Track candidates associated with the EM cluster are fitted using a Gaussian Sum Filter (GSF) to take into account energy losses through bremsstrahlung [96]. For the 8 TeV dataset, the ATLAS reconstruction was modified to account for larger bremsstrahlung energy losses and to improve track-to-cluster matching, resulting in an average increase in electron reconstruction efficiency of 5% for electrons with $E_T > 15$ GeV and 7% for $E_T < 15$ GeV.

ATLAS analyses use a range of cut-based (i.e. a set of cuts on multiple input variables) and likelihood-based selections to identify electrons, where typically the most stringent selections are applied in final states which are subject to higher backgrounds and, to maintain as large as possible an acceptance, looser cuts are used in final states with lower backgrounds. The ATLAS $H \to ZZ^{(*)} \to 4\ell$ analysis

uses the 'loose' likelihood-based identification for the 8 TeV data and the 'multi-lepton' cut-based identification for the 7 TeV data.

The likelihood-based identification, using a discriminant based on signal and background probability density functions obtained from data, improves the rejection of light-flavour jets and photon conversions, objects that may be misidentified as an electron, by a factor of two for the same signal efficiency as the 'multi-lepton' method. The likelihood-based methods additionally allow the inclusion of variables where a cut would impact too strongly on the identification efficiency, for example the fraction of energy contained in the first calorimeter sampling layer. A description of the variables used in the 'loose' likelihood-based and 'multi-lepton' cut-based selections is given in Table 3.2.

The combined electron reconstruction and identification efficiency, for the various likelihood based selection working points used in ATLAS analyses, is shown as a function of p_T and η in Figure 3.14.

(a)   (b)
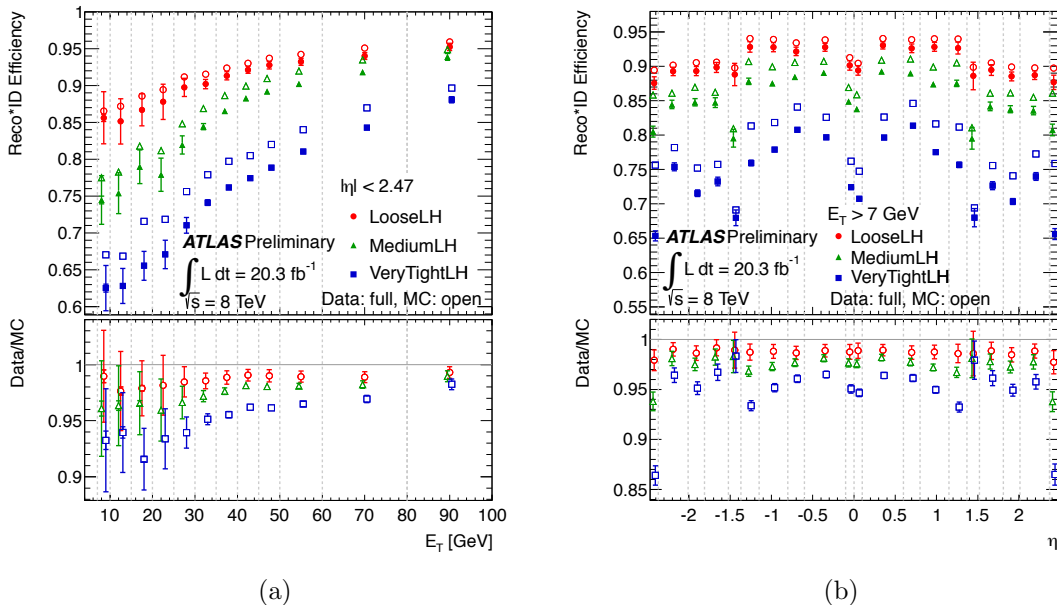
Figure 3.14:   Combined reconstruction and identification efficiency for electrons identified using various likelihood-based selection working points: a) as a function of E_T, and b) as a function of η. Data are shown with full points and simulated data are shown with open points. The panel shows the ratio between the measured and simulated efficiencies. Figure from Ref. [95].

Table 3.2: Definition of discriminating variables used for electron identification using the multilepton cut-based criteria and loose likelihood criteria [95]. The R_ϕ and f_1 variables are not used in the multilepton criteria and the n_{TRT} variable is not used in the loose likelihood criteria.

Type	Description	Name
Hadronic leakage	Ratio of E_{T} in the first layer of the hadronic calorimeter to E_{T} of the EM cluster (used over the range $|\eta| < 0.8$ and $|\eta| > 1.37$)	R_{Had1}
	Ratio of E_{T} in the hadronic calorimeter to E_{T} of the EM cluster (used over the range $|\eta| > 0.8$ and $|\eta| < 1.37$)	R_{Had}
Third layer of EM calorimeter	Ratio of the energy in the third layer to the total energy	f_3
Middle layer of EM calorimeter	Lateral shower width, $\sqrt{(\Sigma E_i \eta_i^2)/(\Sigma E_i) - ((\Sigma E_i \eta_i)/(\Sigma E_i))^2}$, where E_i is the energy and η_i is the pseudorapidity of cell i and the sum is calculated within a window of 3×5 cells	$W_{\eta 2}$
	Ratio of the energy in $3{\times}3$ cells over the energy in $3{\times}7$ cells centered at the electron cluster position (not used for multilepton)	R_ϕ
	Ratio of the energy in $3{\times}7$ cells over the energy in $7{\times}7$ cells centered at the electron cluster position	R_η
Strip layer of EM calorimeter	Shower width, $\sqrt{(\Sigma E_i (i - i_{\mathrm{max}})^2)(\Sigma E_i)}$, where i runs over all strips in a window of $\Delta\eta \times \Delta\phi \approx 0.0625 \times 0.2$, corresponding typically to 20 strips in η, and i_{max} is the index of the highest-energy strip	W_{stot}
	Ratio of the energy difference between the largest and second largest energy deposits in the cluster over the sum of these energies	E_{ratio}
	Ratio of the energy in the strip layer to the total energy (not used for multilepton)	f_1
Track quality	Number of hits in the B-layer (discriminates against photon conversions)	n_{Blayer}
	Number of hits in the pixel detector	n_{Pixel}
	Number of total hits in the pixel and SCT detectors	n_{Si}
	Momentum lost by the track between the perigee and the last measurement point divided by original momentum	$\Delta p/p$
TRT	Total number of hits in the TRT (not used for loose likelihood)	n_{TRT}
	Ratio of the number of high-threshold hits to the total number of hits in the TRT	$F_{\mathrm{HT}}(\mathrm{rTRT})$
Track–cluster matching	$\Delta\eta$ between the cluster position in the strip layer and the extrapolated track	$\Delta\eta_1$
	$\Delta\phi$ between the cluster position in the middle layer and the extrapolated track	$\Delta\phi_2$

The electron E_T is calculated using the measured energy of the calorimeter cluster, corrected for energy lost before the calorimeter or deposited in neighbouring cells, and the direction of the ID track at the interaction point. The precise determination of the scale and resolution of the electron energy is important for the measurement of the Higgs boson mass in this channel and the calibration, described in Ref. [97], exploits multivariate techniques and relies on a detailed knowledge of the detector geometry and material distribution. The energy scale calibration is cross checked as a function of E_T in bins of $|\eta|$ using $J/\psi \rightarrow ee$ and $Z \rightarrow ee$ events, as shown in Figure 3.15.
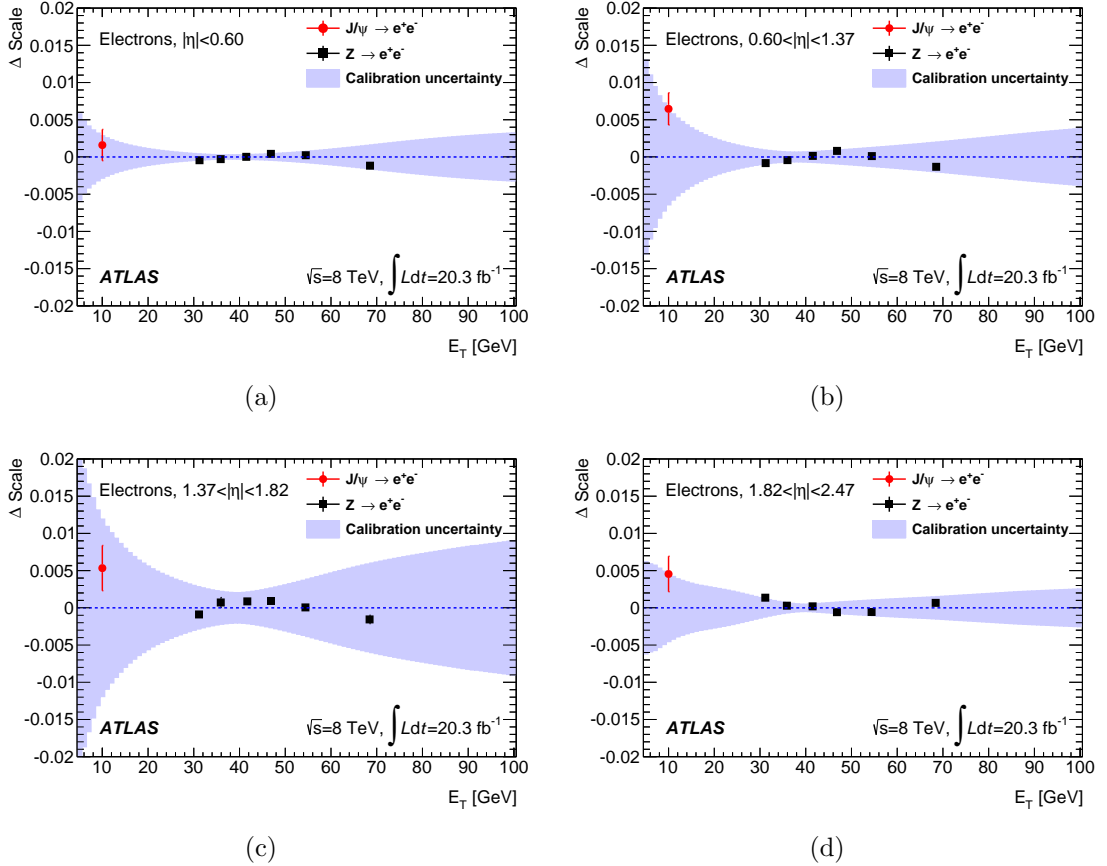
Figure 3.15: Energy scale factors, Δ Scale, between the nominal electron energy scale and the measured energy scale, using the $J/\psi \rightarrow ee$ and $Z \rightarrow ee$ cross check analyses: (a) for $|\eta| < 0.6$, (b) for $0.6 < |\eta| < 1.37$, (c) for $1.37 < |\eta| < 1.82$, and (d) for $1.82 < |\eta| < 2.37$. The systematic uncertainty on the electron energy scale is shown as the shaded area. Figure from Ref. [93].

In the ATLAS $H \rightarrow ZZ^{(*)} \rightarrow 4\ell$ analysis, for electron candidates with $E_T < 30$ GeV whose cluster E_T and track p_T agree within uncertainties, a combined fit of

the cluster energy and track momentum is performed to calculate the electron E_T, improving the four-lepton mass resolution, $m_{4\ell}$ by approximately 4% for final states containing electrons. The improvement is significant for electrons falling in the so-called 'crack-region', $1.37 < |\eta| < 1.52$, where the barrel and end-cap calorimeters overlap and the energy resolution is typically poor.

3.4.3   Photons

Photons are used in the $H \to ZZ^{(*)} \to 4\ell$ analysis as part of the Final State Radiation (FSR) correction described in section 4.2.1. Photons are reconstructed in ATLAS by searching for clusters in the EM calorimeter, where clusters without matching ID tracks are classified as unconverted photon candidates and clusters matched to pairs of tracks consistent with $\gamma \to e^+e^-$ conversions are classified as converted photon candidates [98]. In some cases, clusters are reconstructed with both photon and electron hypotheses.

The reconstruction efficiency for photons is almost 100%, though as some are misidentified as electrons, the identification efficiency for photons with $30 < E_T < 100$ GeV is around 83-95% for unconverted photons, and 87-99% for converted photons [99]. The photon energy scale uncertainty is similar for converted and unconverted photons, and is 0.2-0.3% for $|\eta| < 1.37$ and $|\eta| > 1.82$, and 0.6% for the intermediate region [97]. It does not depend strongly on E_T.

3.4.4   Jets

In the $H \to ZZ^{(*)} \to 4\ell$ analysis, jets are used to distinguish between Higgs boson production mechanisms as described in chapter 5.1. Jets are reconstructed in AT-LAS using topological clusters of calorimeter cells with the anti-k_t algorithm [100], using a distance parameter of $R = 0.4$ for the $H \to ZZ^{(*)} \to 4\ell$ analysis. Jets are calibrated to the hadronic scale using simulation, where a Jet Energy Scale (JES)

correction, estimated using a combination of in situ techniques, is applied to account for differences between data and simulation [101].

The uncertainty on the calibration ranges from below 1% in the central region to 3.5% for low p_T jets at high $|\eta|$ for the $\sqrt{s} = 8$ TeV data, which is reduced significantly compared to the $\sqrt{s} = 7$ TeV data. The uncertainty on the jet energy resolution is around 1% for jets with above $p_T > 100$ GeV and around 3% for jets with $p_T \approx 20$ GeV.

Jets originating from additional interactions in the bunch crossing are removed by requiring that at least 50% (75%) of the energy within $\Delta R = 0.4$ around the jet axis are compatible with the primary vertex for the 7 (8) TeV data.

$H \rightarrow ZZ^{(*)} \rightarrow 4\ell$ with the ATLAS detector

Both the ATLAS and CMS experiments have observed a previously unknown particle in the search for the Higgs boson [12, 13], and subsequent studies indicate that the properties of the observed particle are consistent with those predicted for the Higgs boson by the SM [3, 102]. The $H \rightarrow ZZ^{(*)} \rightarrow 4\ell$ final state, where $\ell = e, \mu$, is one of the most sensitive Higgs boson decay channels and played a key part in these results, in particular due to the high signal-to-background ratio (S/B) and good mass resolution.

This chapter describes the analysis of the $H \rightarrow ZZ^{(*)} \rightarrow 4\ell$ final state using the full dataset collected by ATLAS during LHC Run I, including the measurement of the Higgs boson mass [93]. Chapter 5 is dedicated to a detailed discussion of the categorisation of events by production mechanism and the subsequent measurement of the signal strengths for different production modes in this channel [4]. The corresponding results obtained by the CMS collaboration may be found in Ref [103].

4.1 Event selection

To obtain a sample of $H \rightarrow ZZ^{(*)} \rightarrow 4\ell$ events, single-lepton and dilepton trigger algorithms are used, where the trigger requirements include p_T (E_T) thresholds for muons (electrons). The p_T and E_T thresholds for the range of triggers used, presented in Table 4.1, are higher for the 8 TeV data to account for the increased number of interactions per bunch crossing. The trigger efficiency, with respect to the offline analysis, is almost 100% for events with a four-lepton candidate containing only electrons, and is greater than 97% for events with a four-lepton candidate containing muons.

Table 4.1: Required p_T and E_T thresholds for the triggers used to select events in the 7 TeV and 8 TeV datasets.

Trigger	p_T/E_T threshold(s) (GeV)
7 TeV	
Single muon	18
Single electron	20
Di-muon	10-10
Di-electron	12-12
Muon-electron	6-10
8 TeV	
Single muon	24
Single electron	24
Di-muon	13-13
Di-muon (asymm.)	8-18
Di-electron	12-12
Muon-electron	8-12

Only events with at least one reconstructed vertex that has three associated tracks with $p_T > 400\,\mathrm{MeV}$ are considered, and the primary vertex for a given event is defined as the vertex whose associated tracks correspond to the greatest p_T sum. Higgs boson candidates are reconstructed by selecting two same-flavour, opposite-charge lepton pairs, where the reconstruction and identification of muon and electron candidates is described in Sections 3.4.1 and 3.4.2 respectively. Events are categorised as 4μ, $2e2\mu$, $2\mu2e$ or $4e$ depending on the flavour of the of the lepton pairs and the distinction between the $2e2\mu$ and $2\mu2e$ channels is discussed below.

To maximise the acceptance, all four types of muons introduced in Section 3.4.1 are used, where each lepton quadruplet is allowed to have at most one SA or CaloTag muon. CB, ST and SA muons are required to have $p_T > 6$ GeV and CaloTag muons are required to have $p_T > 15$ GeV. Stand-alone muons are only considered in the pseudorapidity region $|\eta| > 2.5$, outside the ID acceptance, and are required to have hits in all three layers of the MS. CaloTag muons are restricted to $|\eta| < 0.1$ and, in order to reject misidentified electrons, CaloTag muons which have the same ID track as an electron are rejected. Electrons are required to have $E_T > 7$ GeV. To require that all selected leptons are associated with the primary vertex, lepton tracks are required to a have longitudinal impact parameter (along the direction of the beam axis), $|\Delta z_0|$, of less than 10 mm with respect to the primary vertex. To reduce the background from cosmic rays, an additional cut on the transverse impact parameter, $|\Delta d_0| < 1$ mm, is required for muons.

In each quadruplet the p_T thresholds for the three highest p_T leptons, chosen to optimise the median expected significance[1] calculated using simulated signal events with $m_H = 125$ GeV, are 20, 15 and 10 GeV. The four leptons are required to be well separated, with $\Delta R > 0.10$ required for same flavour leptons and $\Delta R > 0.20$ required for different flavour leptons. For 4μ and $4e$ events, events containing an opposite-charge, same-flavor dilepton pair with $m_{\ell\ell} < 5$ GeV are removed to reject $J/\psi \rightarrow \ell\ell$ decays. The lepton pair with mass, m_{12}, closest to the Z boson mass, m_Z, is labelled the leading dilepton, while the second lepton pair, with mass m_{34}, is labelled the sub-leading dilepton.

In each event a mass window requirement, again chosen to maximise the median expected significance, is applied to the invariant mass of each of the lepton pairs. The invariant mass of the leading dilepton is required to be between 50 GeV and 106 GeV, and the invariant mass of the sub-leading dilepton is required to lie in the range $m_{min} < m_{34} < 106$ GeV, where $m_{min} = 12$ GeV for $m_{4\ell} < 140$ GeV, rises

---

[1]The median expected significance under the hypothesis of s signal events and b background events is given by [104]:

$$med[Z_0] = \sqrt{2((s+b)ln(1+s/b) - s}$$

linearly to $m_{min} = 50$ GeV at $m_{4\ell} = 190$ GeV and stays at $m_{min} = 50$ GeV for $m_{4\ell} > 190$ GeV. In the case that more than one quadruplet satisfies the kinematic selection requirements, the one with m_{12} value closest to m_Z is retained. If more than four leptons are identified and multiple quadruplets have the same m_{12} value, the one with the highest m_{34} is selected. For events where the Higgs boson candidate contains both muon and electron pairs, the event is placed in the $2e2\mu$ category if the leading dilepton is a di-electron pair and is placed in the $2\mu2e$ category if the leading dilepton is a di-muon pair. If more than one channel has a quadruplet passing the selection, the channel with the highest expected signal rate, in the order $4\mu \Rightarrow 2e2\mu \Rightarrow 2\mu2e \Rightarrow 4e$ from highest to lowest, is kept. Less than one event per mille is expected to contain two quadruplets.

Track- and calorimeter-based isolation and impact parameter requirements are applied to the leptons to reduce the number of events from reducible background processes containing fake or non-prompt leptons entering the signal region, where selected leptons may result from misidentified jets or in-flight pion or kaon decays.

The normalised track isolation discriminant is defined as the sum of the transverse momenta of tracks, Σp_{T}, inside a cone of $\Delta R < 0.2$ around the lepton, excluding the lepton track, divided by the lepton p_{T}. Each lepton is required to have a normalised track isolation discriminant of less than 0.15. Only tracks with at least four hits in the pixel and silicon strip detectors ("silicon hits") and $p_{\mathrm{T}} > 1$ GeV are considered for muon candidates, and only tracks with at least nine silicon hits, including one hit in the innermost pixel layer, and $p_{\mathrm{T}} > 0.4$ GeV are considered for electron candidates.

The normalised calorimetric isolation discriminant [4] for muons is defined as the sum of the energy collected in calorimeter cells, ΣE_T, inside an isolation cone of 0.20 around the muon, after subtracting the local muon ionisation energy, divided by the muon p_{T}. For electrons, the normalized calorimetric isolation is computed as the sum of the topological cluster transverse energies inside a cone of 0.2 around the electron cluster divided by the electron p_{T}, where the cells corresponding to

the core of the electron cluster are excluded from the sum. Muons are required to have a normalised calorimetric isolation less than 0.30, while for electrons the corresponding value is 0.20. For both the track- and calorimeter-based isolation any contributions arising from other leptons of the quadruplet are subtracted. For the track isolation the contribution from any other lepton in the quadruplet within $\Delta R < 0.2$ is subtracted. For the calorimetric isolation the contribution of any electron in the quadruplet within $\Delta R < 0.18$ is subtracted.

The transverse impact parameter significance, d_0/σ_{d_0}, defined as the impact parameter in the transverse plane divided by its uncertainty, is required to be lower than 3.5 for muons and lower than 6.5 for electrons. A looser cut is used for electrons as the electron impact parameter distribution is broader as a result of bremsstrahlung.

The combined reconstruction, identification and selection efficiency for the 8 TeV dataset, calculated using simulated events with $m_H = 125$ GeV, is 39% for the 4μ final state, 27% for the $2e2\mu/2\mu2e$ final states and 20% for the $4e$ final state. For the 7 TeV dataset the efficiency is reduced to 25% for the $2e2\mu/2\mu2e$ final states and 17% for the $4e$ final state, as some improvements in the electron reconstruction and identification procedure for the 8 TeV data are not applied to the 7 TeV data.

4.2   Higgs boson reconstruction

4.2.1   Final state radiation recovery

The $H \to ZZ^{(*)} \to 4\ell$ process may also include radiative photon production. Where it is identified, the Final State Radiation (FSR) photon is incorporated into the four lepton invariant mass calculation. Applying such a correction improves the four-lepton mass resolution and allows the recovery of events whose reconstructed four-lepton mass lies outside the signal region due to the FSR, avoiding applying a correction for this loss based on simulation.

The FSR process in Z boson decays is well modelled by simulation and ATLAS has developed a method to include both collinear (where the ΔR between the muon and cluster satisfies $\Delta R_{\text{cluster},\mu} < 0.15$) and non-collinear ($\Delta R_{\text{cluster},\mu/e} > 0.15$) FSR photons in the reconstruction of Z bosons. A method to include collinear photons is applied to muons, and exploits the longitudinal segmentation of the ATLAS EM calorimeter to reconstruct photons collinear to muons [105]. For electrons, collinear FSR photons are included in the electromagnetic shower associated with the electron in the calorimeter so no special treatment is necessary. The non-collinear FSR correction is performed both for final states with muons and final states with electrons.

The ATLAS $H \to ZZ^{(*)} \to 4\ell$ analysis searches for FSR photons corresponding to leptons selected as part of the Higgs boson candidate. Since the probability for more than one FSR photon with significant energy in a single event is negligible, at most one FSR photon is allowed per event. FSR corrections are only considered for the leading dilepton pair.

The collinear correction is only applied if $66 < m_{\mu\mu} < 89$ GeV and $m_{\mu\mu\gamma} < 100$ GeV. Photon candidates are required to have $E_T > 1.5$ GeV and $f_0 < 0.2$ for $\Delta R < 0.08$, and $E_T > 3.5$ GeV and $f_0 < 0.1$ for $0.08 < \Delta R < 0.15$, where f_0 is the fraction of the calorimeter cluster energy deposited in the first sampling layer. The f_0 requirement discriminates against cases where the calorimeter activity is induced by the muon itself, and the E_T requirement is applied to reduce the background due to π^0 decays.

If a collinear correction is not applied, a non-collinear correction may be applied if $m_{\ell\ell} < 81\,\text{GeV}$ and $m_{\ell\ell\gamma} < 100\,\text{GeV}$. Photon candidates are required to be isolated and have $E_T > 10\,\text{GeV}$. The upper bound on $m_{\ell\ell}$ is introduced to prevent applying the correction for Initial State Radiation (ISR). If more than one FSR candidate satisfying these requirements is found, then the photon with the highest E_T is selected.

Figure 4.1 shows the invariant mass distribution for $Z \to \mu\mu$ events where a collinear

photon or a non-collinear photon is identified, both before and after applying the correction. The observed and simulated data agree well and the distributions after the correction are centred near m_Z.
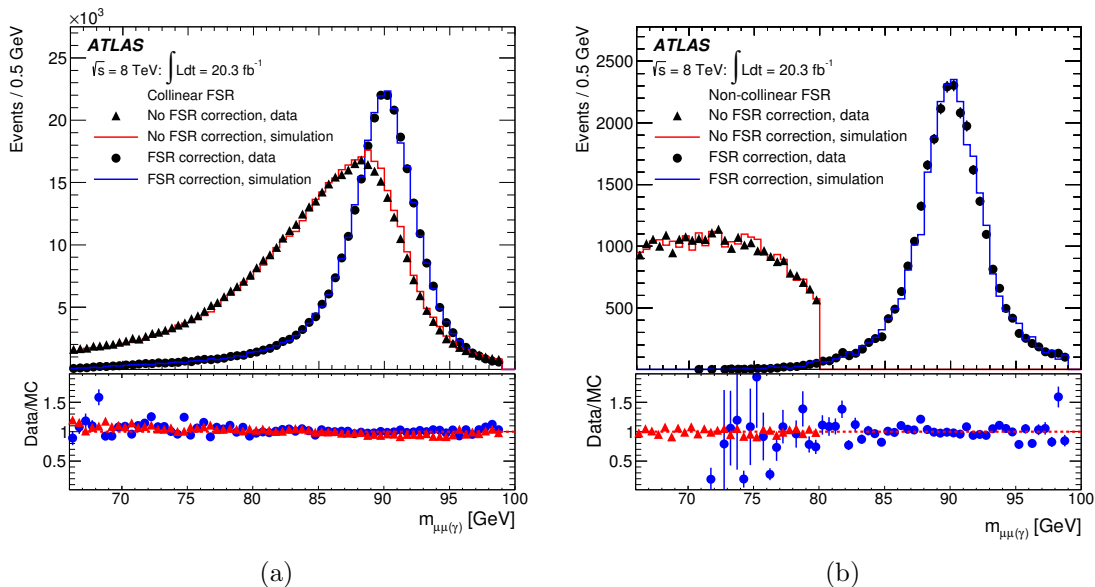

Figure 4.1: The invariant mass distribution for $Z \to \mu\mu$ events where: a) a collinear FSR photon is identified, and b) a non-collinear photon is identified. In both cases the observed data are shown before (triangles) and after (circles) the correction. Simulated data are also shown, where in both cases the red histogram shows the simulated data before the correction and the blue histogram shows the simulated data after the correction. Figure from Ref. [4].

The collinear FSR correction is expected to be applied to approximately 4% of events passing the $H \to ZZ^{(*)} \to 4\ell$ event selection, with an efficiency of 70% and a purity of 85%. The non-collinear FSR correction is expected to be applied to around 1% of events, with an efficiency of 60% and a purity greater than 95%.

4.2.2 Z-Mass Constraint

Exploiting the fact that in $H \to ZZ^{(*)} \to 4\ell$ decays, the leading lepton pair is typically produced by the on-shell decay of a Z boson, the four-lepton mass resolution can be improved by applying a Z-mass-constrained kinematic fit to the leading dilepton pair. The kinematic fit uses a relativistic Breigt-Wigner distribution to

model the Z boson line shape and a Gaussian distribution to model the momentum response function for each lepton, where the width of the Gaussian is fixed to the expected lepton momentum resolution. Though the actual lepton response functions do not precisely correspond to Gaussian distributions, more complicated momentum response functions were found to give a similar performance. Additionally, though the Z boson line shape is not exactly a Breit-Wigner distribution, replacing the Breit-Wigner distribution in the kinematic fit with the Z boson line shape taken directly from simulation has a negligible effect on the results. More details on the procedure can be found in Ref. [106]. The effect of the Z-mass-constrained fit on simulated $H \to ZZ^{(*)} \to 4\mu$ events, using the preliminary analysis documented in Ref. [107], is shown before and after applying the collinear FSR correction in Figure 4.2.

The improvement in the four-lepton mass resolution as a result of the Z-mass constraint is studied by fitting a Gaussian to the peak of the simulated four-lepton invariant mass distribution for $m_H = 125$ GeV in each final state, before and after the constrained fit. The Z-mass constraint improves the four-lepton mass resolution by 18% in the 4μ channel, 23% in the $2e2\mu$ channel, 11% in the $2\mu 2e$ channel and 14% in the $4e$ channel. The simulated distributions after the correction are shown in Figure 4.3 with the fitted Gaussians overlaid.

4.3 Discrimination against SM diboson production

A Boosted Decision Tree (BDT) is used to build a discriminant between the signal and the ZZ^* background events and the BDT reponse is used as a second discriminant in the maximum likelihood fit. The variables used in the BDT are a Matrix Element- (ME) based kinematic discriminant and the transverse momentum, $p_T^{4\ell}$, and pseudorapidity, $\eta^{4\ell}$, of the four-lepton system. The BDT is trained using simulated $H \to ZZ^{(*)} \to 4\ell$ events, generated for $m_H = 125$ GeV, against $qq \to ZZ^{(*)}$ events, where all events are required to pass the full analysis selection and fall in
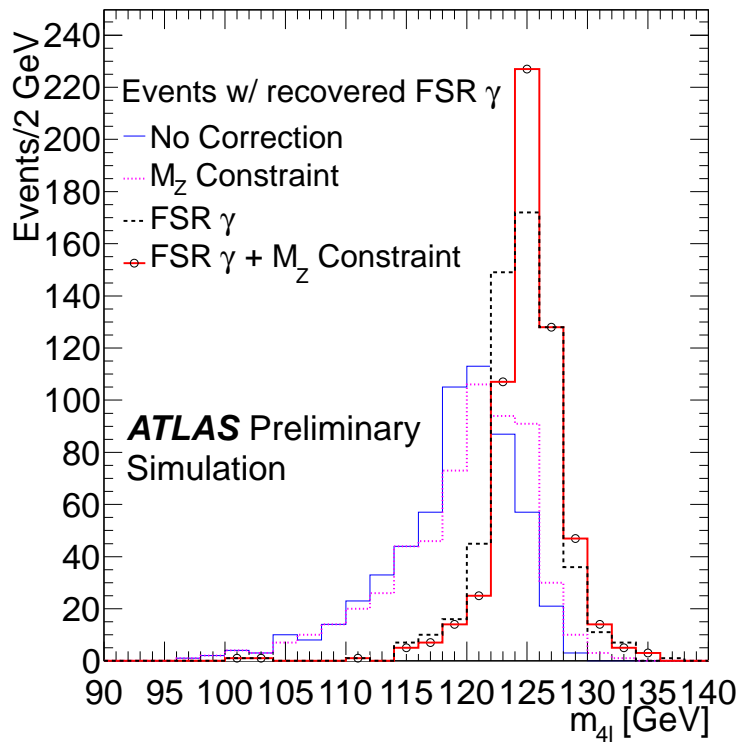
Figure 4.2: Simulated four-muon invariant mass distribution for $m_H = 125$ GeV, for events where a collinear FSR photon has been identified. The mass distribution is shown for uncorrected events (blue histogram) and events where the collinear FSR correction is applied (purple dashed histogram). In both cases, the effect of applying the Z-mass constrained fit is shown, by a black histogram for the case with no FSR correction and a red histogram for the case with the correction. All distributions are normalised to the same area [107].
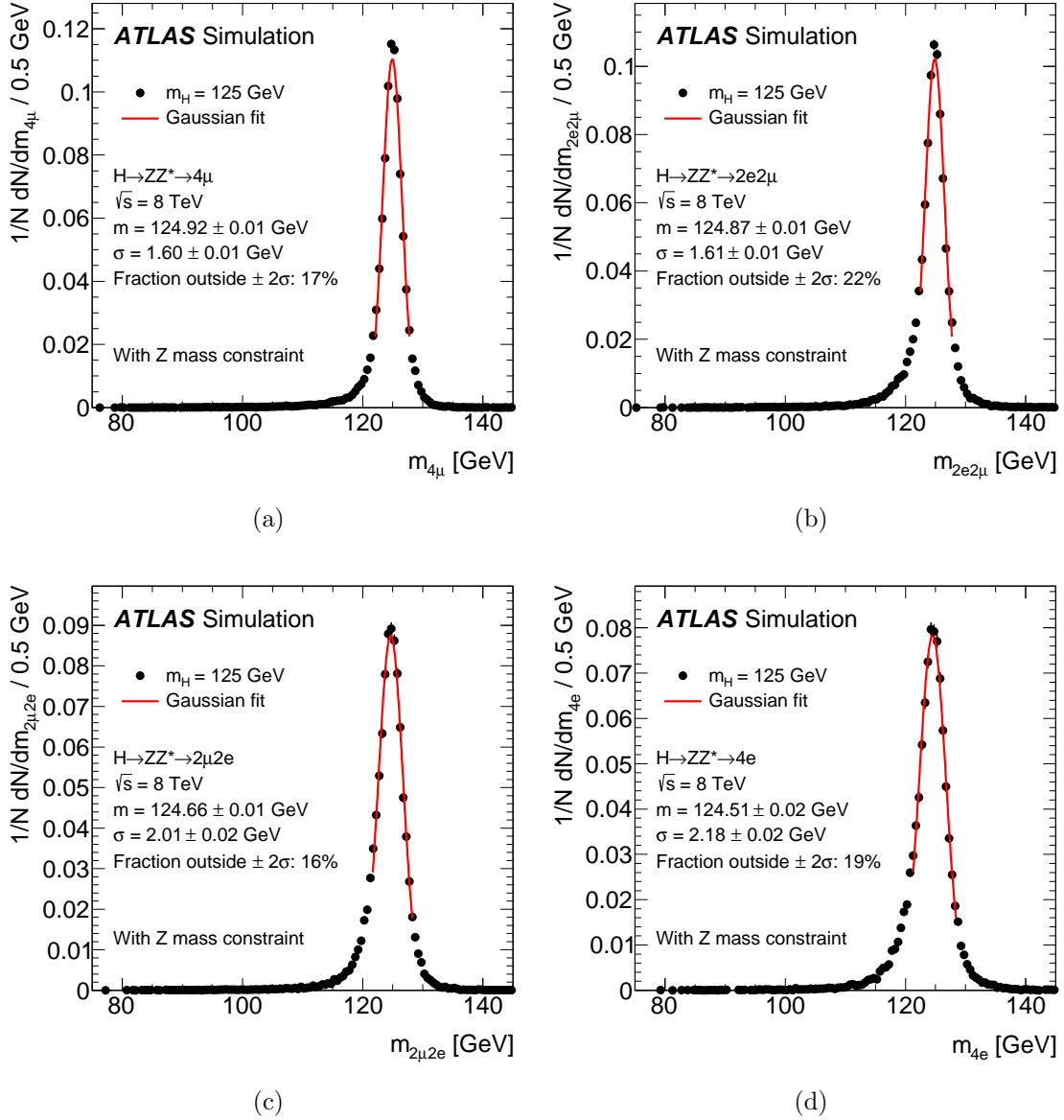
Figure 4.3: Simulated $H \rightarrow ZZ^{(*)} \rightarrow 4\ell$ four-lepton invariant mass distributions including the Z-mass constrained fit for $m_H = 125$ GeV in: a) the 4μ channel, b) the $2e2\mu$ channel, c) the $2\mu2e$ channel, and d) the $4e$ channel. A Gaussian fit to the simulated events is overlaid in each channel, where the fit is performed in a symmetric range for the 4μ channel, and in an asymmetric range for the other channels to accommodate effects in the tail of the distribution due to bremsstrahlung. Figure from Ref. [4].

the the mass window $115 < m_{4\ell} < 130\,\text{GeV}$. The training is performed separately for the different final states. The signal and background distributions used to train the BDT, as well as the BDT response, are shown in Figure 4.4.

The ME kinematic discriminant, D_{ZZ^*} [4], is designed to exploit the differences between the signal and $ZZ^{(*)}$ background kinematics. It is defined as the logarithm of the ratio of the matrix element under the signal hypothesis to the matrix element under the background hypothesis:

$$D_{ZZ^*} = \ln \left(\frac{|\mathcal{M}_{sig}|^2}{|\mathcal{M}_{ZZ^*}|^2} \right) \tag{4.1}$$

where $\mathcal{M}_{sig}$ is the ME for the ggF-produced $H \to ZZ^{(*)} \to 4\ell$ process and $\mathcal{M}_{ZZ^*}$ is the ME for the $qq \to ZZ^{(*)}$ background process. Both the signal and background MEs are computed at LO using MadGraph [108], assuming the SM spin-CP hypothesis $J^P = 0^+$ and $m_H = m_{4\ell}$ on an event-by-event basis for the signal ME. As shown in Figure 4.5, the BDT including $p_T^{4\ell}$ and $\eta^{4\ell}$ in addition to D_{ZZ^*} provides more discrimination, particularly at higher signal efficiencies, than D_{ZZ^*} alone.

4.4   Background estimation

The primary background process contributing to the $H \to ZZ^{(*)} \to 4\ell$ analysis signal region, described in Section 4.1, is SM $ZZ^{(*)}$ production, which is also characterised by the presence of isolated leptons. This background is estimated using simulated events, which are normalised to the SM cross section. In the fiducial region selected by this analysis the estimate, both in terms of shape and normalisation, shows good agreement between the observed and simulated data in the high mass region ($\gtrsim 2m_Z$), where only $ZZ^{(*)}$ production is expected to make a significant contribution. Discrimination between the signal and this background is provided by the BDT introduced in Section 4.3. The small expected background contribution from WZ events is also estimated using simulation.
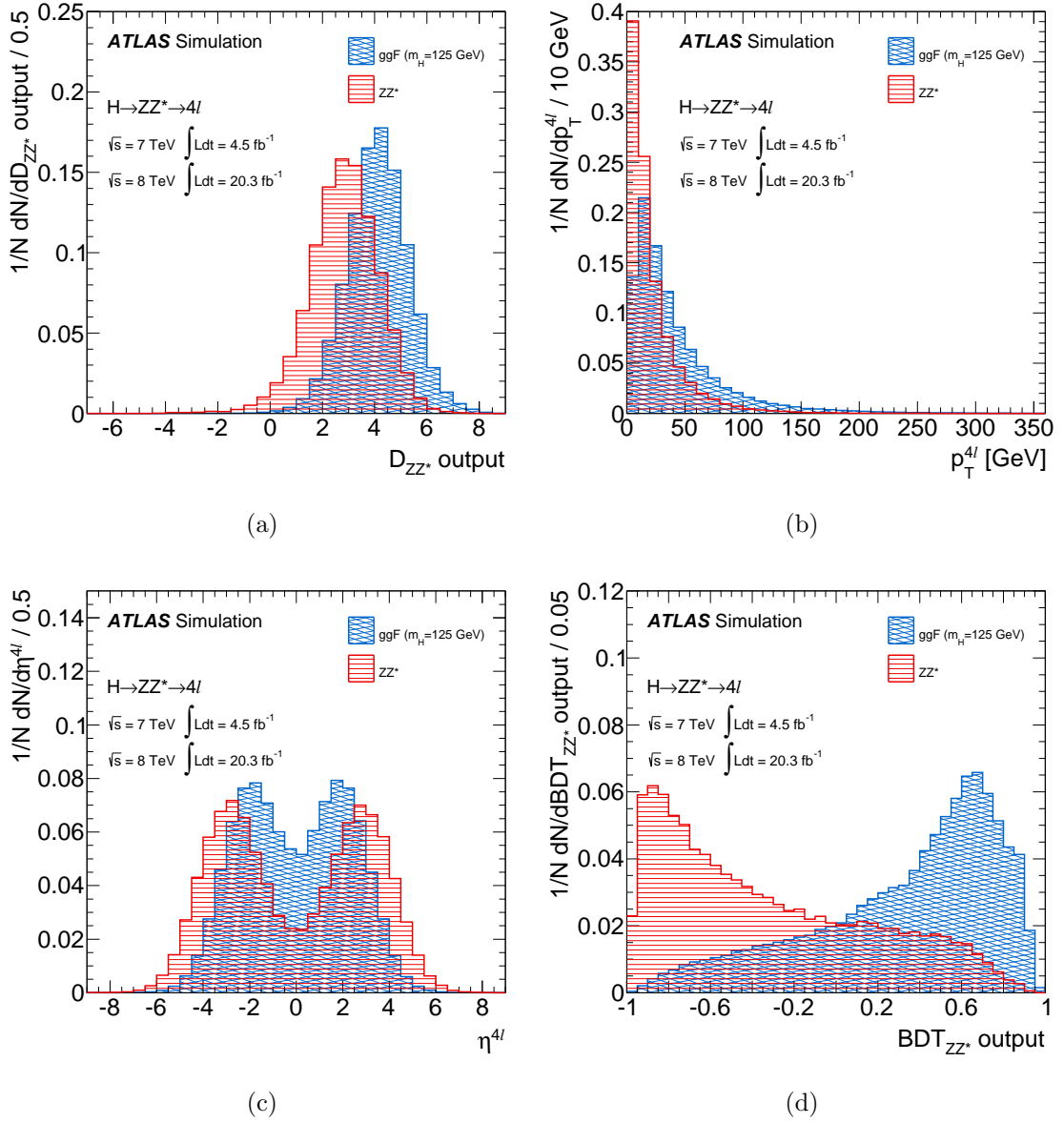
Figure 4.4: Signal (red histograms) and background (blue histograms) event distributions used in the training of the BDT: a) for D_{ZZ^*}, b) for $p_T^{4\ell}$, and c) for $\eta^{4\ell}$. The BDT response distributions are shown in d). All distributions are normalised to the same area [4].
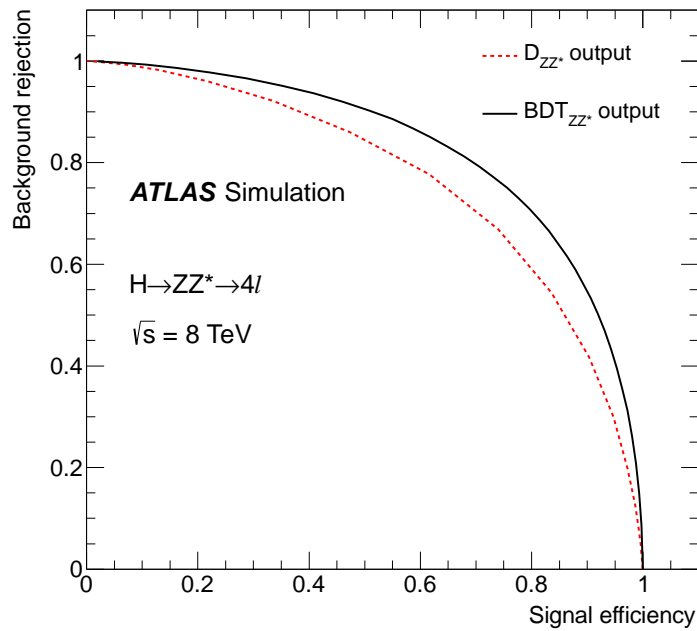
(a)

Figure 4.5: Background rejection fraction versus signal efficiency when using only D_{ZZ^*} to discriminate between signal and background events (red), and when using the full BDT (black). Figure from Ref. [4].

Several background processes with misidentified or non-isolated leptons also contribute to the final state, where the background composition depends on the sub-leading dilepton flavour and is thus different for the $\ell\ell\mu\mu$ and $\ell\ell ee$ channels. The main backgrounds of this type are $\ell\ell + \text{jets}$ and $t\bar{t}$. Their rates are estimated using data-driven techniques. Different methods, described in the following sections, are used to estimate the rates of these backgrounds in the $\ell\ell\mu\mu$ and $\ell\ell ee$ final states.

4.4.1 Estimate of the $\ell\ell\mu\mu$ background

Apart from the dominant $ZZ^{(*)}$ production, the main background process contributing to $\ell\ell\mu\mu$ final states is the production of a Z boson accompanied by jets, denoted $Z + \text{jets}$. Where events enter into the signal region, the muons selected in the sub-leading dilepton come predominantly from heavy quark meson semi-leptonic (heavy-flavour) decays, with the process denoted $Zb\bar{b}$. There is a smaller contribution from muons produced in π/K in-flight decays and this process is denoted $Z + \text{light jets}$. There is also a contribution to the background from t production. To estimate the rates of these background processes, four orthogonal control regions, described below, are defined in order to separate the different background components. A simultaneous maximum likelihood fit to the observed data in each of the control regions is performed, where the mass of the leading dilepton, m_{12}, is used as the discriminating variable. The $Z + \text{jets}$ background is expected to have m_{12} peaking at the mass of the Z boson, whereas $t\bar{t}$ events are expected to have a broader distribution. The selection requirements for each of the control regions include criteria designed to reduce the contributions from the signal and $ZZ^{(*)}$ processes.

The **Inverted impact parameter significance control region** (or 'inverted-d_0' control region) is defined by applying the analysis selection described in Section 4.1, with the exception that the isolation criteria are not applied to the leptons comprising the sub-leading dilepton, and at least one of these leptons is required to fail the impact parameter significance requirements. This control region enhances the $Zb\bar{b}$ and $t\bar{t}$ contributions.

The **Inverted isolation control region** is defined by applying the analysis selection, with the exception that at least one of the leptons comprising the sub-leading dilepton is required to fail either (or both) the track- or calorimeter-based isolation requirements. To ensure orthogonality with the 'inverted-d_0' control region, both leptons in the sub-leading pair are required to pass the impact parameter significance requirements. This control region enhances contributions from Z + light jets and $t\bar{t}$ events and its inclusion in the simultaneous fit complements the 'inverted-d_0' control region as it allows for the extraction of the $Zb\bar{b}$ and Z+light jets components of the Z + jets background, which would be impossible to distinguish from a single control region as their m_{12} distributions are expected to be similar.

The **Same-sign sub-leading dilepton control region** (or 'SS' control region) is defined by applying the analysis selection, with the exception that neither the impact parameter nor the isolation requirements are applied to leptons in the sub-leading pair, and these leptons are required to have the same charge. The 'SS' control region is expected to have significant contributions from the $Zb\bar{b}$, Z + light jets and $t\bar{t}$ processes.

The $e\mu$ **leading dilepton control region** is defined by applying the analysis selection, with the exception that the leading dilepton is made up of an opposite-charge, opposite-flavour lepton pair and neither the impact parameter nor the isolation requirements are applied to leptons in the sub-leading pair. Leptons in the sub-leading pair are required to have the same flavour, and may have the same or opposite charge. An additional requirement on the dilepton invariant mass is applied to remove the contribution of events with a Z boson candidate decaying to a pair of electrons or muons. This control region is dominated by $t\bar{t}$ events.

For each control region, the number of events expected from each of the background processes, as well as the corresponding relative composition, is shown in Table 4.2.

To express the fit results from different control regions in a common way, a **reference control region** is defined where the full analysis selection, except for the impact

Table 4.2: The expected contribution, estimated using simulated events, for each of the background processes in each control region used in the simultaneous fit, in terms of the absolute number of events (first three rows) and their relative fraction (bottom three rows).

Background	inv-d_0 CR	inv-iso CR	SS CR	$e\mu$ CR
	Absolute number of expected events			
$Zb\bar{b}$	70.5 ± 0.6	19.5 ± 0.3	47.0 ± 0.7	0.4 ± 1.9
$Z + \text{light jets}$	20 ± 3	29 ± 3	26 ± 3	0.0 ± 1.3
$t\bar{t}$	124.6 ± 1.3	25.2 ± 0.6	80.6 ± 1.1	159.6 ± 1.6
	Relative fraction of expected events			
$Zb\bar{b}$	0.328 ± 0.005	0.265 ± 0.012	0.306 ± 0.007	0.003 ± 0.012
$Z + \text{light jets}$	0.092 ± 0.013	0.393 ± 0.026	0.169 ± 0.016	0.000 ± 0.008
$t\bar{t}$	0.580 ± 0.009	0.342 ± 0.016	0.525 ± 0.011	0.997 ± 0.010

parameter and isolation criteria for the leptons in the sub-leading pair, is applied. Fit results are expressed in terms of the number of events for each process in this control region, where the ratios between the number of events in each of the fitted control regions and the reference control region are treated as Gaussian-constrained nuisance parameters, with the nominal values and statistical uncertainties taken from simulation. This control region is expected to contain contributions from each of the background processes, but also includes all signal events entering the signal region so is not included directly in the fit. The ratios between the number of events in each of the fitted control regions and the reference control region, calculated using simulated events, are shown in Table 4.3 together with their statistical uncertainties.

Table 4.3: Ratios between the number of events in the control regions used in the fit to the reference region described in the text, calculated using simulation. The uncertainties are due to the number of events in the simulated samples. The ratios for the inverted d_0, $f_{\text{inv}-\text{d0}}$, inverted isolation, $f_{\text{inv}-\text{iso}}$, SS, f_{SS}, and $e\mu$ leading dilepton, $f_{e\mu+\mu\mu}$, control regions are shown.

Background	$f_{\text{inv}-\text{d0}}$	$f_{\text{inv}-\text{iso}}$	f_{SS}	$f_{e\mu+\mu\mu}$
Zbb	0.751 ± 0.010	0.209 ± 0.005	0.653 ± 0.012	0.0005 ± 0.0003
$Z + \text{light jets}$	0.44 ± 0.09	0.52 ± 0.09	0.59 ± 0.10	0.000 ± 0.003
$t\bar{t}$	0.828 ± 0.012	0.167 ± 0.004	0.539 ± 0.009	1.201 ± 0.023

The $Zb\bar{b}$ and $Z + \text{light jets}$ m_{12} distributions are modelled using the convolution of a relativistic Breit-Wigner distribution and a Crystal Ball function, and the $t\bar{t}$ m_{12}

distribution is modelled using a second-order Chebyshev polynomial. The variable parameters of these two functions are required to be the same in each control region. The nominal parameter values are determined by a fit to simulated events, and in the fit to data are treated as Gaussian-constrained nuisance parameters, where the Gaussian widths correspond to the statistical uncertainties on the parameters from the fit to simulated data. The small expected contributions from the WZ and SM $ZZ^{(*)}$ processes that enter the control regions are also modelled in the fit by the convolution of a relativistic Breit-Wigner distribution and a Crystal Ball function, where the yields are fixed to those predicted by simulation.

Several cross-checks are performed to validate the fit:

- The yields resulting from the fit to the simulated data are checked against the number of events expected for each background component. The results are found to be compatible within uncertainties.

- Two alternative fits are performed to the observed data. For the first all parameters are fixed to the predicted values from simulation, and for the second the parameters are unconstrained in the fit. In both cases, the results are compatible with the nominal results within uncertainties.

The m_{12} distribution, as well as the result of the maximum likelihood fit, are shown for the observed data in each of the control regions used in the fit in Figure 4.6. The corresponding estimated number of events in the reference control region is shown in Table 4.4. The number of events for each background component as determined by the simultaneous fit is shown, as well as the number of events determined by independent maximum likelihood fits in each control region. The results are compatible given the uncertainties.

The estimated number of events for each process in the reference control region is extrapolated to the signal region using a 'transfer factor', the per-event probability for the particular background type to fulfil the additional selection criteria (the isolation and d_0 requirements), calculated using simulated events. The calculated
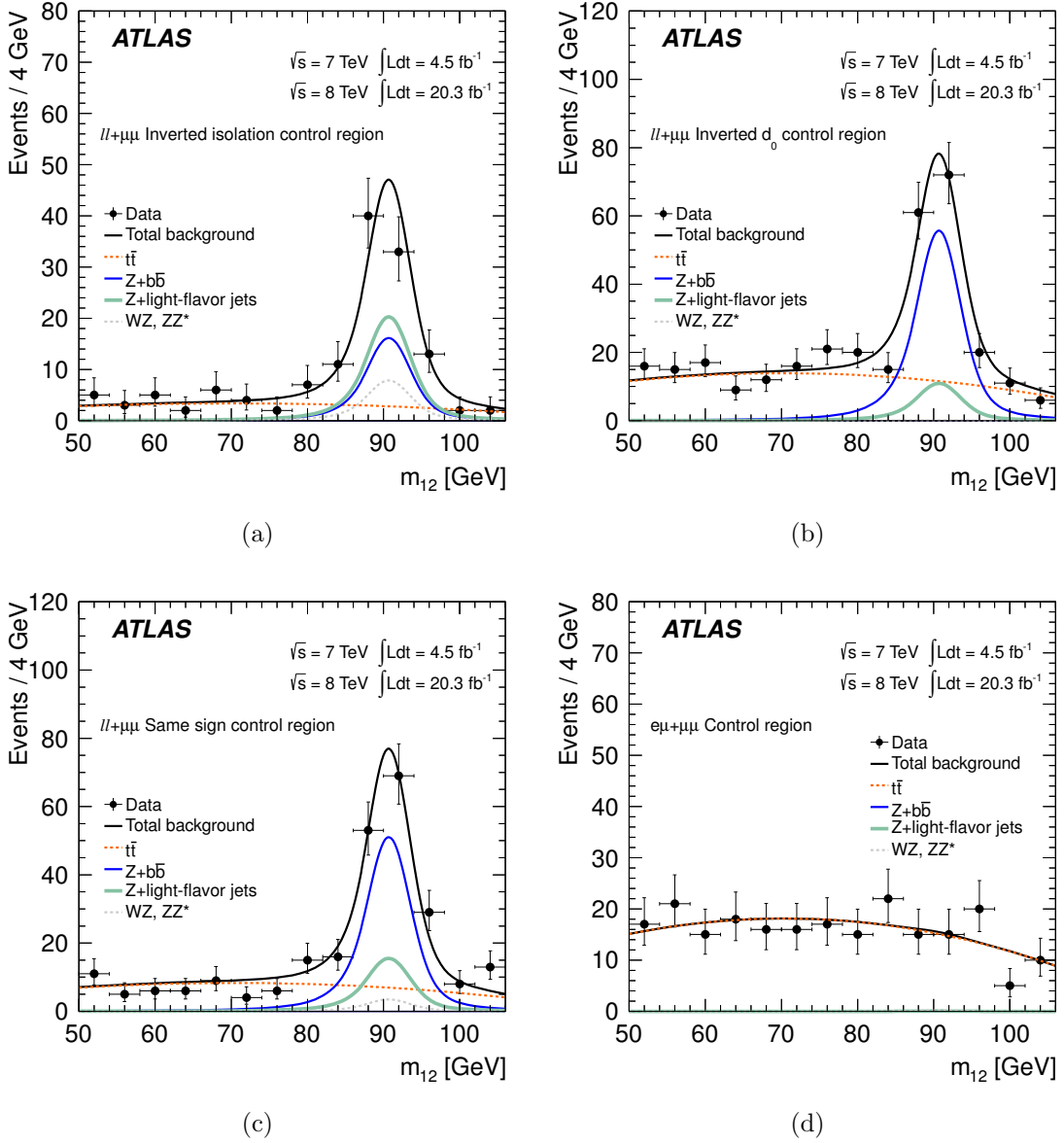
Figure 4.6: Observed m_{12} distributions for the 7 TeV and 8 TeV data, shown as filled points, and the results of the maximum likelihood fit for the four control regions: (a) 'inverted-d_0', (b) 'inverted-isolation', (c) 'SS', and (d) $e\mu$ leading dilepton. The fit results show the total background (black line) as well as the individual components: $Zb\bar{b}$ (blue line) and $Z+$light jets (green line), $t\bar{t}$ (dashed red line), and combined WZ and $ZZ^{(*)}$ (dashed grey line), where the WZ and $ZZ^{(*)}$ contributions are estimated from simulation. Figure from ref. [4].

efficiencies are checked with data using $Z \rightarrow \ell\ell + \mu$ candidate events, where the impact parameter and isolation requirements are applied to the Z boson candidate and events with a fourth lepton or with a dilepton with $m_{\ell\ell} < 5$ GeV are rejected. Based on the difference between data and simulation, a 1.6% uncertainty is added

Table 4.4: Number of estimated events for different background components in the reference $\ell\ell + \mu\mu$ control region for the 7 TeV and 8 TeV data. The results are shown for the simultaneous maximum likelihood fit and for independent maximum likelihood fits in each control region. The statistical uncertainties on the fitted yields are also shown [4].

Reducible background yields for 4μ and $2e2\mu$ in reference control region				
Control region	$Zb\bar{b}$	$Z +$ light jets	Total $Z +$ jets	$t\bar{t}$
Inverted impact parameter			206 ± 18	208 ± 23
Inverted isolation			210 ± 21	201 ± 24
$e\mu + \mu\mu$			$-$	201 ± 12
Same-sign dilepton			198 ± 20	196 ± 22
Combined fit	159 ± 20	49 ± 10	208 ± 22	210 ± 12

to the transfer factor.

The transfer factors are shown in Table 4.5. The quoted uncertainties include the statistical uncertainty due to the size of the simulated sample, as well as the systematic uncertainty based on the agreement between data and simulation. The uncertainties on the transfer factors are significantly larger than the statistical uncertainties from the simultaneous fit, so these uncertainties dominate the uncertainty on the background estimates in the signal region.

Table 4.5: The transfer factors for each background type, calculated using per-event efficiencies for simulated events to pass the analysis selection isolation and impact parameter requirements. The uncertainties are dominated by the statistical uncertainty on the number of simulated events satisfying the full analysis selection requirements for each process.

Reducible Background	Transfer Factor (%)
$Zb\bar{b}$	3.10 ± 0.19
$Z +$ light jets	3.0 ± 1.8
$t\bar{t}$	0.55 ± 0.09

The estimated number of events in the signal regions in the 4μ and $2e2\mu$ final states, as well as the associated uncertainties, are shown for each background type in Table 4.6. The decomposition of the $Z +$ jets background into the $Zb\bar{b}$ and the $Z +$ light jets contributions is also is shown.

Table 4.6: Estimates for the number of background events (excluding the SM $ZZ^{(*)}$ background) in the 4μ and $2e2\mu$ signal regions for the $\sqrt{s} = 7$ TeV and $\sqrt{s} = 8$ TeV data. The $Z + $ jets and $t\bar{t}$ background estimates come from the simultaneous fit described in the text and the WZ contribution comes from simulation. The $Z + $ jets background estimate is also shown separately for the $Zb\bar{b}$ and $Z + $ light jets processes [4].

Background	4μ	$2e2\mu$
	$\sqrt{s} = 7$ TeV	
$Z + $ jets	$0.42 \pm 0.21\text{(stat)} \pm 0.08\text{(syst)}$	$0.29 \pm 0.14\text{(stat)} \pm 0.05\text{(syst)}$
$t\bar{t}$	$0.081 \pm 0.016\text{(stat)} \pm 0.021\text{(syst)}$	$0.056 \pm 0.011\text{(stat)} \pm 0.015\text{(syst)}$
WZ expectation	0.08 ± 0.05	0.19 ± 0.10
	$Z + $ jets decomposition	
$Zb\bar{b}$	$0.36 \pm 0.19\text{(stat)} \pm 0.07\text{(syst)}$	$0.25 \pm 0.13\text{(stat)} \pm 0.05\text{(syst)}$
$Z + $ light-flavor jets	$0.06 \pm 0.08\text{(stat)} \pm 0.04\text{(syst)}$	$0.04 \pm 0.06\text{(stat)} \pm 0.02\text{(syst)}$
	$\sqrt{s} = 8$ TeV	
$Z + $ jets	$3.11 \pm 0.46\text{(stat)} \pm 0.43\text{(syst)}$	$2.58 \pm 0.39\text{(stat)} \pm 0.43\text{(syst)}$
$t\bar{t}$	$0.51 \pm 0.03\text{(stat)} \pm 0.09\text{(syst)}$	$0.48 \pm 0.03\text{(stat)} \pm 0.08\text{(syst)}$
WZ expectation	0.42 ± 0.07	0.44 ± 0.06
	$Z + $ jets decomposition	
$Zb\bar{b}$	$2.30 \pm 0.26\text{(stat)} \pm 0.14\text{(syst)}$	$2.01 \pm 0.23\text{(stat)} \pm 0.13\text{(syst)}$
$Z + $ light-flavor jets	$0.81 \pm 0.38\text{(stat)} \pm 0.41\text{(syst)}$	$0.57 \pm 0.31\text{(stat)} \pm 0.41\text{(syst)}$

4.4.2 Estimate of the $\ell\ell ee$ background

For $\ell\ell ee$ final states, the background in the signal region typically arises from jets which have been misidentified as electrons. Three different methods are used to estimate these background contributions, exploiting two types of control region containing electrons with relaxed identification requirements (X):

- $3\ell + X$: the full analysis selection is applied, except for the requirements on the lowest E_T electron, where the electron identification criteria and isolation and impact parameter significance requirements are relaxed.

- $\ell\ell + XX$: the full analysis selection is applied, except for the requirements on the sub-leading dilepton, where the identification requirements for both of the

electrons are relaxed.

Several methods, described in this section, are used to estimate the background in $\ell\ell ee$ final states. In each method, electron candidates originating from different sources are assigned one of the following classifications:

f - light flavour jets misidentified as electrons.

γ - electrons from photon conversions.

q - electrons from semi-leptonic heavy-flavour meson decays.

The methods for determining the $\ell\ell ee$ background measure inclusively different background sources, and include contributions not only from $Z + \text{jets}$ but also from $t\bar{t}$, WZ and $ZZ^{(*)}$. The expected contribution from $ZZ^{(*)}$, estimated using simulated events, is subtracted from the final estimate.

The baseline method for the background estimate, chosen as the method with the smallest expected total uncertainty, is known as the '$3\ell+X$' method and is described in Section 4.4.2.1. Two further methods provide cross-checks; the 'Transfer Factors' method, described in Section 4.4.2.2, and the 'Reco-Truth Unfolding' method, described in Section 4.4.2.3.

4.4.2.1   The $3\ell + X$ method

The $3\ell + X$ method uses a control region where the full analysis selection is applied, apart from the lowest E_T electron, where relaxed requirements are applied. For the lowest E_T electron, a track with minimal silicon hit requirements (at least 7 silicon hits, with hits in at least two of the pixel layers) matching a calorimeter cluster is required, where no further electron identification criteria, nor impact parameter significance or isolation requirements, are applied. To suppress the $ZZ^{(*)}$ contribution, the electron candidates forming the sub-leading pair are required to have

the same-sign. After this requirement, 5% of the remaining events are estimated to come from $ZZ^{(*)}$ and this contribution is subtracted from the final estimate. In the case that more than one quadruplet per event is built, all the quadruplets with the same m_{12} are considered.

As the $3\ell + X$ control region contains three leptons passing the full selection, the background composition for this method is simpler than methods estimating the background using an $\ell\ell + XX$ control region. This allows the use of a two-dimensional maximum likelihood fit, where the observables used are the number of hits in the innermost layer of the pixel detector, $n_{hits}^{B-layer}$, and the ratio of the number of high-threshold to low-threshold TRT hits, $rTRT$. The fit extracts the yields for the f, γ and q background components. Separation between the components is possible using the fact that for most converted photons, the conversion happens after the first pixel layer, and electrons typically produce a higher number of high-threshold TRT hits than jets.

The templates used to model each of the background components are taken from a simulated sample of events in an $\ell\ell+X$ control region, where only the minimal silicon hit requirements, described above, are applied to X. A correction is applied to the templates to account for the observed difference in the $n_{hits}^{B-layer}$ and $rTRT$ variables between data and simulation. As the expected contribution of the q component in the control region is low, its yield is Gaussian-constrained to the number of events expected from simulation, where the Gaussian width is set to be 20% of the expected yield.

The result of the fit is shown in Figure 4.7. The background contributions from the f, γ and q sources are unfolded as a function of the electron p_T using the *sPlot* method [109], which returns event-by-event a so-called *sWeight* for each component, corresponding to the probability for X to be of f, γ or q type. The *sWeight*s for each component, which sum to one for each event, are extrapolated from the control region to the signal region with transfer factors that depend on the efficiency for an electron of the component type in question to pass all selection requirements.
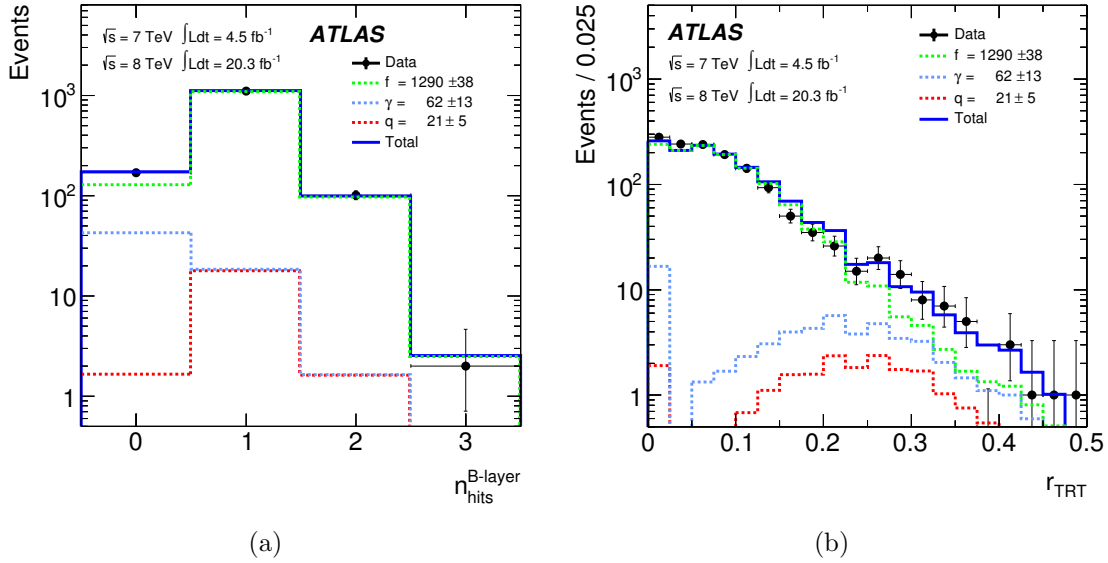
(a)   (b)

Figure 4.7: Results of the two-dimensional maximum-likelihood fit in the $3\ell + X$ control region to: a) $n_{hits}^{B-layer}$ and, b) $rTRT$. The plots show the data (filled points), the total background (solid blue histogram) and its various components, namely f (green dashed histogram), γ (blue dashed histogram) and q (red dashed histogram). All distributions are shown for the sum of the $4e$ and $2\mu 2e$ channels, though the fits are performed separately in each channel. Figure from Ref. [4].

The efficiencies for electron candidates corresponding to each type to pass all selection requirements is found using simulated $Z+X$ events and corrected for differences between data and simulation. The relevant sample is selected by requiring a reconstructed Z boson candidate decaying to a same-flavour, opposite-charge lepton pair with $p_T > 20\,\text{GeV}$, both leptons satisfying the requirements of the analysis event selection. To reduce the number of events in the sample where X is a genuine electron, E_T^{miss} in the events is required to be below 50 GeV. Any additional leptons are required to be well separated from the leptons associated with the Z boson candidate, satisfying $\Delta R > 0.2(0.1)$ for different-(same-) flavour leptons. The electron candidate X is required to satisfy the silicon hit requirements applied throughout this section. The efficiencies used for the extrapolation are obtained in 8 p_T bins for each of the different background sources.

For the f background type, the simulation efficiency is corrected by a scale factor as a function of p_T, which ranges from 1.6 to 2.5 in p_T bins. The γ background type is well

modelled by the simulation, where the data and simulation agree within 10%. For the q background component, the efficiency is well modelled by simulation. Systematic uncertainties of 30%, 20% and 25% are applied to the f, γ and q components, respectively, due to the data-simulation correction. The fit results in the $3\ell + X$ control region, the extrapolation factors and the estimated number of events in the signal region are shown, summed over the $4e$ and $2e2\mu$ channels, for each background type in Table 4.7. The total expected number of background events in the $4e$ and $2e2\mu$ channels, after the subtraction of the expected $ZZ^{(*)}$ contribution, is shown in the Summary Table 4.8.

Table 4.7: Using the $3\ell + X$ method to estimate the $\ell\ell + ee$ background, the fit results for each component in the $3\ell + X$ control region, the transfer factors used for extrapolation and the signal region yields for the reducible $\ell\ell + ee$ background are shown. The estimates for the $2\mu2e$ and $4e$ channels are summed. The uncertainties are the combination of the statistical and systematic uncertainties [4].

Type	Fit yield in control region	Extrapolation factor	Yield in signal region
		$\sqrt{s} = 7$ TeV data	
f	391 ± 29	0.010 ± 0.001	3.9 ± 0.9
γ	19 ± 9	0.10 ± 0.02	2.0 ± 1.0
q	5.1 ± 1.0	0.10 ± 0.03	0.51 ± 0.15
		$\sqrt{s} = 8$ TeV data	
f	894 ± 44	0.0034 ± 0.0004	3.1 ± 1.0
γ	48 ± 15	0.024 ± 0.004	1.1 ± 0.6
q	18.3 ± 3.6	0.10 ± 0.02	1.8 ± 0.5

4.4.2.2 The transfer factors method

This cross-check method uses a $\ell\ell + XX$ control region, where the full analysis selection is applied to the leading dilepton and the sub-leading dilepton is formed using electron candidates with relaxed identification requirements ("X") that each fail at least one of the isolation or impact parameter significance requirements. The yield in this control region is extrapolated to the signal region using the efficiency for electron candidates coming from each background source to pass the full analysis selection.

Electron candidates are classified as 'Electron (E)' or 'Fake (F)' using reconstruction-based discriminating variables and events are placed into categories depending on this classification, where the composition of the different background sources is different in each category. The categorisation allows a more accurate determination of the efficiencies for background electron candidates from each source to pass the full selection requirements.

A $Z + X$ control region is used to estimate the efficiency for X to pass the full selection requirements, needed to extrapolate the measured yield in the control region to the signal region. Two alternative approaches are taken for this estimation, addressing in different ways the different compositions of the $Z + X$ and $\ell\ell + XX$ control regions.

The total expected number of background events in the $4e$ and $2e2\mu$ channels is shown in the Summary Table 4.8.

4.4.2.3   The reco-truth unfolding method

This cross-check method uses an $\ell\ell + XX$ control region, which is similar to the control region used for the method described in Section 4.4.2.2, except that no requirements are placed on the isolation and impact parameter significance for electron candidates comprising the sub-leading dilepton[2]. In the simulated $\ell\ell + XX$ sample, each reconstruction category is further decomposed in terms of all possible paired combinations of the various background sources, f, q, γ and e. The e classification is introduced because of the contributions from the signal and $ZZ^{(*)}$ background processes, which are present in this control region as the isolation and impact parameter significance requirements are no longer inverted. The yield observed in the $\ell\ell + XX$ control region is extrapolated to the signal region in bins of p_T and η, where the transfer factor in each bin is calculated using the weighted sum of each combination of background sources (16) in each reconstruction category (4). The

---

[2]The requirements are inverted for the previous method.

expected contribution from events classified as ee is dominated by the signal and SM $ZZ^{(*)}$ contributions and is removed, where an additional subtraction is made to subtract the remaining $ZZ^{(*)}$ events in other categories.

The total expected number of background events in the $4e$ and $2e2\mu$ channels is shown in Table 4.8.

Table 4.8: Estimated number of background events using each $\ell\ell ee$ background estimation method in the $2e2\mu$ and 4μ categories. Results are displayed for the $\sqrt{s} = 7$ TeV and $\sqrt{s} = 8$ TeV data for the full mass range. The "†" symbol indicates which method is used to estimate the background normalisation applied in the analysis. The other estimates come from methods used as cross-checks. The first uncertainty shown is statistical, the second is systematic [4].

Method	$\sqrt{s} = 7$ TeV data	$\sqrt{s} = 8$ TeV data
$2\mu 2e$		
$3\ell + X^\dagger$	$2.9 \pm 0.5 \pm 0.5$	$2.9 \pm 0.3 \pm 0.6$
$\ell\ell + XX$ Transfer Factor	$2.2 \pm 0.3 \pm 1.1$	$2.5 \pm 0.1 \pm 0.9$
$\ell\ell + XX$ Transfer Factor b-enriched	$2.8 \pm 0.5 \pm 0.8$	$3.2 \pm 0.2 \pm 0.9$
$\ell\ell + XX$ Reco–truth	$2.8 \pm 0.4 \pm 1.0$	$2.9 \pm 0.3 \pm 0.3$
$4e$		
$3\ell + X^\dagger$	$3.3 \pm 0.5 \pm 0.5$	$2.9 \pm 0.3 \pm 0.5$
$\ell\ell + XX$ Transfer Factor	$2.0 \pm 0.3 \pm 0.9$	$2.4 \pm 0.1 \pm 0.9$
$\ell\ell + XX$ Transfer Factor b-enriched	$3.4 \pm 0.9 \pm 0.8$	$2.9 \pm 0.2 \pm 0.8$
$\ell\ell + XX$ Reco–truth	$2.6 \pm 0.4 \pm 0.9$	$2.8 \pm 0.3 \pm 0.3$

4.4.3 Background control plots

The agreement between the observed data and the sum of the background estimates for the different background components is shown to be good in a control region where the full analysis selection is applied, except for the isolation and impact parameter significance requirements on the leptons comprising the subleading dilepton. The invariant mass distributions for the leading dilepton, m_{12}, and subleading dilepton, m_{34} are shown in this control region for $\ell\ell + \mu\mu$ and $\ell\ell + ee$ final states in Figure 4.8. The $Z + $ jets and $t\bar{t}$ components are normalised to the results
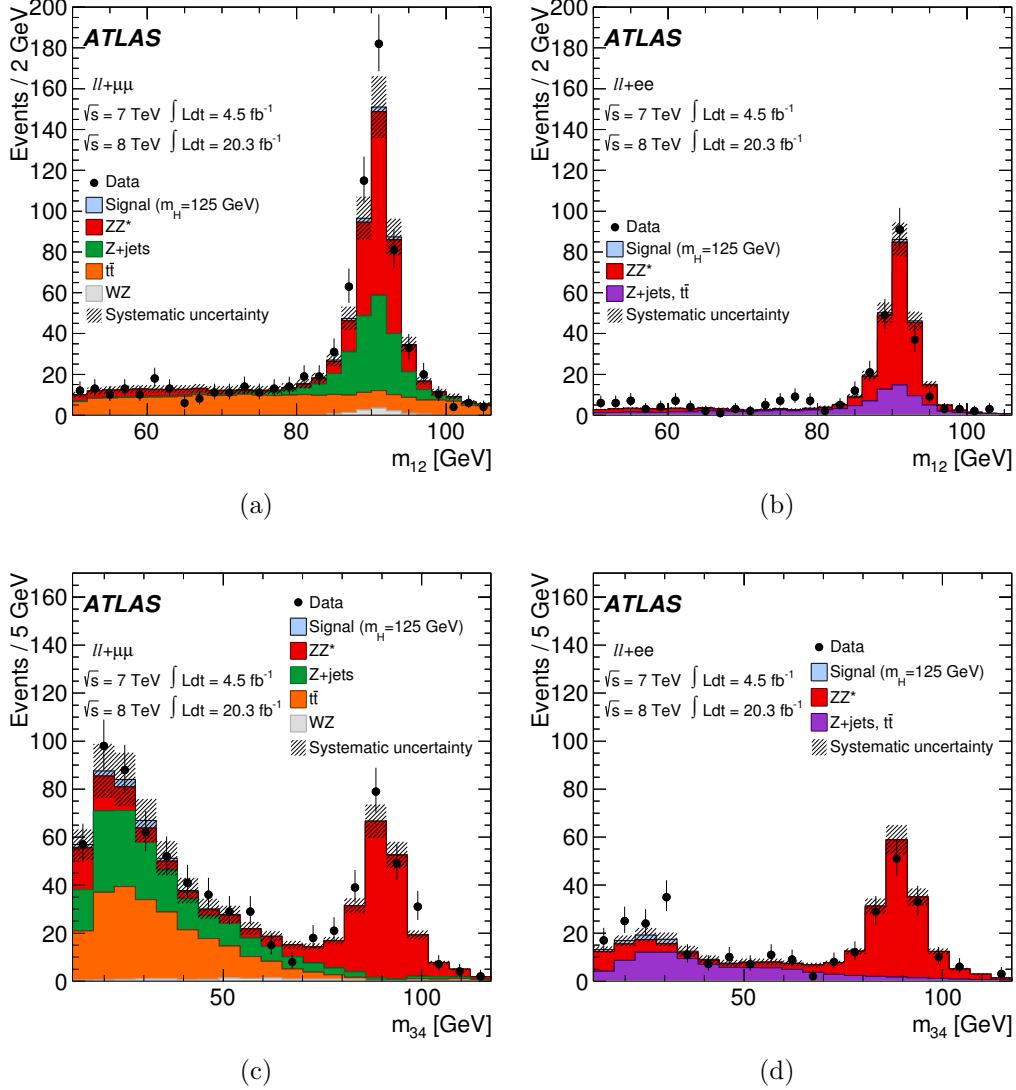
of the baseline data-driven estimates.

Figure 4.8: Leading and subleading dilepton invariant mass distribtuions in a control region where the full analysis selection is applied, except for the isolation and impact parameter significance requirements on the sub-leading dilepton. The sample is divided according to the flavour of the sub-leading dilepton. (a) and (b) show the m_{12} distribution, in (a) for $\ell\ell + \mu\mu$ events, and in (b) for $\ell\ell + ee$ events. (c) and (d) show the m_{34} distribution, in (a) for $\ell\ell + \mu\mu$ events, and in (b) for $\ell\ell + ee$ events. The simulation is normalised to the data-driven background estimates. The data are shown as filled points and the different background sources as filled histograms. The total background systematic uncertainty is represented by the hatched areas. Figure from Ref. [4].

4.5   Signal and background modelling

The ATLAS results in the $H \to ZZ^{(*)} \to 4\ell$ final state, obtained using the inclusive analysis discussed in this chapter, employ a two-dimensional, maximum likelihood fit to the four-lepton invariant mass, $m_{4\ell}$, and the output of the BDT discussed in section 4.3, $O_{BDT_{ZZ^*}}$, in the mass range $110 < m_{4\ell} < 140\,\mathrm{GeV}$. This section describes the procedures used to build the signal and background probability density functions (PDFs) used in the fit.

4.5.1   Signal modelling

The signal PDF used in the two-dimensional fit takes the following form:

$$
\mathcal{P}(m_{4\ell}, O_{\mathrm{BDT}_{ZZ^*}} \mid m_H) = \mathcal{P}(m_{4\ell} \mid O_{\mathrm{BDT}_{ZZ^*}},\ m_H)\, \mathcal{P}(O_{\mathrm{BDT}_{ZZ^*}} \mid m_H)
$$
$$
\simeq \left(\sum_{n=1}^{4} \mathcal{P}_n(m_{4\ell} \mid m_H) \theta_n(O_{\mathrm{BDT}_{ZZ^*}}) \right) \mathcal{P}(O_{\mathrm{BDT}_{ZZ^*}} \mid m_H)
$$

$$(4.2)$$

where θ_n defines four bins in $O_{\mathrm{BDT}_{ZZ^*}}$ (-1 − -0.5, -0.5 − 0, 0 −0.5 and 0.5 − 1) and $\mathcal{P}_n$ is the probability density in $m_{4\ell}$ for the signal in a given θ_n bin. Since the $m_{4\ell}$ distribution doesn't vary significantly as a function of $O_{\mathrm{BDT}_{ZZ^*}}$ in each of the bins, the product of the one-dimensional probability densities of $m_{4\ell}$ and $O_{\mathrm{BDT}_{ZZ^*}}$ is used.

The $m_{4\ell}$ and $O_{\mathrm{BDT}_{ZZ^*}}$ probability densities are obtained using a Kernel Density Estimation technique [110], which sums Gaussian kernels with variable width over an input set of points, provided here by the simulated distributions. The resulting probability densities are smoothed distributions which are statistically consistent with the input distributions and don't suffer from potential effects due to finite bin size that would be present if template histograms were used to model the distributions. Also, since the probability densities are continuous, the $m_{4\ell}$ distributions can

be shifted horizontally by arbitrary $m_{4\ell}$ values, a feature which is exploited in the implementation of the energy scale systematics discussed in Section 4.6.

The $m_{4\ell}$ probability densities are produced using samples generated at 15 different m_H values in the range 115 - 130 GeV (at 0.5 GeV intervals for $123 < m_H < 126$ GeV and at 1 GeV intervals elsewhere) and are parameterised as functions of m_H. This is achieved using B-spline interpolation [111], where the $m_{4\ell}$ value at a given point in the distribution, for a particular m_H, is the weighted sum of the corresponding $m_{4\ell}$ value from distributions associated with the series of m_H control points. The weights are determined for each control point from a cubic B-spline basis function.

The expected signal yields for different values of m_H are obtained from simulation at each of the control points used for the probability density modelling. The yields at intermediate mass points are then obtained using asecond B-spline on the same basis. Combining the signal shapes with the normalisations results in the normalised signal shapes which are continuously parameterised in m_H. Figure 4.9 shows the two dimensional probability density used for the signal process.

4.5.2   Background modelling

The background is modelled using two-dimensional probability densities. The $qq \to ZZ^{(*)}$ and $gg \to ZZ^{(*)}$ background template shapes are obtained separately by performing Kernel Density Estimation, using simulated events as input, in two dimensions to obtain a smooth, two-dimensional $m_{4\ell} - O_{\mathrm{BDT}_{ZZ^*}}$ distribution.

For the other background processes in the $\ell\ell + \mu\mu$ final states, the two-dimensional probability density distributions are also derived from simulation, where the simulation agrees well with the observed data in the control regions discussed in Section 4.4.1. The uncertainty on the shape of the probability density is evaluated by varying the track isolation and impact parameter significance selections applied. For other backgrounds in $\ell\ell + ee$ final states, the number of simulated events is not sufficient to produce a smooth background model, so the probability density is derived
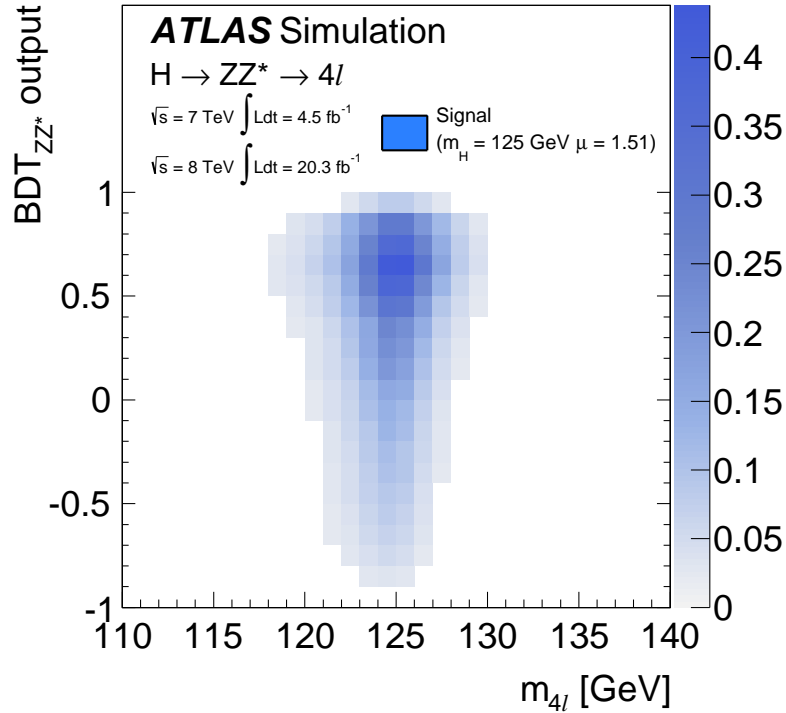
Figure 4.9: Two dimensional probability density for the signal, $\mathcal{P}(m_{4\ell}, O_{\mathrm{BDT}_{ZZ^*}} \mid m_H)$, normalised to the expected total number of events in the sum of all final states for the 2011 and 2012 datasets. The expected total number of events assumes $m_H = 125\,\mathrm{GeV}$ and $\mu = 1.51$. Figure from Ref. [4].

from the $3\ell + X$ data control region, weighted by the transfer factors to reflect the signal region kinematics. Here, the shape uncertainties are obtained by taking the difference between the default probability density and the alternative probability densities obtained by using the control regions used for cross-checks.

The background probability densities for $\ell\ell + \mu\mu$ and $\ell\ell + ee$ final states are shown projected onto $m_{4\ell}$ in Figure 4.10. Figure 4.11 shows the full two-dimensional probability densities for the $ZZ^{(*)}$ and $Z + \mathrm{jets}$ backgrounds.
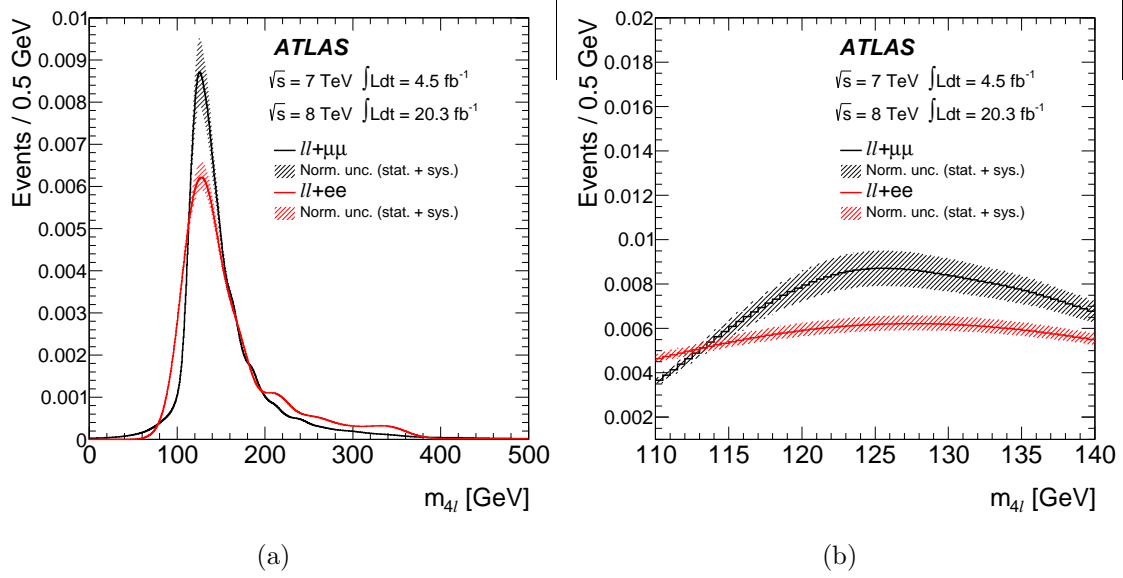
(a)   (b)

Figure 4.10:   One dimensional probability density, $\mathcal{P}(m_{4\ell})$, projected onto $m_{4\ell}$ for the $\ell\ell + \mu\mu$ and $\ell\ell + ee$: a) for $0 < m_H < 500$ GeV, and (b) for the reduced mass range, $110 < m_H < 140$ GeV, in which the maximum likelihood fit is performed [4].
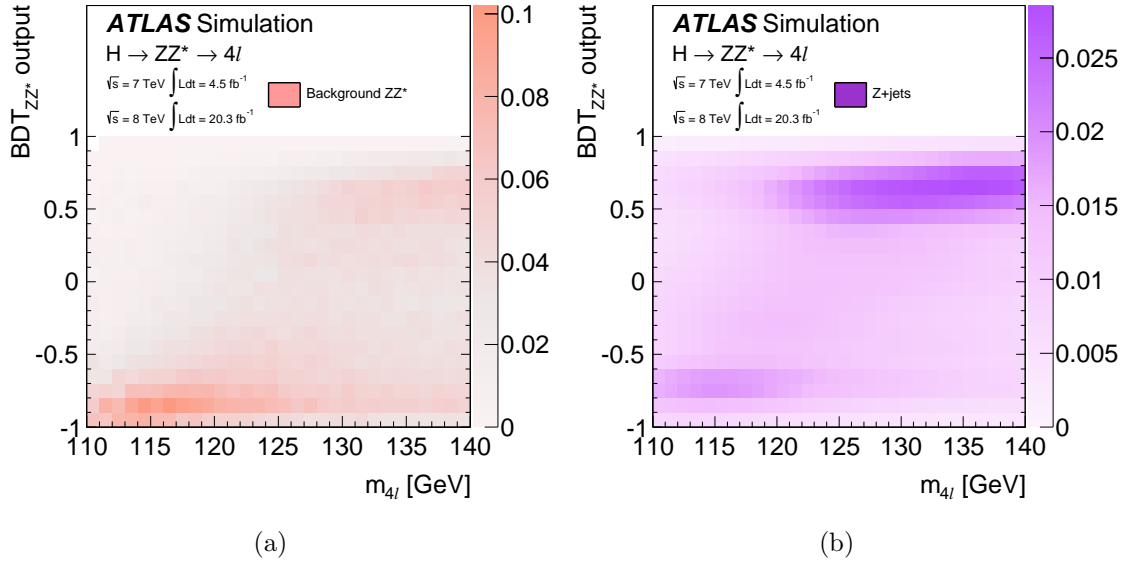

(a)   (b)

Figure 4.11:   Two dimensional probability density, $\mathcal{P}(m_{4\ell}, O_{\mathrm{BDT}_{ZZ^*}})$ for: a) the $ZZ^{(*)}$ background, and (b) the Z + jets background [4].

4.5.3   Likelihood function

The signal and background probability densities discussed above are used to construct a likelihood function, $\mathcal{L}$, that depends on m_H and μ:

$$
\mathcal{L}(m_H, \mu, \boldsymbol{\theta}) = \prod_i^{\text{year}} \prod_j^{\text{final state}} \text{Poisson}(N_{ij} | \mu \cdot S_{ij}(m_H, \boldsymbol{\theta}) + B_{ij}(\boldsymbol{\theta}))
$$
$$
\cdot \prod_{k=1}^{N_{ij}} \mathcal{F}_{ij}((m_{4\ell}, O_{\text{BDT}_{ZZ^*}})_k, m_H, \mu, \boldsymbol{\theta})
$$

(4.3)

which is the product of the Poisson probability of observing N_{ij} events, given the expectation for the signal S_{ij} and background B_{ij}, multiplied with the product of the values of the probability density $\mathcal{F}_{ij}$, for $(m_{4\ell}, O_{\text{BDT}_{ZZ^*}})_k$ of all events in the 2011 and 2012 data sets and each of the four final states. $\mathcal{F}_{ij}$ is the weighted sum of the signal and background probability densities. $\boldsymbol{\theta}$ represents the set of nuisance parameters used to model the effect of the systematic uncertainties described in Section 4.6.

Confidence intervals are based on the profile likelihood ratio technique [104]. The profile likelihood ratio $\Lambda(m_H)$ used for the measurement of the Higgs boson mass is:

$$
\Lambda(m_H) = \frac{\mathcal{L}(m_H, \hat{\hat{\mu}}(m_H), \hat{\hat{\boldsymbol{\theta}}}(m_H))}{\mathcal{L}(\hat{m}_H, \hat{\mu}, \hat{\boldsymbol{\theta}})}
$$

(4.4)

where the signal strength, μ, is a free parameter in the fit. The single circumflex (*e.g.* $\hat{\boldsymbol{\theta}}(\boldsymbol{\mu})$) denotes the unconditional maximum likelihood estimate of a parameter and the double circumflex (*e.g.* $\hat{\hat{\boldsymbol{\theta}}}(\boldsymbol{\mu})$) denotes the conditional maximum likelihood estimate for given fixed values of $\boldsymbol{\mu}$.

For the measurement of the signal strength, m_H is fixed to its best-fit value and the profile likelihood ratio is:

$$\Lambda(\mu) = \frac{\mathcal{L}(\mu, \hat{\hat{\boldsymbol{\theta}}}(\mu))}{\mathcal{L}(\hat{\mu}, \hat{\boldsymbol{\theta}})} \qquad (4.5)$$

4.6   Systematic Uncertainties

Systematic uncertainties are modelled using nuisance parameters in the profile likelihood ratio, as described in Section 4.5.

The dominant sources of systematic uncertainty on the measurement of the Higgs boson mass in the four-lepton final state are the muon momentum scale (see Figure 3.13) and electron energy scale (see Figure 3.15). The corresponding uncertainties are calculated by modifying the momentum (energy) of a muon (electron) by a scale factor and observing the shift in the m_{4l} distribution.

The measurement of the muon momentum scale is discussed in Section 3.4.1. In the muon p_T range 6-100 GeV, the systematic uncertainty on the scale is around 0.04% for $|\eta| < 2.0$, and is up to 0.2% for $|\eta| > 2.0$. The uncertainty is modelled using a single nuisance parameter, where deviations to the scale as measured in both the ID and MS are considered. The uncertainties on the measured Higgs boson mass due to the muon momentum scale uncertainties are estimated to be 0.04% for the 4μ final state and 0.02% for the $2\mu2e$ and $2e2\mu$ final states.

The determination of the electron energy scale is discussed in Section 3.4.2, and its precision is better than 0.1% for the full pseudorapidity and E_T coverage. A total of 24 nuisance parameters are used to model the electron and photon energy scale uncertainties, with the sources described in Ref [97]. An additional nuisance parameter is used to model the electron momentum scale uncertainty, which is relevant for the combination of electron track and calorimeter information. The corresponding uncertainties on the measured Higgs boson mass are 0.04% for the $4e$ and $2\mu2e$ final states and 0.03% for the $2e2\mu$ final state.

For the final Higgs boson mass measurement in the four-lepton channel, final states

including muons have a relatively higher weight than final states containing electrons due to their better mass resolution. Taking this into account, the electron energy scale uncertainty gives rise to a 0.01% uncertainty on the Higgs boson mass, whereas the muon momentum scale uncertainty gives rise to a 0.03% uncertainty. Other sources of systematic uncertainty are negligible for this measurement.

For measurements of the Higgs boson signal rate, there are systematic uncertainties relating to the uncertainty on the trigger, reconstruction and identification efficiencies for muons and electrons. These uncertainties are calculated using simulation by comparing the nominal event yield with the modified yield after applying weights to events or individual physics objects corresponding to the various sources of systematic uncertainty.

Due to the presence of multiple high-p_T leptons in the final state, the trigger efficiency for the $H \to ZZ^{(*)} \to 4\ell$ final state is high. The uncertainties on the trigger efficiency are estimated by calculating the number of events that pass the full selection criteria with and without the trigger requirement in the simulation. The uncertainties on the signal yield due to the electron trigger efficiency uncertainty and the muon trigger efficiency uncertainty are each less than 0.7%.

The uncertainty on the reconstruction and identification efficiency of muons is discussed in Section 3.4.1 and is modelled using a single nuisance parameter. The associated estimated uncertainties on the signal strength measurement are 1.9%, 0.8% and 1.1% in the 4μ, $2\mu2e$ and $2e2\mu$ final states, respectively.

Uncertainties on the electron reconstruction and identification efficiency, discussed in Section 3.4.2, are modelled using seven nuisance parameters, taking into account different E_T ranges: $7 < E_T < 10$ GeV, $10 < E_T < 15$ GeV, $15 < E_T < 20$ GeV and $E_T > 20$ GeV. The method is designed to model the correlations between the systematic uncertainties in the $H \to ZZ^{(*)} \to 4\ell$ analysis and analyses in other Higgs boson decay modes, for example $H \to WW^{(*)} \to \ell\nu\ell\nu$. The systematic uncertainties on the Higgs boson signal strength measurement due to uncertainties in

the electron reconstruction and identification efficiencies, estimated using simulated events with $m_H = 125$ GeV, are 4.4%, 1.7% and 3.3% for $4e$, $2e2\mu$ and $2\mu2e$ final states, respectively.

Based on the data-simulation comparison in a tag-and-probe study of the efficiency of the isolation and impact parameter significance requirements applied in the analysis selection, an additional uncertainty is applied in two E_T bins for electrons with $E_T < 15$ GeV. For electrons with $E_T < 11$ GeV, the uncertainty is 1.4% in the barrel region and 2.5% in the end-cap region. For electrons with 11 GeV $< E_T < 15$ GeV, the uncertainty is 0.7% in the barrel region and 1.2% in the end-cap region. For simulated signal events with $m_H = 125$ GeV, the additional systematic uncertainties induced on the measurement of the Higgs boson signal strength are 1.2%, 0.1% and 1.1% for the $4e$, $2e2\mu$ and $2\mu2e$ final states, respectively. The corresponding uncertainties for muons are found to be negligible.

There are also systematic uncertainties associated with the uncertainty on theoretical calculations, the luminosity measurement and the data-driven estimates of the rates of background processes. These are discussed in Sections 2.2, 3.3 and 4.4 respectively.

A summary of the systematic uncertainties on the measurement of the Higgs boson signal strength in this channel may be found in Table 4.9.

4.7   Results

The event selection described in Section 4.1 is applied to the full 7 TeV and 8 TeV datasets. In total, 428 events are selected with $m_{4\ell} > 100$ GeV, with 137 events selected in the 4μ final state, 212 in total in the $2e2\mu$ and $2\mu2e$ channels and 79 in the $4e$ category. In this mass range, 371 ± 14 events are expected from background processes alone.

Figure 4.12 shows the $m_{4\ell}$ distribution for the selected events, summed over all

Table 4.9: Impact of different sources of systematic uncertainty on the measurement of the Higgs boson signal strength for each of the final states considered in the analysis, as well as their combination. Where a particular source of uncertainty is negligible for a given final state, this is indicated with "–". The systematic uncertainties related to theoretical uncertainties apply equally to all final states [4].

Source of uncertainty	4μ	$2e2\mu$	$2\mu2e$	$4e$	combined
Electron reconstruction/identification efficiencies	–	1.7%	3.3%	4.4%	1.6%
Electron isolation/impact parameter selection	–	0.07%	1.1%	1.2%	0.5%
Electron trigger efficiency	–	0.21%	0.05%	0.21%	<0.2%
$\ell\ell + ee$ backgrounds	–	–	3.4%	3.4%	1.3%
Muon reconstruction/identification efficiencies	1.9%	1.1%	0.8%	–	1.5%
Muon trigger efficiency	0.6%	0.03%	0.6%	–	0.2%
$\ell\ell + \mu\mu$ backgrounds	1.6%	1.6%	–	–	1.2%
QCD scale uncertainty					6.5%
PDF, α_s uncertainty					6.0%
$H \to ZZ^*$ branching ratio uncertainty					4.0%

final states, as well as the expected distributions for the signal and background processes. Distributions are shown for the full mass range considered by the analysis and for a reduced mass range, 80 GeV $< m_{4\ell} <$ 170 GeV. An excess of events above the background-only prediction is visible in the region around $m_{4\ell} =$ 125 GeV. Elsewhere, the data are well described by the background prediction.

Figure 4.13 shows the m_{12} and m_{34} distributions for the selected events, summed over all final states, falling in the mass range used in the maximum likelihood fit, 110 GeV $< m_{4\ell} <$ 140 GeV, and the two-dimensional $m_{12} - m_{34}$ distribution for events with 120 GeV $< m_{4\ell} <$ 130 GeV. In both cases, the expected distributions for signal and background events are also shown. The data are described well by the simulation.

The distribution of $BDT_{ZZ^{(*)}}$ for selected events with 120 GeV $< m_{4\ell} <$ 130 GeV for the sum of all final states is shown in Figure 4.14, along with the two-dimensional $m_{4\ell} - BDT_{ZZ^{(*)}}$ distribution for selected events with 110 GeV $< m_{4\ell} <$ 140 GeV. The expected distributions for signal and background events are again shown. The data are again observed to be compatible with the simulation.

For all of the Figures discussed above, the expected signal distributions are scaled by a factor of $\mu = 1.51$, the best-fit value for the Higgs boson signal strength at $m_H = 125$ GeV, as measured by the categorised analysis described in Chapter 5.

The observed number of events for each final state for the 7 TeV and 8 TeV datasets is shown in Table 4.10 for the mass range 120 GeV $< m_{4\ell} <$ 130 GeV. The expected number of signal and background events in this mass range is also shown, along with the corresponding signal-to-background ratio. The collinear FSR correction is applied to 8 selected events and the non-collinear correction is applied to 2 events. This is in good agreement with the expected numbers from simulation.

The significance of the observed excess around $m_{4\ell} = 125$ GeV is quantified via the local p_0-value, the probability for an excess at least as large as that observed to occur under the background-only hypothesis. The p_0-value is calculated under
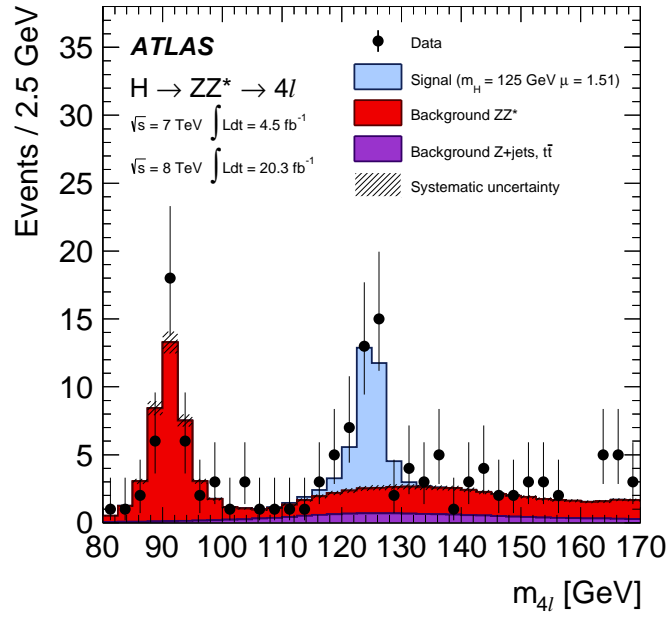
(a)
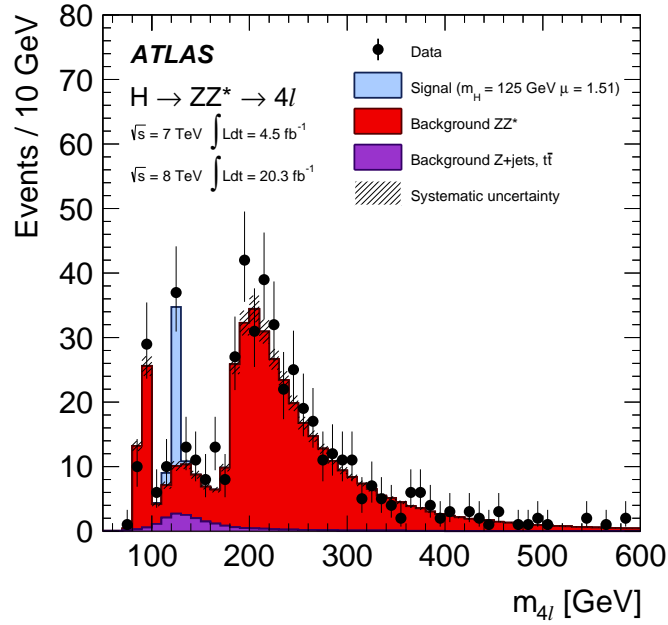
(b)

Figure 4.12: Four-lepton invariant mass distributions for events passing the event selection, summing the 4μ, $2e2\mu$, $2\mu2e$ and $4e$ final states, in the 7 TeV and 8 TeV data sets: a) in the mass range 80 GeV $< m_{4\ell} <$ 170 GeV, and b) in the full mass range. The data are shown as filled circles and the expected signal and background distributions are shown as filled histograms. The $ZZ^{(*)}$ background (red histogram) is shown separately from the Z + jets and $t\bar{t}$ backgrounds (purple histogram). The signal distribution (blue histogram) is shown for $m_H = 125$ GeV and is scaled by a signal strength $\mu = 1.51$. Figure from Ref. [4].
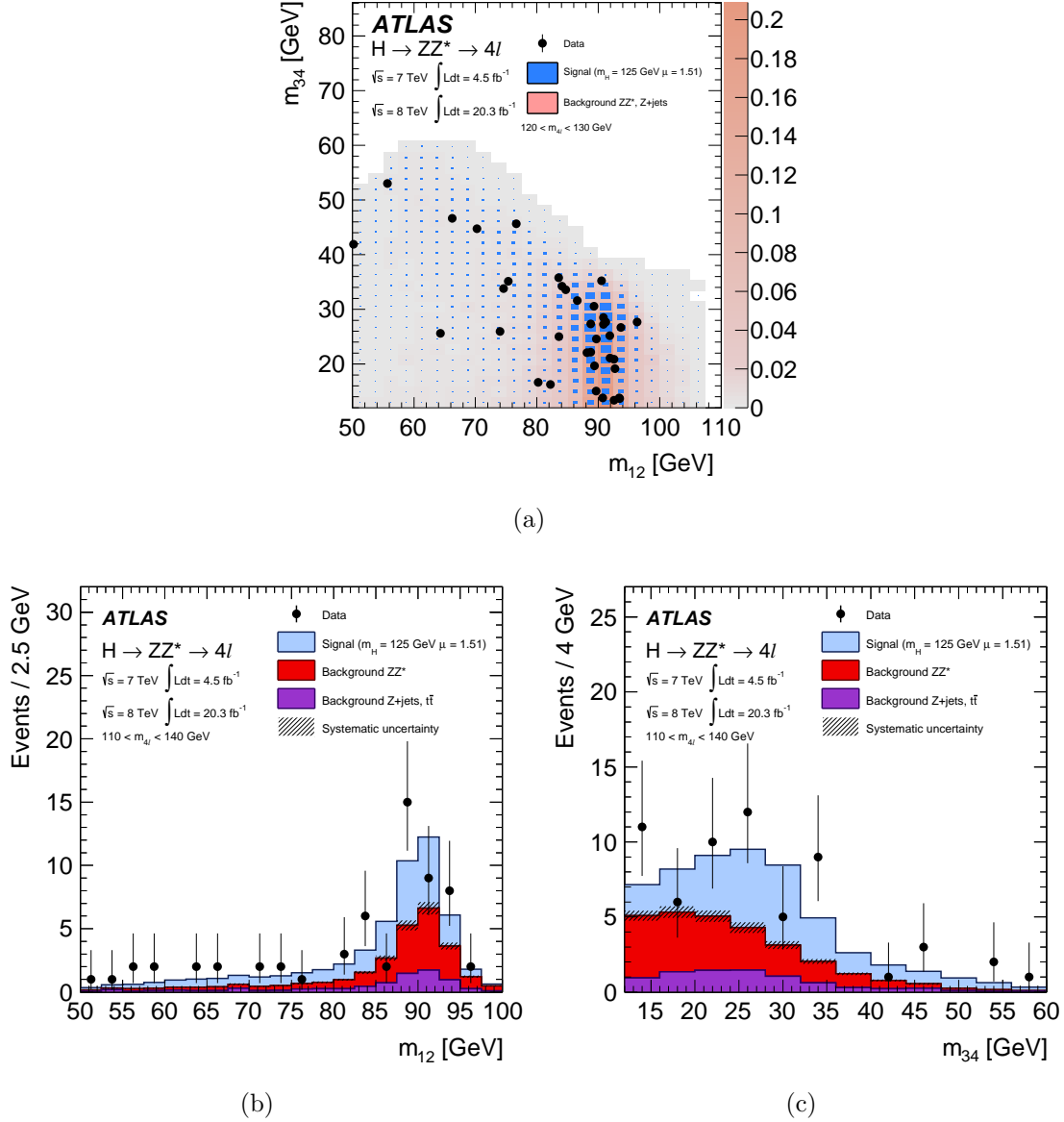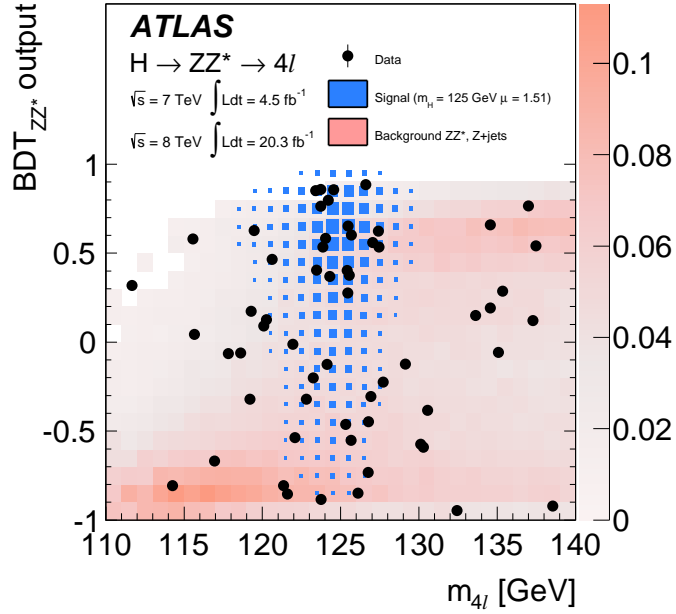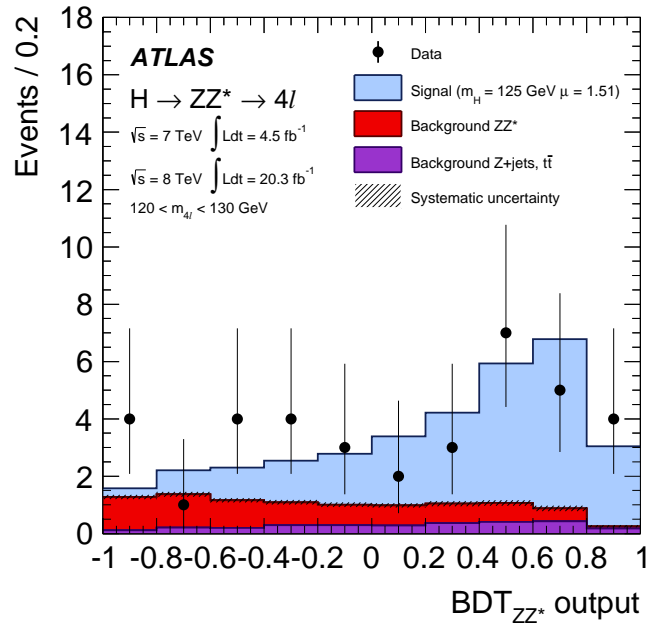
(a)

(b)

(c)

Figure 4.13: a) $m_{12} - m_{34}$, b) m_{12}, and c) m_{34}, distributions for events passing the event selection for all 4ℓ final states in the 7 TeV and 8 TeV data sets. Events in the mass range 120 GeV $< m_{4\ell} <$ 130 GeV are shown in a) and events in the mass range 110 GeV $< m_{4\ell} <$ 140 GeV are shown in b) and c). In a) the expected distributions for the signal (blue) and total background (red) are shown, where the relative density of events is indicated by the box size for the signal and the colour shading for the background. In b) and c) The data are shown as filled circles and the expected signal and background distributions are shown as filled histograms. The $ZZ^{(*)}$ background (red histogram) is shown separately from the Z + jets and $t\bar{t}$ backgrounds (purple histogram). The signal distribution (blue histogram) is shown for $m_H = 125$ GeV and is scaled by a signal strength $\mu = 1.51$. Figure from Ref. [4].

(a)

(b)

Figure 4.14: a) $m_{4\ell} - BDT_{ZZ^{(*)}}$, and b) $BDT_{ZZ^{(*)}}$ distributions for events passing the event selection for all 4ℓ final states in the 7 TeV and 8 TeV data sets: in the mass range 120 GeV $< m_{4\ell} <$ 130 GeV for a), and 110 GeV $< m_{4\ell} <$ 140 GeV for b). In a) the expected distributions for the signal (blue) and total background (red) are shown, where the relative density of events is indicated by the box size for the signal and the colour shading for the background. In b) the data are shown as filled circles and the expected signal and background distributions are shown as filled histograms. The $ZZ^{(*)}$ background (red histogram) is shown separately from the $Z +$ jets and $t\bar{t}$ backgrounds (purple histogram). The signal distribution (blue histogram) is shown for $m_H = 125$ GeV and is scaled by a signal strength $\mu = 1.51$. Figure from Ref. [4].

Table 4.10: The number of events observed after the full event selection for $120 < m_{4\ell} < 130$ GeV for the 7 TeV and 8 TeV datasets. The number of expected signal events under the $m_H = 125$ GeV hypothesis, number of expected $ZZ^{(*)}$ events, number of $Z + $ jets and $t\bar{t}$ events and corresponding signal-to-background ratio are also shown [4].

Final state	Signal full mass range	Signal	$ZZ^{(*)}$	$Z + $ jets, $t\bar{t}$	S/B	Exp.	Obs.
$\sqrt{s} = 7$ TeV							
4μ	1.00 ± 0.10	0.91 ± 0.09	0.46 ± 0.02	0.10 ± 0.04	1.7	1.47 ± 0.10	2
$2e2\mu$	0.66 ± 0.06	0.58 ± 0.06	0.32 ± 0.02	0.09 ± 0.03	1.5	0.99 ± 0.07	2
$2\mu2e$	0.50 ± 0.05	0.44 ± 0.04	0.21 ± 0.01	0.36 ± 0.08	0.8	1.01 ± 0.09	1
$4e$	0.46 ± 0.05	0.39 ± 0.04	0.19 ± 0.01	0.40 ± 0.09	0.7	0.98 ± 0.10	1
Total	2.62 ± 0.26	2.32 ± 0.23	1.17 ± 0.06	0.96 ± 0.18	1.1	4.45 ± 0.30	6
$\sqrt{s} = 8$ TeV							
4μ	5.80 ± 0.57	5.28 ± 0.52	2.36 ± 0.12	0.69 ± 0.13	1.7	8.33 ± 0.6	12
$2e2\mu$	3.92 ± 0.39	3.45 ± 0.34	1.67 ± 0.08	0.60 ± 0.10	1.5	5.72 ± 0.37	7
$2\mu2e$	3.06 ± 0.31	2.71 ± 0.28	1.17 ± 0.07	0.36 ± 0.08	1.8	4.23 ± 0.30	5
$4e$	2.79 ± 0.29	2.38 ± 0.25	1.03 ± 0.07	0.35 ± 0.07	1.7	3.77 ± 0.27	7
Total	15.6 ± 1.6	13.8 ± 1.4	6.24 ± 0.34	2.00 ± 0.28	1.7	22.1 ± 1.5	31
$\sqrt{s} = 7$ TeV and $\sqrt{s} = 8$ TeV							
4μ	6.80 ± 0.67	6.20 ± 0.61	2.82 ± 0.14	0.79 ± 0.13	1.7	9.81 ± 0.64	14
$2e2\mu$	4.58 ± 0.45	4.04 ± 0.40	1.99 ± 0.10	0.69 ± 0.11	1.5	6.72 ± 0.42	9
$2\mu2e$	3.56 ± 0.36	3.15 ± 0.32	1.38 ± 0.08	0.72 ± 0.12	1.5	5.24 ± 0.35	6
$4e$	3.25 ± 0.34	2.77 ± 0.29	1.22 ± 0.08	0.76 ± 0.11	1.4	4.75 ± 0.32	8
Total	18.2 ± 1.8	16.2 ± 1.6	7.41 ± 0.40	2.95 ± 0.33	1.6	26.5 ± 1.7	37

the asymptotic approximation [104] using the profile likelihood ratio test statistic described in Section 4.5. The maximum p_0-value, corresponding to 8.2 standard deviations, is found to be at $m_H = 124.51$ GeV, where the expected significance for a SM Higgs boson of this mass is 5.8 standard deviations. At the ATLAS best-fit value for the Higgs boson mass, $m_H = 125.36$ GeV (discussed in section 4.7.1), the p_0-value corresponds to 8.1 standard deviations, where the expected significance is 6.2 standard deviations. The p_0-value is shown as a function of m_H in Figure 4.15.
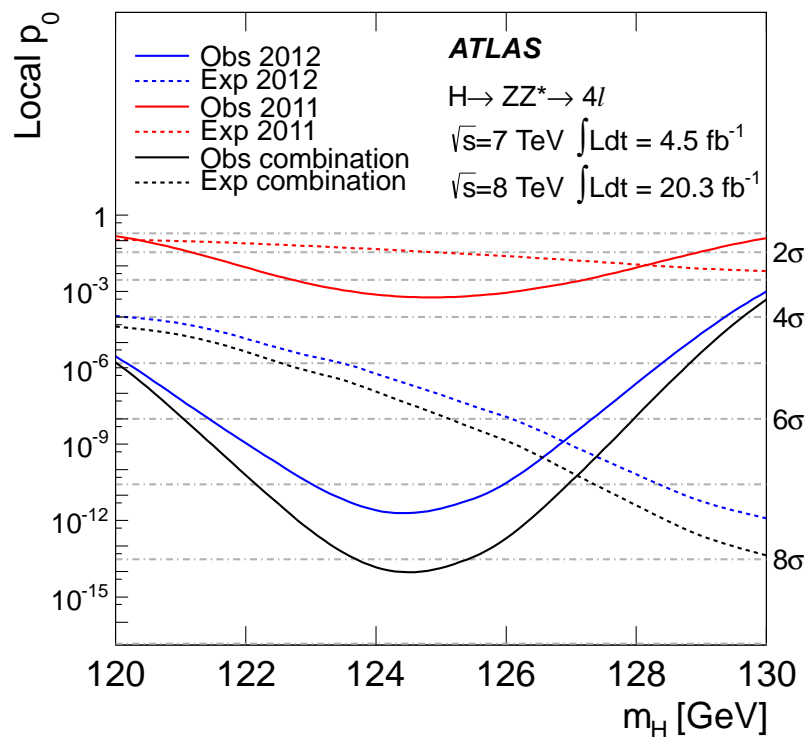
Figure 4.15: Observed (solid lines) and median expected (dashed lines) distributions for the local p_0-value as a function of m_H for the 7 TeV (red) and 8 TeV (blue) datasets and their combination (black). The dashed lines show p_0-values corresponding to integer numbers of standard deviations. Figure from Ref. [4].

4.7.1   Higgs boson mass and inclusive signal strength measurement

The Higgs boson mass is measured using the selected $H \to ZZ^{(*)} \to 4\ell$ events using the profile likelihood ratio test statistic described in Section 4.5. Using the baseline two-dimensional fit method, the best-fit value is:

$$m_H = 124.51 \pm 0.52(\text{stat}) \pm 0.06(\text{syst})\text{GeV}$$

where the systematic uncertainty is calculated by taking the quadrature subtraction of the full fit uncertainty, minus the fit uncertainty when fixing the nuisance parameters corresponding to systematic uncertainties to their best fit values. Using the cross-check methods described in Section 4.5, similar best-fit values are obtained for the Higgs boson mass, with the best-fit value from the one-dimensional method within 120 MeV of the baseline value and the best-fit value from the per-event-errors method with 60 MeV.

At $m_H = 124.51$ GeV, the best-fit inclusive signal strength is $\mu = 1.66^{+0.45}_{-0.38}$. At the best-fit value for the Higgs boson mass obtained using the combination of the $H \to ZZ^{(*)} \to 4\ell$ and $H \to \gamma\gamma$ channels in ATLAS (discussed in Section 4.7.1), the best-fit value is found to be $\mu = 1.50^{+0.35}_{-0.31}(\text{stat})^{+0.19}_{-0.13}(\text{syst})$.

The profile likelihood is shown as a function of the Higgs boson mass in Figure 4.16, and as a function of the Higgs boson signal strength (with the Higgs boson mass fixed to the ATLAS combined best-fit value, $m_H = 125.36\text{GeV}$) in Figure 4.17. In both cases, the results are shown for the individual channels and their combination.

4.7.1.1   ATLAS combined measurement

To improve the precision on the Higgs boson mass measurement, ATLAS performs a combined fit to the observed events selected in the $H \to ZZ^{(*)} \to 4\ell$ and $H \to \gamma\gamma$ final states, where the latter analysis is described in Ref. [93]. The measured Higgs
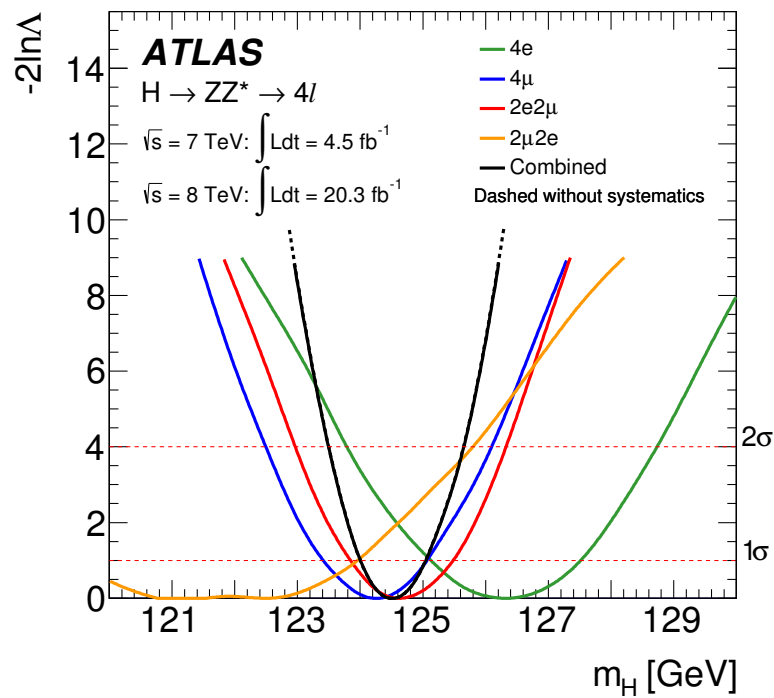
Figure 4.16: Profile likelihood as a function of the Higgs boson mass, m_H, for the combination of the 7 TeV and 8 TeV datasets. The 4μ (blue), $2\mu2e$ (yellow), $2e2\mu$ (red) and $4e$ (green) channels are shown, together with the combination of all channels (black). For the combination, the result is shown with (solid line) and without (dashed line) systematic uncertainties included. Figure from Ref. [93].
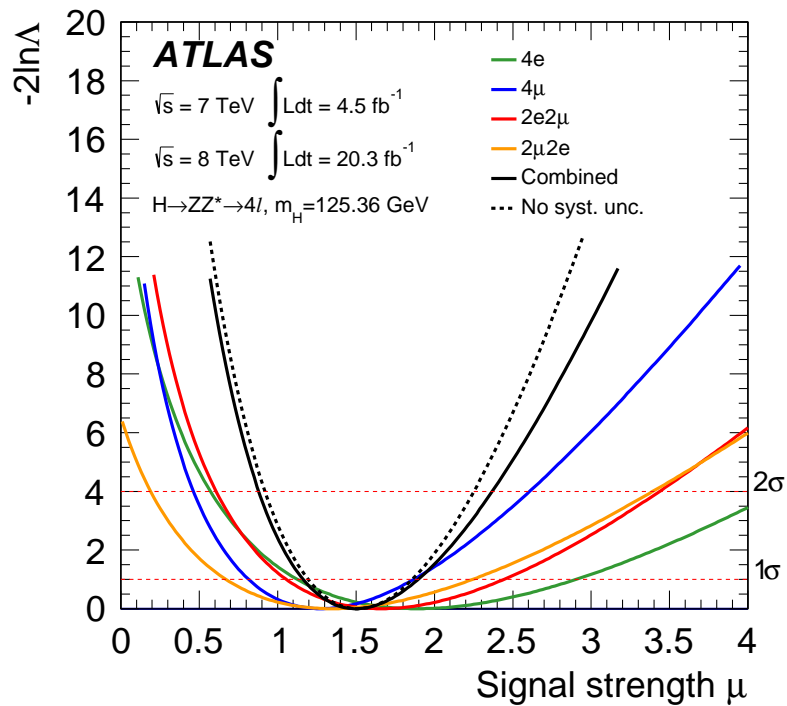
Figure 4.17: Profile likelihood as a function of the Higgs boson signal strength, μ, for the combination of the 7 TeV and 8 TeV datasets. The 4μ (blue), $2\mu2e$ (yellow), $2e2\mu$ (red) and $4e$ (green) channels are shown, together with the combination of all channels (black). For the combination, the result is shown with (solid line) and without (dashed line) systematic uncertainties included. The value of the Higgs boson mass is fixed to the ATLAS combined best-fit value, $m_H = 125.36$ GeV. Figure from Ref. [4].

boson mass using the $H \to \gamma\gamma$ final state alone is $m_H = 125.98 \pm 0.42(\text{stat}) \pm 0.28(\text{syst})\text{GeV}$.

The profile likelihood ratio test statistic used for the combined mass measurement, $\Lambda(m_H)$, is:

$$\Lambda(m_H) = \frac{\mathcal{L}(m_H, \hat{\hat{\mu}}_{4\ell}(m_H), \hat{\hat{\mu}}_{\gamma\gamma}(m_H), \hat{\hat{\boldsymbol{\theta}}}(m_H))}{\mathcal{L}(\hat{m}_H, \hat{\mu}_{4\ell}, \hat{\mu}_{\gamma\gamma}, \hat{\boldsymbol{\theta}})} \qquad (4.6)$$

where the signal strengths for the four-lepton, $\mu_{4\ell}$, and diphoton, $\mu_{\gamma\gamma}$, decay modes are profiled separately. The best-fit value for the Higgs boson mass from the combined fit is $m_H = 125.36 \pm 0.37(\text{stat}) \pm 0.18(\text{syst})\text{GeV}$. As a cross-check, the fit is also performed using a common, fixed signal strength, $\mu = 1$, and the result is found to lie within 80 MeV of the baseline value. The profile likelihood is shown as a function of m_H in Figure 4.18 for the individual decay modes and their combination. For the $H \to ZZ^{(*)} \to 4\ell$ final state the uncertainty is dominated by the statistical component, whereas for the $H \to \gamma\gamma$ final state the systematic uncertainty, though smaller than the statistical uncertainty, has a non-negligable impact.

The compatibility between the mass measurements in the two decay modes is studied by reparameterising the profile likelihood ratio above in terms of the difference between the measured mass in each mode, Δm_H, profiling m_H in the fit. The compatibility, derived from the value of the profile likelihood ratio at $\Delta m_H = 0$, corresponds to a significance of 1.98 standard deviations.

4.7.1.2 Combined ATLAS and CMS measurement

Using the full LHC Run I dataset, the ATLAS and CMS collaborations have performed a simultaneous fit to the observed data samples in the $H \to ZZ^{(*)} \to 4\ell$ and $H \to \gamma\gamma$ final states by each experiment [112]. The results for the Higgs boson mass measurements performed by the CMS collaboration in the $H \to ZZ^{(*)} \to 4\ell$ and $H \to \gamma\gamma$ channels may be found in Refs. [103] and [113] respectively, while the
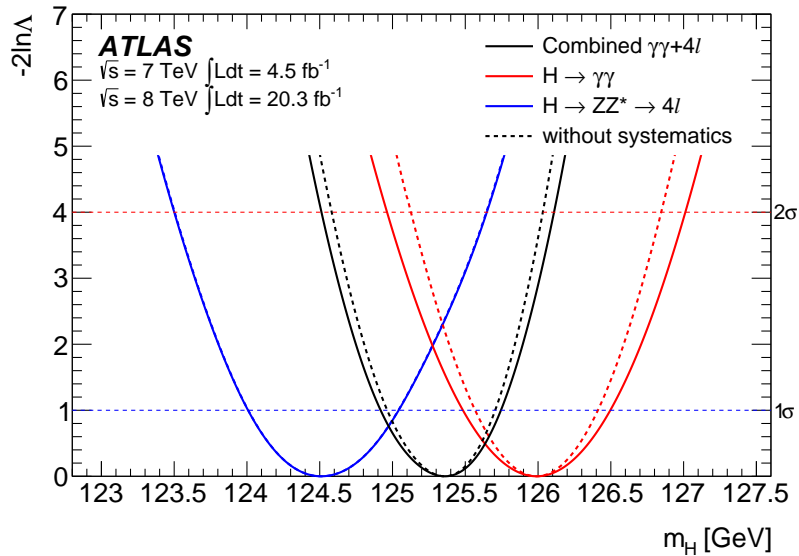
Figure 4.18: Profile likelihood as a function of the Higgs boson mass, m_H, for the combination of the 7 TeV and 8 TeV datasets. The result is shown using the $H \to ZZ^{(*)} \to 4\ell$ decay mode alone (blue), the $H \to \gamma\gamma$ decay mode alone (red) and the combination (black). In each case, the result is shown with (solid line) and without (dashed line) systematic uncertainties included. Figure from Ref. [93].
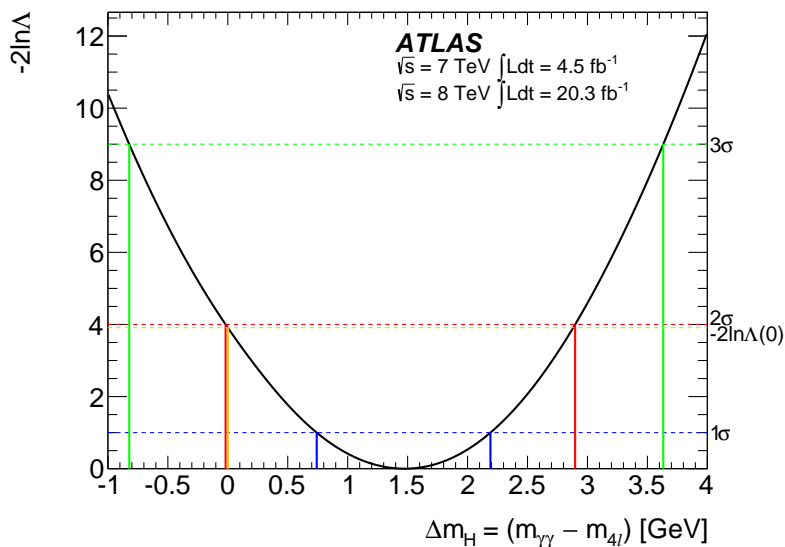

Figure 4.19: Profile likelihood as a function of the difference between the measured Higgs boson masses in the $H \to ZZ^{(*)} \to 4\ell$ and $H \to \gamma\gamma$ channels, Δm_H, for the combination of the 7 TeV and 8 TeV datasets [93].

CMS combined Higgs boson mass measurement may be found in Ref. [114].

The procedure is similar to the procedure used for the ATLAS combination, and the best-fit value for the Higgs boson mass is found to be:

$$m_H = 125.09 \pm 0.21(\text{stat}) \pm 0.11(\text{syst})\text{GeV}$$

A summary of the measured masses in each channel for each experiment is shown in Figure 4.20, along with the combined measurements for each experiment and the overall combined measurement. The individual measurements are consistent with each other.
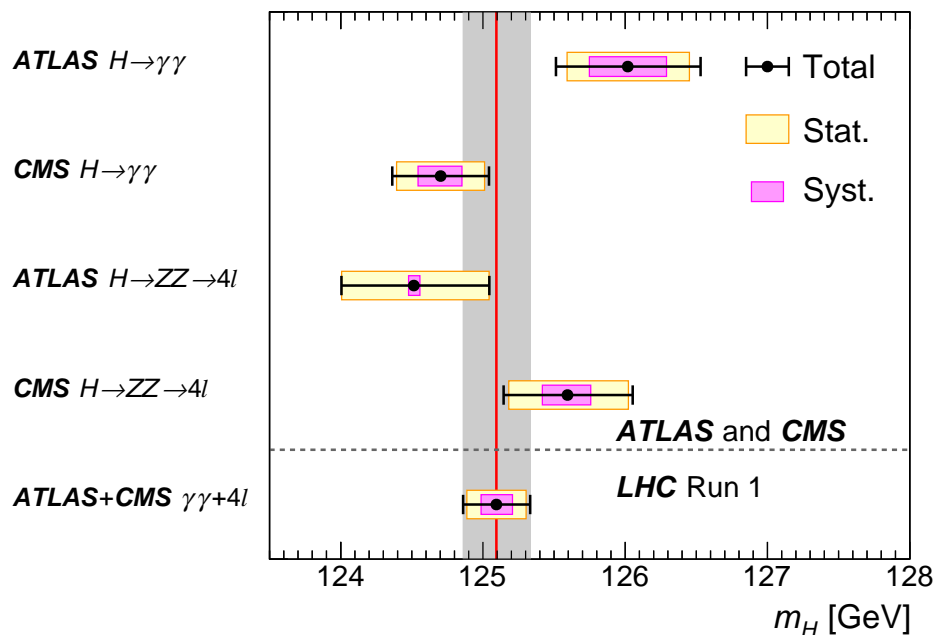

Figure 4.20: Measured mass of the Higgs boson for the $H \to ZZ^{(*)} \to 4\ell$ and $H \to \gamma\gamma$ channels in the ATLAS and CMS experiments, the combined mass measurement for each experiment and the overall combination. The systematic uncertainties (magenta bands), statistical uncertainties (yellow bands) and total uncertainties (error bars) are shown. The red line shows the combined best-fit mass, and the grey line shows the total uncertainty on this measurement. Figure from Ref. [112].

4.7.2   Fiducial and differential cross section measurements

ATLAS has also measured fiducial and differential cross sections for Higgs boson production in the $H \to ZZ^{(*)} \to 4\ell$ final state using the 8 TeV dataset [5]. The differential cross section measurements are performed in bins of six variables: the transverse momentum of the four-lepton systems, $p_T^{4\ell}$, the pseudo-rapidity of the four-lepton system, $y^{4\ell}$, the dilepton invariant mass of the sub-leading lepton pair, m_{34}, the decay angle of the leading dilepton with respect to the beam axis in the four-lepton rest frame, the number of jets per event, N_{jets}, and the transverse momentum of the leading jet, p_T^j.

Figure 4.21 shows the observed and expected distributions in four of these variables - $p_T^{4\ell}$, m_{34}, N_{jets} and p_T^j - for events with 118 GeV $< m_{4\ell} <$ 129 GeV. In each case, the observed data agree well with the prediction.

In a fiducial region designed to be as close as possible to the analysis selection presented in Section 4.1, described in Ref. [5], the cross section is found to be $\sigma_{tot}^{fid} = 2.11^{+0.53}_{-0.47}(\text{stat}) \pm 0.08(\text{syst})$ fb. This is consistent with the theoretical prediction for $m_H = 125.4\,\text{GeV}$ $\sigma_{tot}^{fid} = 1.30 \pm 0.13$ fb [27].

ATLAS has also measured fiducial and differential Higgs boson cross sections in the diphoton final state [115], and these results have been combined [116].
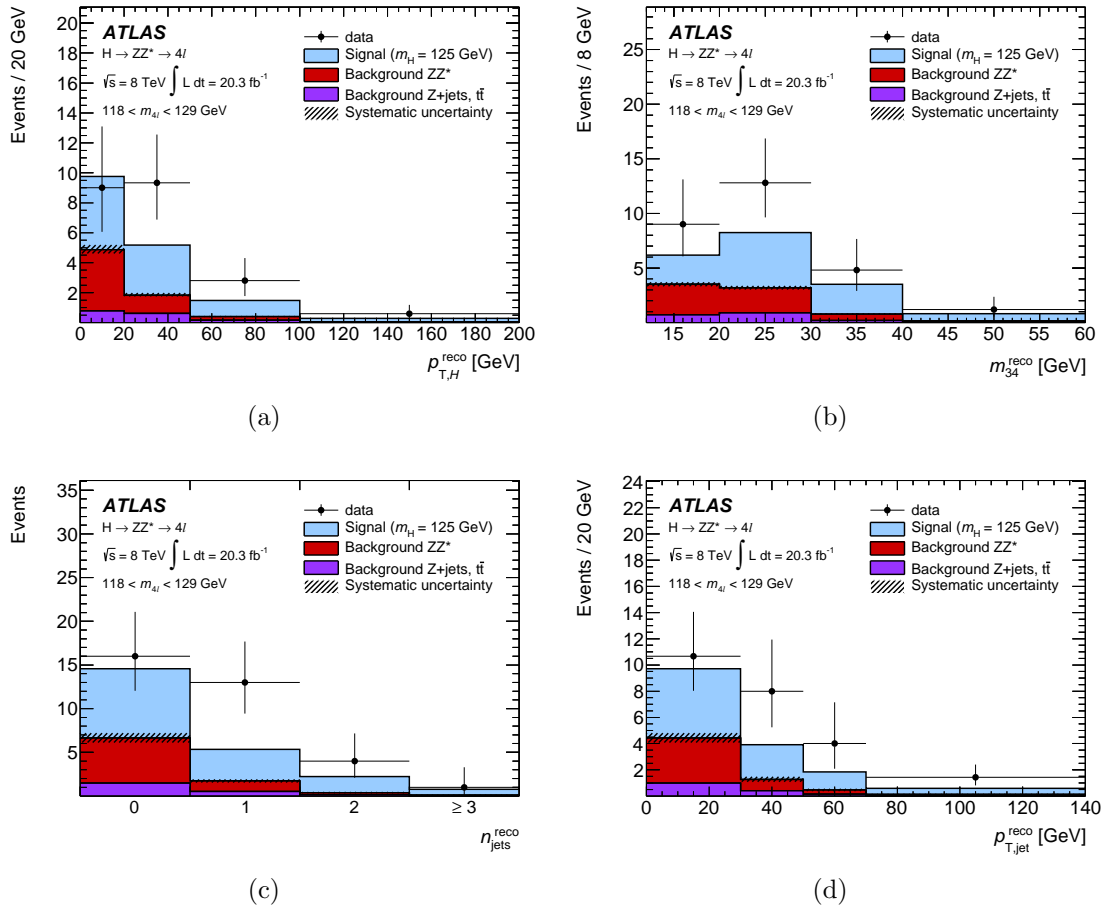
Figure 4.21: a) $p_T^{4\ell}$, b) m_{34}, c) N_{jets}, and d) $p_T^{4\ell}$, for selected events, summing the 4μ, $2e2\mu$, $2\mu2e$ and $4e$ final states, in the mass range 118 GeV $< m_{4\ell} <$ 129 GeV for the 8 TeV data. The expected signal distributions for $m_H = 125$ GeV are shown (blue filled histograms), as are the expected $ZZ^{(*)}$ (red filled histograms) and $Z+$jets and $t\bar{t}$ (purple filled histograms) background distribution. Figure from Ref. [5].

Higgs boson production rates and couplings in the $H \rightarrow ZZ^{(*)} \rightarrow 4\ell$ channel

This chapter contains a detailed discussion of the ATLAS collaboration measurement of the production rates and couplings of the Higgs boson in the $H \rightarrow ZZ^{(*)} \rightarrow 4\ell$ decay mode using the full LHC run I dataset [4]. The results supercede those from the preliminary analysis described in Ref [107].

5.1 Event categorisation

To extract the rates for different Higgs boson production mechanisms, events passing the $H \rightarrow ZZ^{(*)} \rightarrow 4\ell$ selection requirements detailed in 4.1 are categorised to gain the sensitivity to discriminate between Higgs boson production modes. Selected events are assigned to one of the following four categories - *VBF-enriched*, *VH-hadronic enriched*, *VH-leptonic enriched* and *ggF-enriched* - where the first three

categories apply requirements on top of the usual event selection based on the characteristic signatures of the VBF and VH Higgs boson production modes.

This categorisation is summarised in the schematic diagram in Figure 5.1 and the following sections discuss the *VBF-enriched*, *VH-hadronic enriched* and *VH-leptonic enriched* categories in more detail. Candidates not assigned to any of these categories are placed in the *ggF-enriched* category.
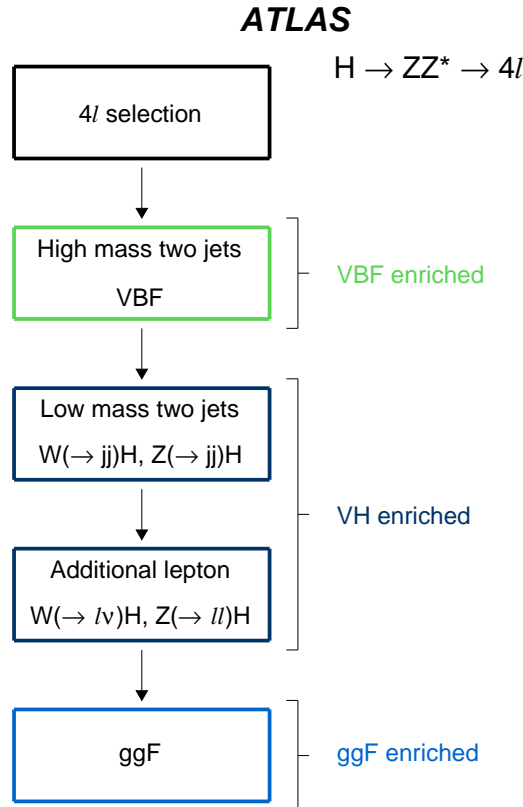

Figure 5.1: Schematic representation of the event categorisation procedure for the $H \rightarrow ZZ^{(*)} \rightarrow 4\ell$ measurement of Higgs boson production rates and couplings. Events passing the selection requirements described in Section 4.1 are assigned to one of four categories which are tested sequentially: *VBF-enriched, VH-hadronic enriched, VH-leptonic enriched* or *ggF-enriched* [4].

5.1.1   VBF enriched category selection criteria

The signature of the VBF Higgs boson production mechanism is the presence of two high transverse momentum jets, well separated in pseudorapidity.

VBF-like events are selected by requiring that the Higgs boson candidate is accompanied by at least two jets with $p_T > 25$ (30) GeV for $|\eta| < 2.5$ ($2.5 < |\eta| < 4.5$). If more than two jets are identified per event, the two highest p_T jets are selected as the VBF-tagged jets. Selecting instead the two jets comprising the highest invariant mass di-jet candidate in the event has negligible impact on the expected sensitivity.

The selection criteria for the *VBF-enriched* and *VH-hadronic enriched* categories are required to be orthogonal, so only events where the di-jet mass of the VBF-tagged jets is greater than 130 GeV are selected as *VBF-enriched*, with negligible impact on the sensitivity of the category.

The selection efficiency of the *VBF-enriched* category is estimated to be 55% using a simulated sample of events in the VBF production mode. A considerable fraction of the events entering the category, estimated to be 54% from simulation, are produced via the ggF mechanism, so to discriminate between VBF and ggF events a BDT classifier, labelled BDT_{VBF}, is used. The response of this BDT is used as an observable in the *VBF-enriched* category in a multi-observable maximum likelihood fit, described in Section 5.4.

5.1.1.1   Boosted Decision Tree classifier for VBF enriched category

The BDT classifier designed to discriminate between events produced by the VBF and ggF production mechanisms, BDT_{VBF}, is trained using simulated VBF events as signal and simulated ggF events as background. The classifier input variables are:

   - The invariant mass of the tagged di-jet system, m_{jj}

- The pseudorapidity separation between the two tagged jets, $|\eta_{jj}|$

- The transverse momentum of each tagged jet, $p_T^{1,2}$

- The pseudorapidity of the highest p_T jet, η_1

where the variables are ranked in order of separation[1], which gives an indication of the relative discriminating power of each of the BDT input variables.

The distributions of the BDT input variables and the overall BDT response are shown in Figure 5.2. As expected, the distributions indicate that Higgs boson events produced via the VBF mechanism typically have a higher di-jet invariant mass and larger pseudorapidity separation than events produced via the ggF mechanism. The p_T spectra of the leading and sub-leading tagged jets peak at higher p_T values for events produced via the VBF mechanism.

The BDT response is found to be similar for ggF produced signal events and for the $ZZ^{(*)}$ background. Combining the simulated ggF and $ZZ^{(*)}$ events to form the background sample for the training has a negligible impact on the results.

Additional variables have been tested as input variables to the BDT. These include additional kinematic observables:

- The di-jet transverse momentum, p_T^{jj}

- The azimuthal separation between the di-jet system and the four-lepton system, $\phi_{4\ell,jj}$

- The pseudo-rapidity of a third jet (when present), η_3

- The angular distance between the four-lepton system and the closest jet $\Delta R_{4\ell,jj}$

---

[1]The separation provided by a variable, x, is calculated via the integral:

$$\frac{1}{2}\int \frac{(\hat{x}_S(x) - \hat{x}_B(x))^2}{\hat{x}_S(x) + \hat{x}_B(x)}$$

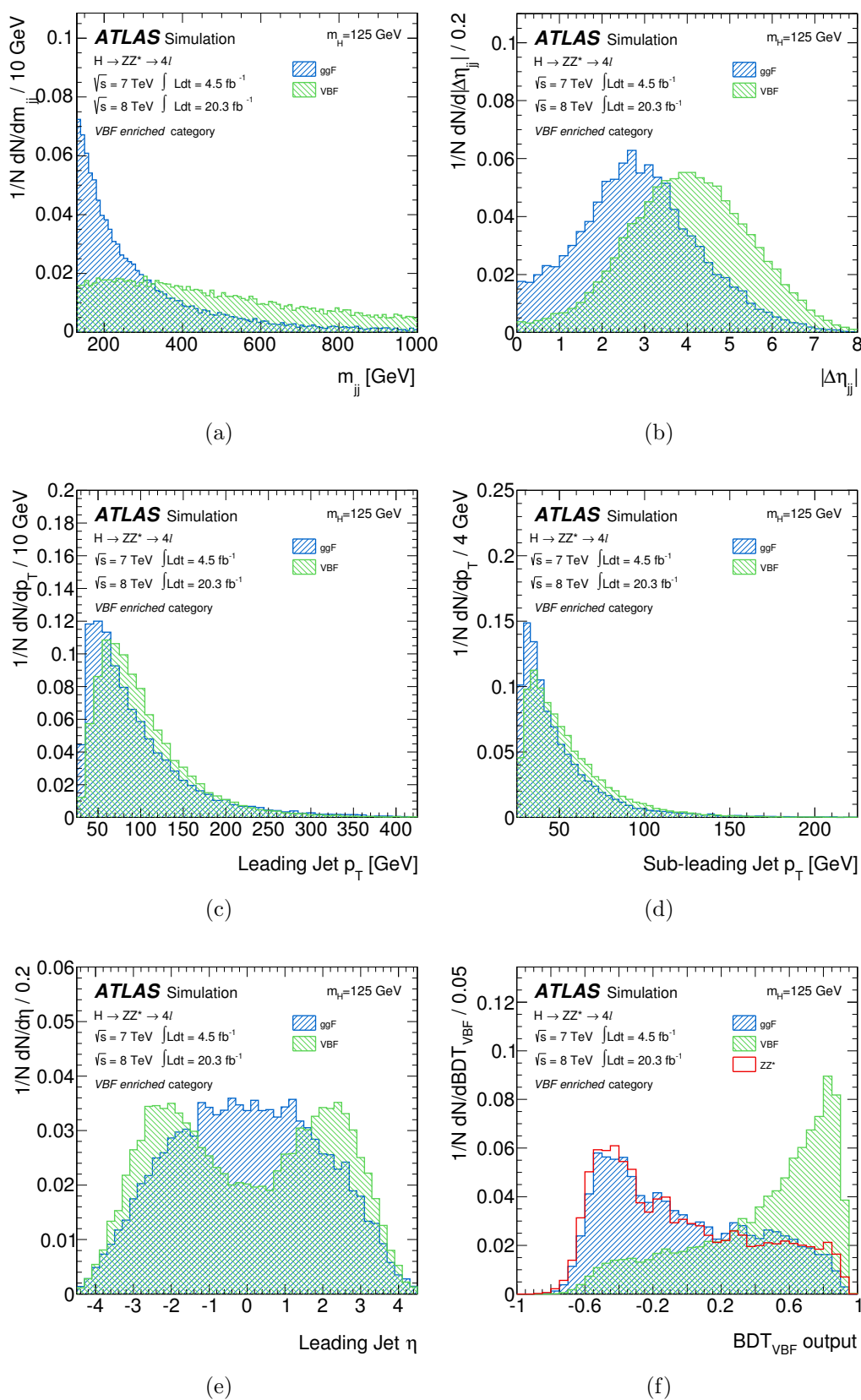where $\hat{x}_S(x)$ and $\hat{x}_B(x)$ are the signal and background PDFs.

Figure 5.2: Distribution of input variables for the VBF (green histograms) and ggF (blue histograms) event samples used in the training of the BDT: (a) dijet invariant mass, (b) dijet η separation, (c) leading jet p_T, (d) sub-leading jet p_T and (e) leading jet η. (f) BDT_{VBF} response for VBF and ggF events, as well as for the ZZ^* background (red). All histograms in a given figure are normalised to the same area [4].

and variables designed to differentiate between gluon-induced and quark-induced jets:

- The number of tracks in a jet

- The jet width, W, which is defined as:

$$W = \frac{\Sigma_i \Delta R^i p_T^i}{\Sigma_i P_T^i}$$

where i are the jet constiuents [117].

For the addition of any of the variables above, at most a small improvement in the discriminating power between VBF and ggF events is achieved. Since for these variables differences are seen between the observed and simulated data, the addition of any of these variables to the BDT would necessitate adding additional systematic uncertainties, negating any improvements in the discriminating power.

The dependence of the output of the BDT discriminant on the Higgs boson mass is negligible, and so the training used four simulated samples with m_H=123, 124, 126 and 127 GeV for each of the ggF and VBF processes. These samples are split evenly into training and testing samples. Training is performed separately for the 7 TeV and 8 TeV datasets to take the difference in kinematics into account.

5.1.2 VH-hadronic enriched category selection criteria

For Higgs boson production in association with a hadronically decaying electroweak boson, a typical event signature is the presence of two jets whose invariant mass peaks at around either $m_{W^\pm} = 80.4$ GeV or $m_Z = 91.2$ GeV. Given the significantly higher cross section for ggF Higgs boson production, events with similar signatures are expected to occur mainly via the ggF process.

VH-like events are selected as *VH-hadronic enriched* by requiring that candidate events contain at least two jets with $p_T > 25$ (30) GeV for $|\eta| < 2.5$ $(2.5 < |\eta| < 4.5)$.

If more than two jets are identified per event, the two highest p_T jets are again selected as the tagged jets. To reduce the proportion of events in this category originating from the ggF process, the di-jet invariant mass is required to satisfy 40 GeV $< m_{jj} <$ 130 GeV. The di-jet invariant mass for selected events containing at least two jets is shown in Figure 5.3.
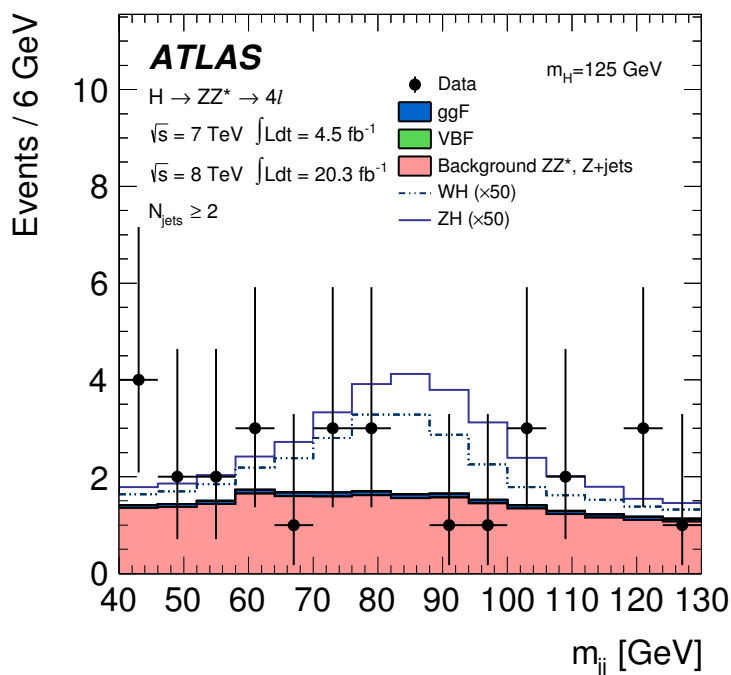

Figure 5.3: Di-jet invariant mass distribution for events containing at least two jets, shown with simulated WH (dot-dash line) and ZH (solid line) events scaled by a factor of 50. Simulated ggF (blue histogram), VBF (blue histogram) and ZZ (pink histogram) events are also shown. The ZH signal is added on top of the WH signal [4].

To further reduce the number of ggF events entering this category, a BDT has been developed to discriminate between the VH and ggF signal processes. The category selection places an additional requirement on the output of this BDT.

5.1.2.1   Boosted Decision Tree classifier for VH-hadronic enriched category

The BDT classifier to discriminate between VH and ggF events, $\mathrm{BDT_{VH}}$, is a BDT using the same input variables as $\mathrm{BDT_{VBF}}$:

- The invariant mass of the tagged di-jet system, m_{jj}

- The transverse momentum of each tagged jet, $p_T^{2,1}$

- The pseudorapidity separation between the two tagged jets, $|\eta_{jj}|$

- The pseudorapidity of the highest p_T jet, η_1

where the variables are again ranked in order of separation (as defined previously), and do not follow the same order as for the $\mathrm{BDT_{VBF}}$ case. The inclusion of the di-jet transverse momentum, p_T^{jj}, was also tested, but was found not to improve the performance of the classifier.

Similarly to the *VBF-enriched* case, simulated samples with m_H=123, 124, 126 and 127 GeV for each of the ggF and VH processes are used, and are combined and split evenly into training and testing samples. Training is performed separately for the 7 TeV and 8 TeV datasets. The response of the $\mathrm{BDT_{VH}}$ classifier for simulated VH and ggF events is shown in Figure 5.4.
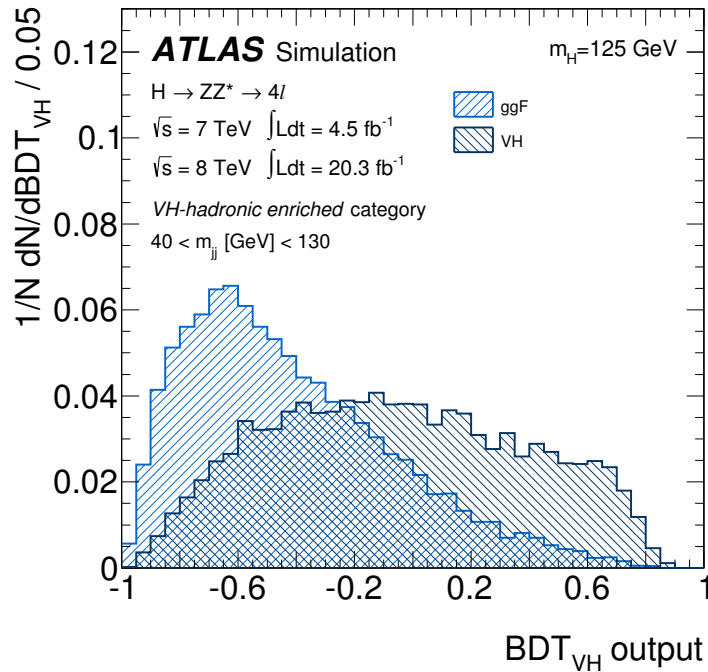

Figure 5.4: Output of the $\mathrm{BDT_{VH}}$ classifier for simulated VH (dark blue) and ggF (light blue) events falling with 40 GeV $< m_{jj} <$ 130 GeV [4].

The requirement placed on the value of $\mathrm{BDT_{VH}}$ is chosen to optimise the median expected significance, considering VH events as signal and all other processes as background, and is -0.4 for the 7 TeV data and 8 TeV data. After this cut the proportion of events selected in this category originating from the ggF production mechanism is 54%. The signal efficiency for the di-jet requirement is 48% for both the WH and ZH production mechanisms, according to the simulation. The addition of the hadronic VH-specific selection, namely the di-jet invariant mass and $\mathrm{BDT_{VH}}$ requirements, reduces the signal efficiency to 25%.

5.1.3   VH-leptonic enriched category selection criteria

A characteristic signature of Higgs boson production in association with a leptonically decaying electroweak boson is the presence of one or two additional isolated leptons. Events are assigned to the *VH-leptonic enriched* category if at least one additional electron or muon is identified in addition to the leptons selected as part of the Higgs boson candidate.

To suppress events produced by other production mechanisms or background processes, the additional lepton is required to pass the same lepton identification criteria as leptons selected as part of the Higgs boson candidate (satisfy the same isolation, impact parameter significance and ΔR requirements) and, to reduce the number of events entering the category where a Higgs boson is produced via the ggF mechanism in association with a fake or non-prompt lepton, to satisfy $p_\mathrm{T} > 8$ GeV. The transverse momentum requirement is chosen to optimise the median expected significance, considering VH-produced Higgs boson events as signal and other Higgs boson and background events as background.

The efficiency of this selection for VH signal events, estimated using simulated events with $m_H = 125$ GeV, is around 90% for leptonic WH events and close to 100% for leptonic ZH events.

5.1.4 Expected yields

The number of expected events satisfying 110 GeV $< m_{4\ell} <$ 140 GeV for each production process is given for each category in Table 5.1 for the 7 TeV and 8 TeV datasets. These yields are estimated using simulated events at $m_H = 125$ GeV. The expected composition for each category is presented schematically for the 8 TeV dataset in Figure 5.5.

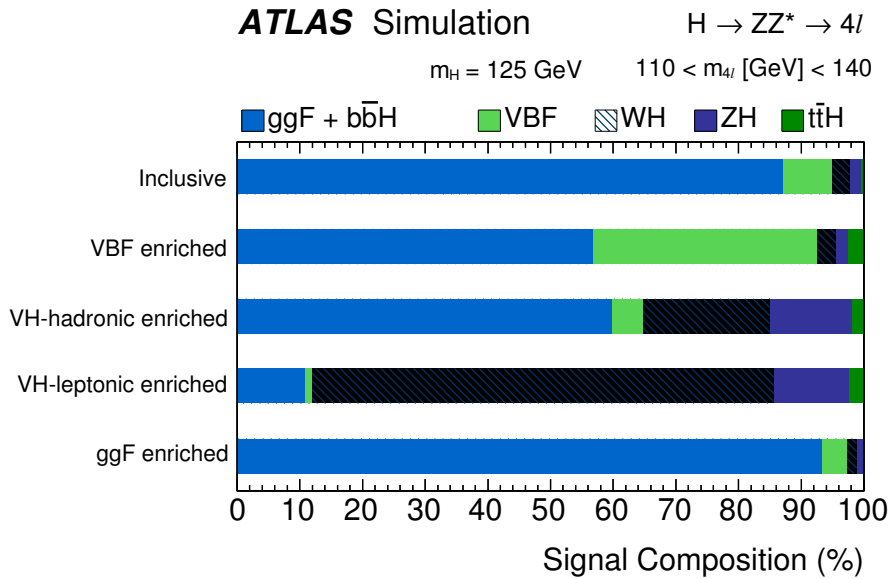
Figure 5.5: Expected composition of each category in terms of Higgs boson production mechanisms for the 8 TeV events with 110 GeV $< m_{4\ell} <$ 140 GeV, calculated using simulated samples with $m_H = 125$ GeV. The overall composition is also shown. Figure from Ref. [4].

5.2 Background estimation in categories

As for the inclusive analysis, the expected $ZZ^{(*)}$ background yields are evaluated in each category using simulation. For the $Z + \mathrm{jets}$ and $t\bar{t}$ backgrounds the fraction of events falling in each category is estimated using simulation, and these fractions are applied to the data-driven background estimates discussed in Section 4.4. The associated systematic uncertainties are estimated by taking the difference between the fractions obtained using simulation, and the equivalent fractions obtained by

Table 5.1: Expected number of events in each category (*ggF-enriched*, *VBF-enriched*, *VH-hadronic enriched*, *VH-leptonic enriched*), calculated using simulated samples with $m_H = 125$ GeV. The number of expected events is specified individually for each production mechanism considered by the analysis.

True origin	Category			
	ggF-enriched	*VBF-enriched*	*VH-hadronic enriched*	*VH-leptonic enriched*
	7 TeV data			
ggF	2.035	0.107	0.046	0.004
VBF	0.114	0.135	0.007	0.000
WH	0.034	0.009	0.023	0.011
ZH	0.026	0.005	0.014	0.002
$b\bar{b}H$	0.022	0.001	0.001	0.000
$t\bar{t}H$	0.000	0.007	0.002	0.000
	8 TeV data			
ggF	11.846	1.084	0.367	0.009
VBF	0.508	0.679	0.030	0.001
WH	0.195	0.059	0.124	0.062
ZH	0.148	0.035	0.080	0.010
$b\bar{b}H$	0.129	0.012	0.004	0.000
$t\bar{t}$H	0.002	0.051	0.012	0.002

applying the event categorisation to the data control regions used for the background estimates. The number of estimated $Z +$ jets and $t\bar{t}$ events for the $\ell\ell\mu\mu$ and $\ell\ell ee$ final states in each category is shown in Table 5.2.

Table 5.2: Background estimates for $\ell\ell\mu\mu$ and $\ell\ell ee$ final states in each category for the 7 TeV and 8 TeV data samples for $80 < m_{4\ell} < 600$ GeV [4]. The uncertainties include the statistical and systematic components.

Channel	*ggF-enriched*	*VBF-enriched*	*VH-hadronic enriched*	*VH-leptonic enriched*
	$\sqrt{s} = 7$ TeV			
$\ell\ell + \mu\mu$	0.98 ± 0.32	0.12 ± 0.08	0.04 ± 0.02	0.004 ± 0.004
$\ell\ell + ee$	5.5 ± 1.2	0.51 ± 0.6	0.20 ± 0.16	0.06 ± 0.11
	$\sqrt{s} = 8$ TeV			
$\ell\ell + \mu\mu$	6.7 ± 1.4	0.6 ± 0.6	0.21 ± 0.13	0.003 ± 0.003
$\ell\ell + ee$	5.1 ± 1.4	0.5 ± 0.6	0.19 ± 0.15	0.06 ± 0.11

5.3 Categorisation-specific systematic uncertainties

After introducing the production-based event categories, the following additional sources of systematic uncertainty become relevant.

Uncertainties on the **theoretical predictions for the expected yields of different production processes** arise due to the requirement on the number of jets introduced as part of the event categorisation. Such uncertainties are also associated with the categories with no jet requirement (*ggF-enriched*, *VH-leptonic enriched*) due to the migration of events between categories. The uncertainties for the signal are taken from the methods described in Refs. [118, 27] and the uncertainties for the $ZZ^{(*)}$ background come from varying the renormalisation and factorisation scales in the simulation and taking the resulting difference with respect to the nominal yield.

Uncertainties due to the potential mismodelling of the **underlying event** are assessed by comparing the nominal efficiencies for the category-specific selections with the ones found when turning off the simulation of multi parton interactions (MPI) for simulated samples of $Z \to \mu\mu$ events.

Uncertainties on the **jet energy scale**, discussed in Section 3.4.4 can lead to the migration of events between categories. For the signal process, systematic uncertainties are modelled in the profile likelihood ratio with nuisance parameters corresponding to the modelling of the absolute and relative in situ jet calibrations, and the flavour composition of the jets. For the $ZZ^{(*)}$ background, a single nuisance parameter is used to model the overall jet energy scale uncertainty.

The systematic uncertainty due to the uncertainty on the **jet energy resolution**, discussed in Section 3.4.4, is found to be small.

The **requirements placed on the additional selected lepton in the VH-leptonic enriched category** lead to systematic uncertainties on the measured rate, which are calculated as discussed in Section 4.6 for the inclusive analysis.

The additional systematic uncertainties due to the categorisation procedure are summarised for the 8 TeV data sample in Table 5.3.

Table 5.3: Systematic uncertainties, on the number of events expected from each production process in the *VBF-enriched, VH-leptonic enriched, VH-hadronic enriched* and *ggF-enriched* categories. Uncertainties that are negligible are denoted by '−' [4].

Process	$ggF/t\bar{t}H/b\bar{b}H$	VBF	VH	ZZ^*
VBF-enriched category				
Theoretical cross section	20.4%	4%	4%	8%
Underlying event	6.6%	1.4%	–	–
Jet energy scale	9.6%	4.8%	7.8%	9.6%
Jet energy resolution	0.9%	0.2%	1.0%	1.4%
Total	23.5%	6.4%	8.8%	12.6%
VH-hadronic enriched category				
Theoretical cross section	20.4%	4%	4%	2%
Underlying event	7.5%	3.1%	–	–
Jet energy scale	9.4%	9.3%	3.7%	12.6%
Jet energy resolution	1.0%	1.7%	0.6%	1.8%
Total	23.7%	10.7%	5.5%	12.9%
VH-leptonic enriched category				
Theoretical cross section	12%	4%	4%	5%
Leptonic VH-specific cuts	1%	1%	5%	–
Jet energy scale	8.8%	9.9%	1.7%	3.2%
Total	14.9%	10.7%	6.6%	5.9%
ggF-enriched category				
Theoretical cross section	12%	4%	4%	4%
Jet energy scale	2.2%	6.6%	4.0%	1.0%
Total	12.2%	7.7%	5.7%	4.1%

5.4   Modelling and statistical treatment

The signal and background modelling strategy described in Section 4.5 is modified for the categorised analysis to allow the measurement of the signal strengths of different production modes.

Selected candidates are placed in production-based categories as described in Section 5.1. The modelling strategy for the *ggF-enriched* category is identical to the

inclusive analysis: events are further divided into sub-categories, where the two-dimensional model using $BDT_{ZZ^{(*)}}$ is used. The construction of the signal probability densities is as described in Section 4.5, where the event samples used as input for the kernel density estimation technique come from the *ggF-enriched* category rather than inclusive samples. The procedure is modified in the same way for the probability densities for the $ZZ^{(*)}$ background, and the $Z + \text{jets}$ and $t\bar{t}$ probability densities are identical to those used for the inclusive analysis.

For the *VBF-enriched* category, the BDT_{VBF} output is used as a second observable in the fit. Here, the two-dimensional probability density, $\mathcal{P}(m_{4\ell}, \text{BDT}_{\text{VBF}})$, may be factorised, since the BDT_{VBF} output does not depend on $m_{4\ell}$ for the signal or background processes. The two dimensional probability density is therefore the product of the one-dimensional probability densities, where the $m_{4\ell}$ distributions are estimated using the usual kernel density estimation technique and a smoothed BDT_{VBF} distribution is produced using interpolated histograms. Again the treatment is the same for the $ZZ^{(*)}$ background, and for the $Z + \text{jets}$ and $t\bar{t}$ probability densities the $m_{4\ell}$ probability density is identical to the one-dimensional probability density used in the inclusive analysis and the same BDT_{VBF} probability density as the $ZZ^{(*)}$ background is used.

In the two VH categories, a one dimensional fit to the $m_{4\ell}$ distribution is performed. The signal and $ZZ^{(*)}$ probability densities are estimated using the usual kernel density estimation technique, with the exception of the $ZZ^{(*)}$ distribution in the *VH-leptonic enriched* category, where the kernel density estimation is performed on an inclusive sample due to the limited number of events entering the category in the simulated samples. The probability densities for the $Z + \text{jets}$ and $t\bar{t}$ processes are again identical to the one-dimensional probability densities used in the inclusive analysis.

For the measurement of the production mode signal strengths, a signal strength factor μ_i, defined as $\mu_i = (\sigma_i \cdot BR_i)/(\sigma_{i,SM} \cdot BR_{i,SM})$, is introduced for each production mode i. Given the level of statistics collected during the LHC run I, the low

cross section production processes, $t\bar{t}H$ and $b\bar{b}H$, are assumed to vary with the same signal strength as the ggF production, $\mu_{ggF+b\bar{b}H+t\bar{t}H}$. This assumption is justified by the fact that in the SM, the ggF, $t\bar{t}H$ and $b\bar{b}H$ production modes all scale with the $q\bar{q}H$ coupling, where $q = b, t$. Similarly, the VBF and VH modes are assumed to scale with a common signal strength, μ_{VBF+VH}, as in the SM both scale with the WH/ZH coupling.

The signal strengths are evaluated at the ATLAS best-fit value for the Higgs boson mass, $m_H = 125.36$ GeV, and the form of the profile likelihood ratio for measuring the inclusive signal strength from section 4.5 is modified to:

$$\Lambda(\mu) = \frac{\mathcal{L}(\mu_{ggF+bbH+ttH}, \mu_{VBF+VH}, \hat{\hat{\boldsymbol{\theta}}}(\mu_{ggF+bbH+ttH}, \mu_{VBF+VH}))}{\mathcal{L}(\hat{\mu}_{ggF+bbH+ttH}, \hat{\mu}_{VBF+VH}, \hat{\boldsymbol{\theta}})} \qquad (5.1)$$

As for the inclusive analyses described in the previous chapter, the maximum likelihood fit is performed in the range 110 GeV $< m_{4\ell} < 140$ GeV.

Figure 5.6 demonstrates the impact each category has on the sensitivity of the $\mu_{ggF+bbH+ttH}$ and μ_{VBF+VH} measurements and the improvement with respect to the categorisation model used for the preliminary results described in Ref. [107].The expected profile likelihood ratio curves for different models are computed by scanning the likelihood in each model for the associated Asimov dataset [104].

Compared to the expected sensitivity of the preliminary analysis, a two-category implementation of the current model, using the *VBF-enriched* and *ggF-enriched* categories provides around 25% improvement on the upper 1σ uncertainty on μ_{VBF+VH}. This is improved further by the addition of the *VH-leptonic enriched* and *VH-hadronic enriched* categories, with a total expected improvement of around 35%. The use of $BDT_{ZZ^{(*)}}$ in the *ggF-enriched* category improves the uncertainty on μ_{VBF+VH} by around 6% and the uncertainty on $\mu_{ggF+ttH+bbH}$ by around 8%.
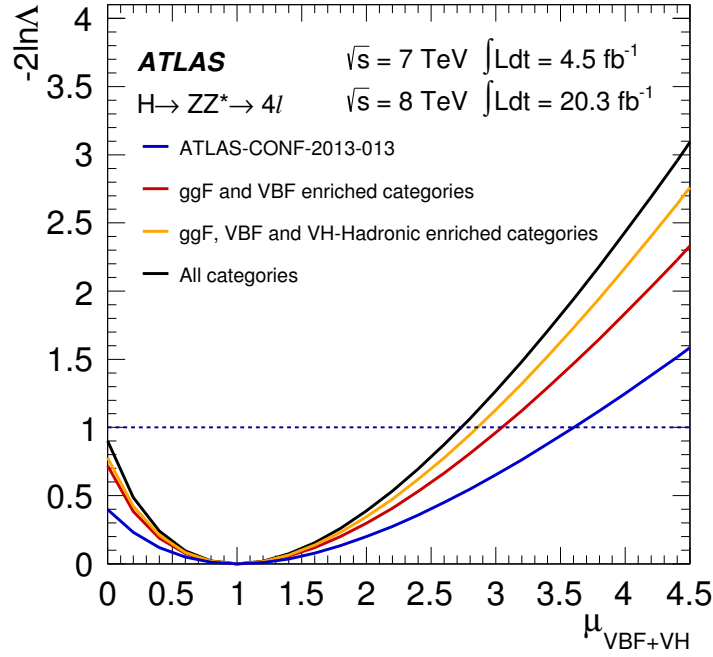
(a)
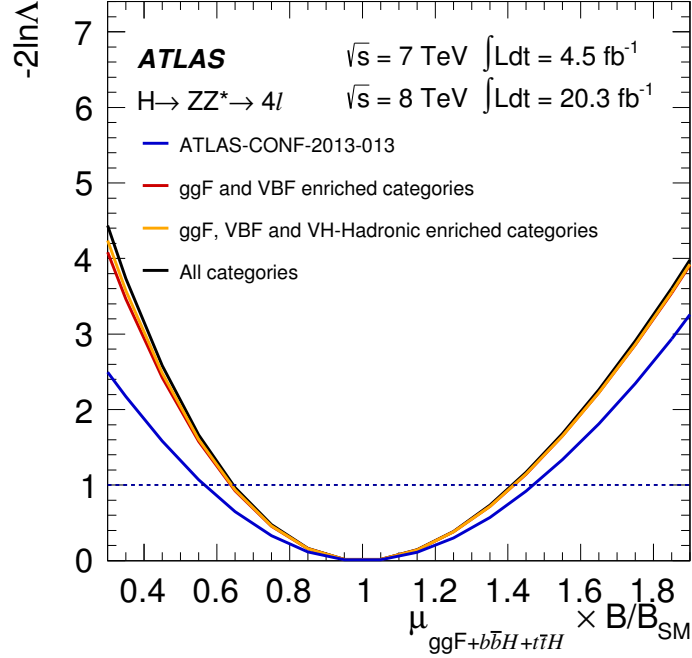
(b)

Figure 5.6: The expected profile likelihood ratio as a function of: a) μ_{VBF+VH}, and b) $\mu_{ggF+ttH+bbH}$, for the categorisation model used for the preliminary results in Ref. [107] (blue), a two-category version of the model described in this chapter using the *VBF-enriched* and *ggF-enriched* categories (red), a three-category version including the *VH-hadronic enriched* category (yellow), and including all categories (black). For each model, the expected profile likelihood ratio is estimated using the associated Asimov dataset. Figure from Ref. [4].

5.5   Results

After the event selection described in Section 4.1 and the classification of events described in Section 5.1, in the mass range 110 GeV $< m_{4\ell} < 140$ GeV, 34 events are observed in the *ggF-enriched* category, 4 events are observed in the *VBF-enriched* category, and no events are observed in either the *VH-hadronic enriched* or *VH-leptonic enriched* categories. Of the events observed in the *VBF-enriched* category, three candidates are found in the mass range 120 GeV $< m_{4\ell} < 130$ GeV, where only one has $\mathrm{BDT_{VBF}} > 0$. The number of expected and observed events in each category is shown for different signal and background processes in two mass ranges in Table 5.4.

The $m_{4\ell}$ and $\mathrm{BDT_{VBF}}$ output distributions for events in the *VBF-enriched* category for the full mass range and for 110 GeV $< m_{4\ell} < 140$ GeV are shown in Fig. 5.7. The two dimensional $m_{4\ell} - \mathrm{BDT_{VBF}}$ distribution is shown in Fig. 5.8. The signal purity, $S/(S+B)$, is shown as a function of the $\mathrm{BDT_{VBF}}$ output, for the case where all Higgs boson events are considered to be signal and for the case where only the events produced via the *VBF* mechanism are considered to be signal, in Fig. 5.9.

Using the categorised analysis, the inclusive signal strength ($\mu = \mu_{ggF+t\bar{t}H+b\bar{b}H} = \mu_{VBF+VH}$) is measured to be $\mu = 1.44^{+0.34}_{-0.31}(\text{stat})^{+21}_{-11}(\text{syst})$, in good agreement with the result, presented in Section 4.7.1, obtained using the inclusive analysis. Similarly, the mass measured using the categorised analysis, $m_H = 124.43^{+0.56}_{-0.54}$ is in good agreement with the inclusive measurement.

Figure 5.10, shows the scans of the profile likelihood ratio described in Section 5.4 as a function of $\mu_{ggF+t\bar{t}H+b\bar{b}H}$ and μ_{VBF+VH}. The resulting measurements of the production mode signal strengths are:

$$
\begin{aligned}
\mu_{\mathrm{ggF}+b\bar{b}H+t\bar{t}H} &= 1.66 \; ^{+0.45}_{-0.41} \; (\text{stat}) \; ^{+0.25}_{-0.15} \; (\text{syst}) \\
\mu_{\mathrm{VBF+VH}} &= 0.26 \; ^{+1.60}_{-0.91} \; (\text{stat}) \; ^{+0.36}_{-0.23} \; (\text{syst})
\end{aligned}
\tag{5.2}
$$

Table 5.4: Expected and observed number of events in each category for each Higgs boson production mode and the ZZ^* Z + jets and $t\bar{t}$ backgrounds for combined 7 TeV and 8 TeV data. Estimates are presented in two mass ranges, 120 GeV $< m_{4\ell} <$ 130 GeV and $m_{4\ell} >$ 110 GeV [4].

| Enriched category	Signal				Background		Total expected	Observed
	$ggF + b\bar{b}H + t\bar{t}H$	VBF	VH-hadronic	VH-leptonic	ZZ^*	Z + jets, $t\bar{t}$		
120 < m$_{4\ell}$ < 130 GeV								
VBF	1.18 ± 0.37	0.75 ± 0.04	0.083 ± 0.006	0.013 ± 0.001	0.17 ± 0.03	0.25 ± 0.14	2.4 ± 0.4	3
(BDT$_{\text{VBF}}$ > 0)	0.48 ± 0.15	0.62 ± 0.04	0.023 ± 0.002	0.004 ± 0.001	0.06 ± 0.01	0.10 ± 0.05	1.26 ± 0.15	1
VH-hadronic	0.40 ± 0.12	0.034 ± 0.004	0.20 ± 0.01	0.009 ± 0.001	0.09 ± 0.01	0.09 ± 0.04	0.80 ± 0.12	0
VH-leptonic	0.013 ± 0.002	< 0.001	< 0.001	0.069 ± 0.004	0.015 ± 0.002	0.016 ± 0.019	0.11 ± 0.02	0
ggF	12.8 ± 1.3	0.57 ± 0.02	0.24 ± 0.01	0.11 ± 0.01	7.1 ± 0.2	2.7 ± 0.4	23.5 ± 1.4	34
m$_{4\ell}$ > 110 GeV								
VBF	1.4 ± 0.4	0.82 ± 0.05	0.092 ± 0.007	0.022 ± 0.002	20 ± 4	1.6 ± 0.9	$24. \pm 4.$	32
(BDT$_{\text{VBF}}$ > 0)	0.54 ± 0.17	0.68 ± 0.04	0.025 ± 0.002	0.007 ± 0.001	8.2 ± 1.6	0.6 ± 0.3	10.0 ± 1.6	12
VH-hadronic	0.46 ± 0.14	0.038 ± 0.004	0.23 ± 0.01	0.015 ± 0.001	9.0 ± 1.2	0.6 ± 0.2	10.3 ± 1.2	13
VH-leptonic	0.026 ± 0.004	< 0.002	< 0.002	0.15 ± 0.01	0.63 ± 0.04	0.11 ± 0.14	0.92 ± 0.16	1
ggF	14.1 ± 1.5	0.63 ± 0.02	0.27 ± 0.01	0.17 ± 0.01	351 ± 20	16.6 ± 2.2	383 ± 20	420

(a)

(b)

(c)

(d)
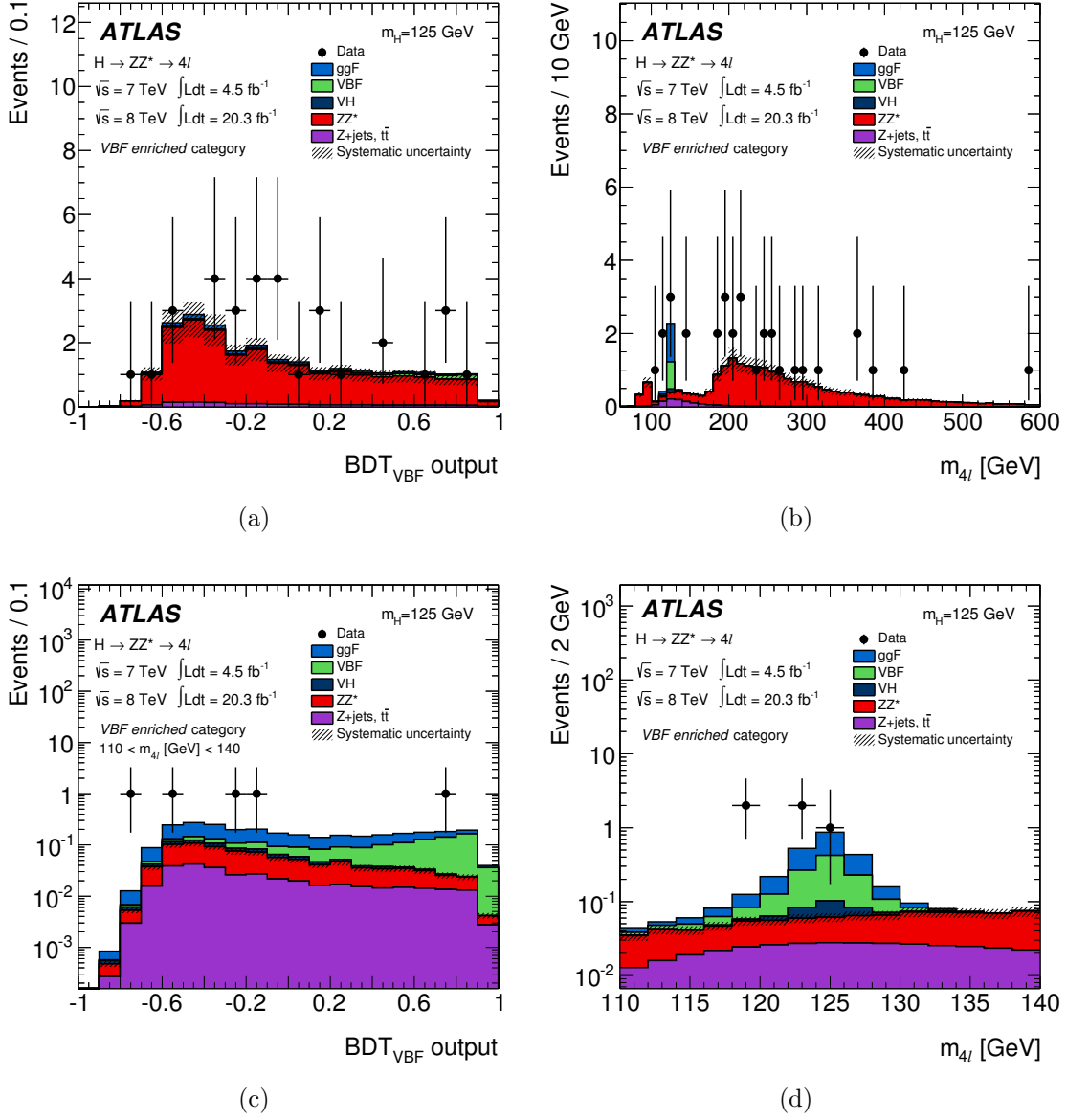
Figure 5.7: Selected events in the *VBF-enriched* category shown as filled circles: a) and b) for the full mass range, and c) and d) for 110 GeV $< m_{4\ell} < 140$ GeV for the 7 TeV and 8 TeV datasets. The BDT_{VBF} output distribution is shown in a) and c), and the $m_{4\ell}$ distribution is shown in b) and d). The ggF (light blue), VBF (green), VH (dark blue) signal processes, and the $ZZ^{(*)}$ (red) and $Z + \text{jets}$ and $t\bar{t}$ (purple) backgrounds, are also shown as filled histograms [4].

Both values are consistent with the SM prediction, $\mu_{ggF+t\bar{t}H+b\bar{b}H} = \mu_{VBF+VH} = 1$.

The sources of any potential deviations from the SM prediction cannot be resolved between production and decay in the above measurements. The ambiguity is resolved by measuring the ratio between the production mode signal strengths, as the

(a)

(b)

(c)
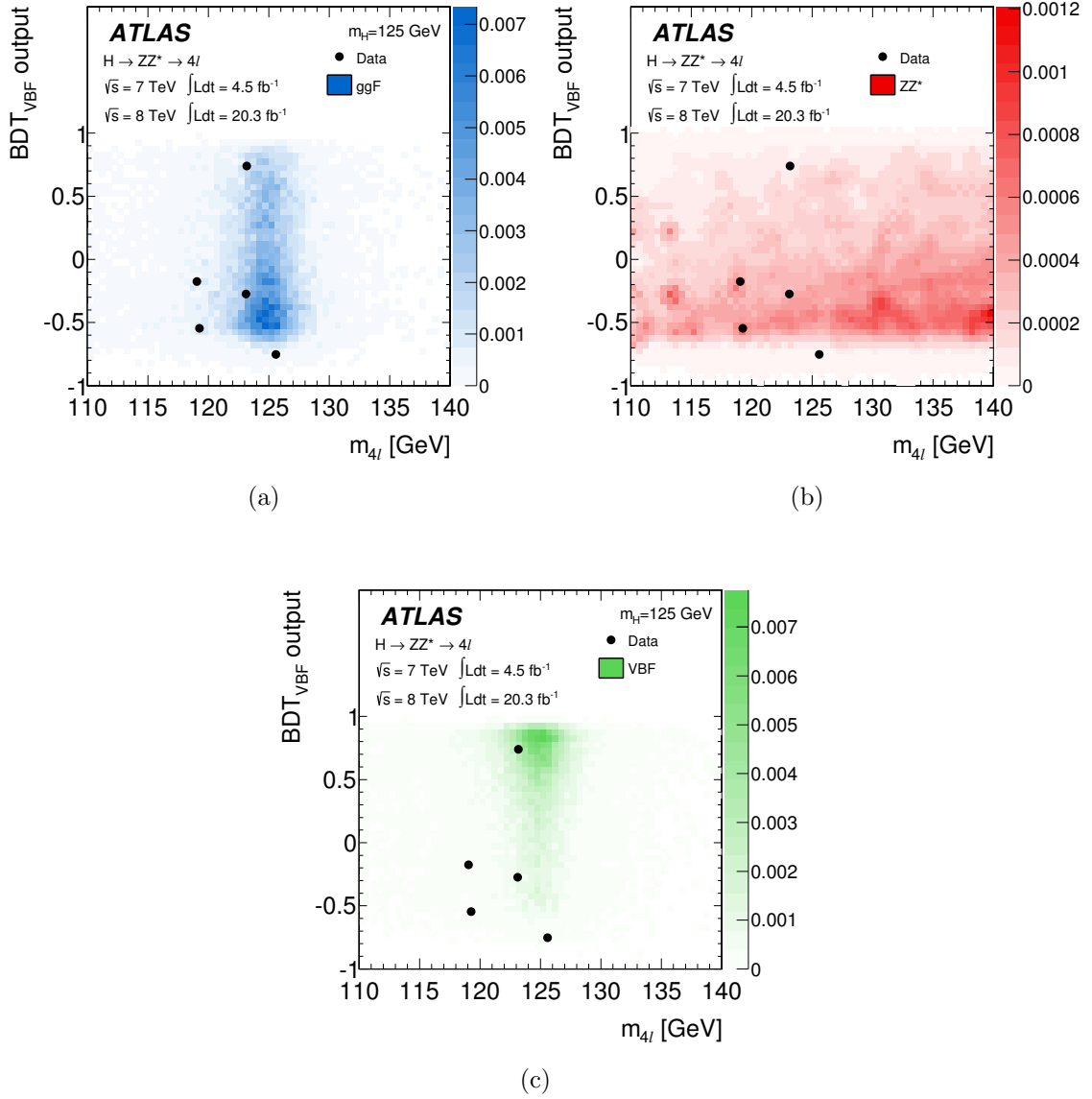
Figure 5.8: Selected events in the *VBF-enriched* category shown as filled circles in the $m_{4\ell} - \mathrm{BDT_{VBF}}$ output plane, where the colour of the filled box represents the expected relative density of events, calculated from simulation, for the: a) *ggF*, b) $ZZ^{(*)}$, and c) *VBF* processes [4].

branching ratio terms cancel:

$$\mu_{\mathrm{VBF+VH}}/\mu_{\mathrm{ggF}+b\bar{b}H+t\bar{t}H} = 0.2^{+1.2}_{-0.5} \tag{5.3}$$

The profile likelihood ratio as a function of $\mu_{\mathrm{VBF+VH}}/\mu_{\mathrm{ggF}+b\bar{b}H+t\bar{t}H}$, along with the two-dimensional profile likelihood ratio contours in the two signal strengths corre-
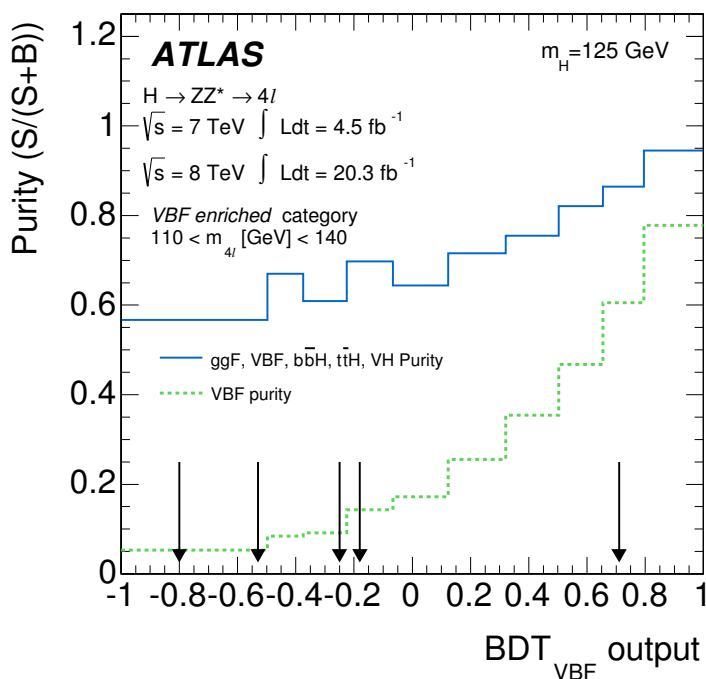
Figure 5.9: Signal purity - $S/(S + B)$ - as a function of the BDT_{VBF} output in the *VBF-enriched* category, considering all Higgs boson production processes as signal (blue solid histogram) and considering only the *VBF* Higgs boson production process as signal (green dashed histogram). The BDT_{VBF} output values for selected events with 110 GeV $< m_{4\ell} < 140$ GeV are indicated by arrows [4].

sponding to the 68% and 95% confidence levels, are shown in Figure 5.11.

Following the κ framework approach introduced in Section 2.3, the measurement is reinterpreted in terms of a measurement of the Higgs boson couplings. Using the benchmark model where a single common scale factor, κ_V, is applied to all vector boson couplings and a single common scale factor, κ_F, is applied to all fermion couplings, the 68% and 95% profile likelihood ratio contours are presented in the κ_V-κ_F plane in Figure 5.12. Also shown is the profile likelihood ratio as a function of $\lambda_{FV} = k_F/k_V$, where the assumptions on the Higgs boson width are relaxed since the branching ratio for $H \to ZZ^{(*)}$ cancels. The value $\lambda_{FV} = 0$ is disfavoured at around the 4σ level in this model.
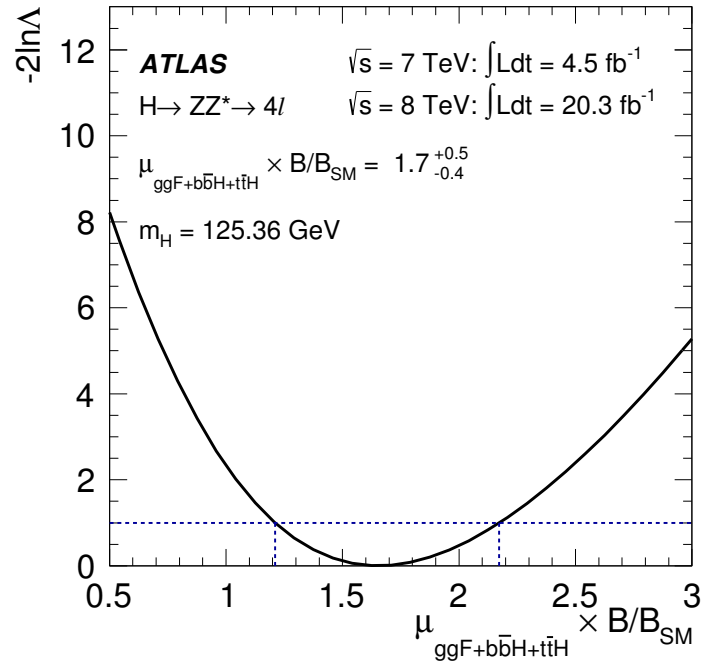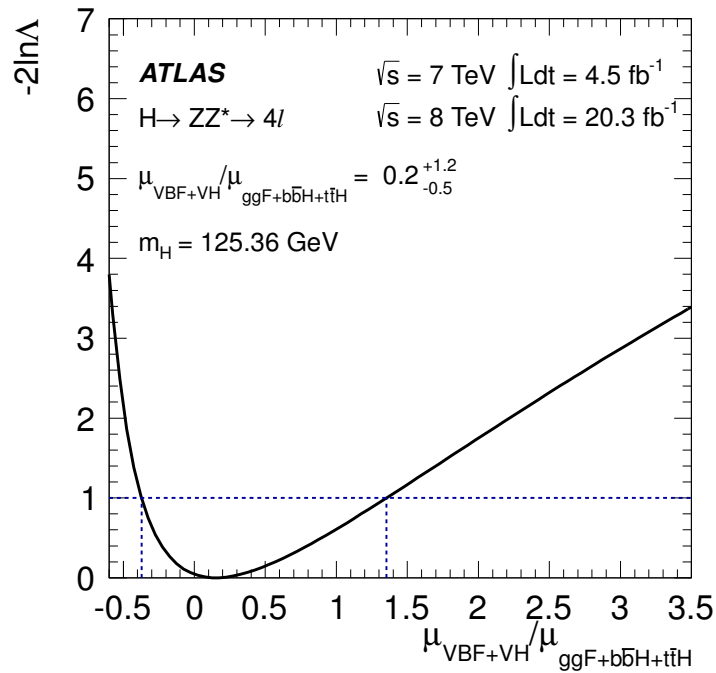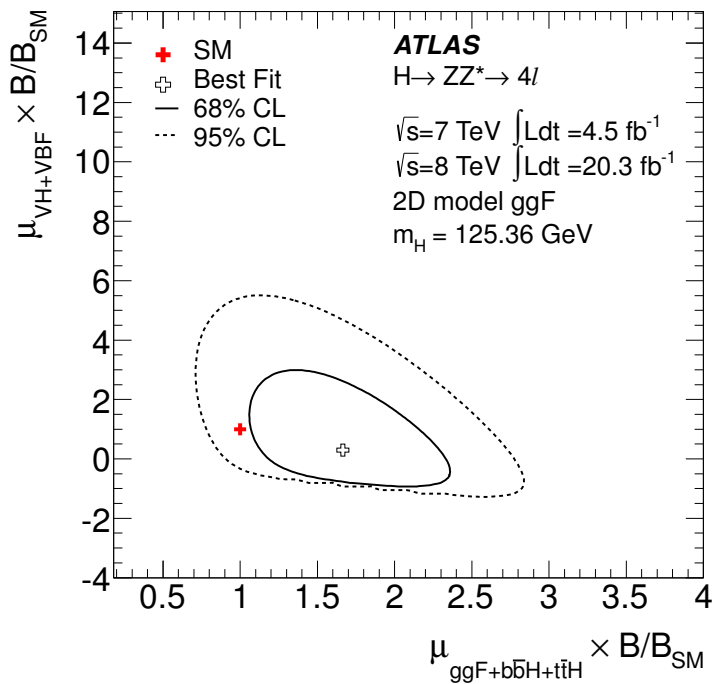
(a)
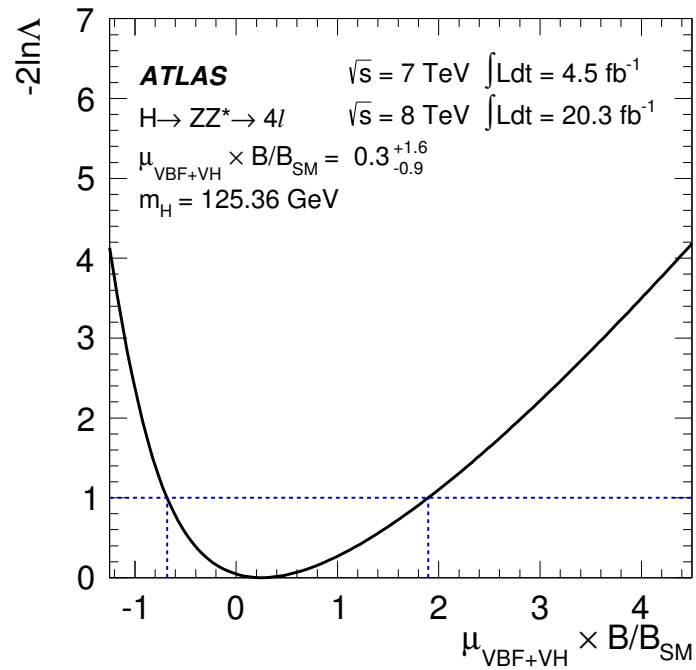
(b)

Figure 5.10: Profile likelihood ratio for a fit to the combined 7 TeV and 8 TeV data sets, as a function of: a) $\mu_{ggF+t\bar{t}H+b\bar{b}H}$, and b) μ_{VBF+VH} [4].
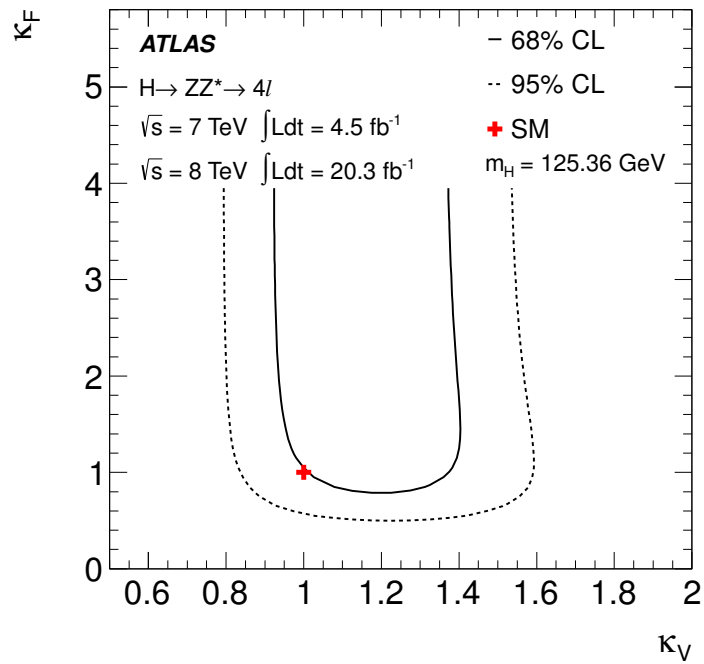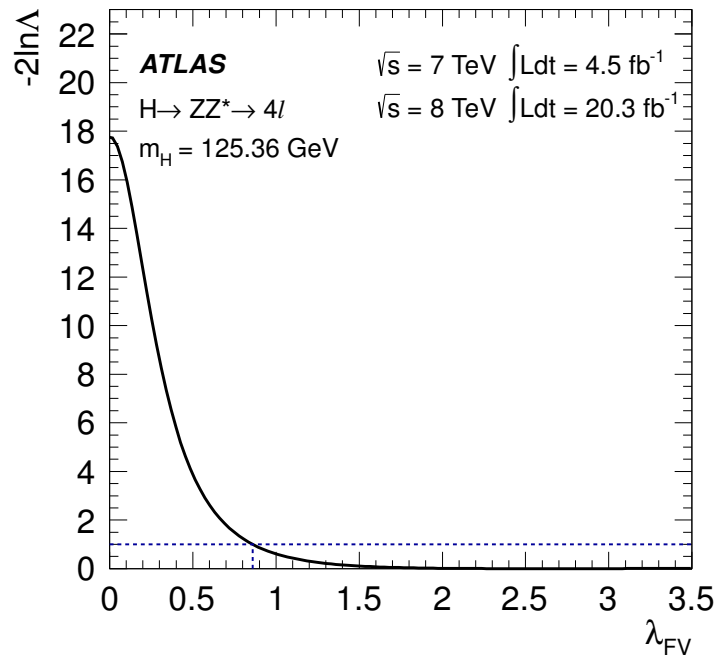
(a)

(b)

Figure 5.11: a) Profile likelihood ratio as a function of $\mu_{VBF+VH}/\mu_{ggF+t\bar{t}H+b\bar{b}H}$. b) 68% and 95% likelihood contours in the $\mu_{VBF+VH}/\mu_{ggF+t\bar{t}H+b\bar{b}H}$ plane. The results are for the combined 7 TeV and 8 TeV datasets [4].

(a)

(b)

Figure 5.12: a) 68% and 95% likelihood contours in the $\kappa_V - \kappa_F$ plane. b) Profile likelihood ratio as a function of $\lambda_{FV} = k_F/k_V$. The results are for the combined 7 TeV and 8 TeV datasets [4].

5.6   Prospects for future measurements of production and decay rates in the $H \to ZZ^{(*)} \to 4\ell$ final state

5.6.1   Up to 100 fb^{-1} at 13 TeV

The projections in this section use the same statistical model and probability densities as for the LHC run I analysis described so far (for the 8 TeV case), but with the expected number of events for each process scaled up to take into account the increase in centre-of-mass energy from 8 TeV to 13 TeV, assuming $m_H = 125$ GeV. The projections do not take into account changes in acceptance, changes to the detector or changes in the level of pile-up. All projections use Asimov data, generated from the relevant model, to produce expected uncertainties.

The production cross section ratios, used to scale the expected yields, are presented for the processes entering the analysis in Table 5.5. The signal cross sections are taken from Ref. [27], while the background cross sections are taken from Ref. [119][2]. The resulting numbers of expected events for 30 fb^{-1} of data collected at 13 TeV, for each process in each category, are presented in Table 5.6. Around 40 signal events are expected in the *ggF-enriched* category, and more than 2 *VBF* events are expected in the *VBF-enriched* category.

Table 5.5: Ratios of cross sections at 13 TeV to those at 8 TeV for processes considered in the analysis.

	Process							
	ggF	VBF	WH	ZH	$t\bar{t}H$	$b\bar{b}H$	$ZZ^{(*)}$	$z+\mathrm{jets}, t\bar{t}$
$\sigma_{13\mathrm{TeV}} / \sigma_{8\mathrm{TeV}}$	2.23	2.38	1.96	2.09	3.93	2.51	1.80	2.00

The profile likelihood ratio, as functions of $\mu_{ggF+t\bar{t}H+b\bar{b}H}$ and μ_{VBF+VH}, is shown for 30 fb^{-1} at 13 TeV in Figure 5.13. The expected uncertainties are reduced with respect to the LHC run I measurements. For LHC run II, ATLAS aims to record at least 100 fb^{-1} by 2018, and the corresponding profile likelihood ratios for

---

[2]Note this is an ATLAS internal report

Table 5.6: Expected number of events in each category (*ggF-enriched, VBF-enriched, VH-hadronic enriched, VH-leptonic enriched*) for 30 fb^{-1} of data collected at 13 TeV, calculated using simulated samples with $m_H = 125$ GeV. The number of expected events is specified individually for each production mechanism considered by the analysis.

True origin	Category			
	ggF-enriched	*VBF-enriched*	*VH-hadronic enriched*	*VH-leptonic enriched*
ggF	36.38	3.31	1.12	0.02
VBF	1.63	2.18	0.09	0.00
WH	0.50	0.16	0.33	0.15
ZH	0.41	0.10	0.22	0.02
$b\bar{b}H$	0.68	0.06	0.02	0.00
$t\bar{t}H$	0.00	0.17	0.04	0.00

this integrated luminosity, as functions of $\mu_{ggF+t\bar{t}H+b\bar{b}H}$ and μ_{VBF+VH}, are shown in Figure 5.14. With this level of collected statistics, the statistical and systematic components of the uncertainty on $\mu_{ggF+t\bar{t}H+b\bar{b}H}$ are expected to be of a similar magnitude.
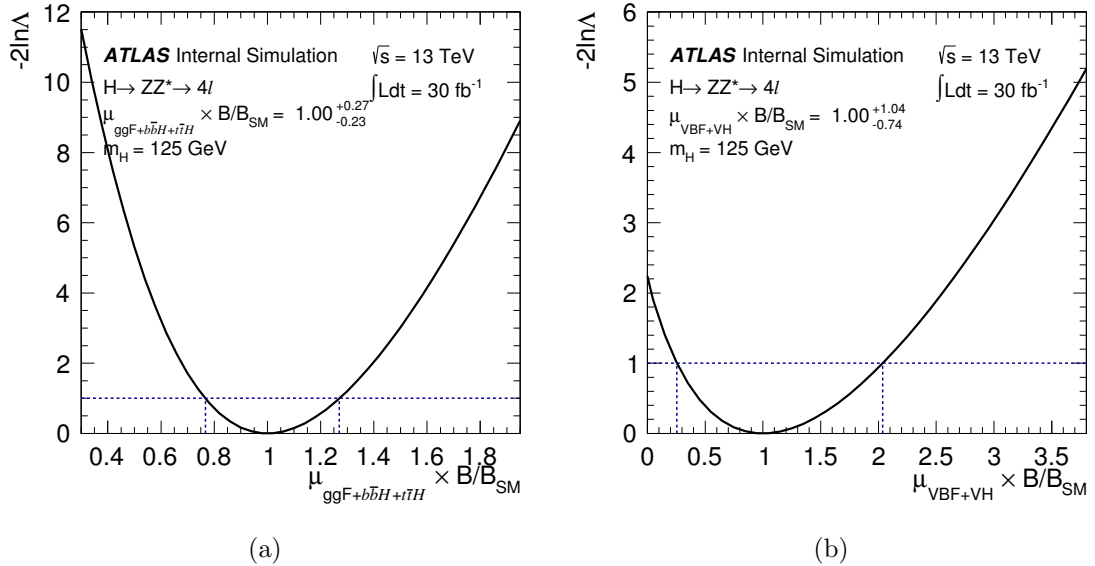

Figure 5.13: Profile likelihood ratio as a function of: a) $\mu_{ggF+t\bar{t}H+b\bar{b}H}$, and b) μ_{VBF+VH}, for 30 fb^{-1} of LHC data collected at 13 TeV.

The profile likelihood ratio is shown as a function of $\mu_{\mathrm{VBF+VH}}$ / $\mu_{\mathrm{ggF}+b\bar{b}H+t\bar{t}H}$ in Figure 5.15. The bosonic production mechanisms may also be separated with a
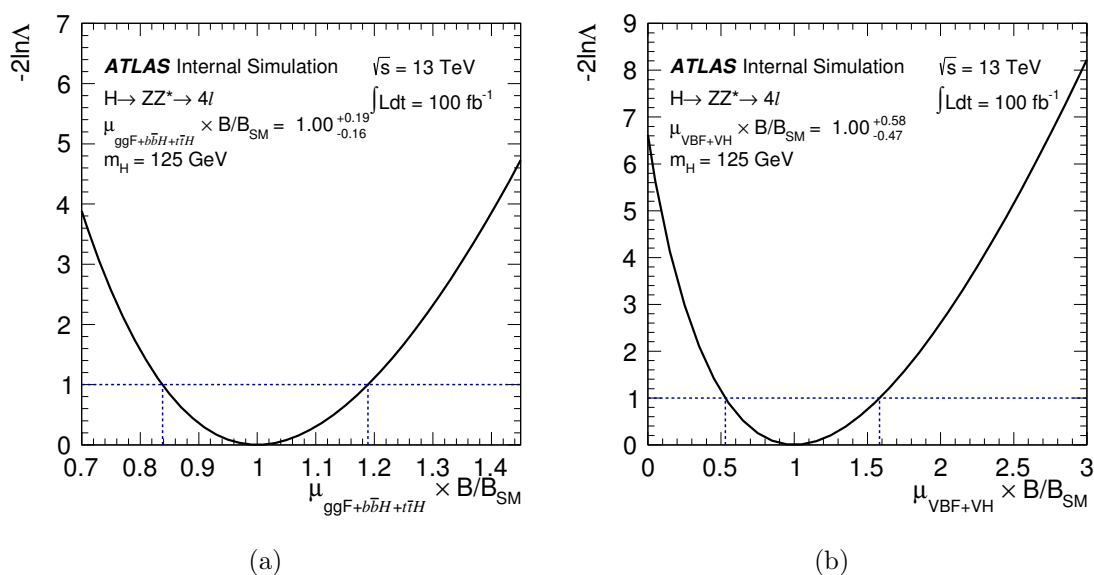
Figure 5.14:   Profile likelihood ratio as a function of: a) $\mu_{ggF+t\bar{t}H+b\bar{b}H}$, and b) μ_{VBF+VH}, for 100 fb^{-1} of LHC data collected at 13 TeV.

sample of this luminosity; the profile likelihood ratio is presented as a function of $\mu_{\text{VBF}} / \mu_{\text{ggF}+b\bar{b}H+t\bar{t}H}$ and $\mu_{\text{VH}} / \mu_{\text{ggF}+b\bar{b}H+t\bar{t}H}$ in the same Figure. For the VH process, the sensitivity with 100 fb^{-1} at 13 TeV is expected to be similar to the sensitivity to the VBF process achieved with the LHC run I data.

5.6.2   Up to 3000 fb^{-1} with an upgraded, HL-LHC

The ATLAS collaboration has presented projections for the sensitivity of measurements of the Higgs boson production and decay rates and couplings at the High Luminosity LHC (HL-LHC) [120], a proposed upgrade of the LHC aiming to deliver around 3000 fb^{-1} of proton-proton collisions, typically with around 140 interactions per bunch crossing.

The design for the upgraded ATLAS detector, required to operate in HL-LHC conditions, is being finalised, with the goal that performance of the upgraded detector at increased instantaneous luminosity should be at least as good as the performance of the current detector under current conditions.
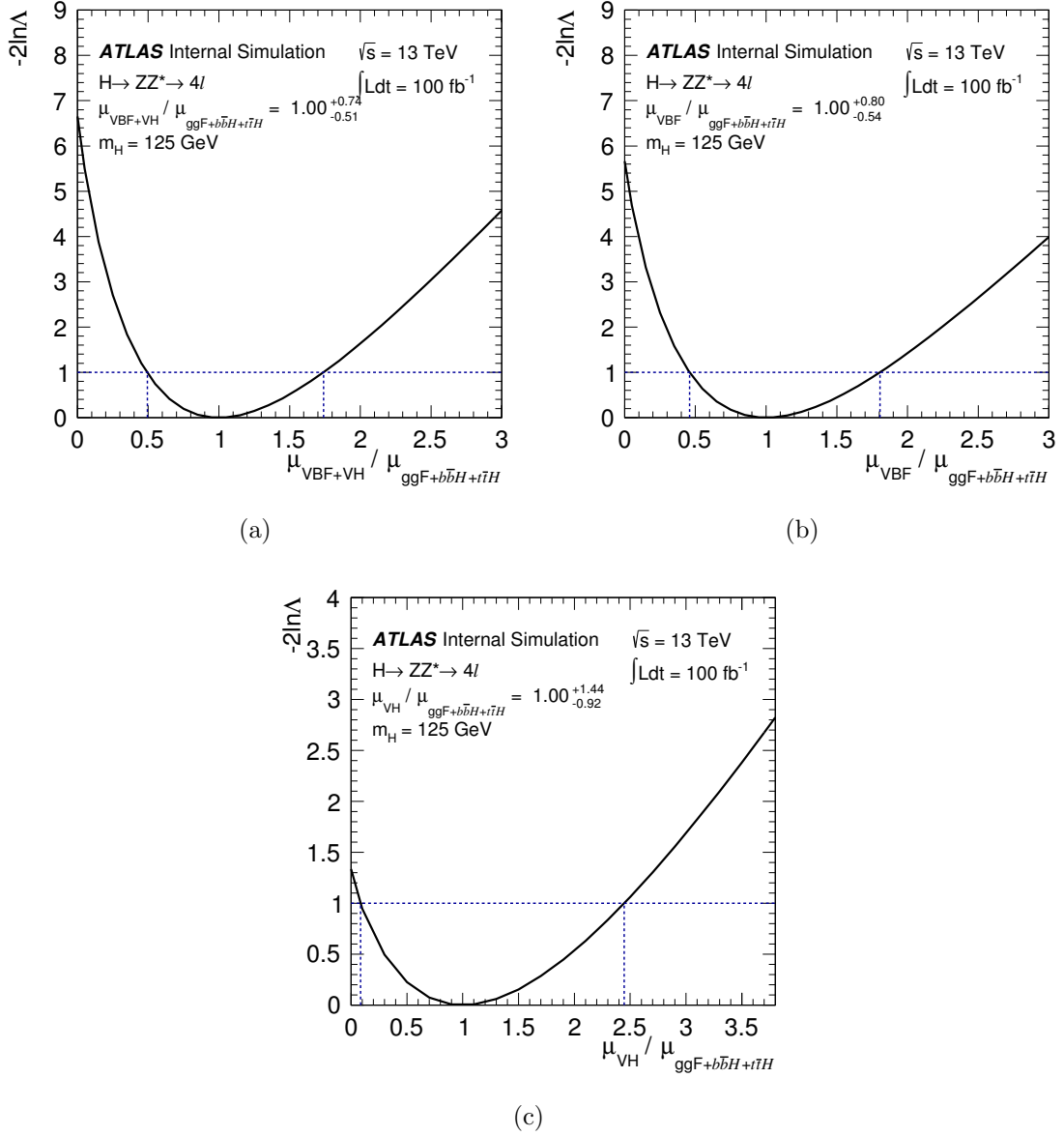
Figure 5.15: Profile likelihood ratio as a function of: a) $\mu_{\mathrm{VBF+VH}} / \mu_{\mathrm{ggF}+b\bar{b}H+t\bar{t}H}$, b) $\mu_{\mathrm{VBF}} / \mu_{\mathrm{ggF}+b\bar{b}H+t\bar{t}H}$, and c) $\mu_{\mathrm{VH}} / \mu_{\mathrm{ggF}+b\bar{b}H+t\bar{t}H}$, for 100 fb^{-1} of data collected at 13 TeV.

The ATLAS projections use generator-level simulation, with parameterised efficiency and resolution functions, based on a full simulation of a preliminary upgraded detector proposal, to model the expected detector performance [121].

This section presents the projections in the $H \to ZZ^{(*)} \to 4\ell$ channel. The selection is based on the preliminary analysis presented in Ref. [107], and a categorisation model designed for sensitivity to the ggF, VBF, WH, ZH and $t\bar{t}H$ production modes is implemented as described below. As in the present analysis, events which do not meet the requirements corresponding to the exclusive, production-tagged categories are placed in the ggF category.

Events are tested for the following categories sequentially:

For events to be placed in the $t\bar{t}H$ category, at least one b-tagged jet is required, exploiting the presence of the two b-jets coming from the top quark decays. To select both leptonic and hadronic W boson decays, either an additional lepton with $p_T > 8$ GeV or at least four additional jets are required.

Events with two additional same-flavour, opposite charge leptons satisfying $m_{\ell\ell} = m_Z \pm 15$ GeV are classified as ZH candidate events and events not meeting this requirement but containing at least one additional lepton with $p_T > 8$ GeV are classified as WH candidate events.

Events with at least two additional jets, where the two highest p_T jets satisfy $m_{jj} > 350$ GeV and $\Delta\eta_{jj} > 3.0$, are classified as VBF candidate events.

The expected number of events in each category for 3000 fb^{-1} is shown in table 5.7, where the events are split by production mechanism. The expected $m_{4\ell}$ distributions for events in each category are presented in Figure 5.16.

The expected uncertainty on the signal strength for each of the production modes studied and their combination is presented in Table 5.8. Fits are performed using a single-observable maximum likelihood fit to the $m_{4\ell}$ distribution. For systematic uncertainties related to theoretical calculations, current uncertainty estimates
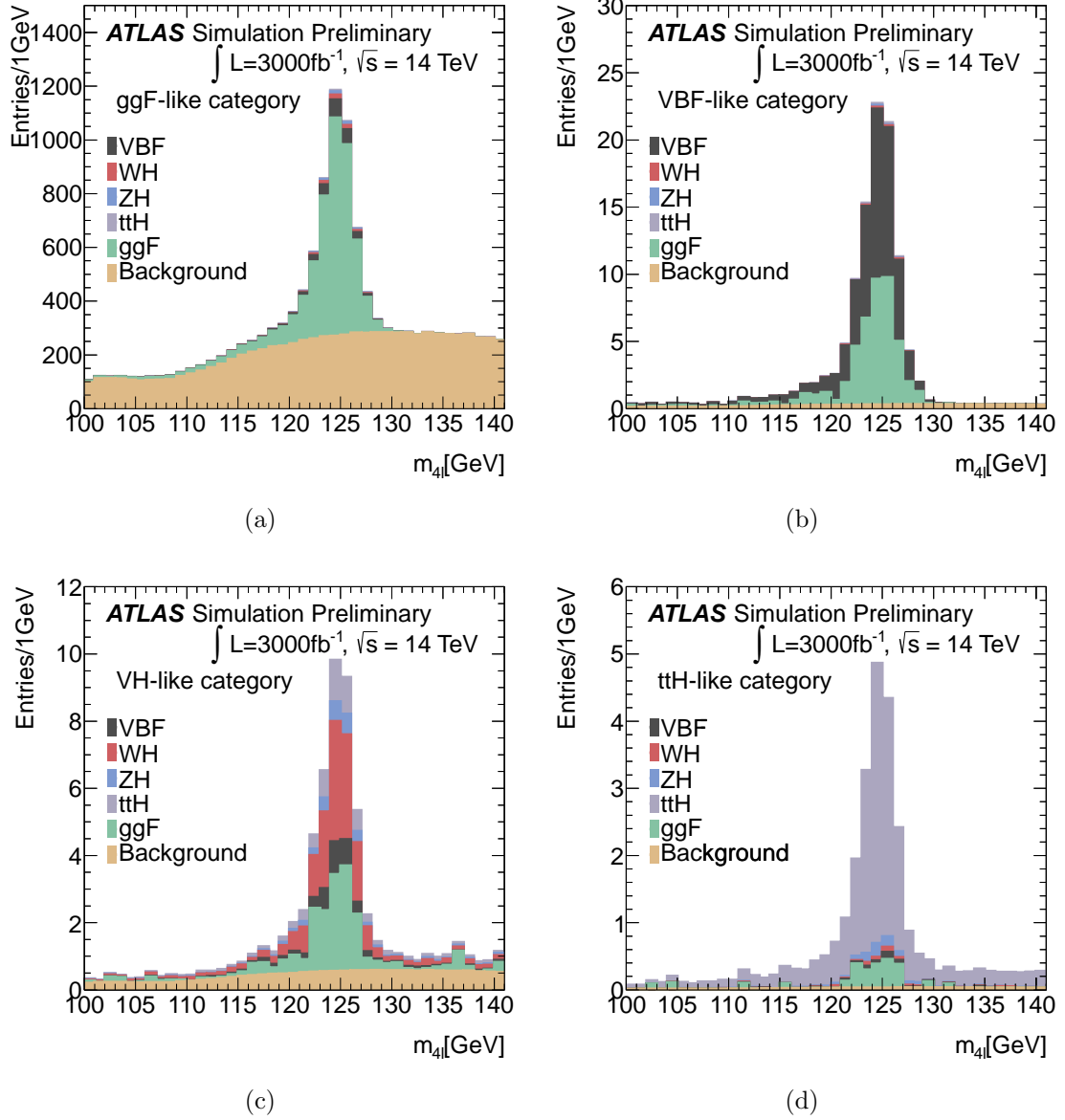
Figure 5.16: Simulated invariant mass distributions, for 3000 fb^{-1} of data collected at 14 TeV with a HL-LHC, for: a) the $ggF - like$ category, b) the $VBF - like$ category, c) the $VH - like$ category, and d) the $t\bar{t}H - like$ category [120].

Table 5.7: Expected number of events in each category for 3000 fb^{-1} of HL-LHC data collected at 14 TeV, assuming $m_H = 125$ GeV [120].

True	Category				
origin	$ggF - like$	$VBF - like$	$WH - like$	$ZH - like$	$t\bar{t}H - like$
ggF	3400	41	22	53	3.1
VBF	270	54	6.6	0.4	1.0
WH	77	0.7	25	0.01	8.8
ZH	54	0.4	4.4	4.4	1.3
$t\bar{t}H$	25	1.0	8.8	1.3	30

are taken and this component dominates the uncertainty on the combined signal strength measurement.

Table 5.8: Expected uncertainties on the signal strength measurements for a m_H = 125 GeV Higgs boson with 3000 fb^{-1} of data at the HL-LHC. Uncertainties are shown for individual production modes and their combination, and are broken down into the statistical (stat.), experimental systematic (exp. syst.) and theoretical systematic (theory syst.) components [120].

$\delta\mu/\mu$	Total	Stat.	Exp. syst.	Theory syst.
Production mode	**3000 fb^{-1}**			
ggF	0.13	0.025	0.04	0.12
VBF	0.37	0.19	0.23	0.23
WH	0.39	0.38	0.061	0.085
ZH	0.53	0.53	0.038	0.073
$t\bar{t}H$	0.22	0.18	0.034	0.12
Combined	0.10	0.0016	0.036	0.093

Higgs boson production and decay rates and couplings using the combination of decay modes

This chapter describes the measurement of the production and decay rates and couplings of the Higgs boson, performed by the ATLAS collaboration using the full LHC run I dataset [9]. The results are evaluated at the ATLAS best-fit value for the Higgs boson mass, $m_H = 125.36$ GeV, and supercede the preliminary results presented in Ref. [122]. The combination is also used to directly place limits on a number of BSM scenarios [10].

The measurements are a result of the combination of the $H \to \gamma\gamma$, $H \to ZZ^{(*)} \to 4\ell$, $H \to WW^{(*)} \to \ell\nu\ell\nu$, $H \to \tau\tau$ and $H \to b\bar{b}$ decay modes, as well as the searches for ttH production, $H \to Z\gamma$ and $H \to \mu\mu$, constraints on the off-shell production of the Higgs boson and direct searches for invisible Higgs boson decays.

6.1   Input channels to the combination

The analyses in different channels that are used as inputs in the combination are briefly described in the following section.

$H \to \gamma\gamma$

The ATLAS $H \to \gamma\gamma$ analysis is described in detail in Ref. [123]. Events with two isolated, well-identified photon candidates are selected, and are grouped into twelve exclusive categories for the 7 TeV and 8 TeV datasets. Categories are assigned sequentially, with the first two categories classifying events as $t\bar{t}H$-like based on signatures of leptonic and hadronic decays of the associated top quarks. Four categories classify events as VH-like, with single-lepton, di-lepton, $E_\mathrm{T}^\mathrm{miss}$ and hadronic requirements. Two categories, with different purities based on a BDT classifier, target VBF production. The remaining categories place requirements on the position of photons in the detector and the p_Tt of the diphoton system, its momentum transverse to its thrust axis in the transverse plane. An unbinned maximum likelihood fit to the diphoton invariant mass distribution is performed to extract the Higgs boson signal.

$H \to ZZ^{(*)} \to 4\ell$

The ATLAS $H \to ZZ^{(*)} \to 4\ell$ analysis is described in detail in Chapters 4 and 5.

$H \to WW^{(*)}$

The ATLAS $H \to WW^{(*)}$ analysis is described in detail in Refs. [124, 125]. For the ggF and VBF processes [124], events are selected by requiring two opposite-charge leptons, and categorised based on the number of jets (N_jet) and the the lepton flavours. Categories classifying events as VBF-like require $N_\mathrm{jet} \geq 2$ and categories

with $N_{\text{jet}} = 0$, 1 and ≥ 2 classify events as ggF-like events. The signal is extracted via a maximum likelihood fit; the observable is the dilepton mass, $m_{\ell\ell}$ for ggF categories, and a BDT, using information sensitive to the production mechanism as input variables, for the VBF categories.

For the VH process, an analysis is performed in categories depending on the lepton multiplicity with two, three or four leptons [125], where the three lepton category, which targets WH produced $H \to WW^*$ decays, is the most sensitive category.

$H \to \tau\tau$

The ATLAS $H \to \tau\tau$ analysis is described in detail in Ref. [126]. $H \to \tau\tau$ final states, including $\tau_{\text{lep}}\tau_{\text{lep}}$, $\tau_{\text{lep}}\tau_{\text{had}}$ and $\tau_{\text{had}}\tau_{\text{had}}$ final states are considered, where in each case events are assigned to either a boosted category, requiring the di-tau transverse momentum to be at least 100 GeV, or a VBF category, requiring two high p_T jets with a large pseudorapidity separation. The Higgs boson signal is extracted via a maximum likelihood fit to the output of a BDT classifier, trained to discriminate between signal and background events, in each category.

$H \to b\bar{b}$

The ATLAS $H \to b\bar{b}$ analysis is described in detail in Ref. [127]. The analysis searches for $H \to b\bar{b}$ decays in the VH production mode, exploiting leptonic decays of the associated vector boson to trigger events and reduce background rates, with $W \to \ell\nu$, $Z \to \ell\ell$, and $Z \to \nu\nu$ final states considered. A b-tagging algorithm is used to identify the Higgs boson decay products. Categories are defined in each final state based on the transverse momentum of the reconstructed W or Z boson, p_T^V, the number of jets contained in an event and the probability for each of the b-tagged jets to correspond to a real b-jet. A binned maximum-likelihood fit to the output of a BDT classifier, using the di-jet invariant mass, b-tagging information and kinematic information as inputs, is performed to extract the Higgs boson signal

for the 8 TeV data. For the 7 TeV data, the di-jet invariant mass is used as the observable in the fit.

The analysis of the 7 TeV data uses an older version of the luminosity calibration compared to other analyses in the combination, resulting in a different integrated luminosity.

$H \to Z\gamma$

The ATLAS $H \to Z\gamma$ analysis is described in detail in Ref. [128]. The analysis searches for a same-flavour, opposite-charge lepton pair, produced along with an isolated photon, and the Higgs boson signal is extracted via a maximum likelihood fit to the $\ell\ell\gamma$ invariant mass distribution.

$H \to \mu\mu$

The ATLAS $H \to \mu\mu$ analysis is described in detail in Ref. [129]. The analysis selects events containing an opposite-charge di-muon, placing events in categories. A VBF category selects events containing two or more jets consistent with the VBF process signature, and the remaining categories place requirements on the pseudorapidity of the muons and the transverse momentum of the di-muon pair. The Higgs boson signal is extracted via a maximum likelihood fit to the di-muon invariant mass distribution.

$t\bar{t}H$ searches

Three separate ATLAS analyses search for Higgs boson production via the $t\bar{t}H$ mechanism, targeting $H \to \gamma\gamma$ [130] decays, $H \to b\bar{b}$ [131] decays and $H \to (WW^*, \tau\tau, ZZ^*)$ decays with leptonic final states [132].

The $t\bar{t}H$ search in the $H \to \gamma\gamma$ channel is part of the $H \to \gamma\gamma$ analysis (see above).

The search for $t\bar{t}H$ production with $H \to b\bar{b}$ uses the 8 TeV dataset and searches for $t\bar{t}$ decays to single-lepton and di-lepton final states, requiring least two b-tagged jets. Events are categorised according to the jet and b-jet multiplicities and a neural network is used to discriminate between signal and background.

The $t\bar{t}H$ search with $H \to WW^*$, $\tau\tau$ and ZZ^* decays searches for multi-lepton final states. Events are categorised based on the number of electron, muon or hadronic τ candidates reconstructed. The signal is extracted using the observed number events in each category.

Off-shell Higgs boson production

The ATLAS analysis targeting off-shell Higgs boson production is described in detail in Ref. [133]. The analysis searches for the off-shell production of a Higgs boson in the $ZZ \to 4\ell$, $ZZ \to 2\ell2\nu$ and $WW \to e\nu\mu\nu$ final states, using the $\sqrt{s} = 8$ TeV data sample.

Since the $H^* \to ZZ$ and $H^* \to WW$ processes are sensitive to off-shell Higgs boson production [134, 135, 136, 137] in the mass range above the $2m_Z$ and $2m_W$ thresholds, the $ZZ \to 4\ell$ analysis searches in the mass range 220 GeV $< m_{4\ell} <$ 1000 GeV, the $ZZ \to 2\ell2\nu$ and $WW \to e\nu\mu\nu$ analyses search in the transverse mass range 380 GeV $< m_{\mathrm{T}}^{ZZ} <$ 1000 GeV.

This analysis is only included in the combination in certain models, where it provides a constraint on the Higgs boson width.

Higgs boson decays to invisible final states

ATLAS searches for invisible Higgs boson decays in final states with large missing transverse energy, considering three signatures: an invisibly decaying Higgs boson produced via the VBF mechanism, produced in association with a Z boson, where the Z boson decaying to a pair of leptons, or in association with a vector boson V

(W or Z), where the vector boson decays hadronically. These searches are combined in Ref. [10].

This analysis is only included in the combination in the combined measurement of the invisible branching ratio.

Table 6.1 summarises the individual analyses described above (with the exception of analyses searching for off shell Higgs boson production and invisible Higgs boson decays), presenting the main results as in the individual publications. Figure 6.1 presents the signal strength measurements in terms of the production processes used as inputs to the combination in each analysis.

Table 6.1: Overview of the individual analyses that are included in all combinations discussed. The searches for off-shell Higgs boson production and Higgs boson decays to invisible final states, which are not included in all combinations, are not shown here. The results are taken directly from the individual publications. Numbers in parentheses are the expected values for the SM Higgs boson. The ✓ symbol indicates whether the analysis is performed for the 7 TeV and/or 8 TeV dataset [9].

| Analysis	Signal		$\int \mathcal{L}dt$ (fb^{-1})	
Categorisation or final states	Strength μ	Significance [σ]	7 TeV	8 TeV
$H \to \gamma\gamma$ [123]	1.17 ± 0.27	$5.2\ (4.6)$	4.5	20.3
ttH: leptonic, hadronic			✓	✓
VH: one-lepton, dilepton, E_T^{miss}, hadronic			✓	✓
VBF: tight, loose			✓	✓
ggF: 4 p_{Tt} categories			✓	✓
$H \to ZZ^{(*)} \to 4\ell$	$1.44^{+0.40}_{-0.33}$	$8.1\ (6.2)$	4.5	20.3
VBF			✓	✓
VH: hadronic, leptonic			✓	✓
ggF			✓	✓
$H \to WW^*$ [124, 125]	$1.16^{+0.24}_{-0.21}$	$6.5\ (5.9)$	4.5	20.3
ggF: (0-jet, 1-jet) $\otimes$ ($ee + \mu\mu$, $e\mu$)			✓	✓
ggF: $\geq$ 2-jet and $e\mu$				✓
VBF: $\geq$ 2-jet $\otimes$ ($ee + \mu\mu$, $e\mu$)			✓	✓
VH: opposite-charge dilepton, three-lepton, four-lepton			✓	✓
VH: same-charge dilepton				✓
$H \to \tau\tau$ [126]	$1.43^{+0.43}_{-0.37}$	$4.5\ (3.4)$	4.5	20.3
Boosted: $\tau_{\text{lep}}\tau_{\text{lep}}, \tau_{\text{lep}}\tau_{\text{had}}, \tau_{\text{had}}\tau_{\text{had}}$			✓	✓
VBF: $\tau_{\text{lep}}\tau_{\text{lep}}, \tau_{\text{lep}}\tau_{\text{had}}, \tau_{\text{had}}\tau_{\text{had}}$			✓	✓
$VH \to Vb\bar{b}$ [127]	0.52 ± 0.40	$1.4\ (2.6)$	4.7	20.3
0ℓ ($ZH \to \nu\nu b\bar{b}$): $N_{\text{jet}} = 2,3$, $N_{\text{btag}} = 1,2$, $p_T^V >$ and < 120 GeV			✓	✓
1ℓ ($WH \to \ell\nu b\bar{b}$): $N_{\text{jet}} = 2,3$, $N_{\text{btag}} = 1,2$, $p_T^V >$ and < 120 GeV			✓	✓
2ℓ ($ZH \to \ell\ell b\bar{b}$): $N_{\text{jet}} = 2,3$, $N_{\text{btag}} = 1,2$, $p_T^V >$ and < 120 GeV			✓	✓
		95% CL limit		
$H \to Z\gamma$ [128]		$\mu < 11\ (9)$	4.5	20.3
10 categories based on $\Delta\eta_{Z\gamma}$ and p_{Tt}			✓	✓
$H \to \mu\mu$ [129]		$\mu < 7.0\ (7.2)$	4.5	20.3
VBF and 6 other categories based on η_μ and $p_T^{\mu\mu}$			✓	✓
ttH production [130, 131, 132]			4.5	20.3
$H \to b\bar{b}$: single-lepton, dilepton		$\mu < 3.4\ (2.2)$		✓
$ttH \to$ multileptons: categories on lepton multiplicity		$\mu < 4.7\ (2.4)$		✓
$H \to \gamma\gamma$: leptonic, hadronic		$\mu < 6.7\ (4.9)$	✓	✓
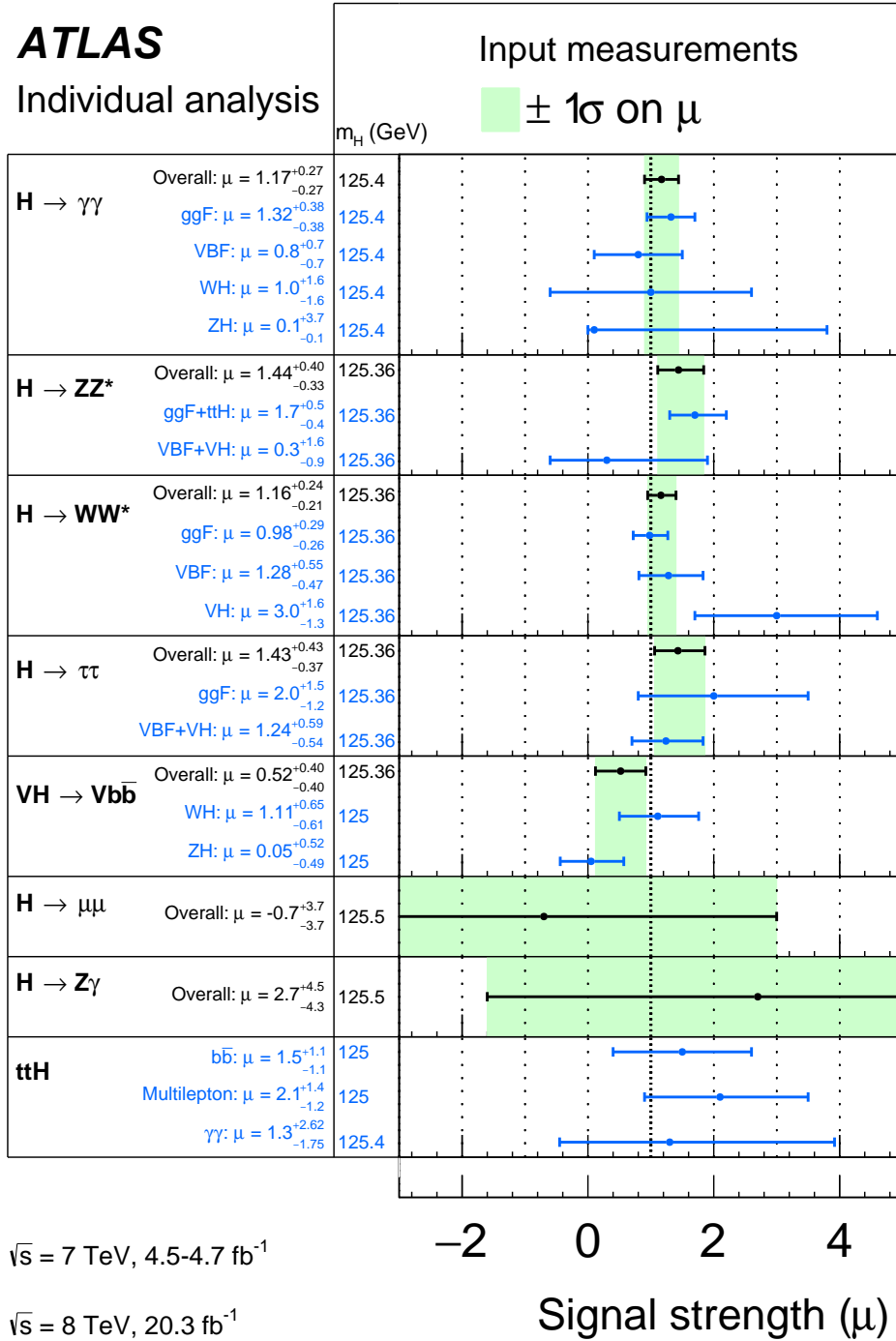
Figure 6.1: Measured signal strength for each input analysis entering the combination, combined per-input (black points) and for individual production modes (blue points). The searches for off-shell Higgs boson production and Higgs boson decays to invisible final states, which are not included in all combinations, are not shown here. Figure from Ref. [9].

6.2 Combination procedure

Compared to the individual publications, a series of small modifications are made to the analyses used as inputs. These are discussed in detail in Ref. [9], and include evaluating the results at a Higgs boson mass of 125.36 GeV (if the original analyses assumed a different mass), treating the cross-feed of Higgs boson decay modes (for example $H \to WW^{(*)}$ events entering the $H \to \tau\tau$ selection) as the appropriate signal mode rather than background, and updating the theoretical QCD scale systematic uncertainty to match the latest calculations (for analyses using older calculations).

As in the rest of this thesis, confidence intervals and hypothesis tests are based on a profile likelihood ratio test statistic, which depends on one or more parameters of interest and a number of nuisance parameters. As part of the combination procedure, parameters of interest may be correlated across different channels, and sources of systematic uncertainty that affect more than one channel are assigned common nuisance parameters.

The majority of the systematic uncertainties affecting the analysis are considered uncorrelated between the 7 TeV and 8 TeV datasets, with the exception of uncertainties relating to the modelling of detector material and some components of the uncertainty on the jet energy scale. Where theoretical uncertainties (e.g. QCD scale uncertainties for a given Higgs boson production process) affect the overall signal rate, they are modelled with a common nuisance parameter across all channels, and where theoretical uncertainties only affect the acceptance in a given channel they are modelled with channel-specific nuisance parameters. PDF uncertainties are treated as correlated for WH, ZH and VBF production, as anti-correlated for $gg \to ZH$ and $qq \to ZH$ production, and as uncorrelated for ggF and $t\bar{t}H$ production. Uncertainties on Higgs boson branching ratios to different final states are treated as uncorrelated, except for the $H \to ZZ^{(*)}$ and $H \to WW^{(*)}$ decay modes where the uncertainty is correlated. The PDF and branching ratio uncertainty approaches

have both been checked against using the full correlation matrix, with differences found to be negligible.

Where different analyses use the same trigger requirements to select events the corresponding uncertainties are modelled with common nuisance parameters. Similarly, where analyses use the same criteria to identify physics objects (for example the $H \to ZZ^{(*)} \to 4\ell$ and $H \to WW^{(*)}$ analyses use the same identification criteria for electrons), these are also modelled using common nuisance parameters.

6.3   Production and decay rates

Figure 6.2 shows the measurement of the signal strength in each decay mode from a simultaneous fit to the combination of all decay modes, where the same signal strength parameter is applied for a given decay mode, regardless of production process. This assumes that the contribution of each production mode is as predicted by the SM. The results are expected to be different to those presented in Figure 6.1, primarily for the following reasons:

- The $t\bar{t}H$ searches in the $H \to b\bar{b}$ and $H \to (WW^*,\ \tau\tau,\ ZZ^*) \to$ leptons decay modes are included in the fit, and this can change significantly the best-fit value for the signal strength in a given mode, with the biggest change observed in the $H \to b\bar{b}$ channel.

- As some systematic uncertainties are now modelled with common nuisance parameters across different channels, this can affect the best-fit signal strength values in the relevant decay modes.

The overall signal strength is measured by applying the same signal strength parameter to all modes, regardless of the production or decay process. This additionally assumes that the ratios of Higgs boson partial widths between different decay modes

are as predicted by the SM. The best fit value is found to be:

$$\mu = 1.18 \pm 0.10(stat) \pm 0.07(syst)^{+0.08}_{-0.07}(theo)\mu \quad = 1.18 \pm 0.15$$

where (stat) refers to the statistical component of the uncertainty, (syst) refers to the experimental component of the systematic uncertainty and (theo) refers theoretical component of the systematic uncertainty. Only theoretical uncertainties relating to signal process are included in the latter category, where theoretical uncertainties on background processes are included in the experimental systematic uncertainty category. The best fit value is compatible with the SM prediction, $\mu = 1$, with a p-value, defined as the probability for a result as or more discrepant as the observed to occur under the SM hypothesis and calculated using the profile likelihood ratio, of 18%.

Under the assumption that the Higgs boson branching ratios are as predicted by the SM, the signal strengths for different Higgs boson production mechanisms can be probed. Here, a common signal strength parameter is assigned to each production process, independently of the decay mode. Four signal strength parameters are introduced: μ_{ggF}, μ_{VBF}, μ_{VH} and $\mu_{t\bar{t}H}$. The $b\bar{b}H$ process is assumed to have the same signal strength as ggF, the WH and ZH processes are assumed to have the same signal strength, and the tH process is assumed to have the same signal strength as $t\bar{t}H$. The best-fit values and associated uncertainties for each of the production mode signal strengths is shown in Figure 6.3, where in each case the result is compatible with the SM prediction.

As for the analysis of production mode signal strengths in the $H \rightarrow ZZ^{(*)} \rightarrow 4\ell$ analysis, the production modes can be further categorised into fermionic production modes (ggF, $t\bar{t}H$) that scale with the $q\bar{q}H$ coupling, and bosonic production modes (VBF, VH) that scale with the WH/ZH coupling. For each final state, two signal strength factors are defined: $\mu^f_{ggF+t\bar{t}H}$ and μ^f_{VBF+VH}. The 68% and 95% CL two-dimensional contours in the profile likelihood ratio are shown for each decay mode
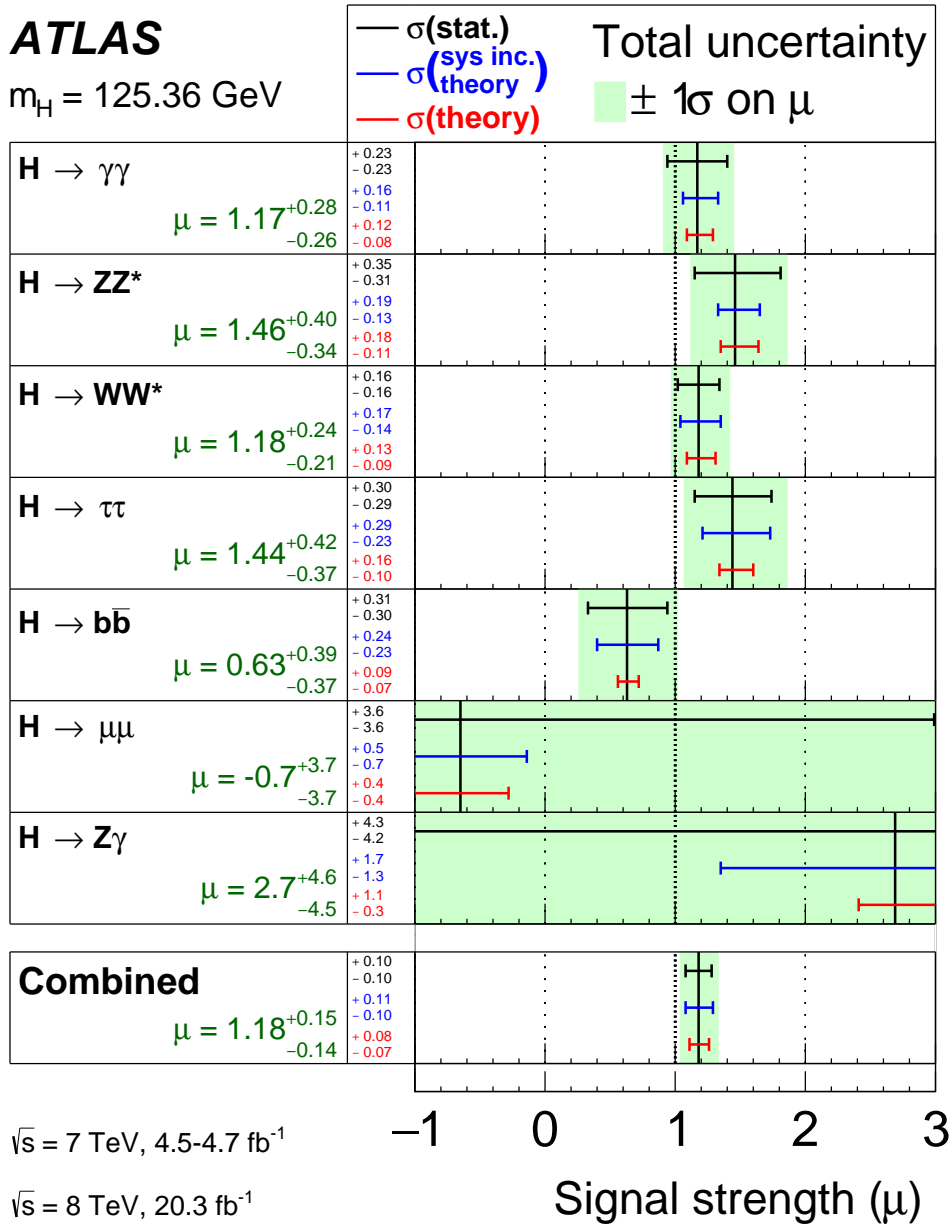
Figure 6.2: Observed Higgs boson signal strengths and uncertainties for the decay modes considered by the analysis and their combination. The results come from a simultaneous fit to the combination of all input channels. The best-fit values are indicated with black vertical lines and the statistical (black), total systematic (blue) and theoretical systematic uncertainties are shown as horizontal error bars. Figure from Ref. [9].
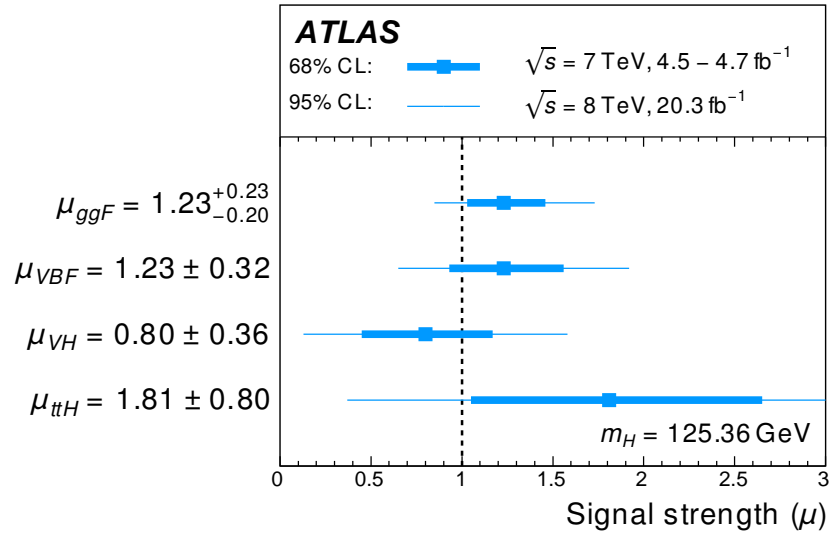
Figure 6.3: Observed Higgs boson signal strengths and uncertainties for ggF, VBF, VH and $t\bar{t}H$ production. The best fit values are shown as blue squares, the 1σ uncertainties are shown as horizontal bars and the 2σ uncertainties are shown as horizontal lines. The SM prediction is shown as a vertical dashed line. Figure from Ref. [9].

in Figure 6.4. The $H \to \mu\mu$ and $H \to Z\gamma$ modes have little sensitivity at present, so are not shown. In the same way as for the $H \to ZZ^{(*)} \to 4\ell$ channel, described in Section 5.5, the $H \to \gamma\gamma$ contour is cut off where the sum of the number of signal and background events in one of the sub-categories is below zero for some values of $\mu^f_{ggF+t\bar{t}H}$ and μ^f_{VBF+VH}. For each decay mode, the results are compatible with the SM prediction.

6.4 Coupling strength measurements

The coupling strength measurements presented in this chapter are based on the framework discussed in Section 2.3. A selection of the results for studied benchmark models are presented here; further results and extended discussion may be found in Ref. [9].
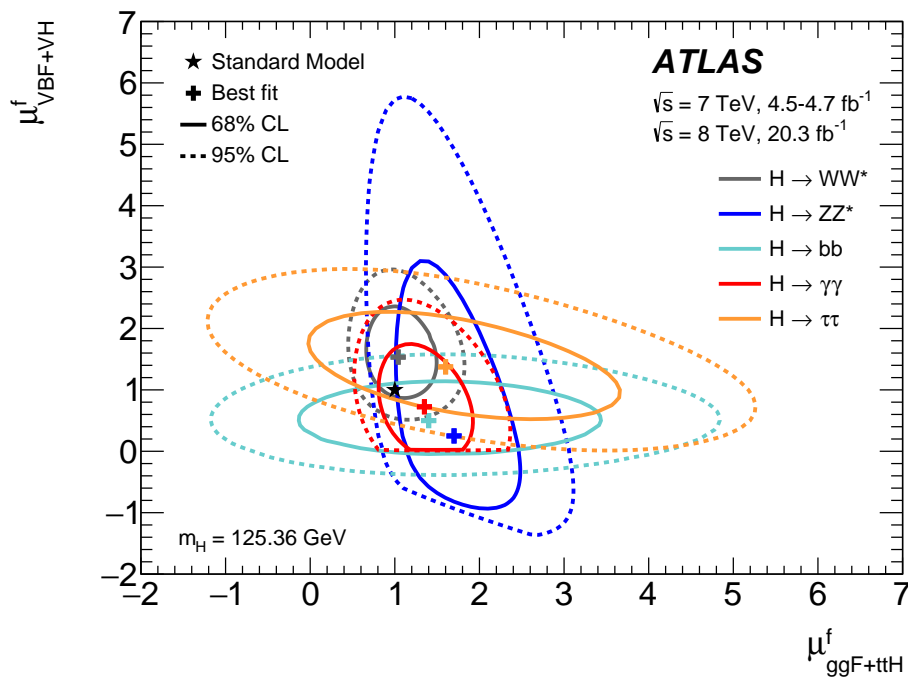
Figure 6.4: Observed best fit (crosses), 68% (solid lines) and 95% (dashed lines) CL contours in the profile likelihood as a function of the fermionic production modes signal strength, $\mu^f_{ggF+t\bar{t}H}$, and bosonic production modes signal strength, μ^f_{VBF+VH}, for the individual decay modes considered in the analysis. The SM prediction is shown by a star symbol. Figure from Ref. [9].

6.4.1 Fermion versus vector coupling strengths

In this benchmark model, a single scale factor, κ_V, is assigned to all vector boson couplings, and a second scale factor, κ_F, is assigned to all fermion couplings. This model is designed to test the coupling structure of the SM Higgs mechanism, since the SM Higgs boson couples in distinctly different ways to bosons and ferimons. For the results presented here, it is assumed that only standard model particles enter in loop processes and the Higgs boson total width. The loop coupling scale factors and total width scale factor therefore scale as a function of κ_V and κ_F.

Since only the relative sign between κ_V and κ_F is physical, $\kappa_V > 0$ is chosen as a convention, and sensitivity to the relative sign comes from interference terms in the loop processes, in particular the $t - W$ interference in the $H \to \gamma\gamma$ decay.

The best-fit values for the coupling scale factors are:

$$\kappa_V = 1.09 \pm 0.07$$

$$\kappa_F = 1.11 \pm 0.16$$

both agreeing well with the SM prediction of $\kappa_F = \kappa_V = 1$. The p-value quantifying the compatibility of the observed data with the SM, interpreted in this benchmark model, is found to be 41%.

Figure 6.5 shows the observed 68% CL profile likelihood ratio contours in $\kappa_V - \kappa_F$ for individual decay modes and their combination, and also shows the one-dimensional profile likelihood ratio for the combination as a function of κ_F. For κ_F, a positive best-fit value is preferred, as in the SM, with a negative relative sign between κ_V and κ_F disfavoured at the 4σ level.

The assumption that only SM particles contribute to the Higgs boson total width can be dropped via a reparameterisation of the benchmark model, where the free parameters are $\lambda_{FV} = \kappa_F/\kappa_V$ and $\kappa_{VV} = \kappa_V \cdot \kappa_V/\kappa_H$. The former is the ratio of the scale factors for the fermionic and bosonic couplings, the latter is an overall scale
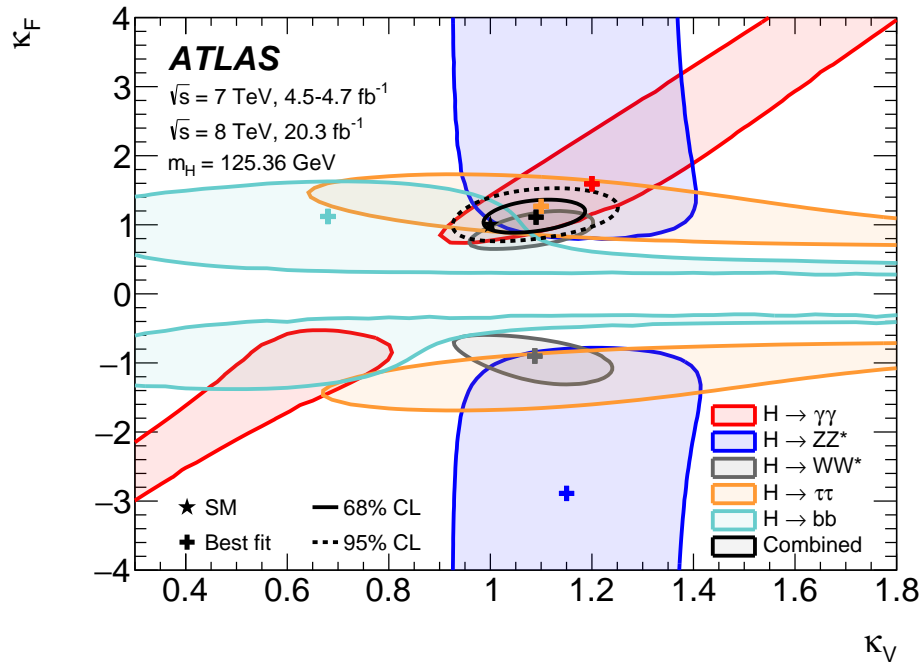
(a)
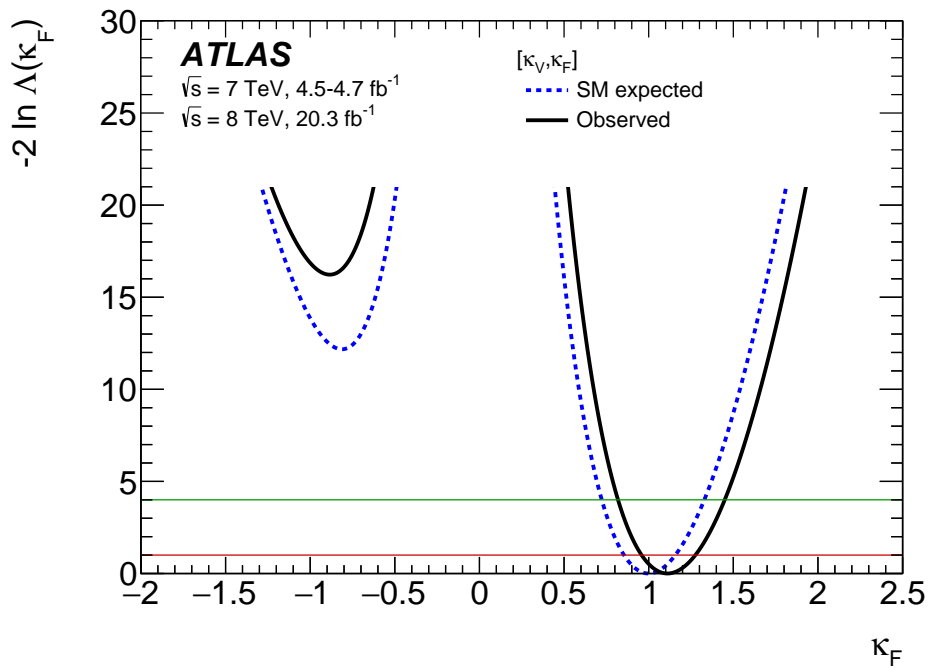
(b)

Figure 6.5: a) Observed 68% CL profile likelihood ratio contours in $\kappa_V - \kappa_F$ for individual decay modes and their combination. Best-fit points are indicated by a cross symbol, the SM predicted value is indicated by a star symbol. b) Observed (solid black line) and expected (dashed blue line) profile likelihood ratio as a function of κ_F (κ_V is profiled) [9].

factor that applies to all couplings.

In this alternative benchmark, the best-fit values for the scale factors are:

$$\lambda_{FV} = 1.02^{+0.15}_{-0.13}$$

$$\kappa_{VV} = 1.07^{+0.14}_{-0.13}$$

A negative relative sign coupling between κ_V and κ_F is again disfavoured at the 4σ level.

6.4.2 Fermion coupling sector

In Section 6.4.1, motivated by the structure of the SM Higgs sector, a single scale factor was applied to all fermion couplings. However, many extensions to the SM predict modified behaviour in the fermion sector. Here, two benchmark models are studied; a first benchmark where one scale factor (κ_u) is applied to all up-type quark couplings and one scale factor (κ_d) is applied to all down-type quark and lepton couplings, and a second benchmark where one scale factor (κ_q) is applied to all quark couplings and one scale factor (κ_ℓ) is applied to all lepton couplings. In both cases, a separate scale factor (κ_V) is applied to vector boson couplings.

Parameterisations in terms of ratios of coupling scale factors are chosen, so no assumption is made on the particles contributing to the Higgs boson total width. This allows the ratios $\lambda_{du} = \kappa_d/\kappa_u$, and $\lambda_{\ell q} = \kappa_\ell/\kappa_q$ to be tested directly. The results presented here assume that only SM particles contribute to loop processes, so loop couplings scale as a function of κ_u, κ_d and κ_V for the first model, and κ_q, κ_ℓ and κ_V for the second.

For the first benchmark model, the parameters of interest in the profile likelihood ratio are chosen to be $\lambda_{du} = \kappa_d/\kappa_u$, $\lambda_{Vu} = \kappa_V/\kappa_u$, and $\kappa_{uu} = \kappa_u \cdot \kappa_u/\kappa_H$. κ_{uu} is an overall scale factor which applies to all couplings. The best-fit values for the

coupling scale factors are:

$$\lambda_{du} = [-1.08, -0.81] \cup [0.75, 1.04]$$

$$\lambda_{Vu} = 0.92^{+0.18}_{-0.16}$$

$$\kappa_{uu} = 1.25 \pm 0.33$$

The parameters are individually compatible with the SM prediction, and the corresponding p-value is 51%.

For the second benchmark model, the parameters of interest in the profile likelihood ratio are chosen to be $\lambda_{\ell q} = \kappa_\ell/\kappa_q$, $\lambda_{Vq} = \kappa_V/\kappa_q$, and $\kappa_{qq} = \kappa_q \cdot \kappa_q/\kappa_H$. Here, κ_{qq} applies to all couplings. The best-fit values for the coupling scale-factors are:

$$\lambda_{\ell q} = [-1.34, -0.94] \cup [0.94, 1.34]$$

$$\lambda_{Vq} = 1.03^{+0.18}_{-0.15}$$

$$\kappa_{qq} = 1.03^{+0.24}_{-0.20}$$

The parameters are again individually consistent with the SM, where the compatibility is calculated as 53%.
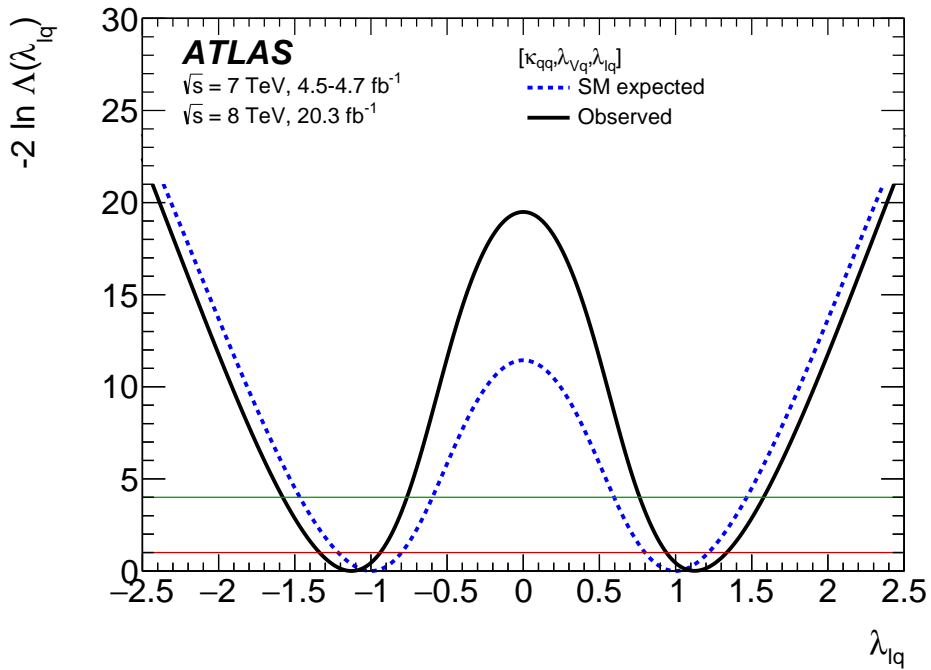
Figure 6.6 shows the profile likelihood ratio as a function of λ_{du} in the first benchmark model and $\lambda_{\ell q}$ in the second. In both cases, there is no significant sensitivity to the relative sign of the couplings. In the first model, a vanishing coupling to down-type quarks and leptons is disfavoured at the 4.5σ level; and in the second, a vanishing coupling to down-type quarks and leptons is disfavoured at the 4.4σ level. In both cases this is driven by the $H \to \tau\tau$ channel.

6.4.3   Beyond the SM contributions

As yet undiscovered particles may contribute directly to the decay width of the Higgs boson and/or in Higgs sector loop processes. This is probed with the coupling measurements by introducing effective scale factors for loop processes (e.g. κ_γ for the
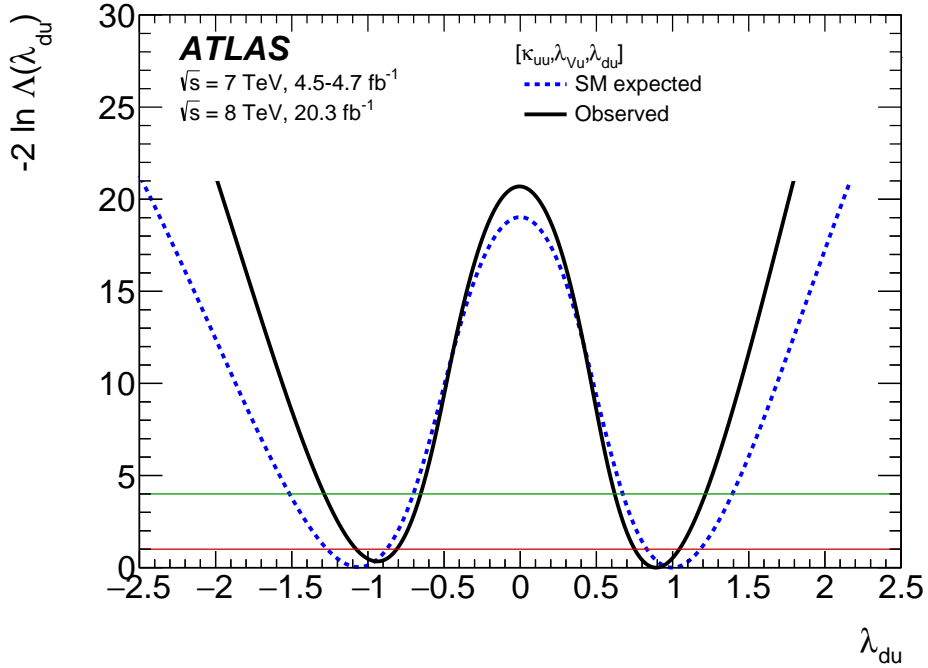
(a)

(b)

Figure 6.6: a) Profile likelihood ratio as a function of λ_{du} in a benchmark model with one scale factor for up-type quarks and one scale factor for down-type quarks and leptons. b) Profile likelihood ratio as a function of $\lambda_{\ell q}$ in a benchmark model with one scale factor for quarks and one scale factor leptons. In both cases the observed profile likelihood ratio is shown as a solid black line and the expected profile likelihood ratio is shown as a dashed blue line [9].

$H \rightarrow \gamma\gamma$ vertex), and by parameterising the total width in terms of the additional branching ratio into additional invisible or undetected final states, $\mathrm{BR}_{\mathrm{i.,u.}}$.

The benchmark model discussed in this section introduces κ_γ, κ_g, and $\kappa_{Z\gamma}$ as effective scale factors corresponding to the $H \rightarrow \gamma\gamma$, $gg \rightarrow H$ and $H \rightarrow Z\gamma$ vertices, as well as $\mathrm{BR}_{\mathrm{i.,u.}}$. The coupling strength parameters corresponding to SM particles are assumed to be equal to the SM prediction of 1.

The fits in this benchmark model are presented in Figure 6.7. The measured values of the effective coupling parameters are found to be in good agreement with the SM prediction. Taking into account the physical constraint that $\mathrm{BR}_{\mathrm{i.,u.}} \geq 0$ by redefining the zero-point of the profile likelihood ratio to be at $\mathrm{BR}_{\mathrm{i.,u.}} = 0$, the observed 95% CL limit on the additional invisible and undetected branching ratio of the Higgs boson is found to be $\mathrm{BR}_{\mathrm{i.,u.}} < 0.27$. The expected 95% CL is $\mathrm{BR}_{\mathrm{i.,u.}} < 0.37$; the observed limit is considerably stronger due to the fact that the profile likelihood ratio minimum falls in the unphysical region.

6.4.3.1   Direct searches for Higgs boson decays to invisible final states

Direct searches for Higgs boson decays to invisible final states have been briefly introduced in Section 6.1 and a combination of these searches is performed in Ref. [10]. Assuming that the Higgs boson production rate, in particular in the VBF and VH modes, is equal to the SM prediction, a 95% CL limit is set on the Higgs boson invisible branching ratio, $BR_{inv.} < 0.25$ (compared to an expected limit of $BR_{inv.} < 0.27$). It should be noted that the limit is placed only on the branching ratio to invisible final states, as opposed to the sum of invisible and undetectable final states, as is the case with the constraints coming from coupling measurements.
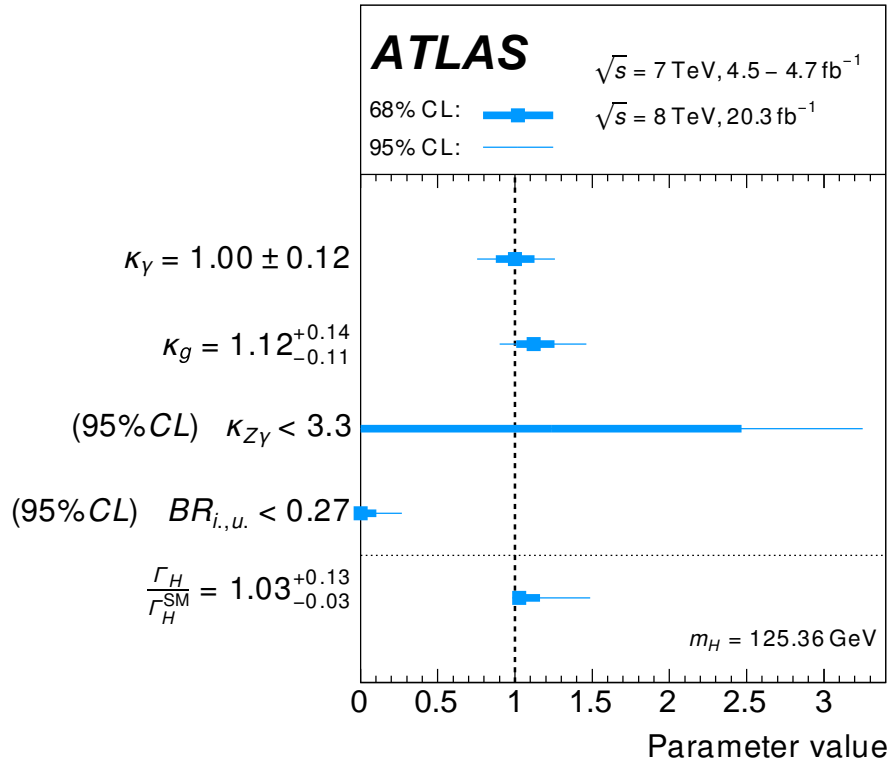
(a)
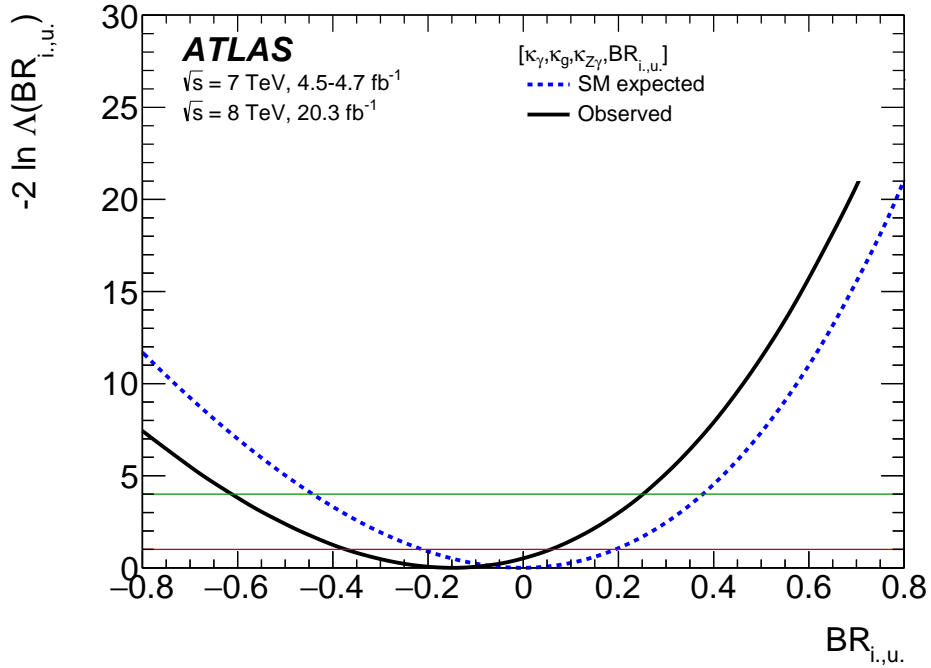
(b)

Figure 6.7: a) Observed best-fit values (blue square), 1σ (horizontal blue bars) and 2σ (horizontal blue lines)uncertainties for the coupling scaled factors κ_γ and κ_g, where for $\kappa_{Z\gamma}$ and $\mathrm{BR_{i.,u.}}$ 95% CL limits are shown. The corresponding allowed ranges of the Higgs boson total width, Γ_H/Γ_H^{SM}, are also shown with respect to the SM prediction. b) Observed (solid black line) and expected (dashed blue line) profile likelihood ratio as a function of $\mathrm{BR_{i.,u.}}$. Figure from Ref. [9].

6.4.4   Generic Models

Rather than grouping together similar couplings in benchmark models, generic models apply individual scale factors to each coupling independently. In this section, two such generic models are presented, the first where only SM particles contribute to the total Higgs boson width and to loop processes, and the second where no assumptions are made on the particle content of loops or the Higgs boson width. A third generic model, parameterised in terms of ratios of coupling scale factors, is presented in Ref. [9].

6.4.4.1   Generic Model 1

The free parameters for this model are κ_W, κ_Z, κ_t, κ_b, κ_τ and κ_μ. The particle content of loop processes is assumed to correspond to the SM, and no additional invisible or undetected Higgs boson decay modes are considered. The convention $\kappa_W > 0$ is chosen.

The fit results in this generic model are summarised in Figure 6.8, where each individual scale factor is found to be compatible with the SM and the p-value describing the compatibility with the SM is 57%. Compared to the benchmark models, the best-fit values for coupling scale factors are typically relatively low. This is due to the low fitted value of κ_b; since the partial width to b quarks dominates the Higgs boson total width, this results in a lower value of Γ_H and has a corresponding effect on the other scale factors.

This model can be reparameterised to highlight the expected mass-dependence of Higgs boson couplings by writing the model in terms of reduced coupling scale factors, y_V for vector bosons and y_F for fermions, where:

$$y_{V,i} = \sqrt{\kappa_{V,i}}\frac{m_{V,i}}{v}, \qquad y_{F,j} = \kappa_{F,j}\frac{m_{F,j}}{v}$$

where $m_{V,i}$ is the mass of a given vector boson, i, $m_{F,i}$ is the mass of a given fermion,
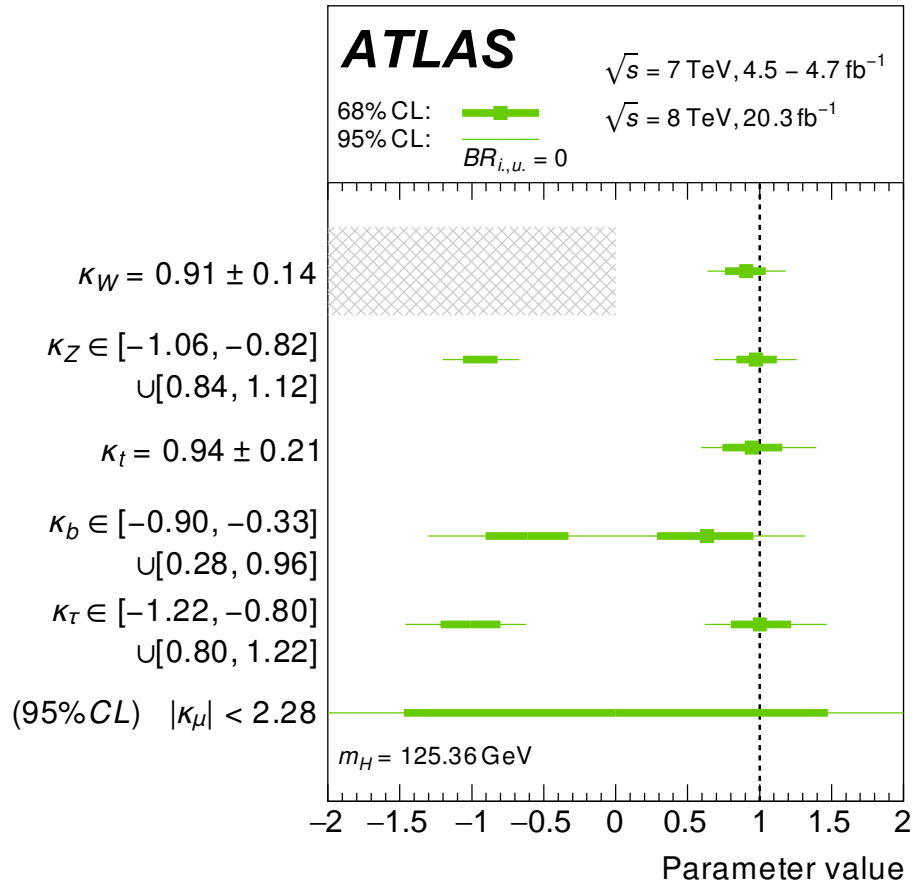
Figure 6.8: Observed best-fit values (green box), 1σ (horizontal green bars) and 2σ (horizontal green lines) uncertainties for fits to the coupling scale factors, κ_W, κ_Z, κ_t, κ_b and κ_τ, in generic model 1, where for κ_μ a 95% CL limit is presented. The sign of κ_W is assumed to be positive, as indicated by the hatched area. Figure from Ref. [9].

j, and v is the SM vacuum expectation value. The fit results in this parameterisation are presented in Figure 6.9.

Furthermore, following the procedure in Ref. [138], the dependence of the couplings on particle masses can be tested directly by expressing the coupling scale factors in terms of a 'mass scaling' parameter, ϵ, and a 'vacuum expectation value' parameter, M, where $\epsilon = 0$ and $M = v \simeq 246$ GeV correspond to the SM prediction. The coupling scale factors for vector bosons and fermions are then re-expressed as:

$$\kappa_{V,i} = v\frac{m_{V,i}^{2\epsilon}}{M^{1+2\epsilon}}, \qquad \kappa_{F,j} = v\frac{m_{F,j}^{\epsilon}}{M^{1+\epsilon}}$$

The observed and expected 68% CL and 95% CL two-dimensional profile likelihood contours in the $\epsilon - M$ plane are also shown in Figure 6.9, where the observed result is in good agreement with the SM prediction.

6.4.4.2   Generic Model 2

The free parameters for this model are κ_W, κ_Z, κ_t, κ_b, κ_τ, κ_μ, κ_γ, κ_g, $\kappa_{Z\gamma}$ and, for two variants of this model, $\mathrm{BR_{i.,u.}}$. The assumption that only SM particles contribute to the loop processes and Higgs boson total width is removed. For the cases where Higgs boson decays to additional invisible or undetected final states are allowed, the Higgs boson total width is constrained either by requiring $\kappa_V < 1$, or by introducing the off-shell Higgs boson signal strength measurements to the combination.

Figure 6.10 presents the results obtained for each variant of this generic model. In all cases, each coupling scale factor tested is compatible with the SM prediction. Where it is not fixed, limits are set on $\mathrm{BR_{i.,u.}}$: $\mathrm{BR_{i.,u.}} < 0.49$ for the $\kappa_V < 1$ constraint and $\mathrm{BR_{i.,u.}} < 0.68$ for the constraint from off shell signal strength measurements. The $\kappa_V < 1$ assumption therefore places stronger constraints on the total Higgs boson width than the inclusion of the off shell Higgs boson production information.
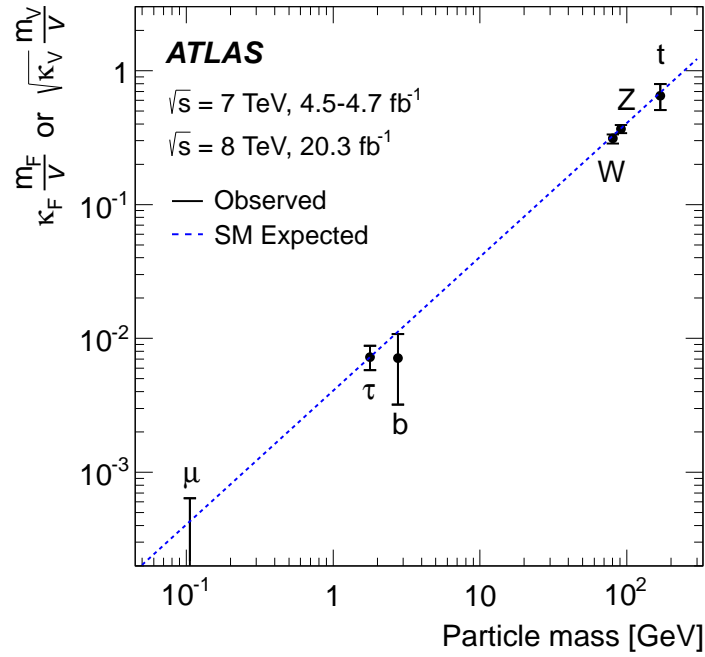
(a)
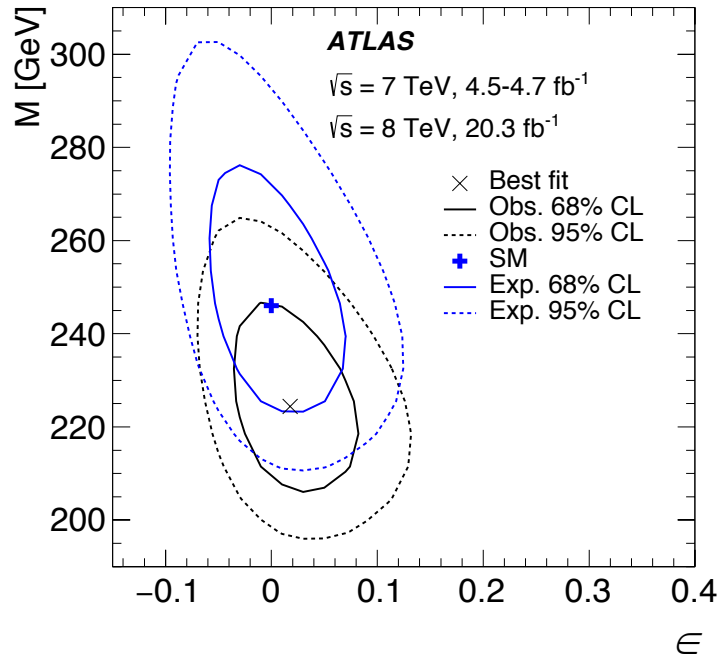
(b)

Figure 6.9: a) Best-fit values and uncertainties for the reduced coupling-strength scale factors, y_V for vector bosons and y_F for fermions, as a function of particle mass, for $m_H = 125.36$ GeV. The dashed line indicates the SM predicted mass dependence [9]. b) Observed (black) and expected (blue) 68% (solid line) and 95% (dashed line) profile likelihood ratio contours as a function of the mass scaling parameter, ϵ, and the vacuum expectation value parameter, M. The best fit value is shown as a black cross symbol and the SM expectation is shown as a blue plus symbol. Figure from Ref. [10].
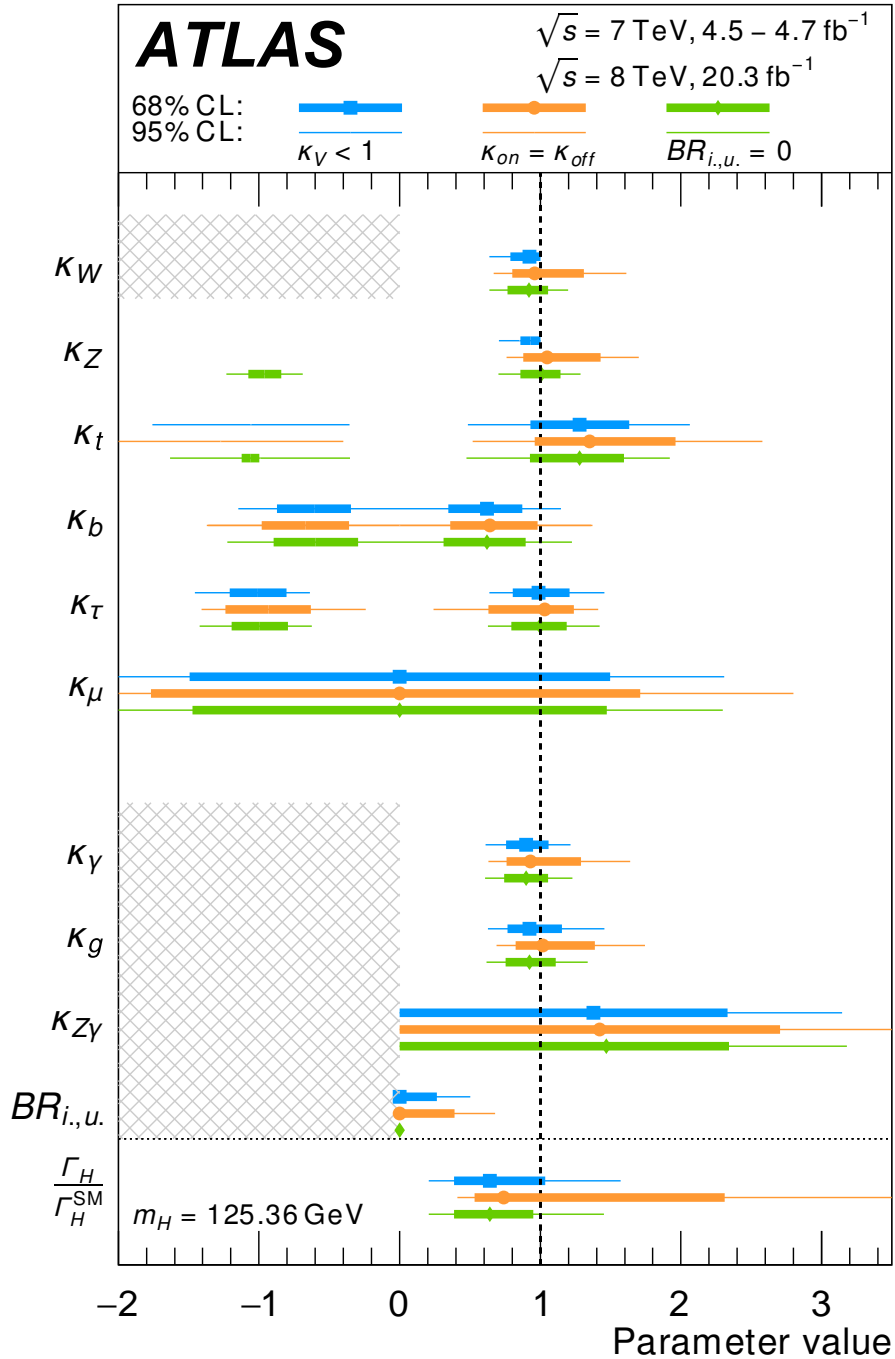
Figure 6.10:   Best-fit values (markers), 1σ (horizontal bars) and 2σ (horizontal lines) for fits to coupling scale factors in generic model 2. Three variants are shown as described in the text, corresponding to the following constraints: $BR_{i.,u.} = 0$ (green, diamond marker), $k_V < 1$ (blue, square marker) and $\kappa_{on} = \kappa_{off}$ (orange, circle marker). The hatched areas indicate regions that are outside the parameter boundaries. Figure from Ref. [10].

6.4.5   Constraints on the Higgs boson invisible branching ratio combining visible and invisible decay modes

In terms of setting limits on the Higgs boson branching ratio to invisible final states, the limits derived from the combination of visible decay modes are complementary to direct searches since they are also sensitive to additional undetected decay modes. Assuming $BR_{undet.} = 0$, the measurements using visible and invisible decay modes can be combined. The invisible decay channels are described in Section 6.1 though the $V(jj)H$ production mode is not included in the combination as its event selection overlaps with the $H \rightarrow b\bar{b}$ event selection. For the combination, the visible decay modes are parameterised in terms of coupling scale factors as in generic model 2, though with the $BR_{undet.} = 0$ assumption and the inclusion of the invisible decay modes, no further assumptions are necessary to constrain the Higgs boson total width. As no assumptions are made on the values of the coupling scale factors, the assumption of SM production rates present in the limits coming from the direct searches for invisible decays is relaxed. The resulting observed (expected) upper 95% CL limit is $BR_{inv.} < 0.23(0.24)$. The profile likelihood ratio, as a function of $BR_{inv.}$, is shown for the visible and invisible decay modes and their combination in Figure 6.11.

Additionally, in terms of measurements of coupling parameters, the combination of visible and invisible decay modes provides an additional variant of generic model 2, since the inclusion of the invisible decay modes (under the assumption that $BR_{undet.} = 0$) provides a constraint on the Higgs boson total width. The numerical fit results for this variant, along with the results corresponding to Section 6.4.4.2, are presented in Table 6.2. For each variant, the observed confidence intervals are similar, and in good agreement with the SM prediction.
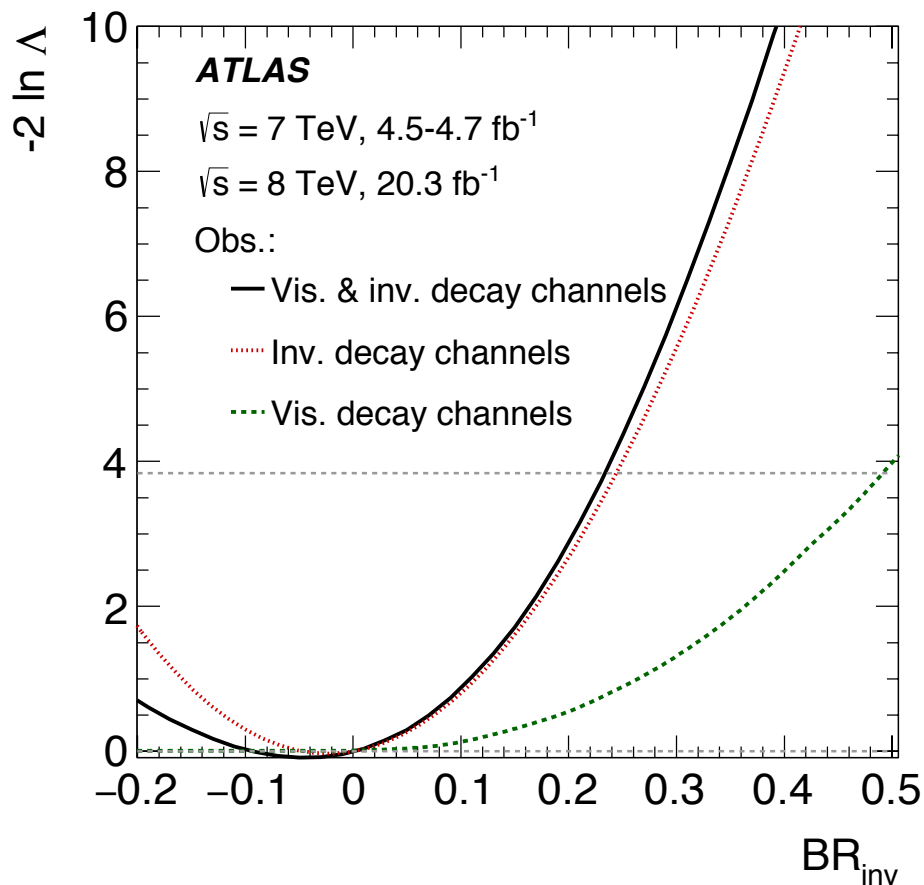
Figure 6.11: Observed profile likelihood ratio as a function of the Higgs boson invisible decay branching ratio for searches for Higgs boson decays to invisible final states (red dashed line), coupling measurements using the combination of visible decay modes in generic model 2 with $\kappa_V < 1$ (green dashed line), and the combination of visible and invisible decay modes (black solid line) dropping the $\kappa_V < 1$ constraint. The $-2ln\Lambda = 0$ point is redefined to reflect the physical boundary at $\xi = 0$. Figure from Ref. [10].

Table 6.2: Summary of numerical results for fits in generic model 2. The first three result columns [9] are illustrated in Fig. 6.10, the fourth comes from a further variant where the direct searches for invisible decays are used to constrain the total Higgs boson width, assuming $\mathrm{BR_{undet.}} = 0$. Confidence intervals for $\mathrm{BR_{inv.,undet.}}$ are estimated with respect to the physical boundary $\mathrm{BR_{inv.,undet.}} > 0$.

Parameter	$\kappa_V < 1$	$\kappa_{on} = \kappa_{off}$	$\mathrm{BR_{inv.,undet.}} = 0$	$\mathrm{BR_{undet.}} = 0$
κ_W	> 0.64 (95% CL)	$= 0.96 \pm^{0.35}_{0.16}$	$= 0.92^{+0.14}_{-0.15}$	$= 0.92 \pm 0.14$
κ_Z	> 0.71 (95% CL)	$= 1.05 \pm^{0.38}_{0.17}$	$\in [-1.08, -0.84] \cup [0.86, 1.14]$	$\in [-1.07, -0.83] \cup [0.85, 1.14]$
κ_t	$= 1.28^{+0.32}_{-0.35}$	$= 1.35^{+0.61}_{-0.39}$	$\in [-1.12, -1.00] \cup [0.93, 1.60]$	$1.26^{+0.32}_{-0.34}$
$|\kappa_b|$	$= 0.62 \pm 0.28$	$0.64^{+0.34}_{-0.28}$	$0.62^{+0.31}_{-0.27}$	0.61 ± 0.28
$|\kappa_\tau|$	$= 0.99^{+0.22}_{-0.18}$	$1.03^{+0.21}_{-0.40}$	1.00 ± 0.20	$0.98^{+0.20}_{-0.18}$
$|\kappa_\mu|$	< 2.3 (95% CL)	2.8 (95% CL)	2.3 (95% CL)	2.3 (95% CL)
κ_γ	$= 0.90^{+0.16}_{-0.14}$	$0.93 \pm^{0.36}_{0.17}$	0.90 ± 0.15	$0.89^{+0.16}_{-0.14}$
κ_g	$= 0.92^{+0.23}_{-0.16}$	$1.02 \pm^{0.37}_{0.19}$	0.92 ± 0.17	$0.92^{+0.18}_{-0.15}$
$\kappa_{Z\gamma}$	< 3.15 (95% CL)	4.03 (95% CL)	3.18 (95% CL)	3.15 (95% CL)
$\mathrm{BR_{inv.,undet.}}$	< 0.49 (95% CL)	< 0.68 (95% CL)	-	0.23(95% CL)

6.5   Constraints on new phenomena using Higgs boson coupling measurements

In Section 6.4, measurements of coupling scale factors are performed in a number of benchmark and generic models within the framework described in section 2.3. Additionally, the same combination of decay modes studied can be used to set limits directly on BSM models, for example those described in Section 2.1.3. The observed constraints for a select number of models are presented here; further results and extended discussion may be found in Ref. [10].

6.5.1   Minimal Composite Higgs Models

MCHMs, in particular the $\mathrm{MCHM_4}$ and $\mathrm{MCHM_5}$ scenarios, are introduced in Section 2.1.3. The coupling scale factors used in Section 6.4 can be rewritten in terms of the ratio, $\xi = v^2/f^2$, which depends on the compositeness scale, f. In both cases, the coupling of the Higgs boson to vector bosons is modified with respect to the SM in the same way:

$$\kappa_V = \sqrt{1-\xi}$$

In the $\mathrm{MCHM_4}$, the Higgs boson coupling to fermions is modified in the same way as the coupling to vector bosons:

$$\kappa_F = \kappa_V = \sqrt{1-\xi}$$

meaning that all production and decay rates scale in the same way (analagous to the overall signal strength measurement presented in Section 6.3), with $\xi = 1 - \mu$.

The best-fit value for ξ is $\xi = -0.18 \pm 0.14$, which is observed to be negative because the overall signal strength is measured to be larger than the SM prediction. Taking into account the physical boundary $\xi \geq 0$, a 95% CL lower limit is placed on the

compositeness scale, $f > 710$ GeV. Compared to the expected limit $f > 510$ GeV, the observed limit is stronger as a result of the larger than expected overall signal strength.

In the MCHM$_5$, the Higgs boson coupling to fermions is modified in a different way to the coupling to vector bosons:

$$\kappa_F = \frac{1 - 2\xi}{\sqrt{1 - \xi}}$$

In this case the best fit ξ is $\xi = -0.12 \pm 0.10$. Again the best-fit value is negative, in this case because the coupling strengths of the Higgs boson to both bosons and fermions is measure to be larger than the SM expectation. The 95% CL limit on the compositeness scale is $f > 780$ GeV, compared to an expected limit $f > 600$ GeV.

The profile likelihood ratio, as a function of the ratio ξ in the MCHM$_4$ and MCHM$_5$ scenarios, is shown in Figure 6.12. The profile likelihood ratio 68% and 95% CL contours are shown in the $\kappa_V - \kappa_F$ plane in Figure 6.13, with the corresponding predicted coupling values for different values of ξ in both scenarios.

6.5.2   Additional EW Singlet Model

Additional EW Singlet Models are also introduced in Section 2.1.3. In this case, all coupling strengths for the light Higgs boson are modified by the same factor, $\mu_h = \kappa^2$, again analagous to the overall signal strength measurement presented in Section 6.3. The model also introduces a heavy Higgs boson, with an associated signal strength μ_H.

Assuming that EWSB fully solves the unitarity problem in $W^+ W^- \rightarrow W^+ W^-$ scattering, the coupling strength of the heavy Higgs boson, κ', can be inferred from a measurement of the coupling strength of the light Higgs boson, κ:
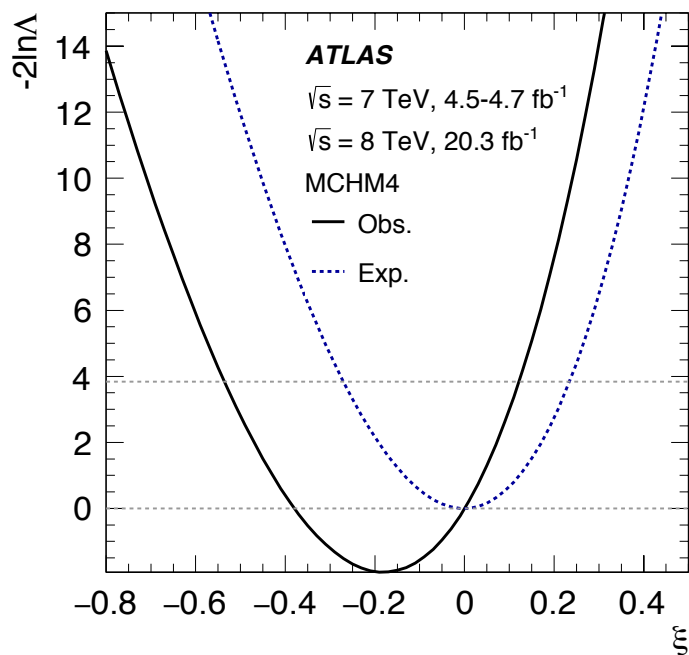
(a)
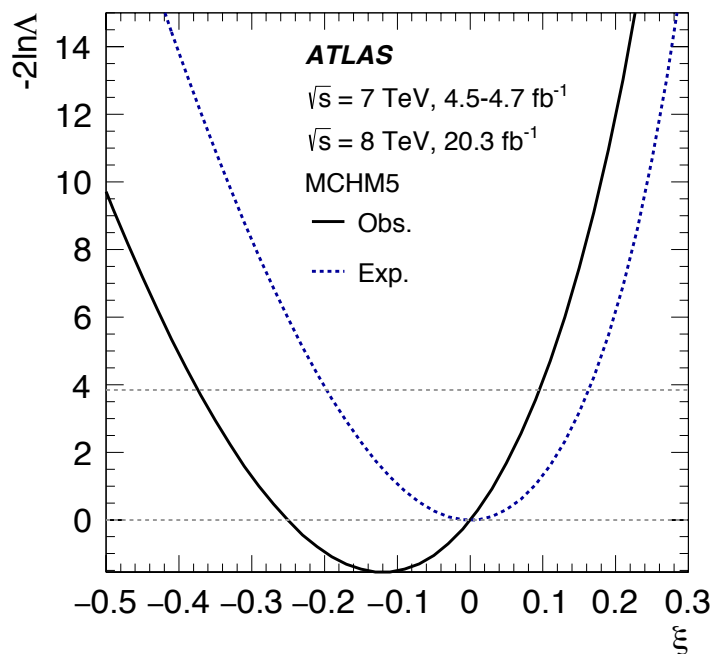
(b)

Figure 6.12: Observed (solid black line) and expected (dashed blue line) profile likelihood ratio as a function of the ratio ξ in: a) MHCM$_4$, and b) MHCM$_5$. The $-2ln\Lambda = 0$ point is redefined to reflect the physical boundary at $\xi = 0$. Figure from Ref. [10].

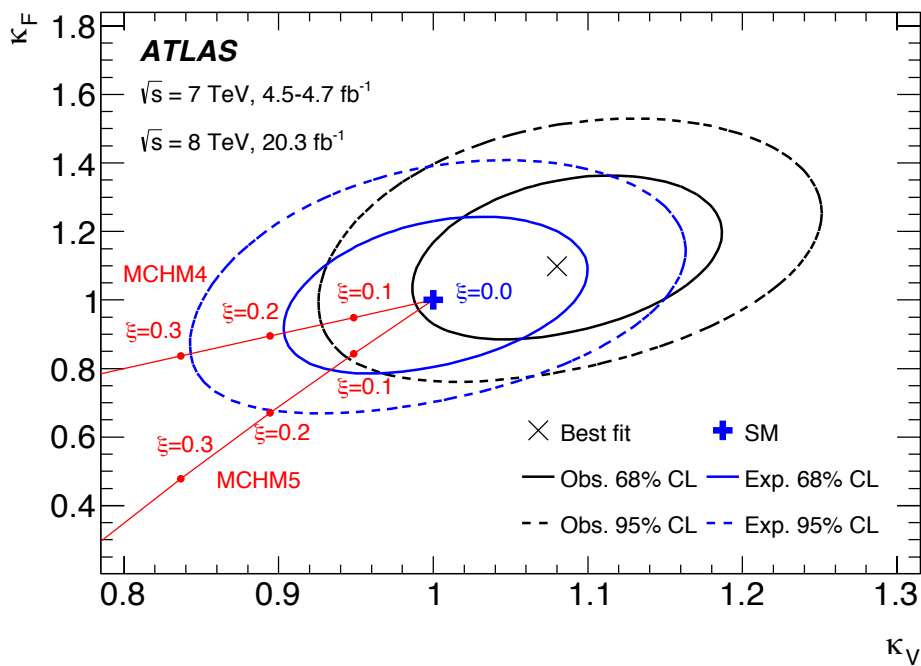Figure 6.13: Observed (black) and expected (blue) 68% (solid lines) and 95% (dashed lines) CL profile likelihood ratio contours in the $\kappa_V - \kappa_F$ plane. The best-fit point is shown by a cross marker, and the SM expectation is shown by a '+' marker. The predictions for the coupling scale factors in $MCHM_4$ and $MCHM_5$ for different values of the ratio ξ are shown as red lines. Figure from Ref. [10].

$$\kappa'^2 = 1 - \kappa^2 \tag{6.1}$$

The best-fit measurement for the heavy Higgs boson coupling strength is $\kappa'^2 = -0.18 \pm 0.14$. The result is again negative because the overall signal strength measured in the combination of decay modes is larger than the SM prediction. Taking into account the physical boundary $\kappa'^2 > 0$, the 95% CL upper limit on the heavy Higgs boson coupling strength is $\kappa'^2 > 0.12$, compared to an expected limit $\kappa'^2 > 0.23$. Figure 6.14 shows the observed and expected limits in the $\kappa'^2 - \mathrm{BR_{H,new}}$ plane, where $\mathrm{BR_{H,new}}$ is the branching ratio for the decay of the heavy Higgs boson to final states unavailable to the light Higgs boson. Contours of the scale factor for the total width of the heavy Higgs boson, $\Gamma_H/\Gamma_{H,SM}$, are also shown.
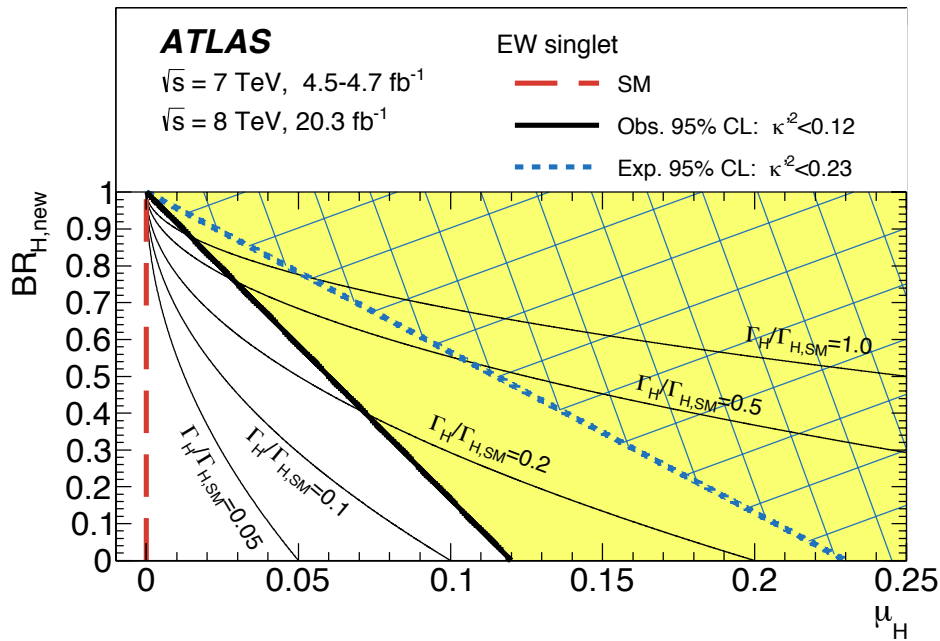
Figure 6.14: Observed (solid black line) and expected (dashed blue line) limit on the additional EW singlet model described in the text in the μ_H-$\mathrm{BR_{H,new}}$ plane, with the SM prediction shown as a dashed red line. The observed and expected excluded regions are shown as a filled yellow area and hatched blue area respectively. Contours corresponding to different values of the width of the heavy Higgs boson, Γ_H, are also shown. Figure from Ref. [10].

CHAPTER 7

Concluding remarks

After many years of searches at a range of experimental facilities, the discovery of a Higgs boson by the ATLAS and CMS collaborations in 2012 has simultaneously presented an opportunity to test the predictions of the Standard Model in a previously unexplored sector and opened new avenues in which to search for new physics. In the subsequent years, the emphasis of experimental Higgs boson physics has shifted from searches to a programme of precision measurements.

Thus far, the Higgs sector measurements performed by the ATLAS and CMS collaborations are in unanimous agreement with the predictions of the Standard Model, and suggest that a non-zero vacuum expectation value of a scalar doublet is largely responsible for electroweak symmetry breaking. Furthermore, the direct observation of Higgs boson decays to $\tau\tau$ pairs, with an observed rate in good agreement with the Standard Model prediction, suggest that the Brout-Englert-Higgs mechanism is also at least partly responsible for generating fermion masses.

Recently, the ATLAS and CMS collaborations have performed a preliminary measurement of the Higgs boson coupling strengths using the combination of decay modes from both experiments [11]. The results serve to further strengthen the conclusions drawn by the individual experiments, with the ATLAS and CMS results typically in good agreement with eachother and with the Standard Model prediction. In Figure 7.1, the combined results are presented in the benchmark model discussed in Section 6.4.4.1, where the particle content of loop processes is assumed to correspond to the Standard Model and no additional invisible or undetected Higgs boson decay modes are considered.
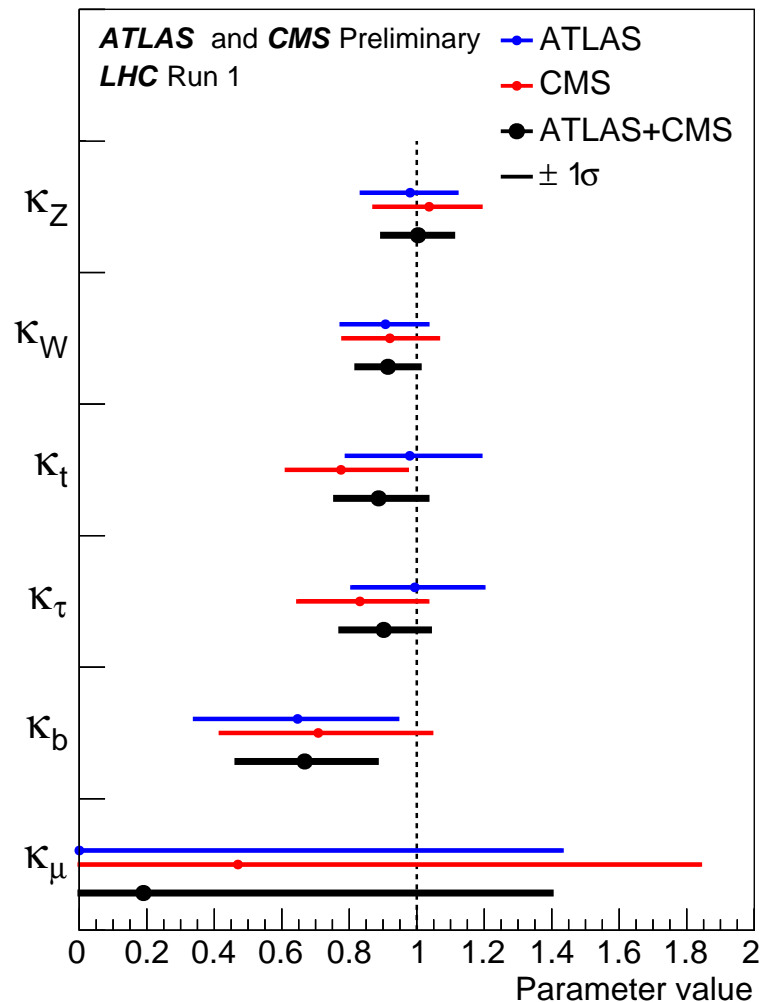

Figure 7.1: Observed best-fit values (markers) and 1σ uncertainties (horizontal bars) for fits to the coupling scale factors, κ_W, κ_Z, κ_t, κ_b and κ_τ, in generic model 1, where for κ_μ a 95% CL limit is presented. Results are shown for the ATLAS (blue), CMS (red) and combined (black) analyses. Figure from Ref. [11].

Direct searches for signatures corresponding to extended Higgs sectors, e.g. additional heavy Higgs bosons, have so far not been observed. This is consistent with the picture outside of the Higgs sector; as of yet no physics beyond the Standard Model has been observed by the ATLAS or CMS collaborations.

With LHC Run II now in its early stages, there is scope for this situation to change. In particular, the higher centre-of-mass energy, $\sqrt{s} = 13$ TeV, allows a probe of an energy regime previously inaccessible. Furthermore, with the LHC Runs II and III anticipated to deliver an integrated luminosity an order of magnitude higher than in Run I, the precision of the measurement of Higgs boson coupling strengths will increase considerably, providing sensitivity to increasingly smaller deviations from the Standard Model predictions.

REFERENCES

[1] H. S. Bansil, J. Bracinik, R. D. Mudd, and P. R. Newman, "Tier-0 Monitoring of the ATLAS Level-1 Calorimeter Trigger Jet and Electromagnetic Trigger Item Efficiencies," Tech. Rep. ATL-DAQ-INT-2012-002, CERN, Geneva, Jul 2012.

[2] B. Barnett, J. Bracinik, S. Hillier, M. Levy, R. Mudd, R. Owen, and M. Watson, "Investigation into the Effect of Isolation on Trigger Rate and Efficiency of Acceptance on Electromagnetic Events in the ATLAS Level-1 Calorimeter," Tech. Rep. ATL-DAQ-INT-2014-001, CERN, Geneva, Jan 2014.

[3] ATLAS collaboration, "Measurements of Higgs boson production and couplings in diboson final states with the ATLAS detector at the LHC," *Phys.Lett.*, vol. B726, pp. 88–119, 2013.

[4] ATLAS collaboration, "Measurements of Higgs boson production and couplings in the four-lepton channel in pp collisions at center-of-mass energies of 7 and 8 TeV with the ATLAS detector," *Phys.Rev.*, vol. D91, no. 1, p. 012006, 2015.

[5] ATLAS collaboration, "Fiducial and differential cross sections of Higgs boson production measured in the four-lepton decay channel in pp collisions at $\sqrt{s}$=8 TeV with the ATLAS detector," *Phys. Lett.*, vol. B738, pp. 234–253, 2014.

[6] ATLAS Collaboration, "Measurements of the properties of the Higgs-like boson in the four lepton decay channel with the ATLAS detector using 25 fb^{-1} of proton-proton collision data," *ATLAS-CONF-2013-013*, Mar 2013.

[7] ATLAS Collaboration, "Measurement of the Higgs boson mass from the $H\to\gamma\gamma$ and $H \to ZZ^{(*)} \to 4\ell$ channels with the ATLAS detector using 25 fb^{-1} of pp collision data," *Submitted to Phys. Rev.*, vol. D, 2014.

[8] ATLAS collaboration, "Search for Higgs and Z Boson Decays to J/ and (nS) with the ATLAS Detector," *Phys. Rev. Lett.*, vol. 114, no. 12, p. 121801, 2015.

[9] ATLAS collaboration, "Measurements of the Higgs boson production and decay rates and coupling strengths using pp collision data at $\sqrt{s} = 7$ and 8 TeV in the ATLAS experiment," *Eur. Phys. J.*, vol. C76, no. 1, p. 6, 2016.

[10] ATLAS collaboration, "Constraints on new phenomena via Higgs boson couplings and invisible decays with the ATLAS detector," *JHEP*, vol. 11, p. 206, 2015.

[11] ATLAS and CMS collaborations, "Measurements of the Higgs boson production and decay rates and constraints on its couplings from a combined ATLAS and CMS analysis of the LHC pp collision data at $\sqrt{s} = 7$ and 8 TeV," Tech. Rep. ATLAS-CONF-2015-044, CERN, Geneva, Sep 2015.

[12] ATLAS collaboration, "Observation of a new particle in the search for the Standard Model Higgs boson with the ATLAS detector at the LHC," *Phys.Lett.*, vol. B716, pp. 1–29, 2012.

[13] CMS Collaboration, "Observation of a new boson at a mass of 125 GeV with the CMS experiment at the LHC," *Phys.Lett.*, vol. B716, pp. 30–61, 2012.

[14] R. Barate *et al.*, "Search for the standard model Higgs boson at LEP," *Phys. Lett.*, vol. B565, pp. 61–75, 2003.

[15] T. Aaltonen *et al.*, "Higgs Boson Studies at the Tevatron," *Phys. Rev.*, vol. D88, no. 5, p. 052014, 2013.

[16] A. L. Read, "Presentation of search results: The CL(s) technique," *J. Phys.*, vol. G28, pp. 2693–2704, 2002. [,11(2002)].

[17] S. L. Glashow, "Partial symmetries of weak interactions," *Nucl. Phys.*, vol. 22, p. 579, 1961.

[18] S. Weinberg, "A model of leptons," *Phys. Rev. Lett.*, vol. 19, p. 1264, 1967.

[19] K. A. Olive *et al.*, "The Review of Particle Physics," *Chin. Phys. C*, vol. 38, 2014.

[20] F. Englert and R. Brout, "Broken Symmetry and the Mass of Gauge Vector Mesons," *Phys. Rev. Lett.*, vol. 13, pp. 321–323, 1964.

[21] P. Higgs, "Broken Symmetries and the Masses of Gauge Bosons," *Phys. Rev. Lett.*, vol. 13, pp. 508–509, 1964.

[22] G. Guralnik, C. Hagen, and T. Kibble, "Global Conservation Laws and Massless Particles," *Phys. Rev. Lett.*, vol. 13, pp. 585–587, 1964.

[23] K. Agashe, R. Contino, and A. Pomarol, "The Minimal composite Higgs model," *Nucl. Phys.*, vol. B719, pp. 165–187, 2005.

[24] R. Contino, L. Da Rold, and A. Pomarol, "Light custodians in natural composite Higgs models," *Phys. Rev.*, vol. D75, p. 055014, 2007.

[25] M. Carena, E. Ponton, J. Santiago, and C. E. M. Wagner, "Electroweak constraints on warped models with custodial symmetry," *Phys. Rev.*, vol. D76, p. 035006, 2007.

[26] ALEPH Collaboration, "Precision electroweak measurements on the *Z* resonance," *Phys. Rept.*, vol. 427, pp. 257–454, 2006.

[27] LHC Higgs Cross Section Working Group, S. Heinemeyer, C. Mariotti, G. Passarino, and R. Tanaka (Eds.), "Handbook of LHC Higgs Cross Sections: 3. Higgs Properties," *CERN-2013-004*, CERN, Geneva, 2013.

[28] A. Hill and J. J. van der Bij, "STRONGLY INTERACTING SINGLET - DOUBLET HIGGS MODEL," *Phys. Rev.*, vol. D36, pp. 3463–3473, 1987.

[29] J. F. Gunion and H. E. Haber, "The CP conserving two Higgs doublet model: The Approach to the decoupling limit," *Phys. Rev.*, vol. D67, p. 075019, 2003.

[30] G. C. Branco, P. M. Ferreira, L. Lavoura, M. N. Rebelo, M. Sher, and J. P. Silva, "Theory and phenomenology of two-Higgs-doublet models," *Phys. Rept.*, vol. 516, pp. 1–102, 2012.

[31] S. L. Glashow and S. Weinberg, "Natural Conservation Laws for Neutral Currents," *Phys. Rev.*, vol. D15, p. 1958, 1977.

[32] E. A. Paschos, "Diagonal Neutral Currents," *Phys. Rev.*, vol. D15, p. 1966, 1977.

[33] LHC Higgs cross section working group, S. Dittmaier, C. Mariotti, G. Passarino, and R. Tanaka (Eds.), "Handbook of LHC Higgs cross sections: 1. Inclusive observables," *CERN-2011-002*, 2011.

[34] LHC Higgs cross section working group, S. Dittmaier, C. Mariotti, G. Passarino, and R. Tanaka (Eds.), "Handbook of LHC Higgs Cross Sections: 2. Differential distributions," *CERN-2012-002*, 2012.

[35] A. Djouadi, M. Spira, and P. M. Zerwas, "Production of Higgs bosons in proton colliders: QCD corrections," *Phys. Lett.*, vol. B 264, p. 440, 1991.

[36] S. Dawson, "Radiative corrections to Higgs boson production," *Nucl. Phys.*, vol. B 359, p. 283, 1991.

[37] M. Spira, A. Djouadi, D. Graudenz, and P. M. Zerwas, "Higgs boson production at the LHC," *Nucl. Phys.*, vol. B 453, p. 17, 1995.

[38] R. V. Harlander and W. B. Kilgore, "Next-to-next-to-leading order Higgs production at hadron colliders," *Phys. Rev. Lett.*, vol. 88, p. 201801, 2002.

[39] C. Anastasiou and K. Melnikov, "Higgs boson production at hadron colliders in NNLO QCD," *Nucl. Phys.*, vol. B 646, p. 220, 2002.

[40] V. Ravindran, J. Smith, and W. L. van Neerven, "NNLO corrections to the total cross section for Higgs boson production in hadron hadron collisions," *Nucl. Phys.*, vol. B 665, p. 325, 2003.

[41] S. Catani, D. de Florian, M. Grazzini, and P. Nason, "Soft-gluon resummation for Higgs boson production at hadron colliders," *J. High Energy Phys.*, vol. 07, p. 028, 2003.

[42] U. Aglietti, R. Bonciani, G. Degrassi, and A. Vicini, "Two-loop light fermion contribution to Higgs production and decays," *Phys. Lett.*, vol. B 595, p. 432, 2004.

[43] S. Actis, G. Passarino, C. Sturm, and S. Uccirati, "NLO electroweak corrections to Higgs Boson production at hadron colliders," *Phys. Lett.*, vol. B 670, p. 12, 2008.

[44] M. Ciccolini, A. Denner, and S. Dittmaier, "Strong and electroweak corrections to the production of Higgs+2jets via weak interactions at the LHC," *Phys. Rev. Lett.*, vol. 99, p. 161803, 2007.

[45] M. Ciccolini, A. Denner, and S. Dittmaier, "Electroweak and QCD corrections to Higgs production via vector-boson fusion at the LHC," *Phys. Rev.*, vol. D 77, p. 013002, 2008.

[46] K. Arnold *et al.*, "VBFNLO: a parton level Monte Carlo for processes with electroweak bosons," *Comput. Phys. Commun.*, vol. 180, p. 1661, 2009.

[47] P. Bolzoni, F. Maltoni, S.-O. Moch, and M. Zaro, "Higgs production via vector-boson fusion at NNLO in QCD," *Phys. Rev. Lett.*, vol. 105, p. 011801, 2010.

[48] T. Han and S. Willenbrock, "QCD correction to the p p $\rightarrow$ W H and Z H total cross- sections," *Phys. Lett.*, vol. B 273, p. 167, 1991.

[49] O. Brein, A. Djouadi, and R. Harlander, "NNLO QCD corrections to the Higgs-strahlung processes at hadron colliders," *Phys. Lett.*, vol. B 579, p. 149, 2004.

[50] M. L. Ciccolini, S. Dittmaier, and M. Kramer, "Electroweak radiative corrections to associated WH and ZH production at hadron colliders," *Phys. Rev.*, vol. D 68, p. 073003, 2003.

[51] W. Beenakker, S. Dittmaier, M. Krämer, B. Plümper, M. Spira, and P. Zerwas, "Higgs radiation off top quarks at the Tevatron and the LHC," *Phys. Rev. Lett.*, vol. 87, p. 201805, 2001.

[52] W. Beenakker, S. Dittmaier, M. Krämer, B. Plümper, M. Spira, and P. Zerwas, "NLO QCD corrections to $t\bar{t}$ H production in hadron collisions," *Nucl. Phys.*, vol. B 653, p. 151, 2003.

[53] S. Dawson, L. Orr, L. Reina, and D. Wackeroth, "Next-to-leading order QCD corrections to $pp \rightarrow t\bar{t}h$ at the CERN Large Hadron Collider," *Phys. Rev.*, vol. D 67, p. 071503, 2003.

[54] S. Dawson, C. Jackson, L. H. Orr, L. Reina, and D. Wackeroth, "Associated Higgs production with top quarks at the Large Hadron Collider: NLO QCD corrections," *Phys. Rev.*, vol. D 68, p. 034022, 2003.

[55] M. Botje *et al.*, "The PDF4LHC Working Group Interim Recommendations," 2011.

[56] H.-L. Lai, M. Guzzi, J. Huston, Z. Li, P. M. Nadolsky, J. Pumplin, and C.-P. Yuan, "New parton distributions for collider physics," *Phys. Rev.*, vol. D 82, p. 074024, 2010.

[57] A. D. Martin, W. J. Stirling, R. S. Thorne, and G. Watt, "Parton distributions for the LHC," *Eur. Phys. J.*, vol. C 63, p. 189, 2009.

[58] R. D. Ball, V. Bertone, F. Cerutti, L. D. Debbio, S. Forte, A. Guffanti, J. I. Latorre, J. Rojo, and M. Ubiali, "Impact of heavy quark masses on parton distributions and LHC phenomenology," *Nucl. Phys.*, vol. B 849, p. 296, 2011.

[59] A. Bredenstein, A. Denner, S. Dittmaier, and M. M. Weber, "Precision calculations for $H \rightarrow WW/ZZ \rightarrow 4$ fermions with PROPHECY4f," 2007.

[60] A. Djouadi, J. Kalinowski, and M. Spira, "HDECAY: a program for Higgs boson decays in the standard model and its supersymmetric extension," *Comput. Phys. Commun.*, vol. 108, p. 56, 1998.

[61] J. Alwall, R. Frederix, S. Frixione, V. Hirschi, F. Maltoni, *et al.*, "The automated computation of tree-level and next-to-leading order differential cross sections, and their matching to parton shower simulations," *JHEP*, vol. 1407, p. 079, 2014.

[62] C. Englert, M. McCullough, and M. Spannowsky, "Gluon-initiated associated production boosts physics," *Phys. Rev.*, vol. D89, p. 013013, 2014.

[63] S. Agostinelli *et al.*, "GEANT4: A Simulation toolkit," *Nucl. Instrum. Meth.*, vol. A506, pp. 250–303, 2003.

[64] J. Allison *et al.*, "Geant4 developments and applications," *IEEE Trans. Nucl. Sci.*, vol. 53, p. 270, 2006.

[65] P. Nason, "A new method for combining NLO QCD with shower Monte Carlo algorithms," *J. High Energy Phys.*, vol. 11, p. 040, 2004.

[66] S. Frixione, P. Nason, and C. Oleari, "Matching NLO QCD computations with parton shower simulations: the POWHEG method," *J. High Energy Phys.*, vol. 11, p. 070, 2007.

[67] S. Alioli, P. Nason, C. Oleari, and E. Re, "A general framework for implementing NLO calculations in shower Monte Carlo programs: the POWHEG BOX," *J. High Energy Phys.*, vol. 06, p. 043, 2010.

[68] S. Alioli, P. Nason, C. Oleari, and E. Re, "NLO Higgs boson production via gluon fusion matched with shower in POWHEG," *J. High Energy Phys.*, vol. 04, p. 002, 2009.

[69] P. Nason and C. Oleari, "NLO Higgs boson production via vector-boson fusion matched with shower in POWHEG," *J. High Energy Phys.*, vol. 02, p. 037, 2010.

[70] T. Sjostrand, S. Mrenna, and P. Z. Skands, "PYTHIA 6.4 physics and manual," *J. High Energy Phys.*, vol. 05, p. 026, 2006.

[71] T. Sjostrand, S. Mrenna, and P. Z. Skands, "A brief introduction to PYTHIA 8.1," *Comput. Phys. Commun.*, vol. 178, p. 852, 2008.

[72] H.-L. Lai, M. Guzzi, J. Huston, Z. Li, P. M. Nadolsky, *et al.*, "New parton distributions for collider physics," *Phys. Rev.*, vol. D82, p. 074024, 2010.

[73] P. M. Nadolsky, H.-L. Lai, Q.-H. Cao, J. Huston, J. Pumplin, *et al.*, "Implications of CTEQ global analysis for collider observables," *Phys. Rev.*, vol. D78, p. 013004, 2008.

[74] D. de Florian, G. Ferrera, M. Grazzini, and D. Tommasini, "Higgs boson production at the LHC: transverse momentum resummation effects in the H to 2gamma, H to WW to lnu lnu and H to ZZ* to 4l decay modes," *J. High Energy Phys.*, vol. 06, p. 132, 2012.

[75] M. Grazzini and H. Sargsyan, "Heavy-quark mass effects in Higgs boson production at the LHC," *J. High Energy Phys.*, vol. 09, p. 129, 2013.

[76] T. Melia, P. Nason, R. Rontsch, and G. Zanderighi, "W^+W^-, WZ and ZZ production in the POWHEG BOX," *J. High Energy Phys.*, vol. 11, p. 078, 2011.

[77] T. Binoth, N. Kauer, and P. Mertsch, "Gluon-induced QCD corrections to $pp \to ZZ \to \ell\bar{\ell}\ell'\bar{\ell}',$" 2008.

[78] M. L. Mangano, M. Moretti, F. Piccinini, R. Pittau, and A. D. Polosa, "ALPGEN, a generator for hard multiparton processes in hadronic collisions," *J. High Energy Phys.*, vol. 07, p. 001, 2003.

[79] M. L. Mangano, M. Moretti, F. Piccinini, and M. Treccani, "Matching matrix elements and shower evolution for top-quark production in hadronic collisions," *J. High Energy Phys.*, vol. 01, p. 013, 2007.

[80] ATLAS collaboration, "The ATLAS experiment at the CERN large hadron collider," *JINST*, vol. 3, 2008.

[81] CMS collaboration, "The CMS experiment at the CERN LHC," *JINST*, vol. 3, 2008.

[82] LHCb collaboration, "The LHCb experiment at the LHC," *JINST*, vol. 3, 2008.

[83] ALICE collaboration, "The ALICE experiment at the CERN LHC," *JINST*, vol. 3, 2008.

[84] ATLAS collaboration, "Readiness of the ATLAS Liquid Argon Calorimeter for LHC Collisions," *Eur.Phys.J.*, vol. C70, pp. 723–753, 2010.

[85] ATLAS collaboration, "Readiness of the ATLAS Tile Calorimeter for LHC collisions," *Eur.Phys.J.*, vol. C70, pp. 1193–1236, 2010.

[86] R. Achenbach *et al.*, "The ATLAS level-1 calorimeter trigger," *JINST*, vol. 3, 2008.

[87] ATLAS Collaboration, "Performance of the ATLAS muon trigger in pp collisions at $\sqrt{s} = 8$ TeV," *Eur. Phys. J.*, vol. C75, no. 3, p. 120, 2015.

[88] "ATLAS Public Results." `http://https://twiki.cern.ch/twiki/bin/view/AtlasPublic`. Accessed: 01/08/2015.

[89] ATLAS collaboration, "Improved luminosity determination in pp collisions at sqrt(s) = 7 TeV using the ATLAS detector at the LHC," *Eur.Phys.J.*, vol. C73, no. 8, p. 2518, 2013.

[90] S. van der Meer, "Calibration of the effective beam height in the ISR," Tech. Rep. CERN-ISR-PO-68-31. ISR-PO-68-31, CERN, Geneva, 1968.

[91] C. Rubbia, "Measurement of the luminosity of p$-overlinep$ collider with a (generalized) Van der Meer Method," Tech. Rep. CERN-p$\bar{p}$-Note-38, CERN, Geneva, Nov 1977.

[92] ATLAS collaboration, "Measurement of the muon reconstruction performance of the ATLAS detector using 2011 and 2012 LHC protonproton collision data," *Eur.Phys.J.*, vol. C74, no. 11, p. 3130, 2014.

[93] ATLAS collaboration, "Measurement of the Higgs boson mass from the $H \to \gamma\gamma$ and $H \to ZZ^* \to 4\ell$ channels with the ATLAS detector using 25 fb^{-1} of pp collision data," *Phys.Rev.*, vol. D90, no. 5, p. 052004, 2014.

[94] ATLAS collaboration, "Electron reconstruction and identification efficiency measurements with the ATLAS detector using the 2011 LHC proton-proton collision data," *Eur.Phys.J.*, vol. C74, no. 7, p. 2941, 2014.

[95] "Electron efficiency measurements with the ATLAS detector using the 2012 LHC proton-proton collision data," Tech. Rep. ATLAS-CONF-2014-032, CERN, Geneva, Jun 2014.

[96] "Improved electron reconstruction in ATLAS using the Gaussian Sum Filter-based model for bremsstrahlung," Tech. Rep. ATLAS-CONF-2012-047, CERN, Geneva, May 2012.

[97] ATLAS collaboration, "Electron and photon energy calibration with the AT-LAS detector using LHC Run 1 data," *Eur.Phys.J.*, vol. C74, no. 10, p. 3071, 2014.

[98] "Expected photon performance in the ATLAS experiment," Tech. Rep. ATL-PHYS-PUB-2011-007, CERN, Geneva, Apr 2011.

[99] "Measurements of the photon identification efficiency with the ATLAS detector using 4.9 fb1 of pp collision data collected in 2011," Tech. Rep. ATLAS-CONF-2012-123, CERN, Geneva, Aug 2012.

[100] M. Cacciari, G. P. Salam, and G. Soyez, "The Anti-k(t) jet clustering algorithm," *JHEP*, vol. 0804, p. 063, 2008.

[101] "Monte Carlo Calibration and Combination of In-situ Measurements of Jet Energy Scale, Jet Energy Resolution and Jet Mass in ATLAS," Tech. Rep. ATLAS-CONF-2015-037, CERN, Geneva, Aug 2015.

[102] ATLAS collaboration, "Evidence for the spin-0 nature of the Higgs boson using ATLAS data," *Phys.Lett.*, vol. B726, pp. 120–144, 2013.

[103] CMS Collaboration, "Measurement of the properties of a Higgs boson in the four-lepton final state," *Phys.Rev.*, vol. D89, no. 9, p. 092007, 2014.

[104] G. Cowan, K. Cranmer, E. Gross, and O. Vitells, "Asymptotic formulae for likelihood-based tests of new physics," *Eur. Phys. J.*, vol. C71, p. 1554, 2011. [Erratum: Eur. Phys. J.C73,2501(2013)].

[105] "Reconstruction of collinear final-state-radiation photons in Z decays to muons in sqrts=7 TeV proton-proton collisions.," Tech. Rep. ATLAS-CONF-2012-143, CERN, Geneva, Nov 2012.

[106] K. Nikolopoulos, D. Fassouliotis, C. Kourkoumelis, and V. Polychronakos, *Discovery Potential for the Standard Model Higgs $\to ZZ^{(*)} \to 4l$ and Contributions to Muon Detection in ATLAS*. PhD thesis, Athens U., Athens, 2010. Presented on 23 Mar 2010.

[107] "Measurements of the properties of the Higgs-like boson in the four lepton decay channel with the ATLAS detector using 25 fb1 of proton-proton collision data," Tech. Rep. ATLAS-CONF-2013-013, CERN, Geneva, Mar 2013.

[108] J. Alwall, M. Herquet, F. Maltoni, O. Mattelaer, and T. Stelzer, "MadGraph 5 : Going Beyond," *JHEP*, vol. 06, p. 128, 2011.

[109] M. Pivk and F. R. Le Diberder, "SPlot: A Statistical tool to unfold data distributions," *Nucl.Instrum.Meth.*, vol. A555, pp. 356–369, 2005.

[110] K. S. Cranmer, "Kernel estimation in high-energy physics," *Comput. Phys. Commun.*, vol. 136, pp. 198–207, 2001.

[111] L. A. Piegl and W. Tiller, *The NURBS book: Monographs in visual communication*, ch. 2. Springer, 2nd ed., 1997.

[112] ATLAS and CMS collaborations, "Combined Measurement of the Higgs Boson Mass in pp Collisions at $\sqrt{s} = 7$ and 8 TeV with the ATLAS and CMS Experiments," *Phys. Rev. Lett.*, vol. 114, p. 191803, 2015.

[113] V. Khachatryan *et al.*, "Observation of the diphoton decay of the Higgs boson and measurement of its properties," *Eur. Phys. J.*, vol. C74, no. 10, p. 3076, 2014.

[114] V. Khachatryan *et al.*, "Precise determination of the mass of the Higgs boson and tests of compatibility of its couplings with the standard model predictions using proton collisions at 7 and 8 TeV," *Eur. Phys. J.*, vol. C75, no. 5, p. 212, 2015.

[115] ATLAS collaboration, "Measurements of fiducial and differential cross sections for Higgs boson production in the diphoton decay channel at $\sqrt{s} = 8$ TeV with ATLAS," *JHEP*, vol. 09, p. 112, 2014.

[116] ATLAS collaboration, "Measurements of the Total and Differential Higgs Boson Production Cross Sections Combining the $H \to \gamma\gamma$ and $H \to ZZ^* \to 4\ell$ Decay Channels at $\sqrt{s} = 8$ TeV with the ATLAS Detector," *Phys. Rev. Lett.*, vol. 115, no. 9, p. 091801, 2015.

[117] ATLAS collaboration, "ATLAS measurements of the properties of jets for boosted particle searches," *Phys. Rev.*, vol. D86, p. 072006, 2012.

[118] I. W. Stewart and F. J. Tackmann, "Theory Uncertainties for Higgs and Other Searches Using Jet Bins," *Phys. Rev.*, vol. D85, p. 034011, 2012.

[119] J. Butterworth, E. Dobson, U. Klein, B. Mellado Garcia, T. Nunnemann, J. Qian, D. Rebuzzi, and R. Tanaka, "Single Boson and Diboson Production Cross Sections in pp Collisions at sqrts=7 TeV," Tech. Rep. ATL-COM-PHYS-2010-695, CERN, Geneva, Aug 2010.

[120] "Projections for measurements of Higgs boson cross sections, branching ratios and coupling parameters with the ATLAS detector at a HL-LHC," Tech. Rep. ATL-PHYS-PUB-2013-014, CERN, Geneva, Oct 2013.

[121] "Performance assumptions based on full simulation for an upgraded ATLAS detector at a High-Luminosity LHC," Tech. Rep. ATL-PHYS-PUB-2013-009, CERN, Geneva, Sep 2013.

[122] "Updated coupling measurements of the Higgs boson with the ATLAS detector using up to 25 fb^{-1} of proton-proton collision data," Tech. Rep. ATLAS-CONF-2014-009, CERN, Geneva, Mar 2014.

[123] ATLAS collaboration, "Measurement of Higgs boson production in the diphoton decay channel in pp collisions at center-of-mass energies of 7 and 8 TeV with the ATLAS detector," *Phys. Rev.*, vol. D90, no. 11, p. 112015, 2014.

[124] ATLAS collaboration, "Observation and measurement of Higgs boson decays to WW* with the ATLAS detector," *Phys. Rev.*, vol. D92, no. 1, p. 012006, 2015.

[125] ATLAS collaboration, "Study of $(W/Z)H$ production and Higgs boson couplings using $H \to WW^*$ decays with the ATLAS detector," 2015.

[126] ATLAS collaboration, "Evidence for the Higgs-boson Yukawa coupling to tau leptons with the ATLAS detector," *JHEP*, vol. 04, p. 117, 2015.

[127] ATLAS collaboration, "Search for the $b\bar{b}$ decay of the Standard Model Higgs boson in associated $(W/Z)H$ production with the ATLAS detector," *JHEP*, vol. 01, p. 069, 2015.

[128] ATLAS collaboration, "Search for Higgs boson decays to a photon and a Z boson in pp collisions at $\sqrt{s}$=7 and 8 TeV with the ATLAS detector," *Phys. Lett.*, vol. B732, pp. 8–27, 2014.

[129] ATLAS collaboration, "Search for the Standard Model Higgs boson decay to $\mu^+\mu^-$ with the ATLAS detector," *Phys. Lett.*, vol. B738, pp. 68–86, 2014.

[130] ATLAS collaboration, "Search for $H \to \gamma\gamma$ produced in association with top quarks and constraints on the Yukawa coupling between the top quark and the Higgs boson using data taken at 7 TeV and 8 TeV with the ATLAS detector," *Phys. Lett.*, vol. B740, pp. 222–242, 2015.

[131] ATLAS collaboration, "Search for the Standard Model Higgs boson produced in association with top quarks and decaying into $b\bar{b}$ in pp collisions at $\sqrt{s} = 8$ TeV with the ATLAS detector," *Eur. Phys. J.*, vol. C75, no. 7, p. 349, 2015.

[132] ATLAS collaboration, "Search for the associated production of the Higgs boson with a top quark pair in multilepton final states with the ATLAS detector," *Phys. Lett.*, vol. B749, pp. 519–541, 2015.

[133] ATLAS collaboration, "Constraints on the off-shell Higgs boson signal strength in the high-mass ZZ and WW final states with the ATLAS detector," *Eur. Phys. J.*, vol. C75, no. 7, p. 335, 2015.

[134] N. Kauer and G. Passarino, "Inadequacy of zero-width approximation for a light Higgs boson signal," *JHEP*, vol. 1208, p. 116, 2012.

[135] F. Caola and K. Melnikov, "Constraining the Higgs boson width with ZZ production at the LHC," *Phys. Rev.*, vol. D88, p. 054024, 2013.

[136] J. M. Campbell, R. K. Ellis, and C. Williams, "Bounding the Higgs width at the LHC using full analytic results for $gg \rightarrow e^- e^+ \mu^- \mu^+$," *JHEP*, vol. 1404, p. 060, 2014.

[137] J. M. Campbell, R. K. Ellis, and C. Williams, "Bounding the Higgs width at the LHC: Complementary results from $H \rightarrow WW$," *Phys. Rev.*, vol. D89, p. 053011, 2014.

[138] J. Ellis and T. You, "Updated Global Analysis of Higgs Couplings," *JHEP*, vol. 06, p. 103, 2013.